A strain smoothing method in finite elements for structural analysis

by

Hung NGUYEN XUAN

Docteur en Sciences appliquées de l'Université de Liège
DES en Mécanique des Constructions, l'Université de Liège
Bachelier en Mathématique et Informatique, l'Université des Sciences
Naturelles de Ho Chi Minh Ville

May 05 2008

DEDICATION

for my loving parent and family

Acknowledgements

I would like to express my deep gratitude and appreciation to my supervisors, Professor Nguyen-Dang Hung and Professor Jean-François Debongnie, for his patient guidance and helpful advices throughout my research work.

I am thankful to Professor Ngo-Thanh Phong and Dr. Trinh-Anh Ngoc from Mathematics and Informatics Department for their assistance and support during my study and work at University of Natural Sciences. I would also like to thank my close friend and colleague PhD candidate Nguyen-Thoi Trung from National University of Singapore for his help-discussion and encouragement during the last time.

I would like to express my sincere acknowledgement to Dr. Stéphane Bordas from Department of Civil Engineering, University of Glasgow, Dr. Timon Rabczuk from Department of Mechanical Engineering, University of Canterbury for his assistance, insightful suggestions, and collaboration in research. I am very grateful to Professor Gui-Rong Liu from National University of Singapore for his enthusiastic support and help during my work at NUS.

I am thankful to Mrs Duong Thi Quynh Mai for her constant help during my stay in Belgium. I also wish to take this opportunity to thank all of friends and the former EMMC students for their continued support and encouragement.

Finally, my utmost gratitude is my parent and family for whose devotion and constant love that have provided me the opportunity to pursue higher education.

Abstract

This thesis further developments strain smoothing techniques in finite element methods for structural analysis. Two methods are investigated and analyzed both theoretically and numerically. The first is a smoothed finite element method (SFEM) where an assumed strain field is derived from a smoothed operator of the compatible strain field via smoothing cells in the element. The second is a nodally smoothed finite element method (N-SFEM), where an assumed strain field is evaluated using the strain smoothing in neighbouring domains connected with nodes.

For the SFEM, 2D, 3D, plate and shell problems are studied in detail. Two issues based on a selective integration and a stabilization approach for volumetric locking are considered. It is also shown that the SFEM in 2D with a single smoothing cell is equivalent to a quasi-equilibrium model.

For the N-SFEM, a priori error estimation is established and the convergence is confirmed numerically by benchmark problems. In addition, a quasi-equilibrium model is obtained and as a result a dual analysis is very promising to estimate an upper bound of the global error in finite elements.

It is also expected that two present approaches are being incorporated with the extended finite element methods to improve the discontinuous solution of fracture mechanics.

Contents

List of Figures

List of Tables

Chapter 1

Introduction

1.1 Review of finite element methods

The Finite Element Method (FEM) was first described by Turner *et al.* (1956) before its terminology was named by Clough (1960). More details for milestones of the FEM history can be found in Felippa (1995, 2001). After more than 40 years of development, the FEM has become one of the most powerful and popular tools for numerical simulations in various fields of natural science and engineering. Commercially available software packages are now widely used in engineering design of structural systems due to its versatility for solids and structures of complex geometry and its applicability for many types of non-linear problems. Theoretically, researchers are attempting to improve the performance of finite elements.

Because of drawbacks associated with high-order elements (Zienkiewicz & Taylor (2000)) which may be capable of providing excellent performance for complex problems including those involving materials with near incompressibility, low-order elements are preferable to employ in practice. Unfortunately, these elements are often too stiff and as a result the elements become sensitive to locking.

Mixed formulations, based on a variational principle, first introduced by Fraeijs De Veubeke (1965) and Herrmann (1965) were developed to handle nearly incompressible materials, see also Brezzi & Fortin (1991). The equivalence between mixed finite element methods and pure displacement approaches using selective reduced integration (SRI) techniques was pointed out by Debongnie (1977, 1978) and Malkus & Hughes (1978). Remedies were proposed by Hughes (1980) to give the B-bar method which can be derived from the three-field Hu-Washizu (1982) variational principle (in fact due to Fraeijs de Veubeke in 1951, see Felippa (2000) for details) is generalized to anisotropic and nonlinear media. Initially, the S(RI) methods were also used to address shear locking phenomenon for plate and shell structures, see Zienkiewicz *et al.* (1971); Hughes *et al.* (1977, 1978).

Although the SRI methods are more advantageous in dynamic analysis and non-linear problems because of their low computational cost, these techniques can lead to instability

due to non-physical deformation (spurious) modes. In addition, their accuracy is often poor in bending-dominated behaviours for coarse or distorted meshes. In order to eliminate the instability of SRI methods, Flanagan & Belytschko (1981) proposed the projection formulation to control the element's hourglass modes while preserving the advantage of reduced integration. The issues of hourglass control were also extended to Mindlin plates (Belytschko *et al.* (1981); Belytschko & Tsay (1983)) and nonlinear problems (Belytschko *et al.* (1985)). An enhanced assumed strain physical stabilization or variational hourglass stabilization which does not require arbitrary parameters for hourglass control was then introduced by Belytschko & Bachrach (1986); Belytschko & Bindeman (1991); Jetteur & Cescotto (1991); Belytschko & Bindeman (1993); Belytschko & Leviathan (1994); Zhu & Cescotto (1996) for solving solid, strain plane, plate and shell problems. It showed that the variational hourglass stabilization based on the three-field variational form is more advantageous to construct efficient elements. Many extensions and improvements of these procedures were given by Reese & Wriggers (2000); Puso (2000); Legay & Combescure (2003); Reese (2005). In addition the incorporation of a scaling factor with stabilization matrix for planes train was formulated by Sze (2000) and for plates by Lyly *et al.* (1993).

In Fraeijs De Veubeke (1965), a complementary energy principle is derived from the restrictive assumption of the mixed Reissner's principle by constraints of variational fields and the equilibrium finite element model is then obtained. Further developments on equilibrium elements were addressed by Nguyen-Dang (1970); Fraeijs De Veubeke *et al.* (1972); Beckers (1972); Geradin (1972)). This approach has overcome volumetric locking naturally, see e.g. Nguyen-Dang (1985). This is also very promising to solve a locking difficulty for three dimensional solids based on the recently equilibrium element by Beckers (2008).

Alternative approaches based on mixed finite element formulations have been proposed in order to improve the performance of certain elements. In these models, the displacement field is identical to that of the standard FEM model, while the strain or stress field is assumed independently of the displacement field.

On the background of assumed stress methods, the two-field mixed assumed stress element introduced and improved by Pian & Tong (1969); Lee & Pian (1978); Nguyen-Dang & Desir (1977); Pian & Sumihara (1984); Pian & Wu (1988) is helpful to alleviate locking problems on regular meshes. A series of new hybrid elements based on the optimized choices of the approximate fields has been then developed. Sze (2000) enhanced the accuracy of the Pian's element by using trapezoidal meshes and introducing a simple selective scaling parameter. Due to the restriction of classically hybrid elements that have drawbacks of fully equilibrated conditions, Wu & Cheung (1995) suggested an alternative way for the optimization of hybrid elements with the penalty-equilibrating approach in which the equilibrium equation is imposed into the individual elements directly. Also, Wu *et al.* (1998) developed an alternative equilibrium approach so-called a quasi-equilibrium model that relaxes the strict condition of the equilibrium element method and provides the lower and upper bounds of path integrals in fracture mechanics. The bound

2

theorem and dual finite elements were extended to piezoelectric crack problems, see e.g. Li *et al.* (2005); Wu & Xiao (2005). All developments of Pian et al.'s work on hybrid elements have been summarized in Pian & Wu (2006). Also, based on a particular set of hybrid finite element, Nguyen-Dang (1979, 1980b); Nguyen-Dang & Desir (1977) proposed a new element type so-called Metis elements. These elements have gained the high reliability for solving elastic, plastic analysis of structures, limit and shakedown analysis, see e.g. Nguyen-Dang *et al.* (1991); De-Saxce & Chi-Hang (1992a); De-Saxce & Chi-Hang (1992b); Nguyen-Dang & Dang (2000); Nguyen-Dang & Tran (2004); Nguyen & Nguyen-Dang (2006). In addition, the formulation of hybrid equilibrium finite elements recently proposed by Alemeida & Freitas (1991), Maunder *et al.* (1996) and Alemeida (2008) may provide an alternative approach to suppress volumetric locking.

Another famous class of mixed formulations are based on assumed strain methods, it can be classed into the Enhanced Assumed Strain (EAS) method and the Assumed Natural Strain (ANS) method:

The concept of the EAS proposed by Simo & Hughes (1986); Simo & Rifai (1990) is based on a three-field mixed approximation with the incorporation of incompatible modes (Taylor *et al.* (1976)). In this approach, the strain field is the sum of the compatible strain term and an added or enhanced strain part. As a result, a two-field mixed formulation is obtained. It was pointed out that additive variables appearing in the enhanced strain field can be eliminated at element level. The method accomplishes high accuracy and robustness and avoids locking , see e.g. Zienkiewicz & Taylor (2000). A further development on the EAS has shown in References (Andelfinger & Ramm (1993); Yeo & Lee (1996); Bischoff *et al.* (1999); Sá & Jorge (1999); Sá *et al.* (2002); Cardoso *et al.* (2006); Armero (2007); Cardoso *et al.* (2007)).

Unfortunately, in all situations, there exist many defects of the EAS methods for shear locking problems of plate and shell elements, especially if distorted meshes employed. Hence the Assumed Natural Strain (ANS) method was promoted in order to avoid these drawbacks and it is now widely applied in commercial softwares such as ANSYS, ADINA, NASTRAN, etc. The main idea of the ANS method is to approximate the compatible strains not directly from the derivatives of the displacements but at discrete collocation points in the element natural coordinates (parent element). It is derived from an engineering view rather than a convincing variational background. The variational form of the original ANS method is not clear, which was showed by Militello & Felippa (1990). The ANS technique for lower-order plate and shell elements was developed by Hughes & Tezduyar (1981); Bathe & Dvorkin (1985, 1986); Dvorkin & Bathe (1984, 1994). An alternative to the ANS method to avoid shear locking is the Discrete-Shear-Gap (DSG) method (Bletzinger *et al.* (2000)). The DSG method is in a way similar to the ANS method since it modifies the course of certain strains within the element. The main difference is the lack of collocation points that makes the DSG method independent of the order and form of the element. Additionally, the DSG method has been proposed to suppress membrane locking, see e. g. Koschnick *et al.* (2005).

The object of above review is not to be exhaustive, but to introduce the main concepts

to be revisited and used in this thesis.

1.2   A review of some meshless methods

Meshfree methods emerged as alternative numerical approaches to, among other feats, alleviate the shortcomings related to element distortion in the FEM. However, except for the case of strong-form based methods such as the point collocation method or Smooth Particle Hydrodynamics –which, unless a satisfying stabilization scheme is employed suffer from numerical isntability– meshfree methods which are based on some sort of a weak form –be it global as in the Element Free Galerkin (EFG) (Belytschko *et al.* (1994); Dolbow & Belytschko (1999)), or local as in some instances of the Meshless Local Petrov Galerkin method (Atluri & Shen (2002))– also require integration of the discretized weak form. Since the shape functions in meshfree methods are often not polynomial –for instance in methods where the shape functions are built using Moving Least Squares (MLS) (Lancaster & Salkauskas (1981))–, exact integration of the weak form is often difficult if not impossible (Dolbow & Belytschko (1999)). In practice, a very high number of Gauss points are used to decrease the integration error, and this is often sufficient in practical cases, while increasing the numerical cost of such meshfree methods. However, because of their high degree of continuity, meshfree methods are also very useful to deal with discontinuities and singularities, as shown by the recent fracture mechanics literature (Duflot (2006); Rabczuk & Belytschko (2007); Rabczuk *et al.* (2007a,b,c, 2008)).

Nodal integration in meshfree methods was proposed by Beissel & Belytschko (1996) and Bonet & Kulasegaram (1999) with the aim to eliminate background meshes for integration of the Element Free Galerkin (EFG) method. Direct nodal integration often leads to numerical instability and suboptimal convergence rates. In Chen *et al.* (2001) it was shown that the vanishing derivatives of the meshfree shape functions at the nodes are the cause of the observed instability. Lower convergence rates were shown to be due to the violation of an integration constraint (IC) by Galerkin methods. The Hellinger-Reissner variational form for stabilized conforming nodal integration in Galerkin meshfree methods is given in Sze *et al.* (2004).

A linear consistent shape function computed from moving least square approximations (Lancaster & Salkauskas (1981)) with linear basis functions does not guarantee linear completeness in meshfree method based on a Galerkin weak form, such as the EFG method. To satisfy this linear completeness, Chen and co-workers proposed a stabilized conforming nodal integration (SCNI) using a strain smoothing method (SSM) for a Galerkin mesh-free method yielding to a more efficient, accurate and convergent method. The stabilized nodal integration was then extended by (Yoo *et al.* (2004); Yvonnet *et al.* (2004); Cescotto & Li (2007)) to the natural element method (Sukumar *et al.* (1998)) for material incompressibility with no modification of the integration scheme.

In mesh-free methods with stabilized nodal integration, the entire domain is discretized into cells defined by the field nodes, such as the cells of a Voronoï diagram (Chen

et al. (2001); Yoo *et al.* (2004); Yvonnet *et al.* (2004); Cescotto & Li (2007); Wang & Chen (2007)). Integration is performed along the boundary of each cell. Based on the SCNI approach, Liu *et al* have applied this technique to formulate the linear conforming point interpolation method (LC-PIM) (Liu *et al.* (2006b); Zhang *et al.* (2007)), the linearly conforming radial point interpolation method (LC-RPIM) (Liu *et al.* (2006a)).

Although meshfree methods such as EFG obtain good accuracy and high convergence rates, the non-polynomial or usually complex approximation space increases the computational cost of numerical integration. However, recent results in computational fracture mechanics show that the EFG method treats three-dimensional crack growth problems with remarkable accuracy (Duflot (2006)), even when crack path continuity is to be enforced (Bordas *et al.* (2008b); Rabczuk *et al.* (2007c, 2008)).

1.3   Motivation

Recently, Liu *et al.* (2007a) have originated the idea of applying the stabilized conforming nodal integration into the standard FEM. The cells form a partition of the elements and domain integration is changed into line integration along the cell boundaries by the introduction of a non-local, smoothed, strain field. Liu *et al* coined this technique a Smoothed Finite Element Method (SFEM) based on the combination of strain smoothing stabilization with the FEM. The theoretical bases of the SFEM for 2D elasticity were then presented in Liu *et al.* (2007b). The SFEM has also been applied to dynamic problems for 2D solids (Dai & Liu (2007)) and the elimination of volumetric locking (Nguyen *et al.* (2007b)). Then, Liu *et al.* (2007c) have proposed a node-based smoothed finite element method (N-SFEM) in which the strain smoothing is formed in neighbouring cells connected with nodes.

Based on the idea of the SFEM and N-SFEM, this thesis aims to study and estimate the reliability of strain smoothing techniques in finite elements, and extends further its applications to more complex problems such as fracture mechanics, three dimension solid, plate and shell structures, etc. A sound variational base, its convergence properties and accuracy are investigated in detail, especially when distorted meshes are employed. The scope of strain smoothing stabilization by showing the clear advantages it brings for incompressible 2D and 3D problems. The thesis also discusses some properties related to equilibrium elements (Fraeijs De Veubeke (1965); Fraeijs De Veubeke *et al.* (1972); Beckers (1972); De-Saxce & Nguyen-Dang (1984); Debongnie *et al.* (1995, 2006); Beckers (2008)) and a priori error estimation.

More importantly, the method shown here may be an important step towards a more efficient and elegant treatment of numerical integration in the context of singular and discontinuous enriched finite element approximations. Another by-procedure is to develop stabilization schemes for partition of unity methods –for example to avoid volumetric locking and allow a simple extension of enriched finite elements to large-scale plasticity or incompressible materials, as well as multi-field extended finite elements.

1.4 Outline

The thesis is organized in nine main chapters.

Chapter 2 recalls governing equations and weak form for solids, plates and shells and introduces the basic concepts of structural analysis by finite element approximations. This chapter also defines a general formulation for a strain smoothing operator.

Chapter 3 is dedicated to a smoothed finite element method for two-dimensional problems.

Chapter 4 extends the smoothed finite element method to three-dimensional elasticity.

A smoothed finite element method for plate analysis is presented in Chapter 5.

Chapter 6 introduces a stabilized smoothed finite element method for free vibration analysis of Mindlin–Reissner plates.

A smoothed finite element method for shell analysis is addressed in Chapter 7.

Chapter 8 presents a node-based smoothed finite element method for two-dimensional elasticity and shows how a mixed approach may be derived from properties of method. A quasi-equilibrium finite element model is then proposed.

Chapter 9 closes with conclusions drawn from the present work and opens ways for further research.

1.5 Some contributions of thesis

According to the author's knowledge, the following points may be considered as the contribution of this thesis:

1) A rigorous variational framework for the SFEM based on the Hu-Washizu assumed strain variational form and an orthogonal condition at a cell level are presented. The method is applied to both compressible and incompressible linear elasticity problems. The thesis points out interesting properties on accuracy and convergence rates, the presence of incompressibility in singularities or distorted meshes, etc. It is shown that the one-cell smoothed four-noded quadrilateral finite element is equivalent to a quasi-equilibrium element and is superconvergent (rate of 2.0 in the energy norm for problems with smooth solutions), which is remarkable. e. g. Nguyen-Xuan *et al.* (2006, 2007b).

2) Strain smoothing in finite elements is further extended to 8-noded hexahedral elements. The idea behind the proposed method is similar to the two-dimensional smoothed-finite elements (SFEM). If the surfaces of the element have low curvature, the stiffness matrix is evaluated by integration on the surface of the smoothing cells. In contrast, the gradients are described in the FEM and the smoothed strains are carried out numerically using Gauss quadrature inside the smoothing cells, following an idea by Stolle & Smith (2004). Numerical results show that the SFEM performs well for analysis of 3D elastic solids. The work on the 3D SFEM was given in Bordas *et al.* (2008a); Nguyen-Xuan *et al.* (2008a).

3) A quadrilateral element with smoothed curvatures for Mindlin-Reissner plates is formulated. The curvature at each point is obtained by a non-local approximation via a

smoothing function. The bending stiffness matrix is calculated by a boundary integral along the boundaries of the smoothing elements (smoothing cells). Numerical results show that the proposed element is free of locking, robust, computational inexpensive and simultaneously very accurate. The performance of the proposed element with mesh distortion is also presented. This resulted in Nguyen-Xuan *et al.* (2008b).

4) A free vibration analysis of Mindlin – Reissner plates using the stabilized smoothed finite element method is studied. The present formula is inherited from the work on smoothed plate elements by Nguyen-Xuan *et al.* (2008b), but the accuracy of the element is increased combining a well-known stabilization technique of Lyly *et al.* (1993) into the shear terms. As a result, the shearing stiffness matrix is obtained by approximating independent interpolation functions in the natural coordinate system associated with a stabilized approach. It is found that the proposed method achieves slightly more accurate and stable results than those of the original MITC4 versions and is free of shear locking as plate thickness becomes very small. The results of this investigation were given in Nguyen-Xuan & Nguyen (2008).

5) A four-node quadrilateral shell element with smoothed membrane-bending based on Mindlin–Reissner theory is exploited. It is derived from the combination of plate bending and membrane elements. It is based on mixed interpolation where the bending and membrane stiffness matrices are calculated on the boundaries of the smoothing cells while the shear terms are approximated by independent interpolation functions in natural coordinates. The performance of the proposed shell element is confirmed by numerical tests. Since the integration is done on the element boundaries for the bending and membrane terms, the element is more accurate than the MITC4 element (Bathe & Dvorkin (1986)) for distorted meshes, see e.g. Nguyen *et al.* (2007a).

6) A node-based smoothed finite element method (N-SFEM) was recently proposed by Liu *et al.* (2007c) to enhance the computational capability for solid mechanics problems. It was shown that the N-SFEM possesses the following properties: 1) it gives an upper bound of the strain energy for fine enough meshes; 2) it is almost immune from volumetric locking; 3) it allows the use of polygonal elements with an arbitrary number of sides; 4) the result is insensitive to element distortion. The first two properties of the N-SFEM are the characteristics of equilibrium finite element approaches. Following the idea of the N-SFEM (Liu *et al.* (2007c)), this thesis shows the following theoretical aspects: 1) a nodally smoothed strain of the N-SFEM is obtained from the justification of a mixed variational principle; 2) accuracy and convergence are verified by a rigorously mathematical theory which is based on the original work of Brezzi & Fortin (1991); 3) a new link between the N-SFEM and an equilibrium finite element model based on four-node quadrilateral formulations is presented. And as a result a quasi-equilibrium element is then proposed.

Chapter 2

Overview of finite element approximations

2.1 Governing equations and weak form for solid mechanics

In what follows, a two-or three dimensional solid is described as an elastic domain Ω with a Lipschitz-continuous boundary Γ. A body force $\mathbf{b}$ acts within the domain, see Figure 2.1. The boundary Γ is split into two parts, namely $\Gamma_{\mathbf{u}}$ where Dirichlet conditions $\bar{\mathbf{u}}$ are prescribed, and $\Gamma_{\mathbf{t}}$ where Neumann conditions $\mathbf{t} = \bar{\mathbf{t}}$ are prescribed. Those two parts form a partition of the boundary Γ.
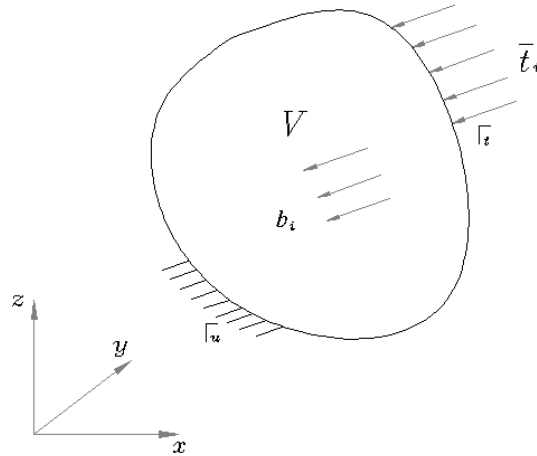
Figure 2.1: The three-dimensional model

The relations between the displacement field $\mathbf{u}$, the strain field $\boldsymbol{\varepsilon}$ and the stress field $\boldsymbol{\sigma}$ are:

1. The compatibility relations

$$\forall i, j \in 1, 2, 3 \, , \; \varepsilon_{ij} = \frac{1}{2}(u_{i,j} + u_{j,i}) \; \text{ (or } \boldsymbol{\varepsilon} = \boldsymbol{\partial} \mathbf{u}) \qquad \text{in} \qquad \Omega \tag{2.1}$$

$$u_i = \bar{u}_i \qquad \text{on} \qquad \Gamma_{\mathbf{u}} \tag{2.2}$$

2. The constitutive relations

$$\sigma_{ij} = D_{ijkl}\varepsilon_{kl} \qquad \text{in} \qquad \Omega \tag{2.3}$$

3. The equilibrium equations

$$\sigma_{ij,j} + b_i = 0 \qquad \text{in} \qquad \Omega \tag{2.4}$$

$$\sigma_{ij}n_j = \bar{t}_i \qquad \text{on} \qquad \Gamma_{\mathbf{t}} \tag{2.5}$$

where $\boldsymbol{\partial} \equiv \nabla_s$ denotes the symmetric gradient operator for the description of the strains from the displacements. Let the two spaces of kinematically admissible displacements, denoted by $\mathcal{V}$ and $\mathcal{V}_0$, respectively, be defined by

$$\mathcal{V} = \{\mathbf{u} \in (H^1(\Omega))^3, \mathbf{u} = \bar{\mathbf{u}} \qquad \text{on} \qquad \Gamma_{\mathbf{u}}\} \tag{2.6}$$

$$\mathcal{V}_0 = \{\mathbf{u} \in (H^1(\Omega))^3, \mathbf{u} = \mathbf{0} \qquad \text{on} \qquad \Gamma_{\mathbf{u}}\} \tag{2.7}$$

The space containing and strains and stresses denoted by $\mathcal{S}$ is defined by

$$\mathcal{S} = \{\boldsymbol{\varepsilon} \text{ or } \boldsymbol{\sigma} \in \{(L^2(\Omega))^6\}\} \tag{2.8}$$

Here, $H^1(\Omega)$ denotes the Sobolev space of order 1 (Debongnie (2001)). Obviously; $\mathcal{V}_0$ contains all differences between two elements of $\mathcal{V}$, that is to say, it is the linear space of admissible displacement variations. These spaces lead to a bounded energy

$$\int_\Omega D_{ijkl}\varepsilon_{ij}(\mathbf{u})\varepsilon_{kl}(\mathbf{u})d\Omega < \infty \tag{2.9}$$

From Equation (2.9), both $\mathcal{V}$ and $\mathcal{V}_0$ may be equipped with the energetical scalar product and the energy norm

$$(\mathbf{u}, \mathbf{v})_E = \int_\Omega D_{ijkl}\varepsilon_{ij}(\mathbf{u})\varepsilon_{kl}(\mathbf{v})d\Omega \tag{2.10}$$

$$\|\mathbf{u}\|_E = \left(\int_\Omega D_{ijkl}\varepsilon_{ij}(\mathbf{u})\varepsilon_{kl}(\mathbf{u})d\Omega\right)^{1/2} \tag{2.11}$$

where $\mathbf{D}$ is a bounded uniformly positive definite matrix.

The displacement approach consists in finding a displacement field $\mathbf{u} \in \mathcal{V}$ for which stresses are in equilibrium. The weak form of this condition is

$$\forall \mathbf{v} \in \mathcal{V}_0, \ \int_\Omega \mathbf{D} : \boldsymbol{\varepsilon}(\mathbf{u}) : \boldsymbol{\varepsilon}(\mathbf{v}) d\Omega = \int_\Omega \mathbf{b} \cdot \mathbf{v} d\Omega + \int_{\Gamma_{\mathbf{t}}} \bar{\mathbf{t}} \cdot \mathbf{v} d\Gamma \qquad (2.12)$$

We here recognize a variational problem of the classical form: Find $\mathbf{u} \in \mathcal{V}$ such that

$$\forall \mathbf{v} \in \mathcal{V}_0, \ a(\mathbf{u}, \mathbf{v}) = f(\mathbf{v}) \qquad (2.13)$$

where

$$a(\mathbf{u}, \mathbf{v}) = \int_\Omega \mathbf{D} : \boldsymbol{\varepsilon}(\mathbf{u}) : \boldsymbol{\varepsilon}(\mathbf{v}) d\Omega \ , \ \ f(\mathbf{v}) = \int_\Omega \mathbf{b} \cdot \mathbf{v} d\Omega + \int_{\Gamma_{\mathbf{t}}} \bar{\mathbf{t}} \cdot \mathbf{v} d\Gamma \qquad (2.14)$$

Equation (2.13) has a unique solution, from a classical inequality of Sobolev spaces. It may also be presented as the solution of the following minimization problem: Find $\mathbf{u} \in \mathcal{V}$ such that

$$\forall \mathbf{v} \in \mathcal{V}, \ \Pi_{TPE}(\mathbf{u}) = \inf \Pi_{TPE}(\mathbf{v}) \qquad (2.15)$$

where

$$\Pi_{TPE}(\mathbf{v}) = \frac{1}{2} a(\mathbf{v}, \mathbf{v}) - f(\mathbf{v}) \qquad (2.16)$$

Functional Π_{TPE} is called the *total potential energy*. Now let $\mathcal{V}^h$ be a finite-dimensional subspace of the space $\mathcal{V}$. Let $\mathcal{V}_0^h$ be the associated finite dimensional subspace of $\mathcal{V}_0$. With each approximate space $\mathcal{V}^h$ is associated the discrete problem: Find $\mathbf{u}^h \in \mathcal{V}^h$ such that

$$\forall \mathbf{v}^h \in \mathcal{V}_0^h, \ a(\mathbf{u}^h, \mathbf{v}^h) = f(\mathbf{v}^h) \qquad (2.17)$$

Equation (2.17) has a unique solution by a Galerkin method. Solution $\mathbf{u}^h$ shall be called the *discrete* solution.

Let $\{N_i\}$ be the basis functions for V^h. The finite element solution $\mathbf{u}^h$ of a displacement model, for instance, in three dimensional is expressed as follows

$$\mathbf{u}^h = \sum_{I=1}^{np} \begin{bmatrix} N_I & 0 & 0 \\ 0 & N_I & 0 \\ 0 & 0 & N_I \end{bmatrix} \mathbf{q}_I \equiv \mathbf{N}\mathbf{q} \qquad (2.18)$$

where np is the total number of nodes in the mesh, the N_I's are the shape functions of degree p associated to node I, the $\mathbf{q}_I = [u_I \ v_I \ w_I]^T$ are the degrees of freedom associated to node I. Then, the discrete strain field is

$$\boldsymbol{\varepsilon}^h = \boldsymbol{\partial}\mathbf{u}^h = \mathbf{B}\mathbf{q} \qquad (2.19)$$

where $\mathbf{B} = \boldsymbol{\partial}\mathbf{N}$ is the discretized gradient matrix.

By substituting Equation (2.18) and Equation (2.19) into Equation (2.13), we obtain a linear system for the vector of nodal unknowns $\mathbf{q}$,

$$\mathbf{Kq} = \mathbf{g} \tag{2.20}$$

with the stiffness matrix given by

$$\mathbf{K} = \int_{\Omega^h} \mathbf{B}^T \mathbf{DB} d\Omega \tag{2.21}$$

and the load vector by

$$\mathbf{g} = \int_{\Omega^h} \mathbf{N}^T \mathbf{b} d\Omega + \int_{\Gamma_{\mathbf{t}}} \mathbf{N}^T \bar{\mathbf{t}} d\Gamma \tag{2.22}$$

where Ω^h is the discretized domain associated with Ω.

2.2 A weak form for Mindlin–Reissner plates

Consider an arbitrary isotropic plate of uniform thickness t, Young's modulus E, and Poisson ratio ν with domain Ω in $\mathbb{R}^2$ stood on the mid-plane of the plate. Let w, $\boldsymbol{\beta} = (\beta_x, \beta_y)^T$ denote the transverse displacement and the rotations in the $x - z$ and $y - z$ planes (see Figure 2.2), respectively. The governing differential equations of the Mindlin-Reissner plate may be expressed as:

$$\nabla \cdot \mathbf{D}^b \boldsymbol{\kappa}(\boldsymbol{\beta}) + \lambda t \boldsymbol{\gamma} + kw + \frac{\rho t^3}{12} \omega \boldsymbol{\beta} = \mathbf{0} \quad \text{in} \quad \Omega \tag{2.23}$$

$$\lambda t \nabla \cdot \boldsymbol{\gamma} + p + \rho t \omega^2 w = 0 \quad \text{in} \quad \Omega \tag{2.24}$$

$$w = \bar{w}, \boldsymbol{\beta} = \bar{\boldsymbol{\beta}} \quad \text{on} \quad \Gamma = \partial\Omega \tag{2.25}$$

where t is the plate thickness, ρ is the mass density of the plate, $p = p(x, y)$ is the transverse loading per unit area, $\lambda = \mu E/2(1+\nu)$, $\mu = 5/6$ is the shear correction factor, k is an elastic foundation coefficient, ω is the natural frequency and $\mathbf{D}^b$ is the tensor of bending moduli, $\boldsymbol{\kappa}$ and $\boldsymbol{\gamma}$ are the bending and shear strains, respectively, defined by

$$\boldsymbol{\kappa} = \begin{bmatrix} \dfrac{\partial \beta_x}{\partial x} \\ -\dfrac{\partial \beta_y}{\partial y} \\ \dfrac{\partial \beta_x}{\partial y} - \dfrac{\partial \beta_y}{\partial x} \end{bmatrix} \equiv \frac{1}{2}\{\nabla \otimes \boldsymbol{\beta} + \boldsymbol{\beta} \otimes \nabla\} \;, \quad \boldsymbol{\gamma} = \begin{bmatrix} \dfrac{\partial w}{\partial x} + \beta_x \\ \dfrac{\partial w}{\partial y} - \beta_y \end{bmatrix} \equiv \nabla w - \boldsymbol{\beta} \tag{2.26}$$

where $\nabla = (\partial/\partial_x, \partial/\partial_y)$ is the gradient vector. Let $\mathcal{V}$ and $\mathcal{V}_0$ be defined as

$$\mathcal{V} = \{(w, \boldsymbol{\beta}) : w \in H^1(\Omega), \boldsymbol{\beta} \in H^1(\Omega)^2\} \cap \mathcal{B} \tag{2.27}$$

11
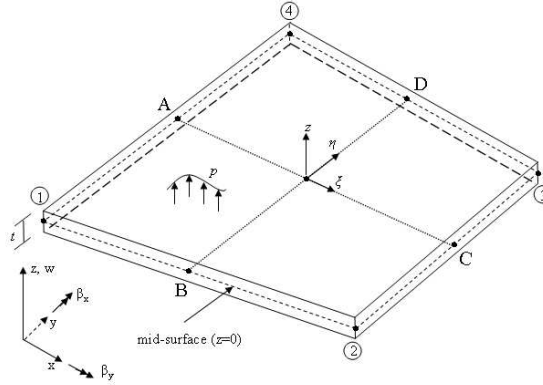
Figure 2.2: Assumption of shear deformations for quadrilateral plate element

$$\mathcal{V}_0 = \{(w, \boldsymbol{\beta}) : w \in H^1(\Omega), \boldsymbol{\beta} \in H^1(\Omega)^2 : v = 0, \boldsymbol{\eta} = \mathbf{0} \text{ on } \Gamma\} \qquad (2.28)$$

with $\mathcal{B}$ denotes a set of the essential boundary conditions and the L^2 inner products are given as

$$(w, v) = \int_\Omega wvd\Omega, \ \ (\boldsymbol{\beta}, \boldsymbol{\eta}) = \int_\Omega \boldsymbol{\beta} \cdot \boldsymbol{\eta} d\Omega, \ \ a(\boldsymbol{\beta}, \boldsymbol{\eta}) = \int_\Omega \boldsymbol{\kappa}(\boldsymbol{\beta}) : \mathbf{D}^b : \boldsymbol{\kappa}(\boldsymbol{\eta}) \, d\Omega$$

The weak form of the static equilibrium equations ($k = 0$) is: Find $(w, \boldsymbol{\beta}) \in \mathcal{V}$ such that

$$\forall(v, \boldsymbol{\eta}) \in \mathcal{V}_0, a(\boldsymbol{\beta}, \boldsymbol{\eta}) + \lambda t(\nabla w - \boldsymbol{\beta}, \nabla v - \boldsymbol{\eta}) = (p, v) \qquad (2.29)$$

and the weak form of the dynamic equilibrium equations for free vibration is: Find $\omega \in \mathbb{R}^+$ and $\mathbf{0} \neq (w, \boldsymbol{\beta}) \in \mathcal{V}$ such that

$$\forall(v, \boldsymbol{\eta}) \in \mathcal{V}_0, \ a(\boldsymbol{\beta}, \boldsymbol{\eta}) + \lambda t(\nabla w - \boldsymbol{\beta}, \nabla v - \boldsymbol{\eta}) + k(w, v) = \omega^2 \{\rho t(w, v) + \frac{1}{12}\rho t^3(\boldsymbol{\beta}, \boldsymbol{\eta})\} \qquad (2.30)$$

Assume that the bounded domain Ω is discretized into ne finite elements, $\Omega \approx \Omega^h = \bigcup_{e=1}^{ne} \Omega^e$. The finite element solution of a low-order[1] element for the Mindlin – Reissner plate is of the form (static problem): Find $(w^h, \boldsymbol{\beta}^h) \in \mathcal{V}^h$ such that

$$\forall(v, \boldsymbol{\eta}) \in \mathcal{V}_0^h, \ a(\boldsymbol{\beta}^h, \boldsymbol{\eta}) + \lambda t(\nabla w^h - \boldsymbol{\beta}^h, \nabla v - \boldsymbol{\eta}) = (p, v) \qquad (2.31)$$

and the finite element solution of the free vibration modes of a low-order element for the Mindlin – Reissner plate is of the form : Find $\omega^h \in \mathbb{R}^+$ and $\mathbf{0} \neq (w^h, \boldsymbol{\beta}^h) \in \mathcal{V}^h$ such that

$$a(\boldsymbol{\beta}^h, \boldsymbol{\eta}) + \lambda t(\nabla w^h - \boldsymbol{\beta}^h, \nabla v - \boldsymbol{\eta}) + k(w^h, v) = (\omega^h)^2 \{\rho t(w^h, v) + \frac{1}{12}\rho t^3(\boldsymbol{\beta}^h, \boldsymbol{\eta})\},$$
$$\forall(v, \boldsymbol{\eta}) \in \mathcal{V}_0^h \qquad (2.32)$$

---

[1] a 4-node quadrilateral full-integrated bilinear finite element

where the finite element spaces, $\mathcal{V}^h$ and $\mathcal{V}_0^h$, are defined by

$$\mathcal{V}^h = \{(w^h, \boldsymbol{\beta}^h) \in H^1(\Omega) \times H^1(\Omega)^2, w^h|_{\Omega^e} \in Q_1(\Omega^e), \boldsymbol{\beta}^h|_{\Omega^e} \in Q_1(\Omega^e)^2\} \cap \mathcal{B} \quad (2.33)$$

$$\mathcal{V}_0^h = \{(v^h, \boldsymbol{\eta}^h) \in H^1(\Omega) \times H^1(\Omega)^2 : v^h = 0, \boldsymbol{\eta}^h = \mathbf{0} \text{ on } \Gamma\} \quad (2.34)$$

where $Q_1(\Omega^e)$ is the set of low-order polynomials of degree less than or equal to 1 for each variable.

As already mentioned in the literature (Bathe (1996); Batoz & Dhatt (1990); Zienkiewicz & Taylor (2000)), shear locking should be eliminated as the thickness becomes small. According to the knowledge of the author, among all the improved elements, the MITC family of elements by Bathe (1996) are the more versatile ones and are widely used in commercial software. Concerning on the MITC4 element, the shear term is approximated by a reduction operator (Bathe & Dvorkin (1985)) $\mathbf{R}_h : H^1(\Omega^e)^2 \to \Gamma^h(\Omega^e)$, where Γ^h is the rotation of the linear Raviart-Thomas space:

$$\Gamma^h(\Omega^e) = \{\boldsymbol{\gamma}^h|_{\Omega^e} = \mathbf{J}^{-1}\widehat{\boldsymbol{\gamma}}^h, \widehat{\boldsymbol{\gamma}}^h = (\gamma_\xi, \gamma_\eta) \in span\{1, \eta\} \times span\{1, \xi\}\} \quad (2.35)$$

where (ξ, η) are the natural coordinates.

The shear strain can be written in the incorporation of reduction operator (Bathe & Dvorkin (1985); Thompson (2003)) as

$$\boldsymbol{\gamma}^h = \nabla w^h - \mathbf{R}_h \boldsymbol{\beta}^h = \mathbf{J}^{-1}(\widehat{\nabla} w^h - \mathbf{R}_{\widehat{\Omega}} \mathbf{J} \boldsymbol{\beta}^h) \quad (2.36)$$

where $\widehat{\nabla} w^h = (w_{,\xi}^h, w_{,\eta}^h)$ and

$$\mathbf{R}_{\widehat{\Omega}} \mathbf{J} \boldsymbol{\beta}^h = \sum_{I=1}^{4} \begin{bmatrix} \xi_I N_{I,\xi} & 0 \\ 0 & \eta_I N_{I,\eta} \end{bmatrix} \mathbf{J}_I \boldsymbol{\beta}_I \quad (2.37)$$

where $\mathbf{J}$ is the Jacobian matrix of the bilinear mapping from the bi-unit square element $\widehat{\Omega}$ into Ω^e, $\mathbf{J}_I$ is the value of Jacobian matrix at node I, and $\xi_I \in \{-1, 1, 1, -1\}, \; \eta_I \in \{-1, -1, 1, 1\}$.

Then, the discretized solutions of the static problem are stated as: Find $(w^h, \boldsymbol{\beta}^h) \in \mathcal{V}^h$ such as

$$\forall (v, \boldsymbol{\eta}) \in \mathcal{V}_0^h, \; a(\boldsymbol{\beta}^h, \boldsymbol{\eta}) + \lambda t(\nabla w^h - \mathbf{R}_h \boldsymbol{\beta}^h, \nabla v - \mathbf{R}_h \boldsymbol{\eta}) = (p, v) \quad (2.38)$$

An explicit form of the finite element solution $\mathbf{u}^h = [w \; \beta_x \; \beta_y]^T$ of a displacement model for the Mindlin-Reissner plate is rewritten as

$$\mathbf{u}^h = \sum_{I=1}^{np} \begin{bmatrix} N_I & 0 & 0 \\ 0 & 0 & N_I \\ 0 & N_I & 0 \end{bmatrix} \mathbf{q}_I \quad (2.39)$$

13

where np is the total number of element nodes, N_I are the bilinear shape functions associated to node I and $\mathbf{q}_I = [w_I \ \theta_{xI} \ \theta_{yI}]^T$ are the nodal degrees of freedom of the variables $\mathbf{u}^h = [w \ \beta_x \ \beta_y]^T$ associated to node I. Then, the discrete curvature field is

$$\boldsymbol{\kappa}^h = \mathbf{B}^b \mathbf{q} \tag{2.40}$$

where the matrix $\mathbf{B}^b$, defined below, contains the derivatives of the shape functions. The approximation of the shear strain is written as

$$\boldsymbol{\gamma}^h = \mathbf{B}^s \mathbf{q} \tag{2.41}$$

with

$$\mathbf{B}_I^s = \left[\begin{array}{ccc} N_{I,x} & 0 & N_I \\ N_{I,y} & -N_I & 0 \end{array} \right] \tag{2.42}$$

By substituting Equation (2.39) - Equation (2.41) into Equation (2.38), a linear system of equations for an individual element is obtained:

$$\mathbf{Kq} = \mathbf{g} \tag{2.43}$$

with the element stiffness matrix

$$\mathbf{K} = \int_{\Omega^e} (\mathbf{B}^b)^T \mathbf{D}^b \mathbf{B}^b d\Omega + \int_{\Omega^e} (\mathbf{B}^s)^T \mathbf{D}^s \mathbf{B}^s d\Omega \tag{2.44}$$

and the load vector

$$\mathbf{g}_I = \int_{\Omega^e} N_I \left[\begin{array}{c} p \\ 0 \\ 0 \end{array} \right] d\Omega \tag{2.45}$$

where

$$\mathbf{D}^b = \frac{Et^3}{12(1-\nu^2)} \left[\begin{array}{ccc} 1 & \nu & 0 \\ \nu & 1 & 0 \\ 0 & 0 & \frac{1-\nu}{2} \end{array} \right] \quad \mathbf{D}^s = \frac{Et\mu}{2(1+\nu)} \left[\begin{array}{cc} 1 & 0 \\ 0 & 1 \end{array} \right] \tag{2.46}$$

2.3 Formulation of flat shell quadrilateral element

Flat shell element benefits are the simplicity in their formulation and the ability to produce reliably accurate solutions while the programming implementation is not as complex as with curved shell elements, see e.g. Zienkiewicz & Taylor (2000). Nowadays, flat shell elements are being used extensively in many engineering practices with both shells and folded plate structures due to their flexibility and effectiveness. In the flat shell elements, the element stiffness matrix is often constituted by superimposing the stiffness matrix of the membrane and plate-bending elements at each node. In principle, shell elements of this type can always be defined by five degrees of freedom (DOF), three displacement DOFs and two in-plane rotation DOFs at each node. A "sixth" degree of freedom is combined with the shell normal rotation, and it may not claim to construct the theoretical

foundation. However, one encounters numerous drawbacks coming from modeling problems, programming, computation, etc. Thus the inclusion of the sixth degree of freedom is more advantageous to solve engineering practices.

Now let us consider a flat shell element in a local coordinate system $\bar{x}\bar{y}\bar{z}$ subjected simultaneously to membrane and bending actions (Figure 2.3)[1].

<center>(a)   (b)</center>
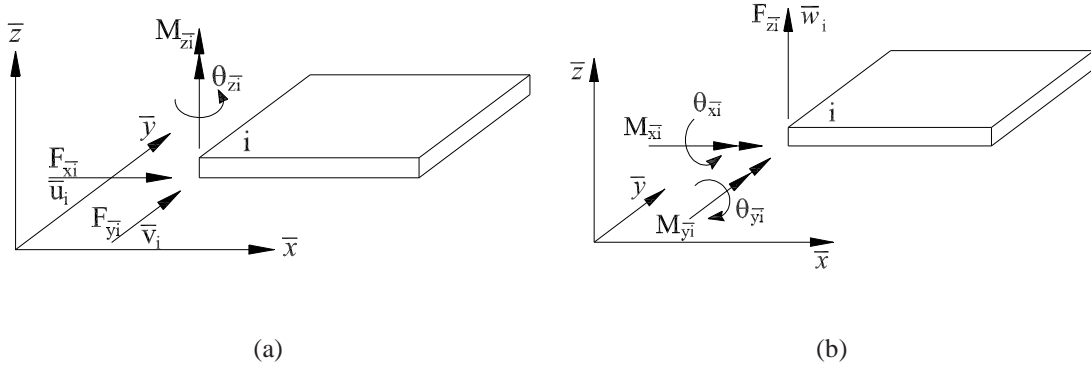
Figure 2.3: A flat shell element subject to plane membrane and bending action : (a) Plane deformations, (b) Bending deformations

The membrane strains in a local coordinate system $\bar{x}\bar{y}\bar{z}$ are given by

$$
\boldsymbol{\varepsilon}^m = \begin{bmatrix} \dfrac{\partial \bar{u}}{\partial \bar{x}} \\ \dfrac{\partial \bar{v}}{\partial \bar{y}} \\ \dfrac{\partial \bar{u}}{\partial \bar{y}} + \dfrac{\partial \bar{v}}{\partial \bar{x}} \end{bmatrix} \tag{2.47}
$$

The bending and transverse shear strains are expressed simply as in the Reissner-Mindlin plates by

$$
\boldsymbol{\kappa} = \begin{bmatrix} \dfrac{\partial \beta_{\bar{x}}}{\partial \bar{x}} \\ -\dfrac{\partial \beta_{\bar{y}}}{\partial \bar{y}} \\ \dfrac{\partial \beta_{\bar{x}}}{\partial \bar{y}} - \dfrac{\partial \beta_{\bar{y}}}{\partial \bar{x}} \end{bmatrix}, \qquad \boldsymbol{\gamma} = \left\{ \begin{array}{c} \gamma_{\bar{x}\bar{z}} \\ \gamma_{\bar{y}\bar{z}} \end{array} \right\} = \left\{ \begin{array}{c} \dfrac{\partial \bar{w}}{\partial \bar{x}} + \beta_{\bar{x}} \\ \dfrac{\partial \bar{w}}{\partial \bar{y}} - \beta_{\bar{y}} \end{array} \right\} \tag{2.48}
$$

The finite element solution $\bar{\mathbf{u}}^h = [\bar{u}\ \bar{v}\ \bar{w}\ \beta_{\bar{x}}\ \beta_{\bar{y}}\ \beta_{\bar{z}}]^T$ of a displacement model for the

---

[1]This figure is cited from Chapter 6 in Zienkiewicz & Taylor (2000)

<center>15</center>

shell is then expressed as

$$
\bar{\mathbf{u}}^h = \sum_{I=1}^{np}
\begin{bmatrix}
N_I & 0 & 0 & 0 & 0 & 0 \\
0 & N_I & 0 & 0 & 0 & 0 \\
0 & 0 & N_I & 0 & 0 & 0 \\
0 & 0 & 0 & 0 & N_I & 0 \\
0 & 0 & 0 & N_I & 0 & 0 \\
0 & 0 & 0 & 0 & 0 & 0
\end{bmatrix}
\bar{\mathbf{q}}_I
\tag{2.49}
$$

where np is the total number of element nodes, N_I are the bilinear shape functions associated to node I and $\bar{\mathbf{q}} = [\bar{u}_I \ \bar{v}_I \ \bar{w}_I \ \theta_{\bar{x}_I} \ \theta_{\bar{y}_I} \ \theta_{\bar{z}_I}]^T$ are the nodal degrees of freedom of the variables $\bar{\mathbf{u}}^h$ associated to node I in local coordinates.

The membrane deformation, the approximation of the strain field is given by

$$
\boldsymbol{\varepsilon}^m = \sum_{I=1}^{4} \mathbf{B}_I^m \bar{\mathbf{q}}_I \equiv \mathbf{B}^m \bar{\mathbf{q}}
\tag{2.50}
$$

where

$$
\mathbf{B}_I^m =
\begin{bmatrix}
N_{I,\bar{x}} & 0 & 0 & 0 & 0 & 0 \\
0 & N_{I,\bar{y}} & 0 & 0 & 0 & 0 \\
N_{I,\bar{y}} & N_{I,\bar{x}} & 0 & 0 & 0 & 0
\end{bmatrix}
\tag{2.51}
$$

The discrete curvature field is

$$
\boldsymbol{\kappa} = \sum_{I=1}^{4} \mathbf{B}_I^b \bar{\mathbf{q}}_I \equiv \mathbf{B}^b \bar{\mathbf{q}}
\tag{2.52}
$$

where

$$
\mathbf{B}_I^b =
\begin{bmatrix}
0 & 0 & 0 & 0 & N_{I,\bar{x}} & 0 \\
0 & 0 & 0 & -N_{I,\bar{x}} & 0 & 0 \\
0 & 0 & 0 & -N_{I,\bar{x}} & N_{I,\bar{y}} & 0
\end{bmatrix}
\tag{2.53}
$$

The approximation of the shear strain is written as

$$
\boldsymbol{\gamma} = \sum_{I=1}^{4} \mathbf{B}_I^s \bar{\mathbf{q}}_I = \mathbf{B}^s \bar{\mathbf{q}}
\tag{2.54}
$$

with

$$
\mathbf{B}_I^s =
\begin{bmatrix}
0 & 0 & N_{I,\bar{x}} & 0 & N_I & 0 \\
0 & 0 & N_{I,\bar{y}} & -N_I & 0 & 0
\end{bmatrix}
\tag{2.55}
$$

The nodal forces is now defined by

$$
\bar{\mathbf{g}} = \begin{bmatrix} F_{\bar{x}_I} & F_{\bar{y}_I} & F_{\bar{z}_I} & M_{\bar{x}_I} & F_{\bar{y}_I} & M_{\bar{z}_I} \end{bmatrix}
\tag{2.56}
$$

The stiffness matrix for *m*embrane and *p*late elements is of the form

$$
\mathbf{k}^m = \int_{\Omega^e} (\mathbf{B}^m)^T \mathbf{D}^m \mathbf{B}^m d\Omega, \ \mathbf{k}^p = \int_{\Omega^e} (\mathbf{B}^b)^T \mathbf{D}^b \mathbf{B}^b d\Omega + \int_{\Omega^e} (\mathbf{B}^s)^T \mathbf{D}^s \mathbf{B}^s d\Omega
\tag{2.57}
$$

where the membrane material matrix is

$$\mathbf{D}^m = \frac{Et}{(1-\nu^2)} \begin{bmatrix} 1 & \nu & 0 \\ \nu & 1 & 0 \\ 0 & 0 & \frac{1-\nu}{2} \end{bmatrix} \tag{2.58}$$

The element stiffness matrix at each node i can now be made up for the following submatrices

$$\bar{\mathbf{k}}_I^e = \begin{bmatrix} [\mathbf{k}^m]_{2\times2} & \mathbf{0}_{2\times3} & 0 \\ \mathbf{0}_{3\times2} & [\mathbf{k}^p]_{3\times3} & 0 \\ 0 & 0 & 0 \end{bmatrix} \tag{2.59}$$

It is clear that the element stiffness matrix at each node I contains zero values of the stiffness corresponding to an additional degree of freedom, $\theta_{\bar{z}_I}$, combined with it a fictitious couple $M_{\bar{z}_I}$. $\theta_{\bar{z}}$ is sometimes called a *drilling* degree of freedom, see e.g. Zienkiewicz & Taylor (2000). The zero stiffness matrix corresponding to $\theta_{\bar{z}}$ can causes the singularity in global stiffness matrix when all the elements meeting at a node are coplanar. To deal with this difficulty, we adopt the simplest approach given in Zienkiewicz & Taylor (2000) to be inserting an arbitrary stiffness coefficient, $\bar{k}_{\theta_{\bar{z}}}$ at the additional degree of freedom $\theta_{\bar{z}_I}$ only and one writes

$$\bar{k}_{\theta_{\bar{z}}}\theta_{\bar{z}_I} = 0 \tag{2.60}$$

Numerously various approaches to estimate and improve the performance of the element with drilling degrees of freedom have published the literature, e.g. Zienkiewicz & Taylor (2000);Cook *et al.* (2001). In this context, the arbitrary stiffness coefficient $\bar{k}_{\theta_{\bar{z}}}$ is chosen to be 10^{-3} times the maximum diagonal value of the element stiffness matrix, see e.g Kansara (2004). Thus the nodal stiffness matrix in Equation (2.59) can be expressed as,

$$\bar{\mathbf{k}}_I^e = \begin{bmatrix} [\mathbf{k}^m]_{2\times2} & \mathbf{0}_{2\times3} & 0 \\ \mathbf{0}_{3\times2} & [\mathbf{k}^p]_{3\times3} & 0 \\ 0 & 0 & 10^{-3}\max(\bar{\mathbf{k}}_{i,i}^e) \end{bmatrix} \tag{2.61}$$

where $\mathbf{k}^e$ is the shell element stiffness matrix before inserting $\bar{k}_{\theta_{\bar{z}}}$.
The transformation between global coordinates xyz and local coordinates $\bar{x}\bar{y}\bar{z}$ is required to generate the local element stiffness matrix in the local coordinate system. The matrix $\mathbf{T}$ transforms the global degrees of freedom into the local degrees of freedom:

$$\bar{\mathbf{q}} = \mathbf{T}\mathbf{q} \tag{2.62}$$

$\mathbf{T}$ consists of direction cosines between the global and local coordinate systems. At each node, the relation between the local and global degrees of freedom is expressed as

$$\begin{Bmatrix} \bar{u} \\ \bar{v} \\ \bar{w} \\ \theta_{\bar{x}} \\ \theta_{\bar{y}} \\ \theta_{\bar{z}} \end{Bmatrix} = \begin{bmatrix} l_{11} & l_{12} & l_{13} & 0 & 0 & 0 \\ l_{21} & l_{22} & l_{23} & 0 & 0 & 0 \\ l_{31} & l_{32} & l_{33} & 0 & 0 & 0 \\ 0 & 0 & 0 & l_{11} & l_{12} & l_{13} \\ 0 & 0 & 0 & l_{11} & l_{12} & l_{13} \\ 0 & 0 & 0 & l_{11} & l_{12} & l_{13} \end{bmatrix} \begin{Bmatrix} u \\ v \\ w \\ \theta_x \\ \theta_y \\ \theta_z \end{Bmatrix} \tag{2.63}$$

17

where l_{ij} is the direction cosine between the local axis $\bar{x}_i$ and the global axis x_j. The transformation matrix for our quadrilateral shell element is given by

$$\mathbf{T} = \begin{bmatrix} \mathbf{T}_d & 0 & 0 & 0 \\ 0 & \mathbf{T}_d & 0 & 0 \\ 0 & 0 & \mathbf{T}_d & 0 \\ 0 & 0 & 0 & \mathbf{T}_d \end{bmatrix} \tag{2.64}$$

where the matrix $\mathbf{T}_d$ is that used in Equation (2.64) of size 6×6. The transformation of the element stiffness matrix from the local to the global coordinate system is given by

$$\mathbf{K} = \mathbf{T}^T \bar{\mathbf{k}}^e \mathbf{T} \tag{2.65}$$

The element stiffness matrix $\mathbf{K}$ is symmetric and positive semi-definite. In Chapter 8, we will introduce the incorporation of a stabilized integration for a quadrilateral shell element and show a convenient approach for shell analysis. According to flat shell formulation aforementioned, the difficulty of transverse shear locking can be eliminated by the independent interpolation of the shear strains in the natural coordinate system (Bathe & Dvorkin (1985)). Consequently, Equation (2.36) provides the way to avoid the transverse shear locking when the shell thickness becomes small.

2.4 The smoothing operator

The smoothed strain method was proposed by Chen *et al.* (2001). A strain smoothing stabilization is created to compute the nodal strain as the divergence of a spatial average of the strain field. This strain smoothing avoids evaluating derivatives of mesh-free shape functions at nodes and thus eliminates defective modes. The motivation of this work is to develop the strain smoothing approach for the FEM. The method developed here can be seen as a stabilized conforming nodal integration method, as in Galerkin mesh-free methods applied to the finite element method. The smooth strain field at an arbitrary point $\mathbf{x}_C$[1] is written as

$$\tilde{\varepsilon}_{ij}^h(\mathbf{x}_C) = \int_{\Omega^h} \varepsilon_{ij}^h(\mathbf{x}) \Phi(\mathbf{x} - \mathbf{x}_C) d\Omega \tag{2.66}$$

where Φ is a smoothing function that generally satisfies the following properties (Yoo *et al.* (2004))

$$\Phi \geq 0 \qquad \text{and} \qquad \int_{\Omega^h} \Phi d\Omega = 1 \tag{2.67}$$

By expanding ε^h into a Taylor series about point $\mathbf{x}_C$,
$$\varepsilon^h(\mathbf{x}) = \varepsilon^h(\mathbf{x}_C) + \nabla \varepsilon^h(\mathbf{x}_C) \cdot (\mathbf{x} - \mathbf{x}_C)$$

$$+ \frac{1}{2} \nabla \otimes \nabla \varepsilon^h(\mathbf{x}_C) : (\mathbf{x} - \mathbf{x}_C) \otimes (\mathbf{x} - \mathbf{x}_C) + \mathcal{O}(\|\mathbf{x} - \mathbf{x}_C\|)^3 \tag{2.68}$$

---

[1] assumed that there exists $\mathbf{x}_C$ such that ε^h is differentiable in its vicinity

Substituting Equation (2.68) into Equation (2.66) and using Equation (2.67), we obtain

$$\tilde{\varepsilon}^h(\mathbf{x}_C) = \varepsilon^h(\mathbf{x}_C) + \nabla\varepsilon^h(\mathbf{x}_C) \cdot \int_{\Omega^h} (\mathbf{x} - \mathbf{x}_C)\Phi(\mathbf{x} - \mathbf{x}_C)d\Omega$$

$$+\frac{1}{2}\nabla \otimes \nabla\varepsilon^h(\mathbf{x}_C) : \int_{\Omega^h} (\mathbf{x} - \mathbf{x}_C) \otimes (\mathbf{x} - \mathbf{x}_C)\Phi(\mathbf{x} - \mathbf{x}_C)d\Omega + \mathcal{O}(\|\mathbf{x} - \mathbf{x}_C\|)^3 \quad (2.69)$$

Equation (2.69) states that the smoothed strain field is defined through the compatibility equations (2.1) and several terms of higher order in the Taylor series. For simplicity, Φ is assumed to be a step function (Chen *et al.* (2001);Liu *et al.* (2007a)) defined by

$$\Phi(\mathbf{x} - \mathbf{x}_C) = \begin{cases} 1/V_C, \mathbf{x} \in \Omega_C \\ 0, \mathbf{x} \notin \Omega_C \end{cases} \quad (2.70)$$

where V_C is the volume of the smoothing 3D cell (using the are A_C for the smoothing 2D cell), $\Omega_C \subset \Omega^e \subset \Omega^h$, as will be shown in next chapter.

Introducing Equation (2.70) into Equation (2.69) for each Ω_C leads to

$$\tilde{\varepsilon}^h(\mathbf{x}_C) = \varepsilon^h(\mathbf{x}_C) + \hat{\varepsilon}^h(\mathbf{x}_C) + \mathcal{O}(\|\mathbf{x} - \mathbf{x}_C\|)^3 \quad (2.71)$$

where

$$\hat{\varepsilon}^h(\mathbf{x}_C) = \frac{\nabla\varepsilon^h(\mathbf{x}_C)}{V_C} \cdot \int_{\Omega_C} (\mathbf{x} - \mathbf{x}_C)d\Omega + \frac{1}{2}\nabla \otimes \nabla\varepsilon^h(\mathbf{x}_C) : \int_{\Omega_C} (\mathbf{x} - \mathbf{x}_C) \otimes (\mathbf{x} - \mathbf{x}_C)d\Omega$$
$$(2.72)$$

can be referred as an *enhanced part* of the strain field (Simo & Hughes (1986); Simo & Rifai (1990)), the enhanced strain field being obtained through the above Taylor series decomposition.

For a four-node quadrilateral finite element (Q4) or an eight-node hexahedral element (H8), the error term in the above Taylor series vanishes and Equation (2.71) becomes

$$\forall \mathbf{x}_C \in \Omega_C, \ \tilde{\varepsilon}^h(\mathbf{x}_C) = \varepsilon^h(\mathbf{x}_C) + \hat{\varepsilon}^h(\mathbf{x}_C) \quad (2.73)$$

Thus we showed that the smoothed strain field for the (Q4) or (H8) elements is sum of two terms; one is the strain field ε^h satisfied the compatibility equation and the other is $\hat{\varepsilon}^h$ that it can be called an enhanced part of the compatibility strain, ε^h.

Remark: If the displacement field is approximated by a linear function such as the case for 3-node triangular or tetrahedral elements, the term $\hat{\varepsilon}^h$ in Equation (2.73) equals zero:

$$\hat{\varepsilon}^h(\mathbf{x}_C) = \mathbf{0} \quad (2.74)$$

The smoothed strain is therefore identical to the compatible strain. Additionally, the SFEM solution coincides with that of the FEM for linear element types.
The next chapters, focus on the smoothing strain technique for four-node quadrilateral finite elements (Q4) or an eight-node hexahedral elements (H8). To follow the original contribution by Liu *et al.* (2007a), the SFEM will be used for most chapters in thesis.

Chapter 3

The smoothed finite element methods 2D elastic problems: properties, accuracy and convergence

3.1 Introduction

In the Finite Element Method (FEM), a crucial point is the exact integration of the weak form –variational principle– leading to the stiffness matrix and residual vector. In the case of curved boundaries, high degree polynomial approximations or enriched approximations with non-polynomial special functions, numerical integration becomes a nontrivial task, and a computationally expensive burden. For mapped, isoparametric elements, Gauss-Lobatto-Legendre quadrature –widely referred to as Gauss quadrature– can lead to integration error. In the isoparametric theory of mapped element, a one-to-one and onto coordinate transformation between the physical and natural coordinates of each element has to be established, which is only possible for elements with convex boundaries. Consequently, severely distorted meshes cannot be solved accurately if the stiffness matrix is obtained by standard Gauss quadrature procedures.

In order to enhance the accuracy of numerical solutions for irregular meshes, Liu *et al.* (2007a) recently proposed a smoothed finite element method (SFEM) for 2D mechanics problems by incorporating the standard FEM technology and the strain smoothing technique of mesh-free methods (Chen *et al.* (2001)). It was found that the SFEM is accurate, stable and effective. The properties of the SFEM are studied in detail by Liu *et al.* (2007b).

Purpose of this chapter is to present the recent contribution on the convergence and stability of the smoothed finite element method (SFEM). Based on the idea of the SFEM in Liu *et al.* (2007a,b), a sound mathematical basis, proving that its solution is comprised between the standard finite element and a quasi-equilibrium finite element solution is revisited. It also is found that one of the SFEM elements is equivalent to a hybrid model. Through numerical studies, a particular smoothed element is shown to be volumetric locking free, leading to superconvergent dual quantities and performing particularly well when

the solution is rough or singular. Moreover, the convergence of the method is studied for distorted meshes in detail.

3.2 Meshfree methods and integration constraints

In mesh-free methods based on nodal integration, the convergence of the solution approximated by linear complete shape functions requires the following integration constraint (IC) to be satisfied (Chen *et al.* (2001))

$$\int_{\Omega^h} \mathbf{B}_I^T(\mathbf{x})d\Omega = \int_{\Gamma^h} \mathbf{n}^T N_I(\mathbf{x})d\Gamma \tag{3.1}$$

where $\mathbf{B}_I$ is the standard gradient matrix associated with shape function N_I such as
-For 2 dimensional

$$\mathbf{B}_I = \begin{bmatrix} N_{I,x} & 0 \\ 0 & N_{I,y} \\ N_{I,y} & N_{I,x} \end{bmatrix}, \quad \mathbf{n}^T = \begin{bmatrix} n_x & 0 \\ 0 & n_y \\ n_y & n_x \end{bmatrix} \tag{3.2}$$

-For 3 dimensional

$$\mathbf{B}_I = \begin{bmatrix} N_{I,x} & 0 & 0 \\ 0 & N_{I,y} & 0 \\ 0 & 0 & N_{I,z} \\ N_{I,y} & N_{I,x} & 0 \\ 0 & N_{I,z} & N_{I,y} \\ N_{I,z} & 0 & N_{I,x} \end{bmatrix}, \quad \mathbf{n}^T = \begin{bmatrix} n_x & 0 & 0 \\ 0 & n_y & 0 \\ 0 & 0 & n_z \\ n_y & n_x & 0 \\ 0 & n_z & n_y \\ n_z & 0 & n_y \end{bmatrix} \tag{3.3}$$

The IC criteria comes from the equilibrium of the internal and external forces of the Galerkin approximation assuming linear completeness (Chen *et al.* (2001) and Yoo *et al.* (2004)). This is similar to the linear consistency in the constant stress patch test in FEM.

By associating the conventional FEM and the strain smoothing method developed for mesh-free nodal integration, Liu *et al.* (2007a) coined the method obtained the smoothed finite element method (SFEM) for two-dimensional problems, the idea being as follows: (1) elements are present, as in the FEM, but may be of arbitrary shapes, such as polygons (2) the Galerkin weak form is obtained by writing a mixed variational principle based on an assumed strain field in Simo & Hughes (1986) and integration is carried out either on the elements themselves (this is the one-cell version of the method), or over smoothing cells, forming a partition of the elements (3) apply the strain smoothing method on each smoothing cell to normalize local strain and then calculate the stiffness matrix.

For instance in 2D problems, there are several choices for the smoothing function. For constant smoothing functions, using Gauss theorem, the surface integration over each smoothing cell becomes a line integration along its boundaries, and consequently, it is unnecessary to compute the gradient of the shape functions to obtain the strains and the

element stiffness matrix. We use 1D Gauss integration scheme on all cell edges. The flexibility of the proposed method allows constructing four-node elements with obtuse interior angles.

3.3 The 4-node quadrilateral element with the integration cells

3.3.1 The stiffness matrix formulation

By substituting Equation (2.70) into Equation (2.66), and applying the divergence theorem, we obtain

$$\tilde{\varepsilon}_{ij}^h(\mathbf{x}_C) = \frac{1}{2A_C} \int_{\Omega_C} \left(\frac{\partial u_i^h}{\partial x_j} + \frac{\partial u_j^h}{\partial x_i} \right) d\Omega = \frac{1}{2A_C} \int_{\Gamma_C} (u_i^h n_j + u_j^h n_i) d\Gamma \qquad (3.4)$$

Next, we consider an arbitrary smoothing cell, $\Omega_C \subset \Omega^e \subset \Omega^h$ illustrated in Figure 3.1
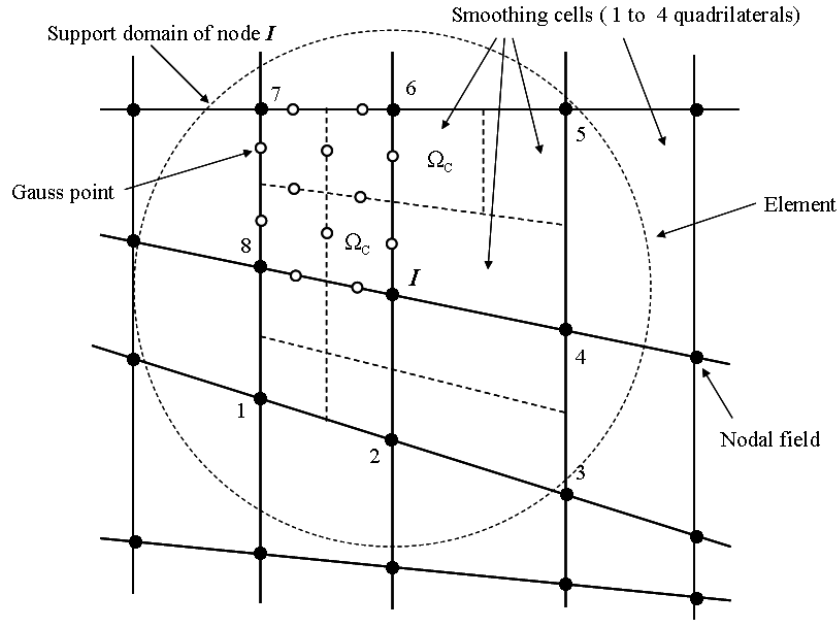
Figure 3.1: Example of finite element meshes and smoothing cells in 2D

with boundary $\Gamma_C = \bigcup_{b=1}^{nb} \Gamma_C^b$, where Γ_C^b is the boundary lines of Ω_C, and nb is the total number of edges of each smoothing cell (Liu *et al.* (2007a)). The relationship between the strain field and the nodal displacement is modified by replacing $\mathbf{B}$ into $\tilde{\mathbf{B}}$ in Equation (2.19) and

$$\tilde{\varepsilon}^h = \tilde{\mathbf{B}}\mathbf{q} \qquad (3.5)$$

The smoothed element stiffness matrix then is computed by

$$\tilde{\mathbf{K}}^e = \sum_{C=1}^{nc} \int_{\Omega_C} \tilde{\mathbf{B}}^T \mathbf{D} \tilde{\mathbf{B}} d\Omega = \sum_{C=1}^{nc} \tilde{\mathbf{B}}^T \mathbf{D} \tilde{\mathbf{B}} A_C \tag{3.6}$$

where nc is the number of the smoothing cells of the element (see Figure 3.1).
Here, the integrands are constant over each Ω_C and the non-local strain displacement matrix reads

$$\tilde{\mathbf{B}}_{CI} = \frac{1}{A_C} \int_{\Gamma_C} \begin{pmatrix} N_I n_x & 0 \\ 0 & N_I n_y \\ N_I n_y & N_I n_x \end{pmatrix} d\Gamma = \frac{1}{A_C} \int_{\Gamma_C} \mathbf{n}^T N_I(\mathbf{x}) d\Gamma \quad \forall I = 1, 2, 3, 4 \tag{3.7}$$

Introducing Equation (3.7) into Equation (3.6), the smoothed element stiffness matrix is evaluated along boundary of the smoothing cells of the element:

$$\tilde{\mathbf{K}}^e = \sum_{C=1}^{nc} \frac{1}{A_C} \left(\int_{\Gamma_C} \mathbf{n}^T \mathbf{N}(\mathbf{x}) dS \right)^T \mathbf{D} \left(\int_{\Gamma_C} \mathbf{n}^T \mathbf{N}(\mathbf{x}) d\Gamma \right) \tag{3.8}$$

From Equation (3.7), we can use Gauss points for line integration along with each segment of Γ_C^b. In approximating bilinear fields, if the shape function is linear on each segment of a cell's boundary, one Gauss point is sufficient for an exact integration.

$$\tilde{\mathbf{B}}_{CI}(\mathbf{x}_C) = \frac{1}{A_C} \sum_{b=1}^{nb} \begin{pmatrix} N_I(\mathbf{x}_b^G) n_x & 0 \\ 0 & N_I(\mathbf{x}_b^G) n_y \\ N_I(\mathbf{x}_b^G) n_y & N_I(\mathbf{x}_b^G) n_x \end{pmatrix} l_b^C \tag{3.9}$$

where $\mathbf{x}_b^G$ and l_b^C are the midpoint (Gauss point) and the length of Γ_b^C, respectively.
It is essential to remark that the smoothed strain field, $\tilde{\varepsilon}^h$, as defined in Equation (3.5) does not satisfy the compatibility relations with the displacement field at all points in the discretized domain. Therefore, the formula (2.17) is not suitable to enforce a smoothed strain field. Although the strain smoothing field is estimated from the local strain by integration of a function of the displacement field, we can consider the smooth, non-local strain, and the local strain as two independent fields. The local strain is obtained from the displacement field, $\mathbf{u}^h$, the non-local strain field can be viewed as an assumed strain field, $\tilde{\varepsilon}^h$. Thus a two-field variational principle is suitable for this approximation.

3.3.2 Cell-wise selective integration in SFEM

The element is subdivided into nc non-overlapping sub-domains also called smoothing cells. Figure 3.2 is the example of such a division with nc = 1, 2, 3 and 4 corresponding to SC1Q4, SC2Q4, SC3Q4 and SC4Q4 elements. Then the strain is smoothed over each sub-cell. As shown in Section 3.5, choosing a single subcell yields an element which is superconvergent in the H1 norm, and insensitive to volumetric locking while the locking

reappears for $nc > 1$. To overcome this drawback, we implement a method in which an arbitrarily high number of smoothing cells can be used to write the volumetric part of the strain tensor, while the deviatoric strains are written in terms of a single subcell smoothing. The method may be coined a stabilized method with selective cell-wise strain smoothing. The smoothed stiffness matrix is built as follows

- Using $nc > 1$ subcells to evaluate the deviatoric term

- Using one single subcell to calculate the volumetric term

This leads to the following elemental stiffness matrix with smoothed strains

$$\tilde{\mathbf{K}}^e = \mu \sum_{C=1}^{nc} \tilde{\mathbf{B}}_C^T \mathbf{D}_{dev} \tilde{\mathbf{B}}_C A_C + K \tilde{\mathbf{B}}_e^T \mathbf{D}_\lambda \tilde{\mathbf{B}}_e A^e \tag{3.10}$$

where

$$\tilde{\mathbf{B}}_e = \frac{1}{A^e} \int_{\Gamma^e} \mathbf{n}^T \mathbf{N}(\mathbf{x}) d\Gamma, \mathbf{D}_{dev} = \frac{1}{3} \begin{bmatrix} 4 & -2 & 0 \\ -2 & 4 & 0 \\ 0 & 0 & 3 \end{bmatrix}, \mathbf{D}_\lambda = \begin{bmatrix} 1 & 1 & 0 \\ 1 & 1 & 0 \\ 0 & 0 & 0 \end{bmatrix} \tag{3.11}$$

$\mu \mathbf{D}_{dev}$ and $K \mathbf{D}_\lambda$ are the deviatoric projection and the volumetric projection of the elastic matrix $\mathbf{D}$, respectively, μ is the shear modulus, K is the bulk modulus defined by $K = E/3(1 - 2\nu)$ and A^e is the area of the element, Ω^e.
Using the one-subcell formulation for the volumetric part of the strain field and multiple subcell formulations for the deviatoric part yields multiple-subcell elements which are not subject to locking (Nguyen *et al.* (2007b); Nguyen-Xuan *et al.* (2006, 2007a)).

3.3.3   Notations

The four node quadrilateral (Q4) with association of the smoothing strain technique for k subcells is denoted by the $SCkQ4$ element –for Smoothed k subcell 4 node quadrilateral. For instance, we will refer a lot to the case where only one subcell is used to integrate the Q4 element: the $SC1Q4$ element.

3.4   A three field variational principle

The three field variational principle given by Washizu (1982) is a possible start for constructing the variational base for the proposed method. The Hu–Washizu functional for an individual element is of the form

$$\Pi_{HW}^e(\mathbf{u}, \tilde{\boldsymbol{\varepsilon}}, \boldsymbol{\sigma}) = \frac{1}{2} \int_{\Omega^e} (\mathbf{D} : \tilde{\boldsymbol{\varepsilon}}) : \tilde{\boldsymbol{\varepsilon}} d\Omega - \int_{\Omega^e} \boldsymbol{\sigma} : (\tilde{\boldsymbol{\varepsilon}} - \boldsymbol{\varepsilon}) d\Omega - \int_{\Omega} \mathbf{b} \cdot \mathbf{u} d\Omega - \int_{\Gamma_{\mathbf{t}}} \bar{\mathbf{t}} \cdot \mathbf{v} d\Gamma \tag{3.12}$$

where $\mathbf{u} \in \mathcal{V}^h$, $\tilde{\boldsymbol{\varepsilon}} \in \mathcal{S}$ and $\boldsymbol{\sigma} \in \mathcal{S}$. For readability, we define, for all admissible $\mathbf{u}$, $f(\mathbf{u}) = \int_\Omega \mathbf{b} \cdot \mathbf{u} d\Omega - \int_{\Gamma_\mathbf{t}} \bar{\mathbf{t}} \cdot \mathbf{v} d\Gamma$, and, substituting Equation (2.73) into the second term of Equation (3.12) yields

$$\Pi^e_{HW}(\mathbf{u}, \tilde{\boldsymbol{\varepsilon}}, \boldsymbol{\sigma}) = \frac{1}{2} \int_{\Omega^e} (\mathbf{D} : \tilde{\boldsymbol{\varepsilon}}) : \tilde{\boldsymbol{\varepsilon}} d\Omega - \int_{\Omega^e} \boldsymbol{\sigma} : \hat{\boldsymbol{\varepsilon}} d\Omega - f(\mathbf{u}) \qquad (3.13)$$

In Simo & Hughes (1986); Simo & Rifai (1990), an enhanced strain field, $\hat{\boldsymbol{\varepsilon}}$, that satisfies the orthogonality condition with the stress field is constructed:

$$\int_{\Omega^e} \boldsymbol{\sigma} : \hat{\boldsymbol{\varepsilon}} d\Omega = 0 \qquad (3.14)$$

With the orthogonality condition in Equation (3.14), Simo & Hughes (1986) proposed an assumed strain variational principle for two fields:

$$\Pi^e_{SH}(\mathbf{u}, \tilde{\boldsymbol{\varepsilon}}) = \frac{1}{2} \int_{\Omega^e} (\mathbf{D} : \tilde{\boldsymbol{\varepsilon}}) : \tilde{\boldsymbol{\varepsilon}} d\Omega - f(\mathbf{u}) \qquad (3.15)$$

The purpose of the following is to construct an SFEM variational form as follows:

$$\Pi^e_{SFEM}(\mathbf{u}, \tilde{\boldsymbol{\varepsilon}}) = \frac{1}{2} \sum_{ic=1}^{nc} \int_{\Omega^e_{ic}} (\mathbf{D} : \tilde{\boldsymbol{\varepsilon}}_{ic}) : \tilde{\boldsymbol{\varepsilon}}_{ic} d\Omega - f(\mathbf{u}) \qquad (3.16)$$

where

$$\tilde{\boldsymbol{\varepsilon}}_{ic} = \frac{1}{A_{ic}} \int_{\Omega^e_{ic}} \boldsymbol{\varepsilon}(\mathbf{x}) d\Omega^e_{ic} \text{ and } A^e = \sum_{ic=1}^{nc} A_{ic} \qquad (3.17)$$

with A_{ic} the area of the smoothing cell, Ω^e_{ic}.

In this context, the stress field $\boldsymbol{\sigma}$ is expressed through the stress-strain relation as $\boldsymbol{\sigma} = \mathbf{D} : \tilde{\boldsymbol{\varepsilon}}$. To obtain the variational principle (3.16), we need to find a strict condition on the smoothing cell, Ω_C such that the orthogonality condition (3.14) is satisfied. Partitioning the element into nc sub-cells such that the sub-cells are not overlapping and form a partition of the element Ω^e, $\Omega^e = \bigcup_{ic=1}^{nc} \Omega^e_{ic}$, we consider the orthogonality condition:

$$\int_{\Omega^e} \boldsymbol{\sigma} : \hat{\boldsymbol{\varepsilon}} d\Omega = \sum_{ic=1}^{nc} \int_{\Omega^e_{ic}} (\mathbf{D} : \tilde{\boldsymbol{\varepsilon}}) : (\tilde{\boldsymbol{\varepsilon}} - \boldsymbol{\varepsilon}) d\Omega^e_{ic}$$

$$= \sum_{ic=1}^{nc} \int_{\Omega^e_{ic}} (\mathbf{D} : \tilde{\boldsymbol{\varepsilon}}) : \left(\frac{1}{A_C} \int_{\Omega_C} \boldsymbol{\varepsilon} d\Omega_C - \boldsymbol{\varepsilon} \right) d\Omega^e_{ic}$$

$$= \sum_{ic=1}^{nc} (\mathbf{D} : \tilde{\boldsymbol{\varepsilon}}) : \int_{\Omega^e_{ic}} \left(\frac{1}{A_C} \int_{\Omega_C} \boldsymbol{\varepsilon} d\Omega_C - \boldsymbol{\varepsilon} \right) d\Omega^e_{ic}$$

$$= \sum_{ic=1}^{nc} (\mathbf{D} : \tilde{\varepsilon}) : \left(\frac{\int_{\Omega_{ic}^e} d\Omega_{ic}^e}{A_C} \int_{\Omega_C} \varepsilon d\Omega_C - \int_{\Omega_{ic}^e} \varepsilon d\Omega_{ic}^e \right)$$

$$= \sum_{ic=1}^{nc} (\mathbf{D} : \tilde{\varepsilon}) : \left(\frac{A_{ic}}{A_C} \int_{\Omega_C} \varepsilon d\Omega_C - \int_{\Omega_{ic}^e} \varepsilon d\Omega_{ic}^e \right) \quad (3.18)$$

where $\tilde{\varepsilon} = \frac{1}{A_C} \int_{\Omega_C} \varepsilon(\mathbf{x}) d\Omega$ is a smoothed strain field defined for every $\Omega_C \subset \Omega^e$ and note that $\int_{\Omega_{ic}^e} \mathbf{D} : \tilde{\varepsilon} d\Omega_{ie}^e = \mathbf{D} : \tilde{\varepsilon} A_{ic}$ because the smoothed strain $\tilde{\varepsilon}$ does not depend on the integration variable. For equation Equation (3.18) to be identically zero, a necessary and sufficient condition is that

$$A_C = A_{ic} \ \text{and} \ \Omega_C \equiv \Omega_{ic}^e \quad (3.19)$$

That is to say that to satisfy the orthogonality condition (3.14) the smoothed cell Ω_C must be chosen to coincide with the smoothing cell Ω_{ic}^e. We then obtain a modified variational principle for the SFEM of the form given in Equation (3.16).

By considering the SFEM variational principle based on an assumed strain field and introducing the approximation $\mathbf{u}^h = \sum_{I=1}^{np} \mathbf{N}_I \mathbf{q}_I = \mathbf{N}\mathbf{q}$ and Equation (3.5), the discretized equations are obtained:

$$\tilde{\mathbf{K}}\mathbf{q} = \mathbf{g} \quad (3.20)$$

Equation (3.20) defines the stiffness matrix $\tilde{\mathbf{K}}$ with strain smoothing. This definition of the stiffness matrix will lead to high flexibility and allow to select elements of arbitrary polygonal shape (Liu *et al.* (2007a);Dai *et al.* (2007)).

Now it needs to be shown that the SFEM total energy approaches the total potential energy variational principle (TPE) when nc tends to infinity, e.g. Liu *et al.* (2007b). Based on the definition of the double integral formula, when $nc \to \infty$, $A_{ic} \to dA_{ic}$ – an infinitesimal area containing point $\mathbf{x}_{ic}$, applying the mean value theorem for the smoothed strain,

$$\tilde{\varepsilon}_{ic} = \int_{\Omega_{ic}^e} \frac{\varepsilon(\mathbf{x})}{A_{ic}} d\Omega_{ic}^e \longrightarrow \varepsilon(\mathbf{x}_{ic}) \quad (3.21)$$

where $\varepsilon(\mathbf{x})$ is assumed to be a continuous function. Equation (3.21) simply says that the average value of $\varepsilon(\mathbf{x})$ over a domain Ω_{ic}^e approaches its value at point $\mathbf{x}_{ic}$.
Taking the limit of Π_{SFEM}^e as the number of subcells tends to infinity,

$$\lim_{nc\to\infty} \Pi_{SFEM}^e(\mathbf{u}, \tilde{\varepsilon}) = \frac{1}{2} \lim_{nc\to\infty} \sum_{ic=1}^{nc} \int_{\Omega_{ic}^e} \mathbf{D} : \left(\int_{\Omega_{ic}^e} \frac{\varepsilon(\mathbf{x})}{A_{ic}} d\Omega_{ic}^e \right) : \left(\int_{\Omega_{ic}^e} \frac{\varepsilon(\mathbf{x})}{A_{ic}} d\Omega_{ic}^e \right) d\Omega_{ic}^e$$

$$-f(\mathbf{u}) = \frac{1}{2} \lim_{nc\to\infty} \sum_{ic=1}^{nc} \mathbf{D} : \varepsilon(\mathbf{x}_{ic}) : \varepsilon(\mathbf{x}_{ic}) dA_{ic} - f(\mathbf{u})$$

$$= \frac{1}{2} \int_{\Omega^e} \mathbf{D} : \varepsilon(\mathbf{x}) : \varepsilon(\mathbf{x}) d\Omega - f(\mathbf{u}) = \Pi_{TPE}^e(\mathbf{u}) \quad (3.22)$$

The above proves that the TPE variational principle is recovered from the SFEM variational formulae as nc tends to infinity. This property has been shown previously by Liu *et al.* (2007b).

3.4.1 Non-mapped shape function description

In this section, we focus on a possible description of the non-mapped shape functions for the SFEM using quadrilateral elements. A quadrilateral element may be divided into integration cells (Liu *et al.* (2007a)), as shown in Figure 3.2. Strain smoothing is calculated over each cell and the area integration over the cell's surface is modified into line integration along its boundary. For completeness, we illustrate four forms of the smoothed integration cells in Figure 3.2. In SFEM, the shape functions themselves are used to compute the smoothed gradient matrix $\widetilde{\mathbf{B}}$ and the stiffness matrix is obtained from line integration along the boundaries of the integration cells, therefore, the shape function is only required *along the edges of the cells* (Liu *et al.* (2007a)). Let us consider a four noded quadrilateral element as shown in Figure 3.2. The shape function is interpolated simply by a linear function on each boundary of the cell and its values are easily known at the Gauss points on these boundary lines.

In order to make very clear how the SFEM is computed, we present a complete algorithm for the method in Table 3.1.

3.4.2 Remarks on the SFEM with a single smoothing cell

3.4.2.1 Its equivalence to the reduced Q4 element using one-point integration schemes: realization of quasi-equilibrium element

It is now shown that the stiffness matrix of the SC1Q4 element is identical to that of FEM using the reduced integration (one Gauss point). The non-local strain displacement matrix in Equation (3.7) becomes

$$\widetilde{\mathbf{B}}_I = \frac{1}{A^e} \begin{bmatrix} \frac{1}{2}(n_x^i l_i + n_x^j l_j) & 0 \\ 0 & \frac{1}{2}(n_y^i l_i + n_y^j l_j) \\ \frac{1}{2}(n_y^i l_i + n_y^j l_j) & \frac{1}{2}(n_x^i l_i + n_x^j l_j) \end{bmatrix} \tag{3.23}$$

where the indices i, j are defined by the recursive rule, $ij = 14, 21, 32, 43$ and (n_x^i, n_y^i) is the normal vector on edge l_i. By writing explicitly the normal vectors and length edges l_i for all edges of the element and substituting all to the smoothed strain displacement matrix in Equation (3.5), we have

$$\widetilde{\mathbf{B}} = \frac{1}{2A^e} \begin{bmatrix} y_{24} & 0 & y_{31} & 0 & y_{42} & 0 & y_{13} & 0 \\ 0 & x_{42} & 0 & x_{13} & 0 & x_{24} & 0 & x_{31} \\ x_{42} & y_{24} & x_{13} & y_{31} & x_{24} & y_{42} & x_{31} & y_{13} \end{bmatrix} \tag{3.24}$$

where $x_{ij} = x_i - x_j, y_{ij} = y_i - y_j$ and A^e is the area of the element. It is found that $\widetilde{\mathbf{B}}$ in (3.24) is identical to that of 4-node quadrilateral element with one-point quadrature given

27
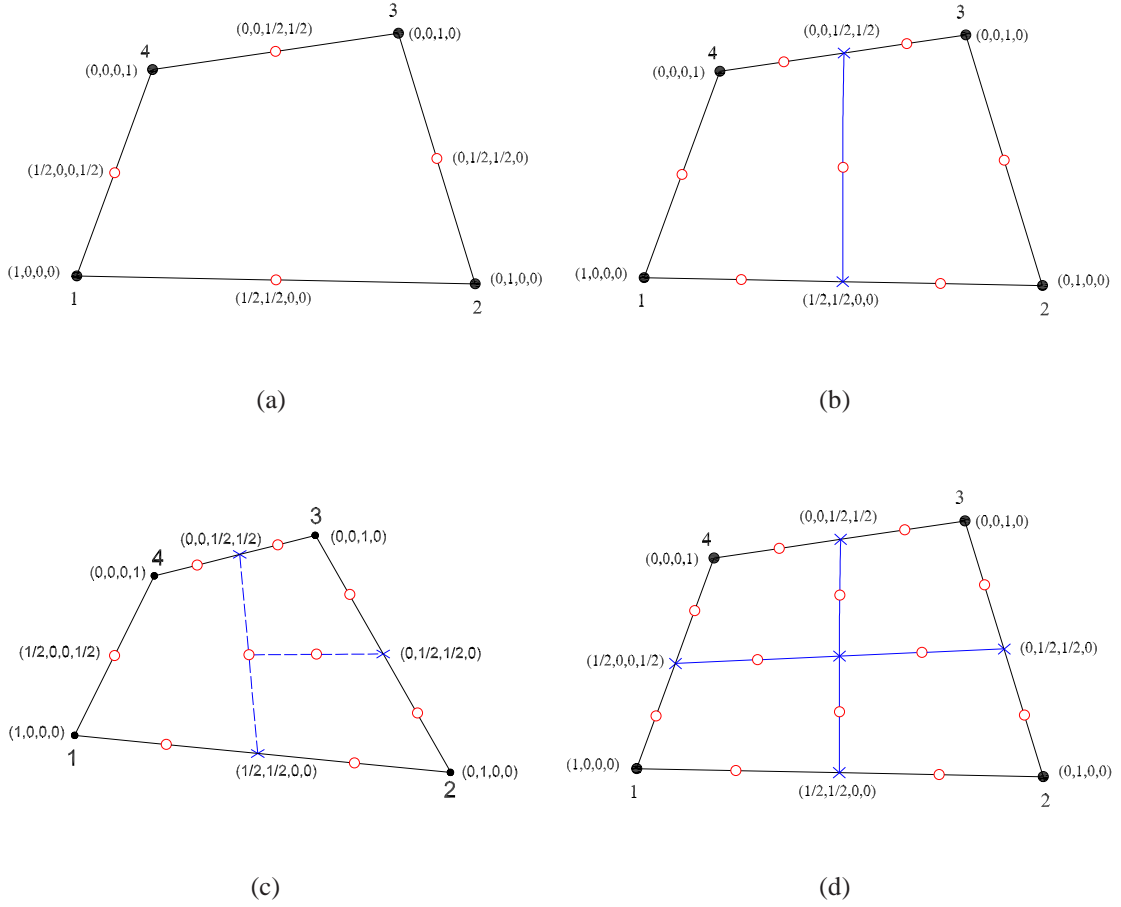
Figure 3.2: Division of an element into smoothing cells (nc) and the value of the shape function along the boundaries of cells: (a) the element is considered as one subcell, (b) the element is subdivided into two subcells, and (c) the element is partitioned into three subcells and (d) the element is partitioned into four subcells. The symbols (•) and (○) stand for the nodal field and the integration node, respectively.

Table 3.1: Pseudo-code for constructing non-maped shape functions and stiffness element matrices

---

1. Determine linear shape functions interpolated along boundaries of element and their values at nodal points, $\mathbf{N}(\mathbf{x}_{node})$(Figure 3.2)
2. Get number of sub-cells (nc) over each element
   - Create auxiliary nodes at locations marked " $\times$ " (Figure 3.2) if $nc > 1$
   - Set connectivity matrix ($cells$) of each smoothing cell at the element level
   - Calculate values of shape function at the auxiliary nodes
   - For all auxiliary nodes belonging to the boundaries of the element, the values of the shape function are based on step 1
   - For all auxiliary nodes interior to the element, the values of the shape function are evaluated by linear interpolation between auxiliary nodes on two confronting edges of the element, $\mathbf{N}(\mathbf{x}_{midpoint})$.
3. Loop over subcells
   {
   - Calculate the outward normal vector $\mathbf{n}$ on each side and the area A_{ic} for cell Ω_{ic}
   - Loop over 4 sides of each sub-cell
     {
     - Loop over Gauss points on each side of the current sub-cell
     - Evaluate the value of the shape function at the Gauss points
     }
     - Compute the stiffness matrix $\tilde{\mathbf{K}}^{ic} = \tilde{\mathbf{B}}_{ic}^{T}\mathbf{D}\tilde{\mathbf{B}}_{ic}A_{ic}$ corresponding to the Ω_{ic}
     - Update the smoothed stiffness element matrices $\tilde{\mathbf{K}}^{e}$ and assemble
   $\tilde{\mathbf{K}}^{e} \longleftarrow \tilde{\mathbf{K}}^{e} + \tilde{\mathbf{K}}^{ic}$
   }

---

by Belytschko & Bachrach (1986). This proves that the solution of the SC1Q4 element coincides with that of the 4-node quadrilateral element with one-point quadrature, also see Liu *et al.* (2007a) for details. By analyzing the eigenvalue of the stiffness matrix, it is realized that $\tilde{\mathbf{K}}$ has 5 zero eigenvalues. It hence exists two spurious kinematic modes associated with zero strain energy. Therefore, Belytschko & Bachrach (1986) introduced a physical stabilization matrix in order to maintain a proper rank for stiffness matrix. In the other investigation, Kelly (1979, 1980) enforced linear combination of boundary displacements to suppress these modes. Moreover, Kelly showed the equivalence between a four-node equilibrium element assembled from *two* De Veubeke equilibrium triangles and the four-node displacement element using the reduced integration via the transformation of the connectors. However, it was recently verified that his method is only suitable for the rectangular elements. In order to extend Kelly's work for arbitrarily quadrilateral elements, it is proposed to consider the four-node equilibrium element assembled from *four* De Veubeke equilibrium triangles. As a result, the formulation proposed in Appendix B will be useful for all cases.

3.4.2.2   Its equivalence to a hybrid assumed stress formulation

The purpose of this part is to demonstrate an equivalence of the classical hybrid variational principle (see Pian & Tong (1969)) with the variational principle of a nodally integrated finite element method with strain smoothing, when one single subcell is used.

The variational basis of the classical hybrid model for one element is written as

$$\Pi^e_{Hyb}(\mathbf{u}, \boldsymbol{\sigma}) = -\int_{\Omega^e} \frac{1}{2} D^{-1}_{ijkl} \sigma_{ij} \sigma_{kl} d\Omega + \int_{\Gamma^e} \sigma_{ij} n_j u_i d\Gamma - \int_{\Gamma^e_{\mathbf{t}}} \bar{t}_i u_i d\Gamma \qquad (3.25)$$

where Γ^e is the entire boundary of Ω^e and $\Gamma^e_{\mathbf{t}}$ is the portion of the element boundary over which the prescribed surface tractions $\bar{t}_i$ are applied.

Here the approximate displacement only needs to satisfy the continuity requirements along the interelement boundaries and the trial stress field satisfies the homogeneous equilibrium equations in each element. The stresses are expressed as

$$\boldsymbol{\sigma} = \mathbf{P}\boldsymbol{\beta} \qquad (3.26)$$

in which $\boldsymbol{\beta}$ contains unknown coefficients and $\mathbf{P}$ is the stress mode matrix. Substitution of Equations (2.18) and (3.26) into (3.25) yields the equation of the form

$$\Pi^e_{Hyb} = -\frac{1}{2}\boldsymbol{\beta}^T \mathbf{F} \boldsymbol{\beta} + \boldsymbol{\beta}^T \mathbf{G} \mathbf{q} - \mathbf{q}^T \mathbf{g} \qquad (3.27)$$

where

$$\mathbf{F} = \int_{\Omega^e} \mathbf{P}^T \mathbf{D}^{-1} \mathbf{P} d\Omega \quad \mathbf{G} = \int_{\Gamma^e} \mathbf{P}^T \mathbf{n}^T \mathbf{N} d\Gamma \quad \mathbf{g} = \int_{\Gamma^e_t} \mathbf{N}^T \bar{\mathbf{t}} d\Gamma \qquad (3.28)$$

The stationary condition of the functional Π^e_{Hyb} with respect to the coefficients $\boldsymbol{\beta}$, leads to

$$\mathbf{F}\boldsymbol{\beta} = \mathbf{G}\mathbf{q} \qquad (3.29)$$

By solving for $\boldsymbol{\beta}$ from Equation (3.29) and then replacing into Equation (3.28), the functional Π^e_{Hyb} can be written in terms of the generalized displacements $\mathbf{q}$ only,

$$\Pi^e_{Hyb} = \frac{1}{2}\mathbf{q}^T\mathbf{K}^e_{Hyb}\mathbf{q} - \mathbf{q}^T\mathbf{g} \tag{3.30}$$

where $\mathbf{K}^e_{Hyb} = \mathbf{G}^T\mathbf{F}^{-1}\mathbf{G}$ is the element stiffness matrix

Now if $\mathbf{P}$ is chosen to be the identity matrix $\mathbf{I}$ of the stress space, the global stiffness matrix of the hybrid model becomes

$$\mathbf{K}^e_{hyb} = \frac{1}{A^e}\left(\int_{\Gamma^e}\mathbf{n}^T\mathbf{N}d\Gamma\right)^T\mathbf{D}\left(\int_{\Gamma^e}\mathbf{n}^T\mathbf{N}d\Gamma\right) \tag{3.31}$$

where $\mathbf{n}^T$ is defined by Equation (3.2).

Because the shape function $\mathbf{N}$ is linear on the boundaries of elements, the integration in the right hand side of Equation (3.31) is exactly computable with one point Gauss quadrature, located at the midpoint of the boundary edges. Therefore, we obtain an equivalence between the hybrid stiffness matrix and the 1–subcell stiffness matrix of the $SC1Q4$ element. So that the $SC1Q4$ element is nothing other than a disguised form of the four-nodal constant stress hybrid quadrilateral element.

3.5 Numerical results

3.5.1 Cantilever loaded at the end

A 2-D cantilever beam subjected to a parabolic load at the free end is examined as shown in Figure 3.3. The geometry is: length $L = 8$, height $D = 4$ and thickness $t = 1$. The material properties are: Young's modulus $E = 3 \times 10^7$, and the parabolic shear force $P = 250$.

The exact solution of this problem is available as given by Timoshenko & Goodier (1987), giving the displacements in the x and y directions as

$$u_x(x,y) = \frac{Py}{6\bar{E}I}\left[(6L-3x)x + (2+\bar{\nu})\left(y^2 - \frac{D^2}{4}\right)\right] \tag{3.32}$$

$$u_y(x,y) = -\frac{P}{6\bar{E}I}\left[3\bar{\nu}y^2(L-x) + (4+5\bar{\nu})\frac{D^2x}{4} + (3L-x)x^2\right] \tag{3.33}$$

where

$$\bar{E} = \left\{\begin{array}{l} E, \\ E/(1-\nu^2), \end{array}\right. \quad \bar{\nu} = \left\{\begin{array}{ll} \nu, & \text{for plane stress} \\ \nu/(1-\nu) & \text{for plane strain} \end{array}\right.$$

and the stress components are

$$\sigma_{xx}(x,y) = \frac{P(L-x)y}{I} \tag{3.34}$$
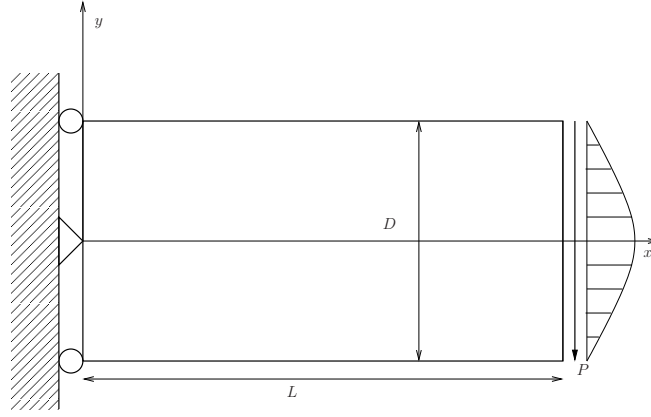
Figure 3.3: A cantilever beam and boundary conditions

$$\sigma_{yy}(x, y) = 0 \tag{3.35}$$

$$\tau_{xy}(x, y) = -\frac{P}{2I}\left(\frac{D^2}{4} - y^2\right) \tag{3.36}$$

where $I = tD^3/12$. In this problem, two types of mesh are considered: one is uniform and regular, the other is irregular, with the coordinates of interior nodes following Liu *et al.* (2007a):

$$\begin{aligned} x' &= x + r_c s\Delta x \\ y' &= y + r_c s\Delta y \end{aligned} \tag{3.37}$$

where r_c is a generated random number of the computer given values between -1.0 and 1.0, $s \in [0, 0.5]$ is an irregularity factor controlling the *s*hapes of the distorted elements and $\Delta x, \Delta y$ are initial regular element sizes in the x–and y–directions, respectively. Discretizations with 512 quadrilateral elements using regular and irregular meshes are shown as an illustration in Figure 3.4. Under plane stress conditions and for a Poisson's ratio $\nu = 0.3$, the exact strain energy is 0.03983333. Tables 3.2, 3.3 and Figures 3.5 - 3.6 present the results for a sequence of uniform meshes, $\alpha_{ir} = 0$. The relative error in displacement norm is defined as follows

$$Re_d = \sqrt{\sum_{i=1}^{ndof}\left(u_i^h - u_i^{exact}\right)^2 / \sum_{i=1}^{ndof}\left(u_i^{exact}\right)^2} \times 100 \tag{3.38}$$

It is important to define a relative error

$$\eta = \frac{\left\|u - u^h\right\|_E}{\|u\|_E} \tag{3.39}$$

where $\left\|u - u^h\right\|_E$ is the discretization error in the energy norm. Figure 3.5 shows the relative error and the rate of convergence in the displacement norm for a sequence of

(a)   (b)
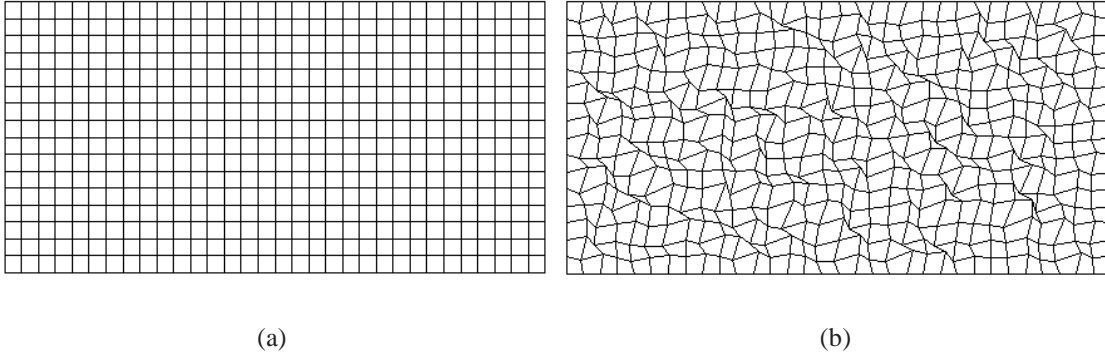
Figure 3.4: Meshes with 512 elements for the cantilever beam:(a) The regular mesh; and (b) The irregular mesh with extremely distorted elements

uniform meshes. Figure 3.6 illustrates the convergence of strain energy and the rate of convergence in the energy norm of elements built using the present method compared to that of the standard FEM four-node quadrilateral element.

Table 3.2: Relative error in the energy norm for the cantilever beam problem

Meshes	D.O.F	Q4	SFEM			
			SC1Q4	SC2Q4	SC3Q4	SC4Q4
16×8	288	0.1327	0.0238	0.0964	0.1048	0.1151
32×16	1088	0.0665	0.0061	0.0474	0.0525	0.0577
64×32	4224	0.0333	0.0016	0.0236	0.0263	0.0289
128×64	16640	0.0167	0.0004	0.0118	0.0132	0.0144

From Tables 3.2–3.3, and Figures 3.5–3.6, the proposed method gives results comparable to a 4-node FEM discretization. In addition, the SC2Q4, SC3Q4 and SC4Q4 elements enjoy the same convergence rate in both the $\mathcal{L}_2$ and H_1 (energy) norms as the standard FEM, as shown in Figures 3.5b and 3.6b. Moreover, displacement results for the SC3Q4 and SC4Q4 discretization are more accurate than the standard bilinear Q4-FEM solution. The proposed elements also produce a better approximation of the global energy. In addition, the CPU time required for all elements with the smoothed strain technique presented here appears asymptotically lower than that of the Q4-FEM, as the mesh size tends to zero. It is remarkable that the SC1Q4 enjoys a form of superconvergence in the energy norm, the convergence rate approaching 2. A reason for this interesting property may seem the equivalence of this SC1Q4 element with an *equilibrium element* (Johnson & Mercier (1979)).

From a mathematical point of view, each finite element is divided into nc–subcells. It is also shown, by the mean-value theorem, that the SFEM solution approaches the FEM solution, when nc approaches infinity. From a numerical point of view, the SFEM solution

33

(a)

(b)

(c)
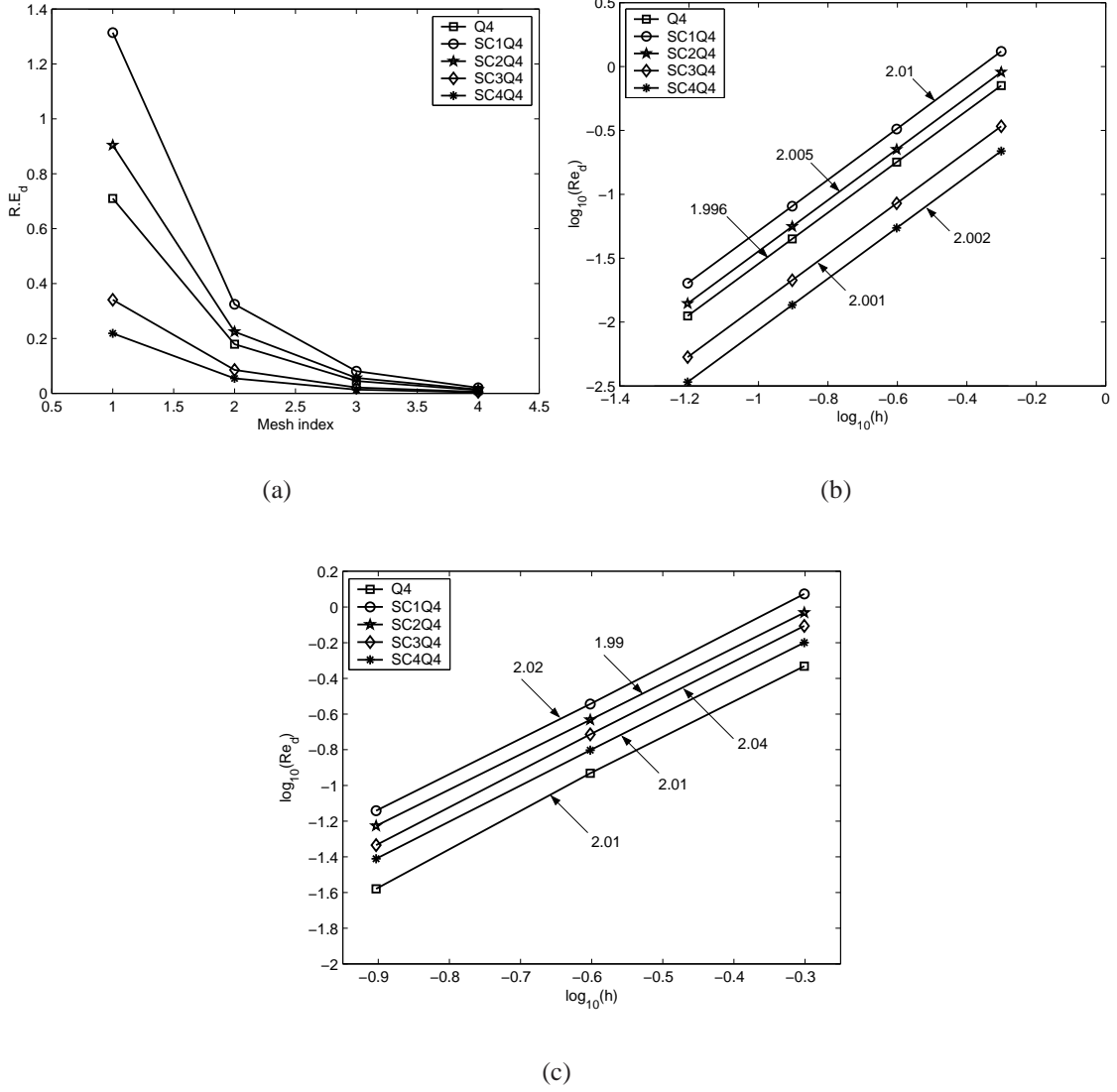
Figure 3.5: The convergence of the displacements for the cantilever beam: (a) relative error with $\nu = 0.3$, plane stress; (b) convergence rate $\nu = 0.3$, plane stress; and (c) convergence rate $\nu = 0.4999$, plane strain

(a)

(b)

(c)
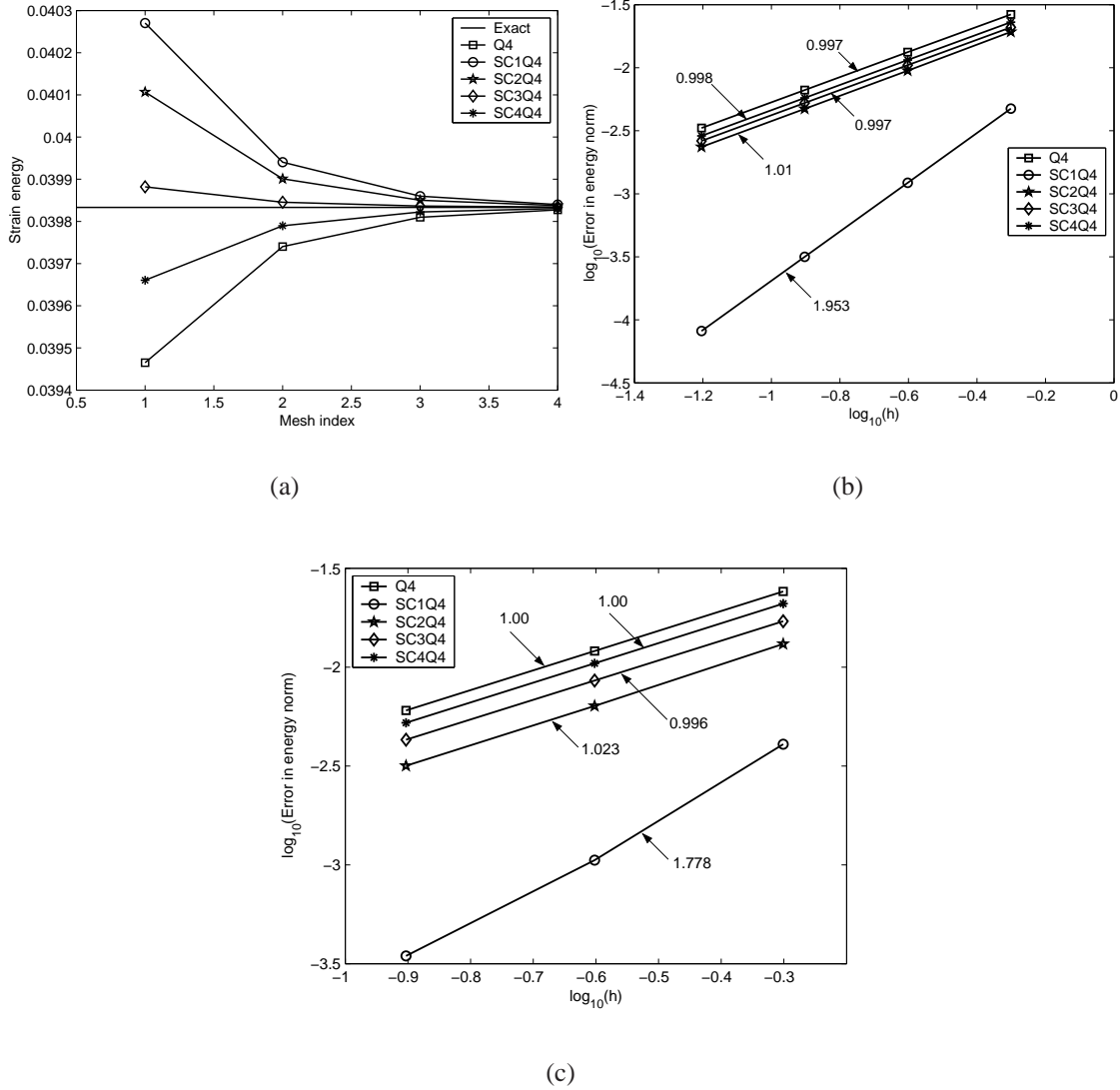
Figure 3.6: The convergence of the energy norm for the cantilever beam: (a) Strain energy with $\nu = 0.3$, plane stress; (b) convergence rate $\nu = 0.3$, plane stress; and (c) convergence rate $\nu = 0.4999$, plane strain. We note that the best element is the SC1Q4 element if error is measured by the H_1 (energy) norm. Moreover, this SC1Q4 element is superconvergent compared to standard displacement-based finite elements.

Table 3.3: Comparing the CPU time (s) between the FEM and the present method. Note that the SC1Q4 element is always faster than the standard displacement finite element.

Meshes	Q4	SFEM			
		SC1Q4	SC2Q4	SC3Q4	SC4Q4
16×8	0.78	0.75	0.81	0.92	0.95
32×16	1.81	1.60	1.80	1.98	2.13
64×32	9.45	8.05	8.25	9.34	9.78
128×64	101.19	81.61	82.75	92.92	94.94

is always comprised within a solution domain bounded by two finite element solutions: the displacement FEM solution[1] and the quasi-equilibrium FEM solution[2].

As presented in Section 2.4, surface integrals appearing in the element stiffness computation are changed into line integration along elements' boundaries and shape functions themselves are used to compute the field gradients as well as the stiffness matrix. This permits to use the distorted elements that create difficulty in the standard FEM. Figure 3.4b is an example of an irregular mesh with severe element distortion. The relative error corresponding to the displacement norm and the energy norm exhibited in Figure 3.7 proves that the SFEM is more reliable than the FEM with irregular meshes, the rate of convergence being shown in Figure 3.8. However, the convergence for both norms now exhibits a non-uniform behavior. An estimation of the convergence rate for each segment is performed for completeness. Results show that the asymptotic rate of convergence given by the standard FEM and the stabilized conforming nodally integrated finite elements are quite comparable.

Table 3.4: Normalized end displacement $(u_y^h(L,0)/u_y(L,0))$

ν	Q4	SFEM			
		SC1Q4	SC2Q4	SC3Q4	SC4Q4
0.3	0.9980	1.0030	1.0023	1.0008	0.9993
0.4	0.9965	1.0029	1.0024	1.0003	0.9981
0.4999	0.5584	1.0028	1.0366	0.6912	0.5778
0.4999999	0.4599	1.0323	1.3655	0.5143	0.4622

Next we estimate the accuracy of the SFEM elements for the same beam problem, assuming a near incompressible material. Under plane strain condition, Table 3.4 describes the normalized end displacement for varying Poisson's ratio. In Figure 3.9, the displacements along the neutral axis for Poisson's ratio $\nu = 0.4999$ are represented.

The results show that Q4, SC2Q4, SC3Q4 and SC4Q4 solutions yield poor accuracy as

---

[1]obtained when $nc \to \infty$

[2]obtained when $nc = 1$
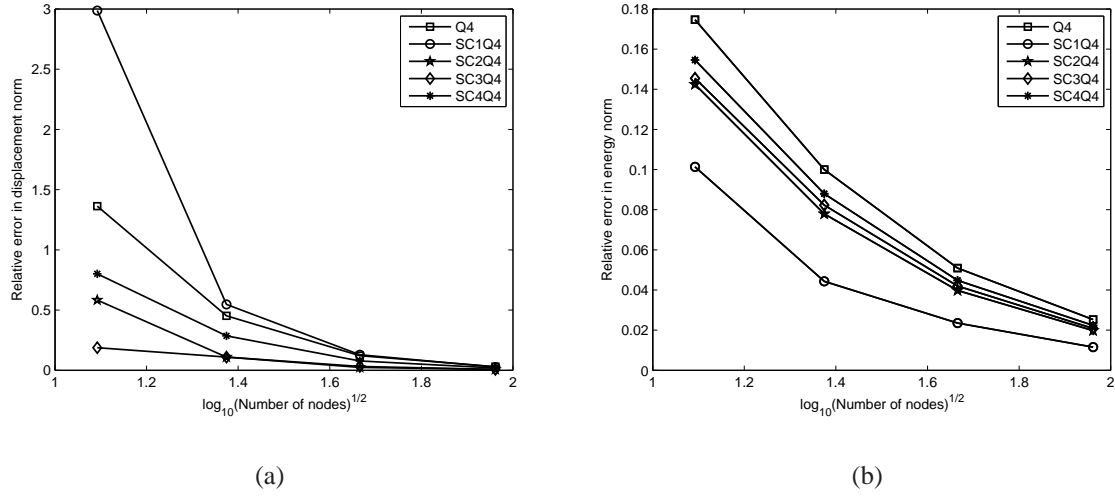
Figure 3.7: The relative error for the beam problem with extremely distorted elements:(a) Displacement norm; (b) Energy norm
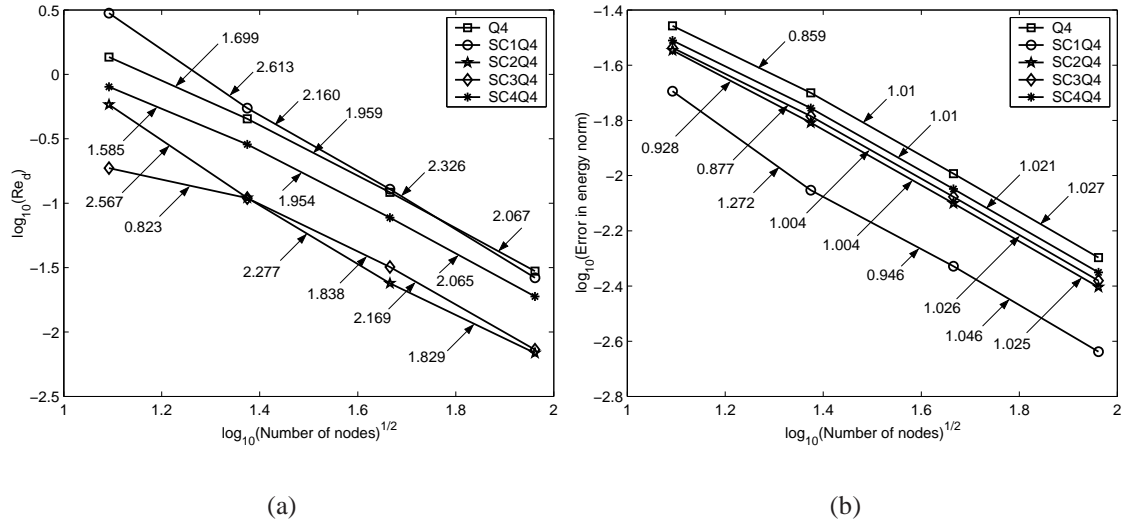
Figure 3.8: Rate of convergence for the beam problem with extremely distorted elements:(a) Displacement; (b) Energy. We note that in the energy norm, the SC1Q4 element gives the lowest error, and a convergence rate comparable to that of the other elements.

(a)

(b)

(c)
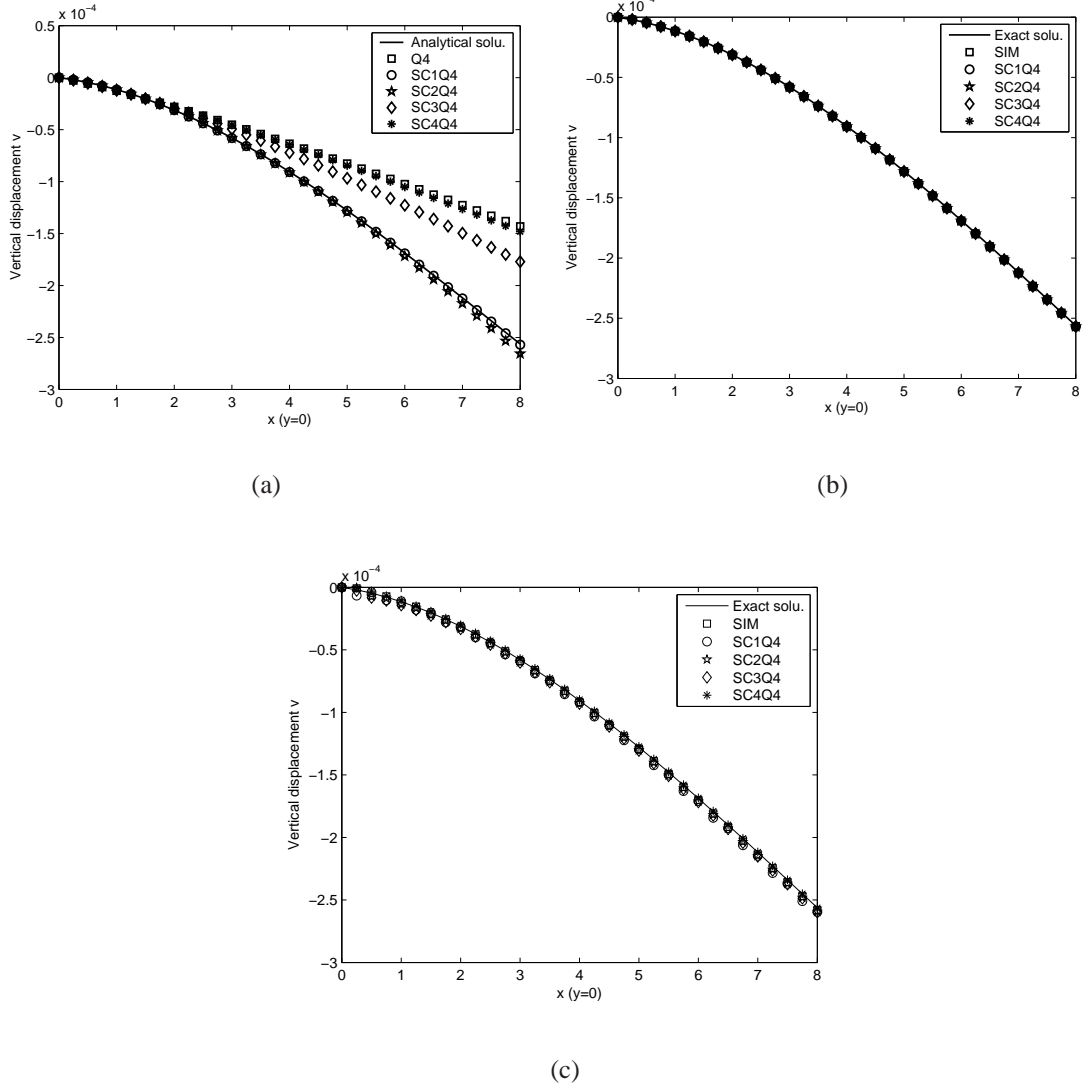
Figure 3.9: Vertical displacement for cantilever beam at the nodes along the x-axis (y =0) in plane strain : (a) without using the selective technique; (b) applying the selective method $\nu = 0.4999$; and (c) applying the selective method $\nu = 0.4999999$

the Poisson's ratio ν tends toward 0.5. In contrast, the SC1Q4 model still is in very good agreement with the analytical solution. To remedy this locking phenomenon, selective integration techniques are considered.

Figures 3.9(b) - 3.9(c) presents the results for selectively integrated (SIM) (Hughes (1980); Malkus & Hughes (1978)) Q4-FEM element and selective cell-wise smoothing method for the SFEM. In addition, the rate of convergence in displacement and energy norm is also displayed on Figures 3.5c –3.6c, which show that the displacement of the SIM-Q4 is more accurate than that of the SFEM formulation while the proposed elements produce a better approximation of the global energy.

3.5.2 Hollow cylinder under internal pressure

Consider a hollow cylinder as in Figure 3.10 with an internal radius $a = 1$, an external radius $b = 5$ and Young's modulus $E = 3 \times 10^7$, subjected to a uniform pressure $p = 3 \times 10^4$ on its inner surface ($r = a$), while the outer surface ($r = b$) is traction free. The analytical solution of this linear elasticity problem is given in Timoshenko & Goodier (1987).

$$\sigma_r(r) = \frac{a^2 p}{b^2 - a^2}\left(1 - \frac{b^2}{r^2}\right); \quad \sigma_\varphi(r) = \frac{a^2 p}{b^2 - a^2}\left(1 + \frac{b^2}{r^2}\right); \quad \sigma_{r\varphi} = 0 \qquad (3.40)$$

while the radial and tangential exact displacement are given by

$$u_r(r) = \frac{(1+\nu)a^2 p}{E(b^2 - a^2)}\left\{(1 - 2\nu)r + \frac{b^2}{r^2}\right\}; \quad u_\varphi = 0 \qquad (3.41)$$

where r, φ are the polar coordinates, and φ s measured counter-clockwise from the positive x-axis.

Because of the symmetry of the problem, only one-quarter of the cylinder is modelled. In the analyses, six different nodal discretizations are considered, namely, 576 elements, 2304 elements, 6400 elements and 9801 elements. The 576 quadrilateral element mesh is shown in Figure 3.11. Under plane stress conditions and Poisson's ratio $\nu = 0.25$, the exact strain energy given by Sukumar *et al.* (1998) as 31.41593.

Figure 3.12a shows that, for regular meshes, the strain energy obtained with SFEM agrees well with the exact solution for compressible and incompressible cases. Moreover, results obtained with the present method appear to be more accurate than the corresponding FEM results. The SC1Q4 element exhibits a superconvergence in energy with a rate of 2.0 in the energy norm, identical to its convergence rate in the L^2 norm.

In the case of a distorted mesh, the proposed method also maintains a higher accuracy than the standard FEM solutions (see Figure 3.13a) but the convergence rates of become non-uniform. However, asymptotically, the SC1Q4 element appears to converge faster than the standard FEM.

We now consider the same problem for a nearly incompressible material ($\nu = 0.4999$) in plane strain conditions. As shown in Figures 3.14a and 3.15a, the radial and hoop
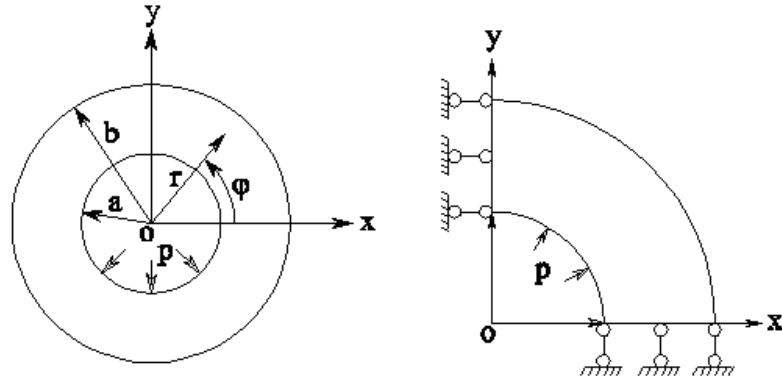
Figure 3.10: A thick cylindrical pipe subjected to an inner pressure and its quarter model

(a)   (b)
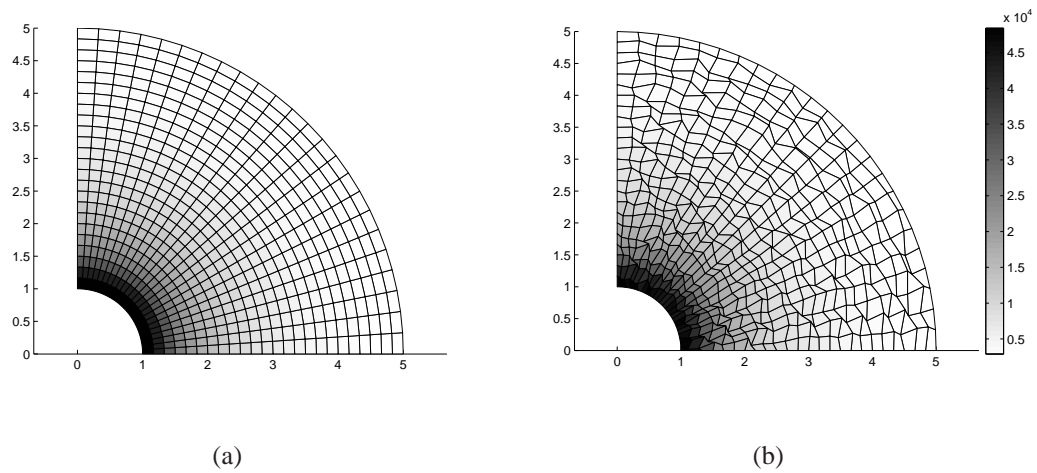
Figure 3.11: Sample discretizations of 576 quadrilateral elements and distribution of von Mises stresses for the SC1Q4 element: (a) regular elements; (b) distorted elements
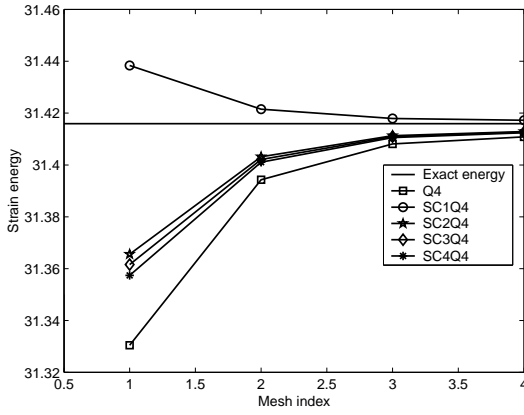
(a) Convergence to the exact energy
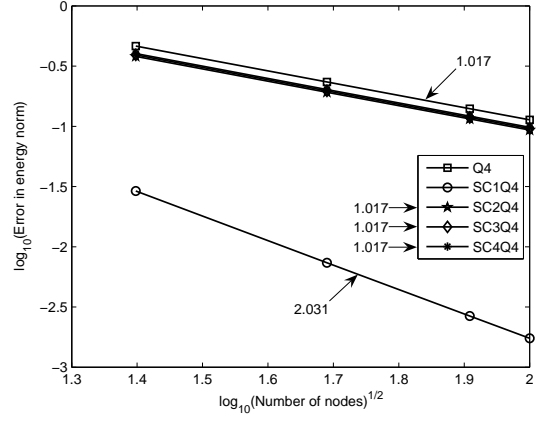
(b) Convergence study in the H_1 norm
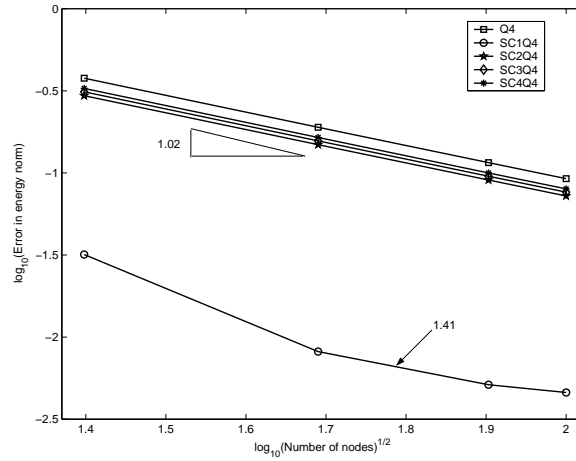
(c)

Figure 3.12: The convergence of the strain energy and convergence rate for the hollow cylinder problem : (a) strain energy ($\nu = 0.25$), plane stress; and (b) error in energy norm ($\nu = 0.25$), plane stress; and (c) error in energy norm ($\nu = 0.4999$), plain strain

41
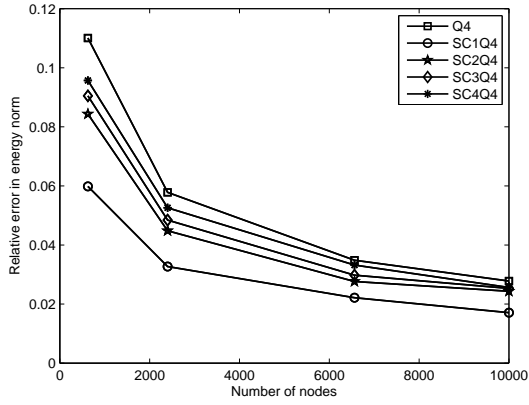
(a) Relative error in energy norm
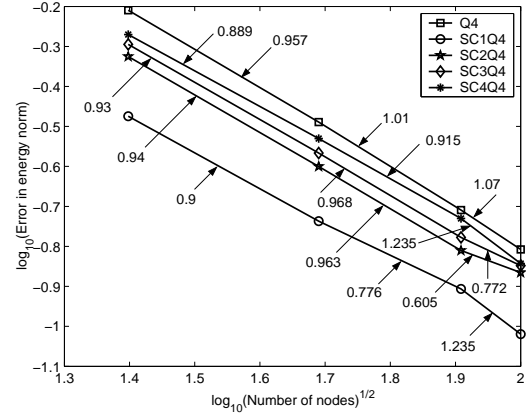
(b) Convergence study in the H_1 norm

Figure 3.13: Convergence rate for the hollow cylinder problem with irregular meshes
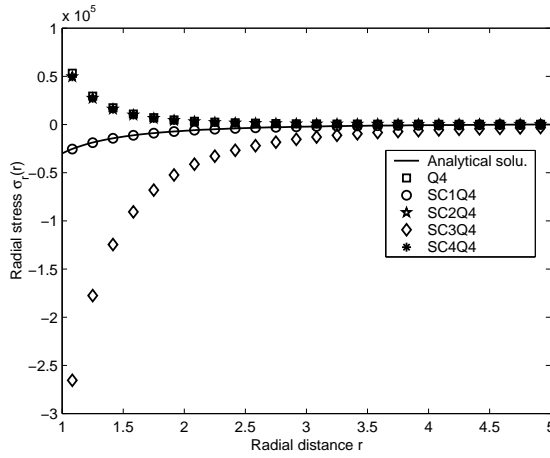
(a)
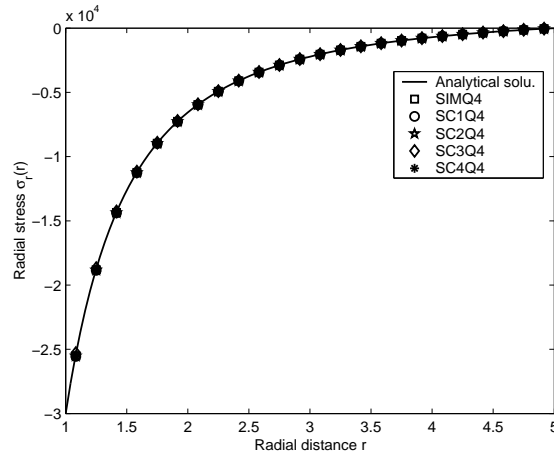
(b)

Figure 3.14: Radial stress $\sigma_r(r)$ for the hollow cylinder under internal pressure condition without and with selective technique

(a)   (b)
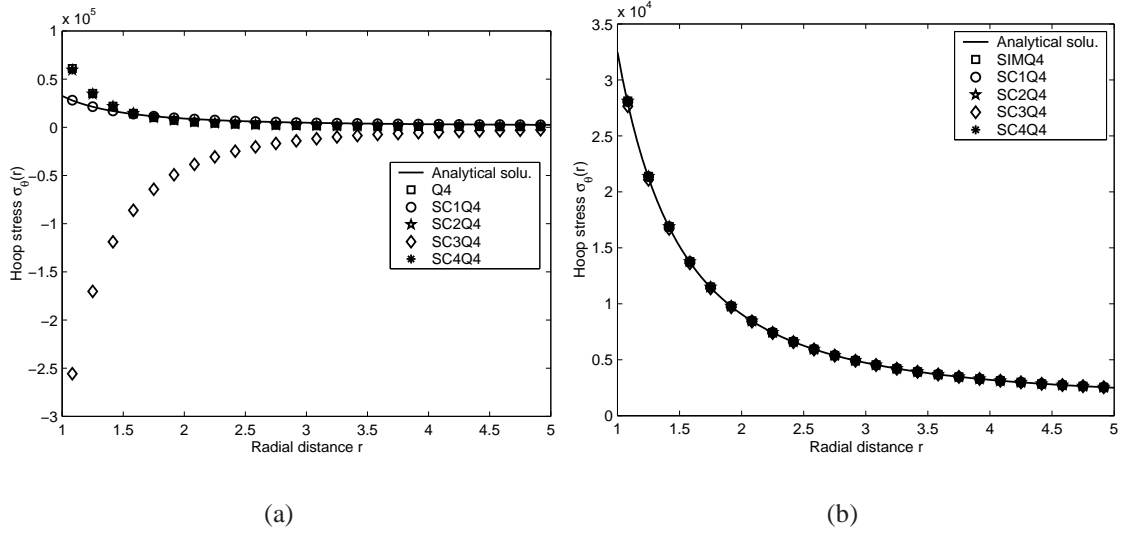
Figure 3.15: Hoop stress $\sigma_\theta(r)$ for the hollow cylinder under internal pressure condition without and with selective technique

stresses are very accurate for the SC1Q4 element, while locking is observed for all other nodally integrated FEMs, as in standard finite elements. This is a very promising property of the SC1Q4 version of the method. Applying the selective cell-wise smoothing method for the SFEM, stable results are obtained, as shown in Figures 3.14b and 3.15b for all proposed elements.

3.5.3   Cook's Membrane
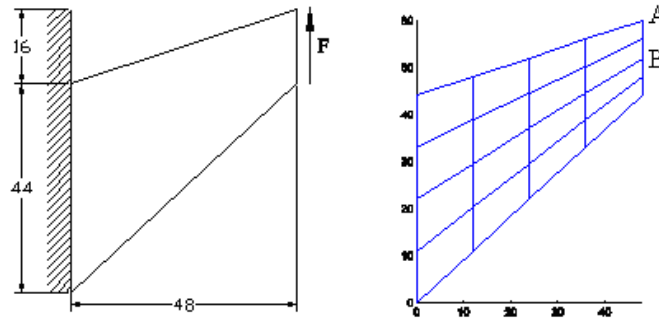
Figure 3.16: Cook's membrane and initial mesh

This benchmark problem given by Cook (1974), shown in Figure 3.16, refers to a clamped tapered panel is subjected to an in-plane shearing load, $F = 100$, resulting

43

in deformation that is dominated by a bending elastic response. Assuming plane strain conditions, Young's modulus $E = 1.0$ and Poisson's ratio $\nu = 0.4999$ or $\nu = 0.4999999$ and thickness = 1, Figure 3.17 plots the vertical displacement at the top right corner. In this problem, the present elements are also compared to the assumed strain stabilization of the 4-node quadrilateral element by Belytschko & Bindeman (1991). It shows that the displacement element (Q4) provides poor results while the other elements based on strain smoothing formulations are reliable, even for very incompressible materials.
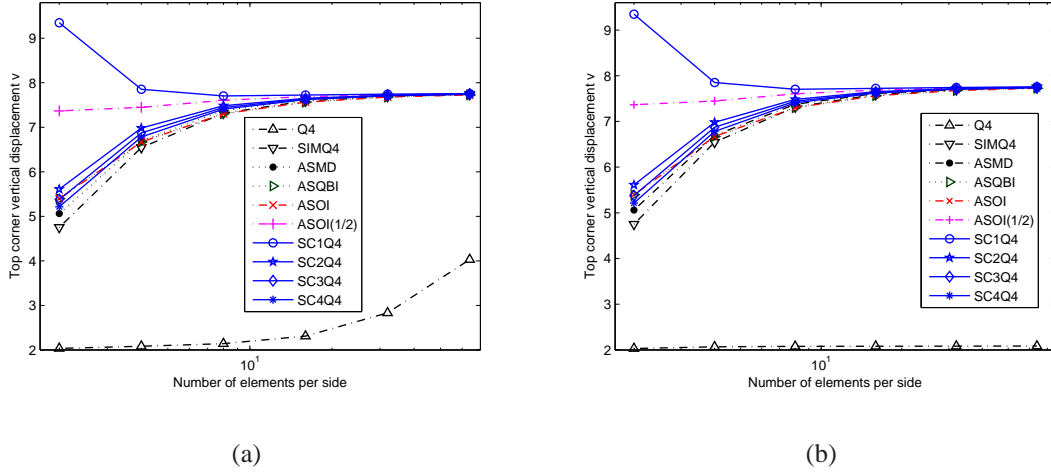
Figure 3.17: Vertical displacement at the top right corner of Cook's membrane; (a) $\nu = 0.4999$, (b) $\nu = 0.4999999$

3.5.4   L–shaped domain

Consider a L–shaped domain with applied tractions and boundary conditions shown in Figure 3.18. The parameters of the structure are: Young's modulus $E = 1.0$, Poisson's ratio $\nu = 0.3$, and thickness $t = 1$.

   The exact strain energy for this problem is not available. However, it can be replaced by an estimated solution through the procedure of Richardson's extrapolation (Richardson (1910)) for the displacement models and equilibrium models. Then the estimated precision is determined by the mean value of these two extrapolated strain energies. The estimated strain energy given by Beckers *et al.* (1993) is 15566.46. The relative error and convergence rates are evaluated based on this estimated global energy. Figure 3.19 illustrates the convergence rate of both the FEM and the presented method. In this example, a stress singularity occurs at the re-entrant corner. The strain energy and relative error results are given in Table 3.5. The convergence of the overall strain energy is shown in Figure 3.19a, and the convergence rates are shown in Figure 3.19b. The accuracy of

Table 3.5: The results on relative error in energy norm of L-shape.

Meshes	D.O.F	Q4	SFEM			
			SC1Q4	SC2Q4	SC3Q4	SC4Q4
1	288	0.1715	0.0827	0.1241	0.1405	0.1535
2	1088	0.1082	0.0394	0.0819	0.0905	0.0976
3	4224	0.0695	0.0192	0.0546	0.0592	0.0631
4	16640	0.0454	0.0099	0.0366	0.0392	0.0415

SFEM is here higher than that of the standard FEM. The SC1Q4 provides the best solutions particularly for the coarser meshes. We note that the SC2Q4 and SC3Q4, both lead to lower error than their SC4Q4 counterpart and than the standard FEM. Additionally, all smoothed finite element models converge from below toward the exact energy, except for the SC1Q4 version, which converges at the optimum rate despite the presence of the singularity in the solution. Besides, we note that a refined mesh or partition of unity enrichment (Belytschko & Black (1999); Belytschko *et al.* (2001)) in the vicinity of the corner is necessary to reduce the error and computational cost.
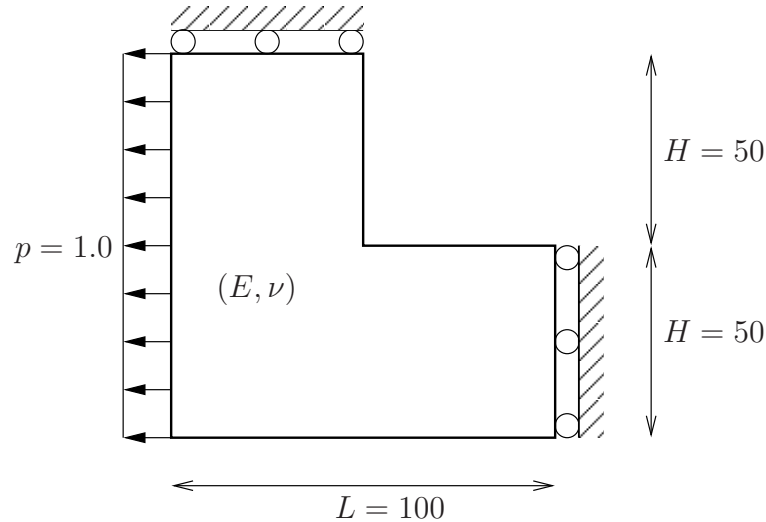
Figure 3.18: L-shape problem set-up.

3.5.5 Crack problem in linear elasticity

Consider a crack problem in linear elasticity, as in Figure 3.20a. The data for this problem is: Young's modulus $E = 1.0$, Poisson's ratio $\nu = 0.3$, and thickness $t = 1$. By symmetry, only half of domain is modelled. By incorporating dual analysis (Debongnie *et al.* (1995); Fraeijs De Veubeke (1965)) and the procedure of Richardson's extrapolation with very

(a)   (b)
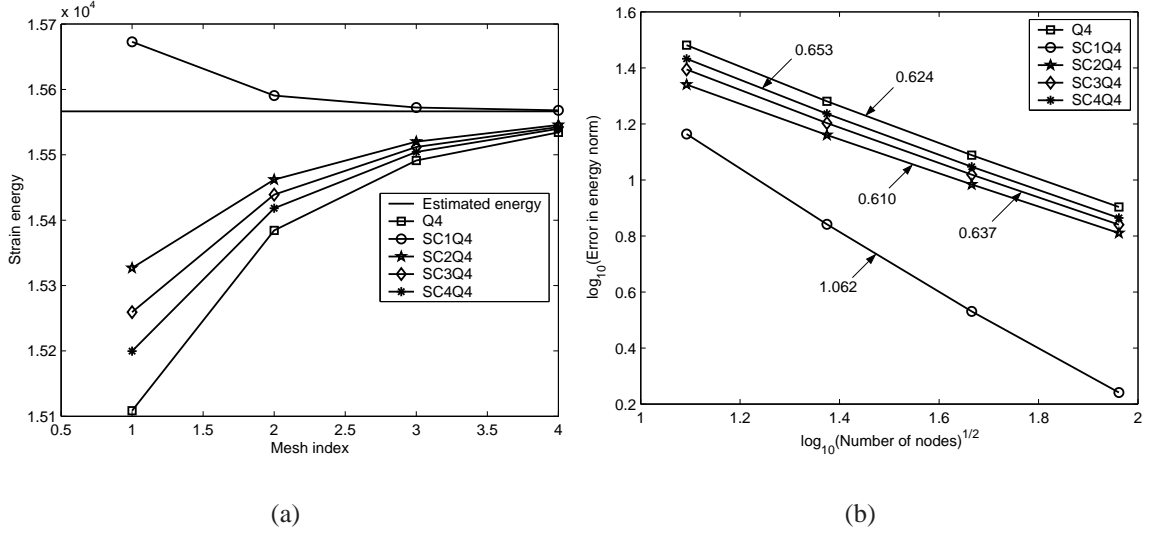
Figure 3.19: The convergence of energy and rate for the L-shaped domain: (a) Strain energy; and (b) Convergence rate. We note that the SC1Q4 element still displays a super-convergence in the energy norm. However, the rate is decreased from 2.0 to 1.0, because of the stress singularity. Again, the SC1Q4 element overestimates the energy, while all other element formulations underestimate it.

fine meshes, Beckers *et al.* (1993) proposed a good approximation of the exact strain energy for this crack problem to be 8085.7610.

Figures 3.20b and 3.20c give an example of a regular mesh ($s = 0$) and an extremely distorted mesh ($s = 0.4$) for a total number of 256 elements.

Table 3.6: The results on relative error based on the global energy for crack problem

Meshes	D.O.F	Q4	SFEM			
			SC1Q4	SC2Q4	SC3Q4	SC4Q4
1	157	0.3579	0.1909	0.2938	0.3163	0.3333
2	569	0.2628	0.0936	0.2154	0.2318	0.2445
3	2161	0.1893	0.0472	0.1551	0.1669	0.1761
4	8417	0.1350	0.0249	0.1105	0.1190	0.1256
5	33217	0.0957	0.0147	0.0783	0.0843	0.0890

Figure 3.21 shows the strain energy and the convergence rate for the crack problem. For this example, whose solution contains a stronger singularity (namely a $r^{-1/2}$ in stress) than the re-entrant corner of the L-shape previously studied, the numerical results shown in Tables 3.6–Figure 3.21 for all uniform meshes show that the SC1Q4 element exhibits a convergence rate of almost 1.0 in the energy norm: twice the convergence rate obtained by standard FEM and the other smoothed finite elements. This is a remarkable property
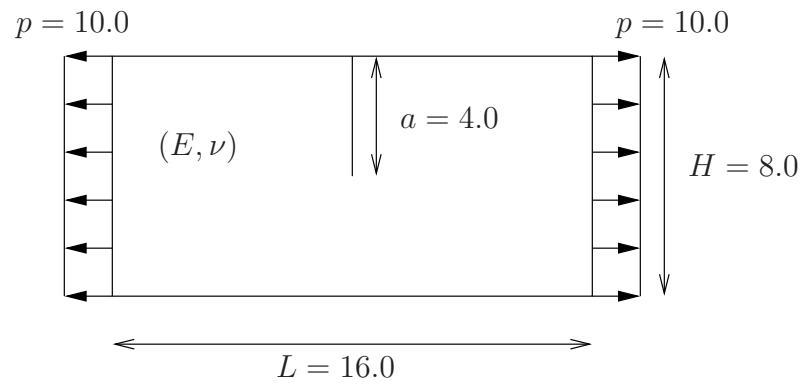
(a) Boundary value problem
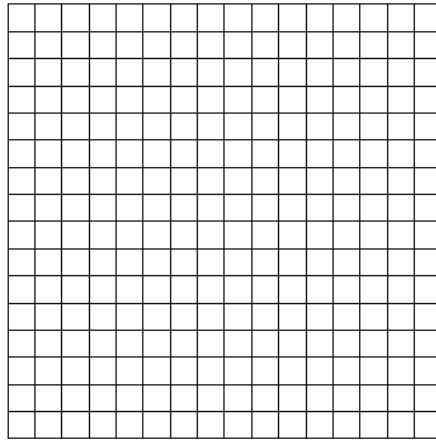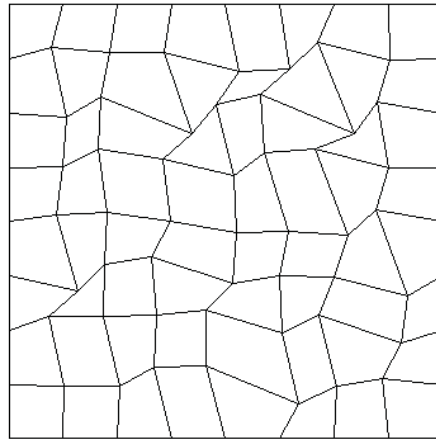
(b) Regular mesh   (c) Distorted mesh

Figure 3.20: Crack problem and coarse meshes

of the proposed method and leads to the conjecture that partition of unity enrichment in (Babuška & Melenk (1997); Melenk & Babuška (1996)) of properly integrated asymptotic fields to the finite element approximation space may lead to recovery of the rate of convergence of 2.0 obtained for the other test cases with the SC1Q4 element.

(a)   (b)
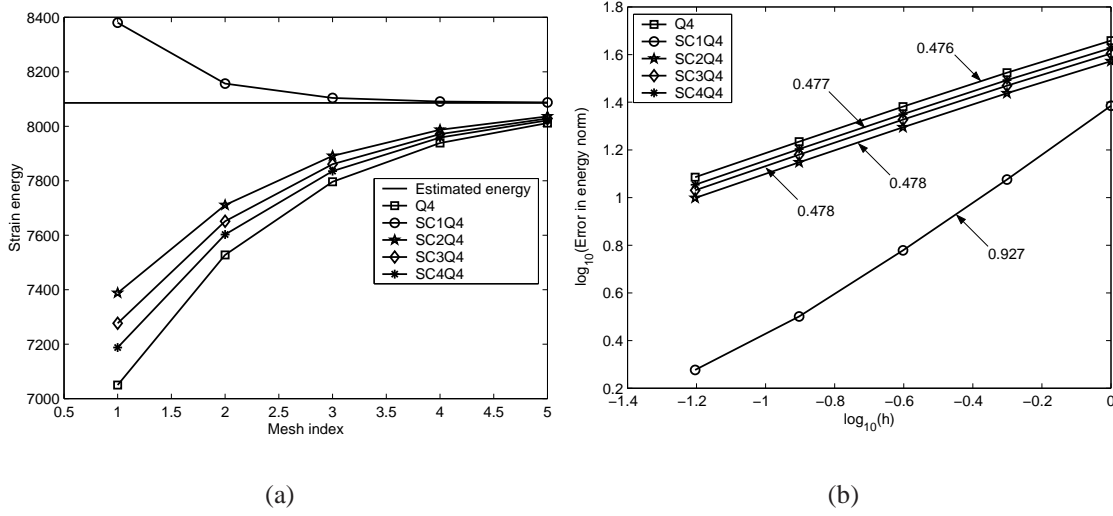
Figure 3.21: The convergence of energy and convergence rate for the crack problem: (a) Strain energy and (b) The rate of convergence

Figure 3.22 illustrates the relative error of the strain energy and the rate of convergence for distorted meshes ($s = 0.4$). Again, SFEM is more accurate than FEM for distorted meshes. However, both in FEM and SFEM, distorted meshes lead to non-uniform convergence rates.

For coarse meshes, the relative error remains large since the methods fail to capture the stress singularity. Adaptive meshes or partition of unity enrichment should be use to keep the computational time and the error reasonable.

Last but not least, we summarize the rate of convergence for regular and irregular meshes in the energy norm for all examples in Table 3.7 and Table 3.8.

Table 3.7: The rate of convergence in the energy error for regular meshes

Problems	Q4	SFEM			
		SC1Q4	SC2Q4	SC3Q4	SC4Q4
Cantilever beam	0.997	1.953	1.010	0.997	0.998
Hollow cylinder	1.017	2.031	1.017	1.017	1.017
L-shape	0.624	1.062	0.610	0.637	0.653
Crack	0.476	0.927	0.478	0.478	0.477

(a)   (b)
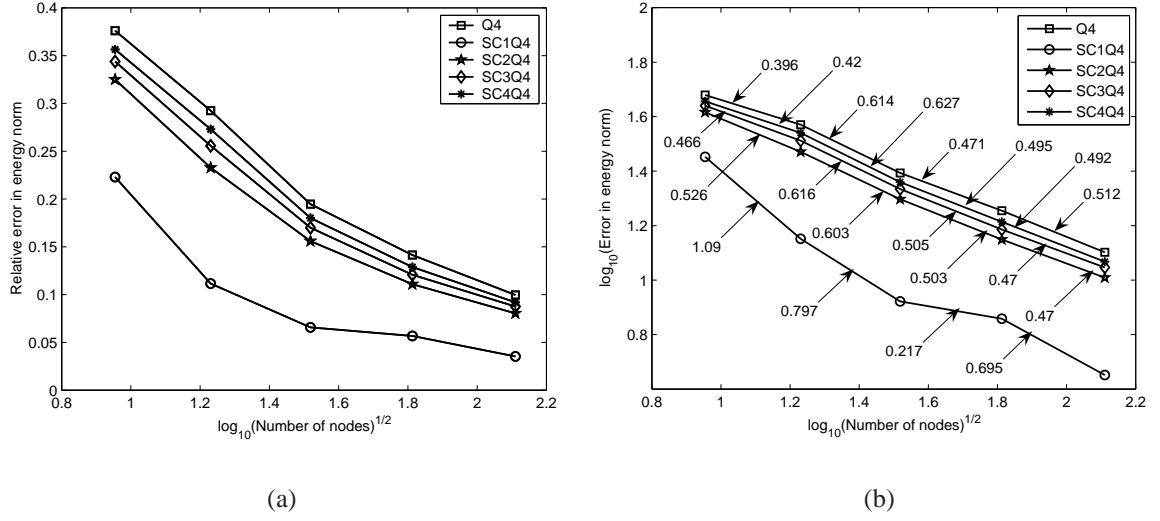
Figure 3.22: The convergence for the crack problem using a sequence of extremely distorted meshes: (a) Relative error in the energy norm and (b) The rate of convergence

Table 3.8: The average rate of convergence in the energy error using distorted elements

Problems	Q4	SFEM			
		SC1Q4	SC2Q4	SC3Q4	SC4Q4
Cantilever beam	0.965	1.086	0.986	0.970	0.966
Hollow cylinder	0.993	0.905	0.897	0.919	0.951
Crack	0.499	0.693	0.525	0.514	0.510

3.6   Concluding Remarks

In this chapter, a very simple method was presented, which can help alleviate some of the difficulties met by conventional displacement finite element methods for two-dimension problems, while maintaining ease of implementation, and low computational costs.

A variational theory behind the class of stabilized integrated finite elements with strain smoothing is analyzed, and carried out convergence studies for compressible and incompressible elastostatics including problems with rough stress solutions, among which a simple fracture mechanics problem.

The method is based on a strain smoothing technique, similar to that used in stabilized conforming nodal integration for meshfree methods. The stiffness matrix is calculated by boundary integration, as opposed to the standard interior integration of the traditional FEM. In all the numerical examples that were tested, at least one of the four element formulations presented is more accurate than the standard four-noded quadrilateral element, for an asymptotically (when the mesh size tends to zero) lower computational cost.

Numerical results show that the four-noded quadrilateral $SC1Q4$ element is consistently superconvergent in the sense of the energy norm, and yields, for problems with a smooth solution, a convergence rate of 2.0 both in the H^1 norm and the L^2 norm. This is explained by the equivalence of the $SC1Q4$ element with the associated Q4 equilibrium element. For problems with rough solutions such as the L-shape or crack problems, the stabilized conforming nodal integration confers the method the same convergence rate as that of a displacement finite element method for problems with smooth solutions, i.e. 1.0 in the energy norm, and 2.0 in the L^2 norm.

Another advantage of the method, emanating from the fact that the weak form is integrated on element boundaries and not on their interiors is that the proposed formulation still gives accurate and convergent results –although not uniformly convergent– for distorted meshes. For the three problems tested, the average convergence rate in the energy norm is always very close to the standard finite element convergence rate, and, except for the case of the hollow cylinder, surpasses this standard rate. Although an in depth convergence analysis for distorted meshes is yet to be performed, the preliminary results obtained here tend to show improved asymptotic convergence rates for the $SC1Q4$ element over the standard FEM.

It seems that the method presented here is very attractive by

- Its simplicity;

- Its sound variational basis and closeness with the standard FEM;

- Its formal equivalence with quasi-equilibrium finite element methods for the single smoothing cell, and with displacement finite element methods for which number of the smoothing cells tend to infinitive;

- Its insensibility to volumetric locking;

- Its efficiency and accuracy on distorted meshes;

- Its improved convergence rate for problems with rough solutions including finite element problems;

The above points will be further investigated in the coming chapters.

Chapter 4

The smoothed finite element methods for 3D solid mechanics

4.1 Introduction

Theoretical developments, accuracy, convergence and stability results of the SFEM for 2D elasticity were presented in Liu *et al.* (2007b). The idea behind this technique is to use a strain measure calculated as the spatial average of the standard (symmetric gradient of the displacements), compatible, strain field. Different numbers of smoothing cells (nc) per element confer the method different properties. A recent review on SFEM is given in Bordas *et al.* (2008a) where these properties are given in detail, and examples of applications to plates, shells, plasticity and coupling with partition of unity enrichment for cracks are addressed. For completeness, the most salient features of the 2D SFEM can be summarized as follows: Integration can be performed on the boundary of the smoothing cells, which simplifies the formulation of polygonal elements; No isoparametric mapping is necessary, thus, highly distorted meshes are acceptable and the computational cost is slightly reduced; Because the divergence theorem is used to write the strain field, the derivatives of the shape functions are not needed to compute the stiffness matrix. The compliance of the resulting stiffness matrix increases with the number of subcells, as do the stress error, total energy and sensitivity to volumetric locking. On the contrary, the displacement error decreases with an increasing number of subcells (Liu *et al.* (2007b)). In Nguyen-Xuan *et al.* (2007b), the well-known L-shape problem and a simple crack problem were solved for various numbers of subcells. The numerical results given in chapter 3 show that for the linear elastic crack problem, the convergence rate attained by the one subcell four noded quadrilateral (SC1Q4) reaches 1.0 in the energy (H1) norm, as opposed to the theoretical (for FEM) rate of 1/2. The reason for this behaviour can be explained as follows: the SC1Q4 results in using average strains on the overall element and is identical to the Q4 with the one-point integration scheme. As proved by Zienkiewicz & Taylor (2000), superconvergent sampling points coincides the one-point integration scheme for the Q4. Hence the SC1Q4 achieves the superconvergent in energy

norm and optimal stresses. In other front on the Q4, Kelly (1979, 1980) showed that the Q4 with reduced integration inherited properties of an equilibrium element. The super-convergent property of equilibrium elements was proved mathematically by Johnson & Mercier (1979).

The purpose of this chapter is to extend the strain smoothing technique to the 8-node hexahedral element. Conceptually, the idea of method is similar to the 2D SFEM but the following alternative reasons for changing the approach to the smoothed strain calculation should be considered:

- If the surfaces of the element are not too curved, i.e. the variation of the normal vector at points belonging to the faces of the elements is small, the stiffness matrix formulation is evaluated by the boundary integration of the smoothing cells and one Gauss point may be used to compute the smoothed strain-displacement matrix.

- When the boundary surfaces of the element have a large curvature, the normal vector is no longer constant along the faces of the elements. This demands higher numbers of integration points on the boundary of the smoothing cells, which can defeat the initial purpose of the technique. Therefore a technique to compute the smoothed strain-displacement matrix through volume averaging inside of boundary averaging is shown. It is recommended to use this technique for highly curved elements. The gradients are calculated in the FEM and the smoothed strains are carried out numerically using Gauss quadrature inside the smoothing cells. The choice of such approaches was mentioned recently by Stolle & Smith (2004). However, the proposed technique is more flexible than that of Stolle et al. The present method is studied in detail for compressible and nearly incompressible materials and propose a stabilization formulation for the SFEM.

Numerical results show that the SFEM performs well for analysis of 3D elastic solids. The work on the 3D SFEM was submitted recently for publication in Nguyen-Xuan *et al.* (2008a).

4.2   The 8-node hexahedral element with integration cells

4.2.1   The stiffness matrix formulations

Consider an element Ω^e contained in the discretized domain Ω_h. Ω^e is partitioned into a number of smoothing cells noted Ω_C. Consider now an arbitrary smoothing cell, $\Omega_C \subset \Omega^e \subset \Omega^h$, as illustrated in Figure 4.1 with boundary $S_C = \bigcup_{b=1}^{nb} S_C^b$, where S_C^b is the bth boundary surface of S_C and nb is the total number of surfaces composing S_C.
The following notations are used in the remainder of the derivation:

- nc: number of smoothing cells in element Ω_e (see Figure 4.3);

- $V_C = \int_{\Omega_C} d\Omega$: volume of cell Ω_C;

- $\mathbf{D}$: matrix form of Hooke's elasticity tensor;

- $N_I(\mathbf{x})$ is the shape function associated with node I evaluated at point $\mathbf{x}$

Given a point $\mathbf{x}_C \in \Omega^e$, assume that $\mathbf{x}_C \in \Omega_C$. Similarly to the 2D SFEM formulation, the smoothed strains for 8-node hexahedral element are written as

$$\tilde{\varepsilon}_{ij}^h(\mathbf{x}_C) = \frac{1}{2V_C} \int_{\Omega_C} \left(\frac{\partial u_i^h}{\partial x_j} + \frac{\partial u_j^h}{\partial x_i} \right) d\Omega = \frac{1}{2V_C} \int_{S_C} (u_i^h n_j + u_j^h n_i) dS \qquad (4.1)$$

The smoothed strain is formulated by replacing $\mathbf{B}$ into $\tilde{\mathbf{B}}$ in Equation (2.19) and

$$\tilde{\varepsilon}^h = \tilde{\mathbf{B}}\mathbf{q} \qquad (4.2)$$

The smoothed element stiffness matrix then is computed by

$$\tilde{\mathbf{K}}^e = \sum_{C=1}^{nc} \int_{\Omega_C} \tilde{\mathbf{B}}_C^T \mathbf{D} \tilde{\mathbf{B}}_C d\Omega = \sum_{C=1}^{nc} \tilde{\mathbf{B}}_C^T \mathbf{D} \tilde{\mathbf{B}}_C V_C \qquad (4.3)$$

where nc is the number of the smoothing cells of the element (see Figure 4.3) and $\tilde{\mathbf{B}}_C$ is constant over each Ω_C and is of the following form

$$\tilde{\mathbf{B}}_C = \begin{bmatrix} \tilde{\mathbf{B}}_{C1} & \tilde{\mathbf{B}}_{C2} & \tilde{\mathbf{B}}_{C3} & \ldots & \tilde{\mathbf{B}}_{C8} \end{bmatrix} \qquad (4.4)$$

Here, the 6×3 submatrix $\tilde{\mathbf{B}}_{CI}$ represents the contribution to the strain displacement matrix associated with shape function at each node I and cell C and writes

$$\tilde{\mathbf{B}}_{CI} = \frac{1}{V_C} \int_{S_C} \mathbf{n}^T N_I(\mathbf{x}) dS, \quad \forall I \in \{1, ..., 8\}, \forall C \in \{1, ..., nc\} \qquad (4.5)$$

Inserting Equation (4.5) into Equation (4.3), the smoothed element stiffness matrix is computed along the surface of the smoothing cells of the element:

$$\tilde{\mathbf{K}}^e = \sum_{C=1}^{nc} \frac{1}{V_C} \left(\int_{S_C} \mathbf{n}^T \mathbf{N}(\mathbf{x}) dS \right)^T \mathbf{D} \left(\int_{S_C} \mathbf{n}^T \mathbf{N}(\mathbf{x}) dS \right) \qquad (4.6)$$

where $\mathbf{N}$ is the shape matrix given in Appendix C.
Equation (4.5) is computed on surfaces of Ω_C. The smoothed gradient matrix can be formulated as

$$\tilde{\mathbf{B}}_{CI}(\mathbf{x}_C) = \frac{1}{V_C} \sum_{b=1}^{nb} \begin{pmatrix} N_I\left(\mathbf{x}_b^G\right) n_x & 0 & 0 \\ 0 & N_I\left(\mathbf{x}_b^G\right) n_y & 0 \\ 0 & 0 & N_I\left(\mathbf{x}_b^G\right) n_z \\ N_I\left(\mathbf{x}_b^G\right) n_y & N_I\left(\mathbf{x}_b^G\right) n_x & 0 \\ 0 & N_I\left(\mathbf{x}_b^G\right) n_z & N_I\left(\mathbf{x}_b^G\right) n_y \\ N_I\left(\mathbf{x}_b^G\right) n_z & 0 & N_I\left(\mathbf{x}_b^G\right) n_x \end{pmatrix} A_b^C \qquad (4.7)$$

where $\mathbf{x}_b^G$ and A_b^C are the midpoint (Gauss point) and the area of Γ_b^C, respectively.

In principle, 2×2 Gauss quadrature points (the same as the isoparametric Q4 element) on each surface are sufficient for an exact integration because the bilinearly shape function is met on surfaces of the H8 element. Hence the mapping from the facets of cell into the parent element (the square element) needs to be evaluated. Then the determinant of the Jacobian matrix over the cell boundaries needs to be computed, it increases the computational cost when many cells are employed and consequently the element stiffness matrix becomes stiffer. One can address this behaviour to the Q4 or H8 element. To alleviate these disadvantages, a reduced one-point quadrature on each surface of the cell is carried out. However, the use of reduced integration may cause instability of the element due to a deficient rank of stiffness matrix when small number of smoothing cells are exploited. To ensure a sufficient rank, many cells can be used. Hence this may be considered as a form of the assumed strain method for one-point quadrature eight-node hexahedral elements, e.g. Belytschko & Bindeman (1993); Fredriksson & Ottosen (2007), where the reduced (constant) stiffness matrix is enhanced by the stabilization matrix in order to ensure proper rank while for the present element the stability is included by a necessarily large number of cells employed. More details will be given in numerical tests.

Next it will be shown how to compute the smoothed strain-displacement matrix inside of the smoothing cells instead of evaluating it on their boundaries. This is used in case of elements with highly curved surfaces.

From Equations (4.1) and (4.5), the smoothed strain-displacement matrix in the original form writes as follows

$$\tilde{\mathbf{B}}_{CI} = \frac{1}{V_C} \int_{\Omega_C} \begin{bmatrix} N_{I,x} & 0 & 0 \\ 0 & N_{I,y} & 0 \\ 0 & 0 & N_{I,z} \\ N_{I,y} & N_{I,x} & 0 \\ 0 & N_{I,z} & N_{I,y} \\ N_{I,z} & 0 & N_{I,x} \end{bmatrix} d\Omega \equiv \frac{1}{V_C} \int_{\Omega_C} \mathbf{B}_I d\Omega, \quad \forall I \in \{1, ..., 8\} \quad (4.8)$$

Let $\mathbf{x}_C = [x_C \ y_C \ z_C]^T$ contain the coordinates of vertices of the smoothing cell, C. Now the smoothing cell, C is mapped to a parent element ((a) as shown in Figure 4.2) similarly to the standard FEM. The coordinates of an arbitrary point in the cell can be determined by linear combination of the coordinates of the cell vertices multiplied with the shape function of the standard eight-node brick element. One has

$$\mathbf{x}^{cell} (\xi^c, \eta^c, \zeta^c) = \sum_{I=1}^{8} N_I (\xi^c, \eta^c, \zeta^c) \mathbf{x}_{CI} \equiv \sum_{I=1}^{8} N_I (\boldsymbol{\xi}^c) \mathbf{x}_{CI} \quad (4.9)$$

where $\boldsymbol{\xi}^c = (\xi^c, \eta^c, \zeta^c)$ denote the natural coordinate system for the parent element that is used to describe for the cell, C. By using $2 \times 2 \times 2$ Gauss quadrature points, the smoothed strain-displacement matrix writes

$$\tilde{\mathbf{B}}_{CI} = \frac{1}{V_C} \sum_{j=1}^{2} \sum_{k=1}^{2} \sum_{l=1}^{2} \mathbf{B}_I^{(b)}(\xi_j^G, \eta_k^G, \zeta_l^G) \left| \mathbf{J}^{(c)}(\xi_j^c, \eta_k^c, \zeta_l^c) \right| w_j w_k w_l \quad (4.10)$$
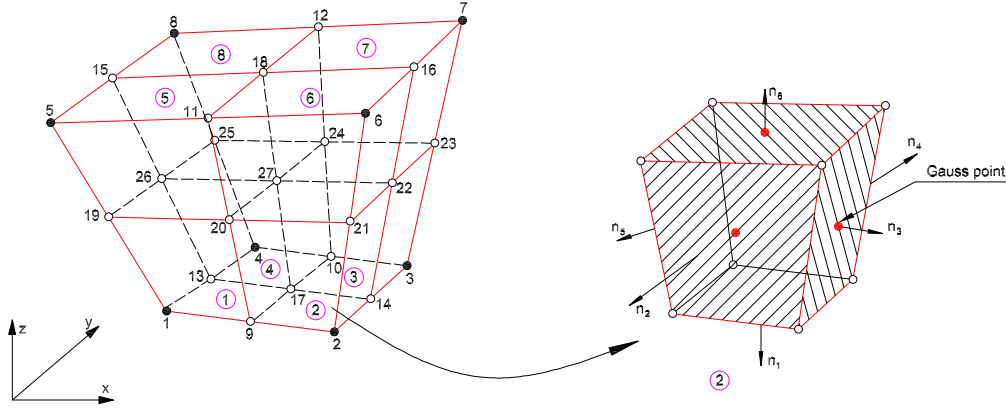
Figure 4.1: An illustration of single element subdivided into eight smoothing solid cells and numbering of the cells

where the index (b) denotes the transformation from the finite element to a parent element, the index (c) denotes the transformation from the smoothing cell to the parent element (see Figure 4.2), $(\xi_j^c, \eta_k^c, \zeta_l^c)$ and (w_j, w_k, w_l) are Gauss points and their weights, $(\xi_j^G, \eta_k^G, \zeta_l^G)$ will be discussed below. As mentioned above, the Jacobian matrix $\mathbf{J}^{(c)}$ for the cell is evaluated by

$$\mathbf{J}^{(c)} = \sum_{I=1}^{8} \begin{bmatrix} \frac{\partial N_I}{\partial \xi^c} x_{CI} & \frac{\partial N_I}{\partial \xi^c} y_{CI} & \frac{\partial N_I}{\partial \xi^c} z_{CI} \\ \frac{\partial N_I}{\partial \eta^c} x_{CI} & \frac{\partial N_I}{\partial \eta^c} y_{CI} & \frac{\partial N_I}{\partial \eta^c} z_{CI} \\ \frac{\partial N_I}{\partial \zeta^c} x_{CI} & \frac{\partial N_I}{\partial \zeta^c} y_{CI} & \frac{\partial N_I}{\partial \zeta^c} z_{CI} \end{bmatrix} \tag{4.11}$$

Similarly to the H8 element, $\mathbf{J}^{(c)}$ for each smoothing cell is also evaluated at $2 \times 2 \times 2$ Gauss quadrature points.

Another issue involved at this stage is the mapping of a point from the global coordinate system (the element) to the local coordinate system which required solving the solution of the following equations:

$$\mathbf{x} = \sum_{I=1}^{8} N_I \left(\xi^G, \eta^G, \zeta^G \right) \mathbf{x}_I \equiv \sum_{I=1}^{8} N_I \left(\boldsymbol{\xi}^G \right) \mathbf{x}_I \tag{4.12}$$

where $\mathbf{x}_I$ are the nodal coordinates of the element and $\mathbf{x}$ is the global coordinate vector of the point in the cell C contained in the element while (ξ^G, η^G, ζ^G) are the local coordinates and unknowns of the equations (4.12). For the H8 element, this is a nonlinear system of equations which can be solved by the Newton-Raphson method. Equation (4.12) is rewritten as

$$\mathbf{F}(\mathbf{x}) = \sum_{I=1}^{8} N_I \left(\boldsymbol{\xi}^G \right) \mathbf{x}_I - \mathbf{x} = \mathbf{0} \tag{4.13}$$

56
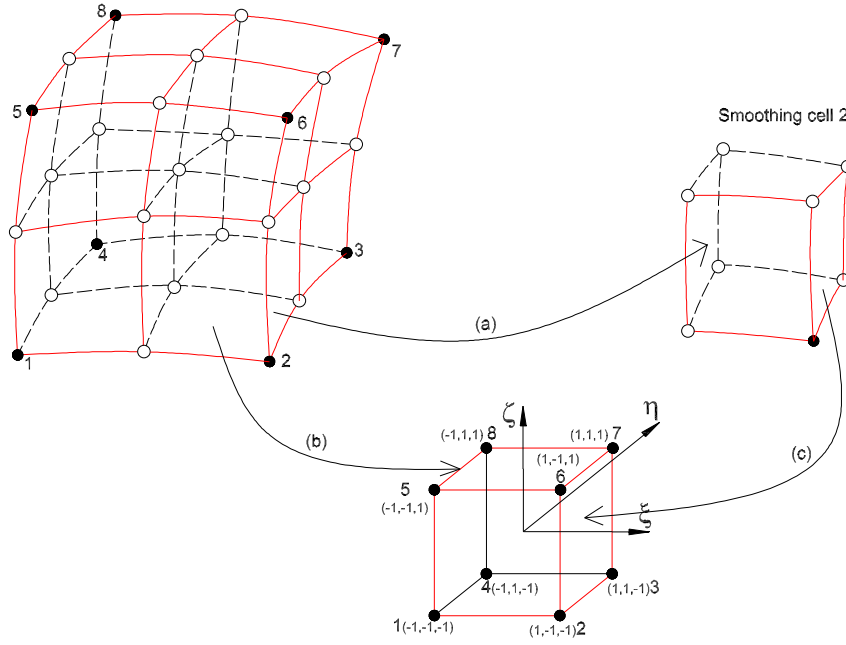
Figure 4.2: Transformation from the cell to the parent element

An expansion of $\mathbf{F}(\mathbf{x})$ in a Taylor series at $\boldsymbol{\xi}^G = \boldsymbol{\xi}_0^G$ is done and kept the linear terms only. It leads to

$$\nabla \mathbf{F} \delta \boldsymbol{\xi}^G + \mathbf{F}(\boldsymbol{\xi}_0^G) = \mathbf{0} \tag{4.14}$$

Then Equation (4.14) with unknowns of $\delta \boldsymbol{\xi}^G$ is solved and the values of $\boldsymbol{\xi}^G$ is updated:

$$\boldsymbol{\xi}^G = \boldsymbol{\xi}_0^G + \delta \boldsymbol{\xi}^G \tag{4.15}$$

After $\boldsymbol{\xi}^G$ is found, $\mathbf{B}_I^{(b)}$ is completely determined. The procedure in Equations (4.10) to (4.15) is repeated for all Gauss points $(\xi_j^c, \eta_k^c, \zeta_l^c)$.

4.2.2 Notations

The eight-node hexahedral (H8) with smoothed strains for k subcells is named by the $SCkH8$ element –for Smoothed k subcell eight-node hexahedral. Figure 4.3 illustrates a division with $nc = 1, 2, 4$ and 8 corresponding to SC1H8, SC2H8, SC4H8 and SC8H8 elements.

4.2.3 Eigenvalue analysis, rank deficiency

By analyzing the eigenvalue of the stiffness matrix, SC4H8, SC8H8 contain six zero eigenvalues corresponding to the six rigid body modes. Hence these elements always

57

have sufficient rank and no spurious zero-energy modes. In contrast, SC1H8 and SC2H8 exhibit twelve and six spurious zero energy modes, respectively. Hence, they do not possess a proper rank. However, for the examples tested below, the important property that the SC1H8 and SC2H8 elements exhibit high accuracy for stresses while displacements are slightly poorer is obtained. This feature is the same as in equilibrium approaches (Fraeijs De Veubeke (1965)) in which the equilibrium equations are a priori verified, but the proposed formulation is simpler and closely related to displacement approaches.

4.2.4   A stabilization approach for SFEM

In this section, a stabilized approach for the 3D SFEM providing the basis for the construction of hexahedral elements with sufficient rank and higher stress accuracy is proposed. Note that this technique still performs well for the 2D SFEM. However, in this method, we only illustrate numerical benchmark problems for the 3D model.

As shown in Section 4.5, choosing a single subcell yields the SC1H8 element which yields accurate and superconvergent stresses and less accurate displacements, for all examples tested. Additionally, this element is insensitive to volumetric locking. However, as noted above, the SC1H8 element is rank deficient.

Otherwise, the SC4H8 and SC8H8 elements are stable but are still sensitive to volumetric locking and locking due to bending.

The idea is to construct an element whose stiffness matrix is a combination of that of the SC1H8 and SC4H8. The idea is the same as the stabilized nodal integration for tetrahedral elements in Puso & Solberg (2006) and in Puso *et al.* (2007) for meshfree methods. The stabilized element stiffness matrix is formulated as follows

$$\tilde{\mathbf{K}}^e_{stab} = \tilde{\mathbf{K}}^e_{SC1H8} + \tilde{\mathbf{K}}^e_{SC4H8} \tag{4.16}$$

Here $\tilde{\mathbf{K}}^e_{SC1H8}$ and $\tilde{\mathbf{K}}^e_{SC4H8}$ denote the stiffness matrix of the SC1H8 and SC4H8 elements, respectively, defined by

$$\tilde{\mathbf{K}}^e_{SC1H8} = \tilde{\mathbf{B}}^T(\mathbf{D} - \alpha\tilde{\mathbf{D}})\tilde{\mathbf{B}}V^e, \quad \tilde{\mathbf{K}}^e_{SC4H8} = \sum_{C=1}^{4} \alpha\tilde{\mathbf{B}}_C^T\tilde{\mathbf{D}}\tilde{\mathbf{B}}_C V_C \tag{4.17}$$

where $\tilde{\mathbf{B}}$ is determined on the element having the volume V^e, α is a stabilization parameter belonging to interval of $0 \leq \alpha \leq 1$ and $\tilde{\mathbf{D}}$ is a stabilization material matrix. It is verified that the stabilization element is equivalent to the SC1H8 as $\alpha = 0$ and when $\alpha = 1, \tilde{\mathbf{D}} = \mathbf{D}$, the SC4H8 element is recovered by the stabilization element. It is also noted that material matrix $\tilde{\mathbf{D}}$ chosen aims to minimize the effects of volumetric locking phenomenon and to preserve the global stability of stiffness matrix. These reasons were discussed in details by Puso & Solberg (2006). For isotropic elastic materials, Lamé parameters $\tilde{\mu}$ and $\tilde{\lambda}$ in $\tilde{\mathbf{D}}$ are chosen such as

$$\tilde{\mu} = \mu \text{ and } \tilde{\lambda} = min(\lambda, 25\tilde{\mu}) \tag{4.18}$$

where λ, μ and $\mathbf{D}$ are given in Appendix C.

Such a stabilization procedure was used for the FEM to obtain a mid-way between the fully and under integrated H8 element. In the following, the stabilized elements are denoted as H8s, SC4H8s and SC8H8s.

Numerical results indicated that a suitable choice of the stabilization parameter $\alpha \in [0, 1]$ can be chosen to obtain stable results when the deformation is bending dominated.

According to benchmarks in Section 4.5, the value of the stabilization parameter is chosen such that the element maintains the sufficient rank and inherits the high accuracy in the stress of the SC1H8.

4.3   A variational formulation

Similarly the 2D case (Liu *et al.* (2007b)), a two field variational principle is suitable for the present method. Consequently, the SFEM solution is identical to the FEM solution when nc tends to infinity. However, if $nc = 1$, the SFEM element (SC1H8) is not always equivalent to the reduced H8 element using one-point integration schemes. This is different from plane conditions where the equivalence of the SC1Q4 element and the Q4 element with the reduced integration always holds. Referring to the reduced integration in the three-dimension case, Fredriksson & Ottosen (2007) provide for more detail. Additionally, it is observed that the SC1H8 element passes the patch test a priori with the distorted element while the reduced H8 element using one-point integration fails the patch test.

4.4   Shape function formulation for standard SFEM

In this section, a possible formulation of the shape functions for the SFEM is shown for the element surfaces having a small curvature. An eight-node hexahedral element may be divided into smoothing cells, as shown in Figure 4.3. Strain smoothing is calculated over each cell and the volume integration on the smoothing cell is changed into surface integration on the boundary of the cell. Here, four forms of the smoothed integration solids are illustrated in Figure 4.3. In the SFEM, the shape functions themselves can be used to compute the smoothed gradient matrix $\tilde{\mathbf{B}}$ and the stiffness matrix is derived from surface integration on the boundary of the smoothing cells, therefore, the shape functions are only required on the surfaces of the smoothing cells. The shape functions are constructed simply through linear interpolation on each edge of a cells boundary surface and its values at the Gauss points on these boundary surfaces are easily evaluated.
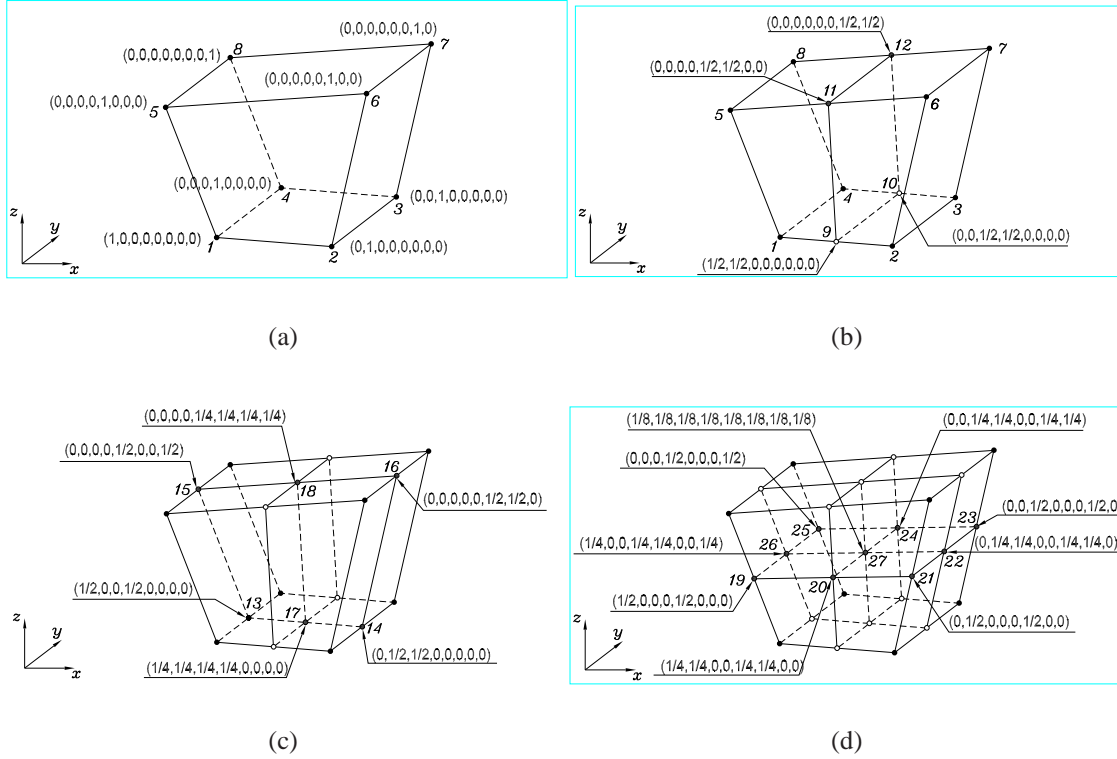
Figure 4.3: Division of an element into smoothing cells (nc) and the value of the shape function on the surfaces of cells: (a) the element is considered as one cell, (b) the element is subdivided into two cells, and (c) the element is partitioned into three cells and (d) the element is partitioned into four cells. The symbols (●) and (○) stand for the nodal field and the integration node, respectively

4.5 Numerical results

4.5.1 Patch test

The patch test for 3D FEM, proposed by MacNeal & Harder (1985) is here employed to test the new elements. The purpose of this illustration is to examine the convergence of the present method under linear displacements imposed along the boundaries. Prescribed displacements at the exterior nodes only (9,...,16) are of the analytical solution given by

$$u(x, y, z) = 5(2x + y + z) \times 10^{-4}, \; v(x, y, z) = 5(x + 2y + z) \times 10^{-4},$$
$$w(x, y, z) = 5(x + y + 2z) \times 10^{-4} \tag{4.19}$$

Figure 4.4 describes a unit cube with 7 hexahedral distorted elements. A comparison of analytical solution and the SFEM (for all smoothing cells considered) is presented in Table 4.1. It is observed that the exact values is to machine precision. The SFEM passes the patch test, it is therefore capable of reproducing a linear field to machine precision. This property ensures convergence of the new elements with mesh refinement.
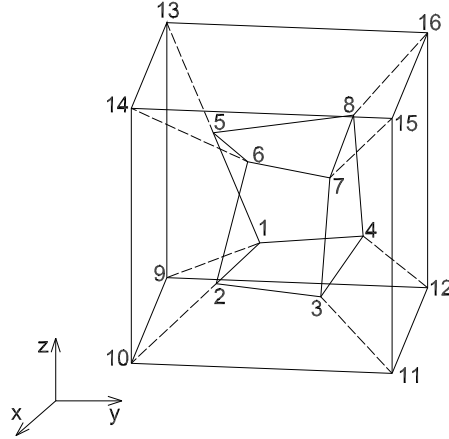
Figure 4.4: Patch test for solids: $E = 1 \times 10^6$, $\nu = 0.25$

4.5.2 A cantilever beam

A cantilever beam, see Figure 4.5a, as studied in Chapter 3 is considered in 3D. Figure 4.5b illustrates the discretization with a regular mesh of eight-node hexahedral elements. Next the accuracy of the SFEM elements is analyzed, assuming a near incompressible material, $\nu = 0.4999$. Figure 4.7 plots the results of vertical displacements, normal tresses and shear stresses along the neutral axis for mesh of 256 hexahedral elements. It is clear that the poor accuracy in the displacement for all elements is observed for all elements, especially the the SC1H8 and SC2H8 elements while these elements

Table 4.1: Patch test for solid elements

Node	Analytical/10^4			SFEM/10^4		
	u	v	w	u	v	w
1	5.16	5.625	4.875	5.16	5.625	4.875
2	11.14	8.45	8.45	11.14	8.45	8.45
3	13.06	12.06	10.13	13.06	12.06	10.13
4	7.63	10.02	7.415	7.63	10.02	7.415
5	7.345	6.675	8.96	7.345	6.675	8.96
6	11.71	9.85	11.74	11.71	9.85	11.74
7	14.57	14.09	13.85	14.57	14.09	13.85
8	8.885	11.79	11.57	8.885	11.79	11.57
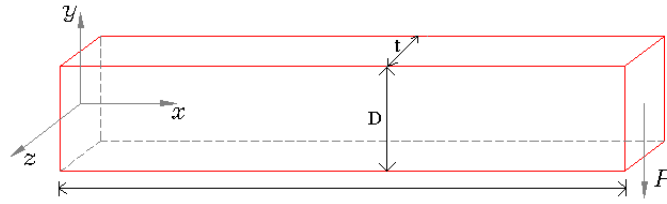
(a)
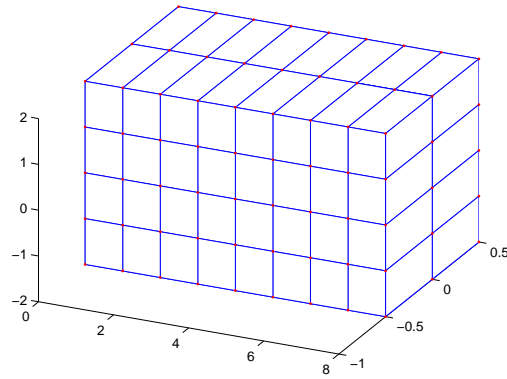
(b)

Figure 4.5: A 3D cantilever beam subjected to a parabolic traction at the free end; (a) Problem, (b) 64 eight-node hexahedral elements
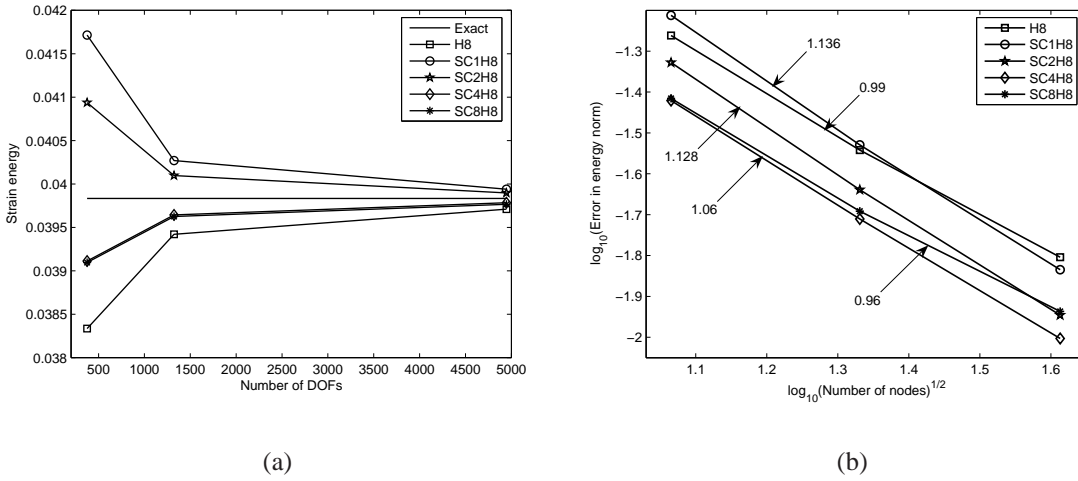
Figure 4.6: Convergence in energy norm of cantilever beam; (a) strain energy, (b) convergence rate

yield more accurate stresses than the H8, SC4H8 and SC8H8. Note that the SC1H8 and SC2H8 elements suffer also from slow displacement accuracy for the compressible case. In contrast, all stabilized elements ($\alpha = 0.1$) are results that are in good agreement with the analytical solution, as indicated by Figure 4.8.

4.5.3 Cook's Membrane

A tapered panel (of unit thickness) given in Chapter 3, but a 3D model now is considered, see Figure 4.9. Purpose of this example is to test behaviour of the elements under an in-plane shearing load, $F = 1$, resulting in deformation dominated by a bending response. Therefore, this benchmark problem has investigated by many authors in order to verify the performance of their elements. Because the exact solution is unknown, the best reference solutions are exploited. With $\nu = 1/3$, the reference value of the vertical displacement at center tip section (C) is 23.9642 (Fredriksson & Ottosen (2004)) and the reference value of the strain energy is 12.015 (Mijuca & Berković (1998)).

In this example, the present elements are also compared to the assumed strain stabilization element (ASQBI) developed by Belytschko & Bindeman (1993). The figures in energy norm correspond to dimensionless length $h = 1/\sqrt{N}$, where N is the number of degrees of freedom (D.O.F) remaining after applying boundary conditions. As resulted in Figure 4.10 and Figure 4.11a, although the SFEM elements are significantly better than the H8 element, the their convergence are too slow, especially very coarse meshes used. As expected, their responses in bending are in general far too stiff while the ASQBI performs well. As seen from Figures 4.11b–4.11d, it is admirable to observe that the SFEM elements with stabilization version exhibit the very high accuracy compared to the H8s

(a)

(b)

(c)
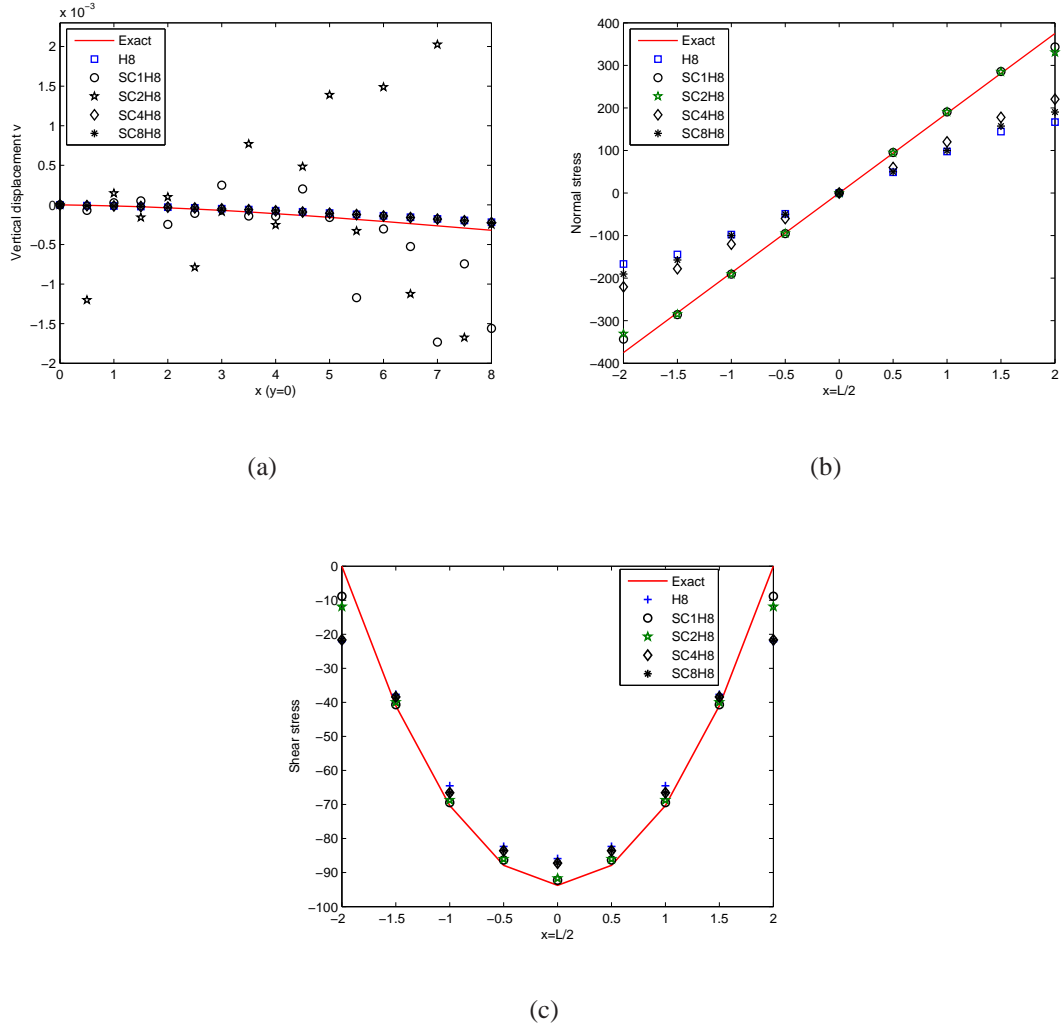
Figure 4.7: Solutions of 3D cantilever in near incompressibility : (a) vertical displacement ($0 \leq x \leq L$, y=0); (b) Normal stress ($-D/2 \leq y \leq D/2$); (c) Shear stress ($-D/2 \leq y \leq D/2$)
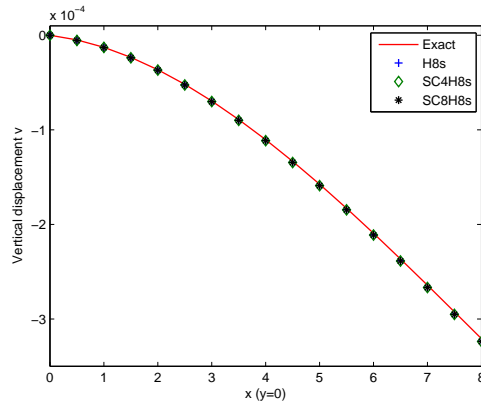
(a)
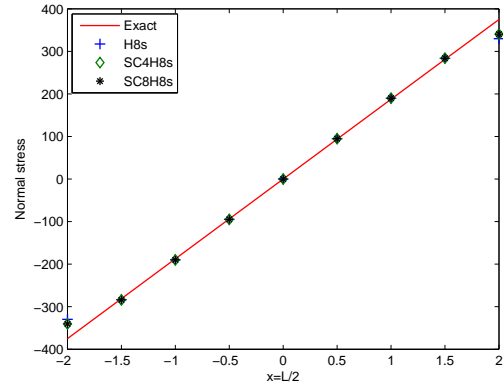
(b)
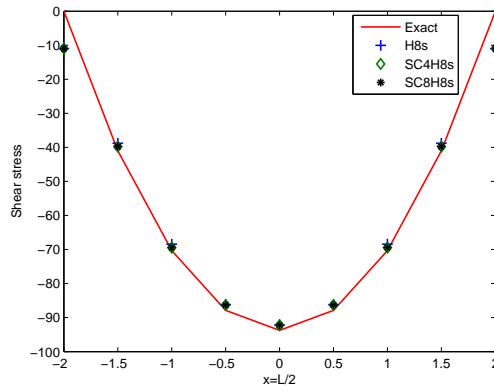
(c)

Figure 4.8: Solutions of 3D cantilever in near incompressibility using stabilization technique: (a) vertical displacement ($0 \leq x \leq L$, y=0); (b) Normal stress ($-D/2 \leq y \leq D/2$); (c) Shear stress ($-D/2 \leq y \leq D/2$)

and ASQBI. However, the stabilization approach for this problem do not make to improve the convergence rate of the SFEM elements. It is noted that for this problem the marginal difference between the SC4H8s and SC8H8s is addressed.
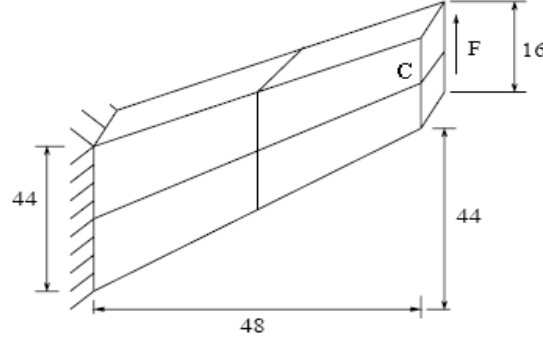
Figure 4.9: 3D Cook's membrane model and coarse mesh

(a)   (b)
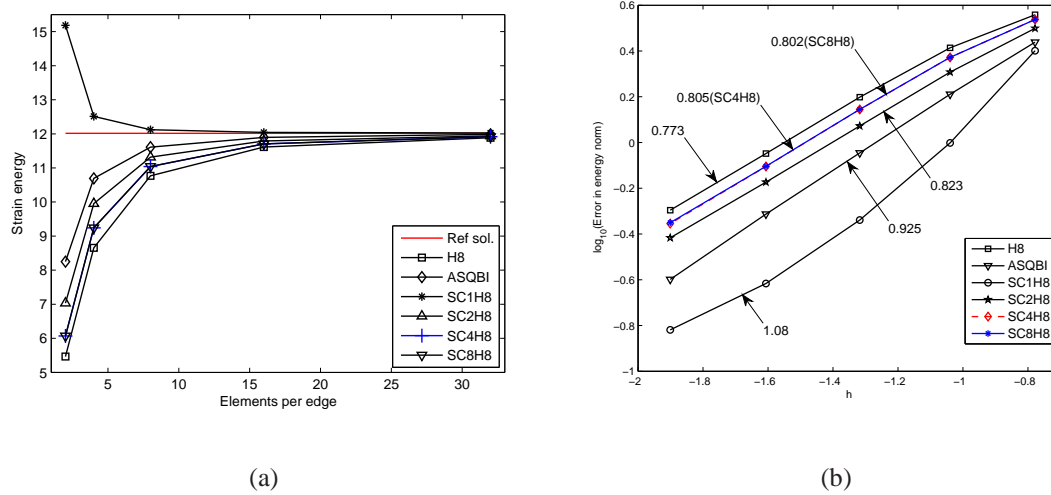
Figure 4.10: The convergence in energy norm; (a) Strain energy, (b) Convergence rate

4.5.4 A 3D squared hole plate

Consider the 3D squared hole plate subjected to the surface traction q as given by Figure 4.16. Due to its symmetry, a quarter of the domain is modelled. The numerical parameters are as follows: $q = 1, a = 1, t = 1, E = 1, \nu = 0.3$. Figure 4.13 plots deformation of domain after applying surface load. The estimated strain energy derived from the procedure of Richardson's extrapolation by Cugnon (2000) is 6.203121186.
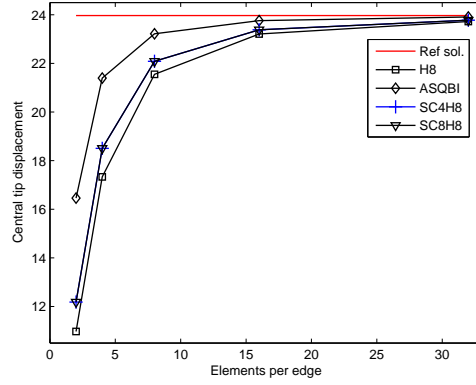
(a)
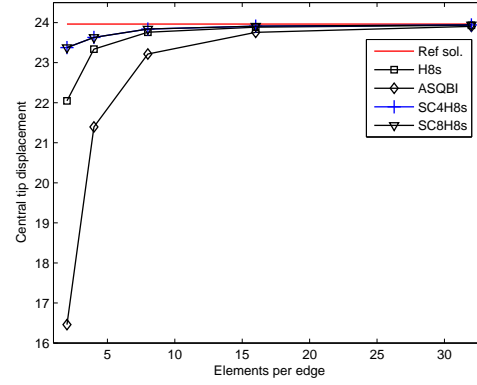
(b)
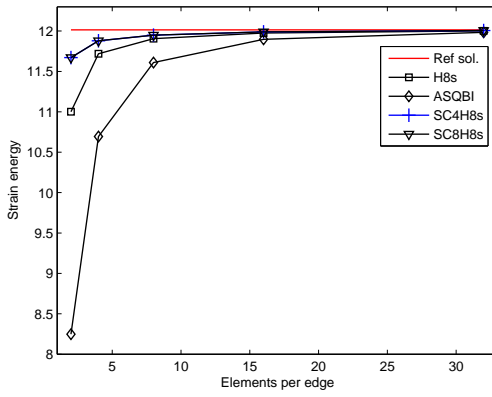
(c)
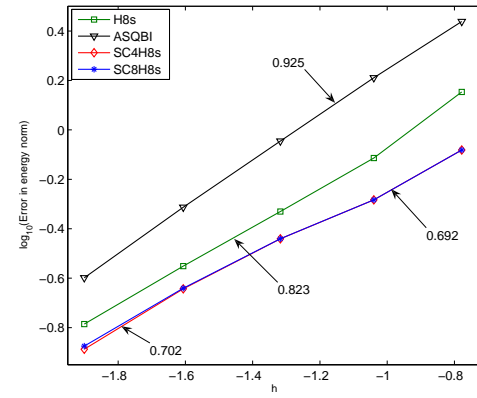
(d)

Figure 4.11: The convergence of tip displacement: (a) Without stabilization, (b) With stabilization ($\alpha = 0.1$); and (c), (d) Strain energy and convergence rate with stabilization ($\alpha = 0.1$), respectively

As mentioned in Chapter 3, a stress singularity exists at the re-entrant corner. The percentage of relative energy error is obtained in Table 4.2. The convergence of the strain energy is displayed on Figure 4.14a, and the convergence rates are given in Figure 4.14b. It is seen that the SFEM elements are more accurate than the standard FEM. Additionally, the SC1H8 provides the optimum rate for this singular problem.

Table 4.2: The results on percentage of relative error in energy norm of 3D L-shape

Mesh No.	D.O.F	H8	SC1H8	SC2H8	SC4H8	SC8H8
1	171	34.10	32.07	12.18	28.44	29.21
2	925	20.43	13.45	9.75	17.12	17.49
3	5913	12.01	6.45	6.37	10.24	10.42
4	11011	10.15	5.14	5.53	8.71	8.85
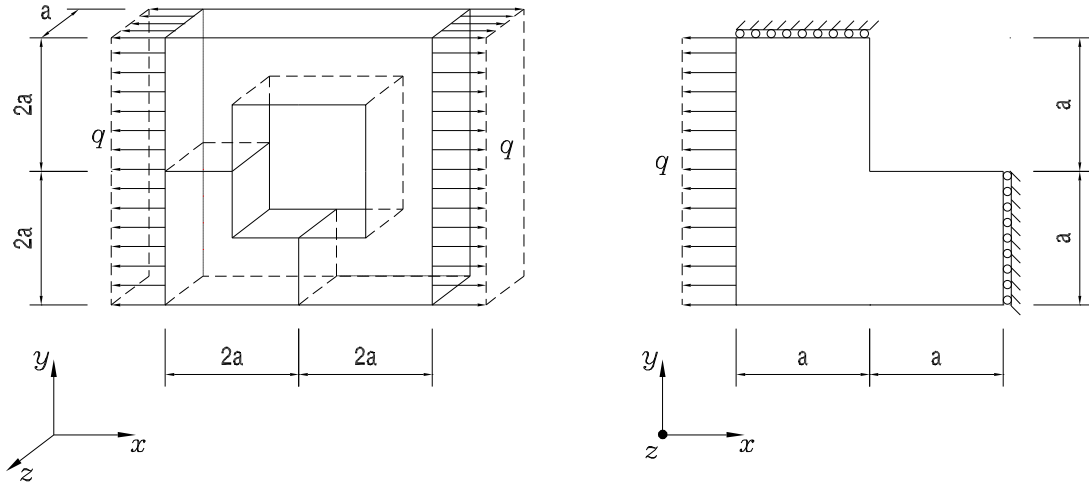
Figure 4.12: Squared hole structure under traction and 3D L-shape model

4.5.5 Finite plate with two circular holes

Figure 4.15a illustrates a finite plate with two holes of radius $r = 0.2m$ subjected to an internal pressure $p = 5kPa$. Due to its symmetry, only the below left quadrant of the plate is modeled. The material properties are: Young's modulus $E = 2.1 \times 10^{11} Pa$, poisson's ratio $\nu = 0.3$. The analytical solution is unknown. In order to estimate the reliability of
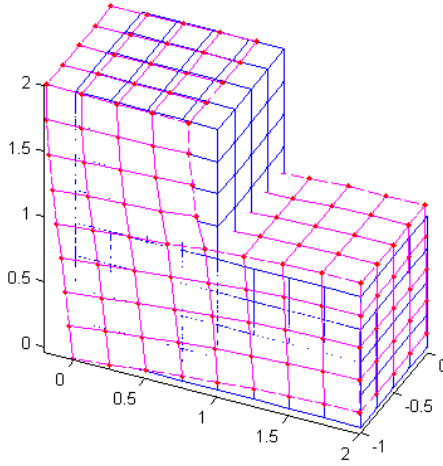
Figure 4.13: An illustration for deformation of 3D L-shape model
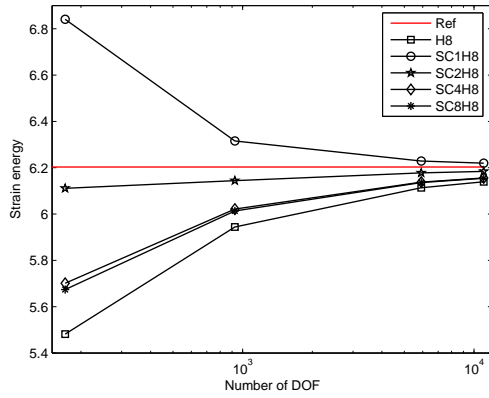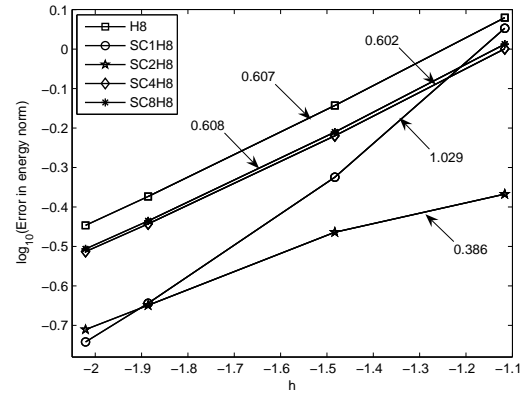
(a) (b)

Figure 4.14: The convergence in energy norm for the 3D square hole problem; (a) Strain energy, (b) Convergence rate

69

the present method, the procedure of Richardson's extrapolation (Richardson (1910)) is used for the SFEM solution and find that the best estimated strain energy obtained by the SC1H8 element is 0.61026×10^{-5}. The relative error and convergence rates are evaluated based on this estimated global energy. The convergence of energy norm is plotted in Figure 4.17. It is clear that superior accuracy of the SFEM elements over the standard H8 element is observed.

(a)   (b)
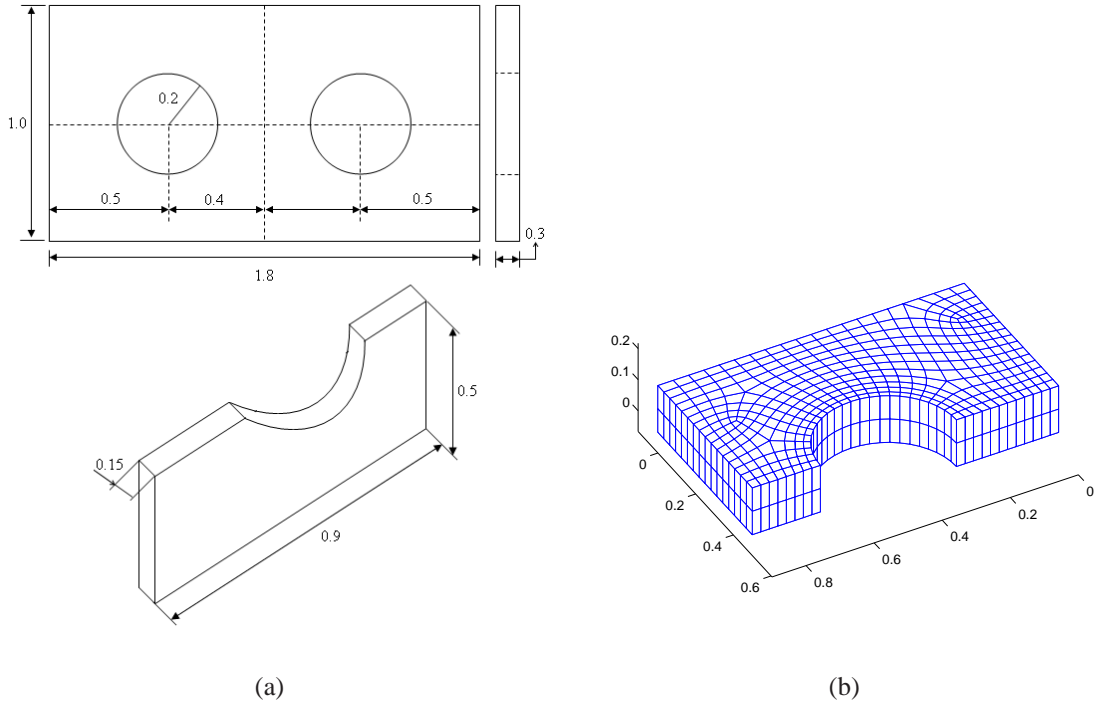
Figure 4.15: Finite plate with two circular holes and coarse mesh; (a) Model, (b) Mesh of 768 eight-node hexahedral elements

4.6 Concluding Remarks

This chapter formulated new 8 noded hexahedral elements based on the smoothed finite element method (SFEM) with various numbers of subcells. These elements are coined SCkH8 where k is the number of subcells. Low numbers of subcells lead to higher stress accuracy but instabilities; high numbers yield lower stress accuracy but are always stable.

A stabilization procedure is proposed where the stiffness matrix is written as a linear combination of the one subcell element and the four or eight subcell element, resulting in higher dual (stress) accuracy and the disappearance of zero energy modes.

For the element with highly curved boundaries, a modified volume averaging technique is proposed to replace the boundary averaging commonly used in SFEM (see also

Table 4.3: The results on percentage of relative error in energy norm of finite plate with two holes

Mesh No.	N	H8	SFEM			
			SC1H8	SC2H8	SC4H8	SC8H8
1	263	24.52	14.04	19.71	23.02	23.12
2	908	13.35	7.63	9.98	12.05	12.29
3	3350	7.38	3.77	5.15	6.23	6.70
4	12842	4.51	1.82	2.63	3.19	4.04
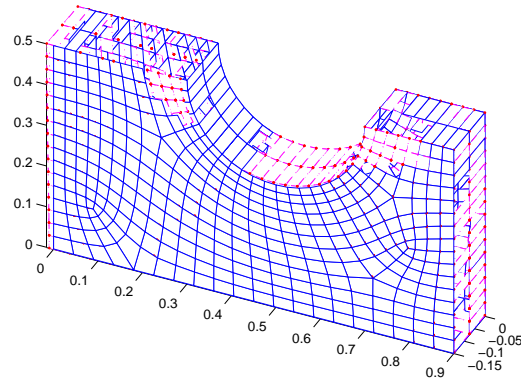
Figure 4.16: An illustration of deformation of the finite plate

(a)

(b)
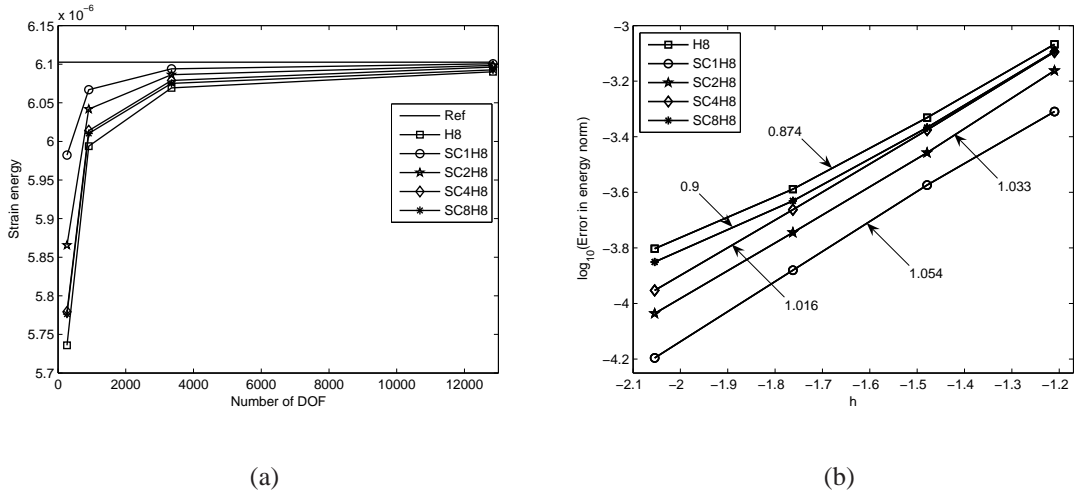
Figure 4.17: The convergence in energy norm; (a) Strain energy, (b) Convergence rate

the seminal work of Stolle & Smith (2004)).

- All the SCkH8 elements always pass the patch test, even for distorted meshes.

- Except for the SC1H8 and SC2H8 elements that exhibit zero energy modes, all other smoothed elements tested are rank sufficient.

- For all examples treated, the proposed elements provide more accuracy than the FEM brick elements and are insensitive to volumetric locking when suitably stabilized.

- The SC4H8 (without stabilization) and the SC4H8s (with stabilization) seem to be the best candidates for practical applications since they are both stable and accurate.

- The theoretical bases associated with the stabilization parameter need to be further investigated.

Based on the SFEM formulation coupling with partition of unity enrichment proposed by Bordas *et al.* (2008a) for two-dimensional crack, it will be interesting to mention how the present SFEM can improve current extended finite elements for three-dimensional fracture mechanics. Further studies on the behaviour of the method for distorted meshes are required to fully assess the performance of the proposed elements. Additionally, more complex problems with variable thickness should be examined.

Chapter 5

A smoothed finite element method for plate analysis

5.1 Introduction

Plate structures play an important role in science and engineering fields. There are two different plate theories, the Kirchhoff plate and the Mindlin-Reissner plate theory. Kirchhoff plates are only applicable for thin structures where shear stresses in the plate can be ignored. Moreover, Kirchhoff plate elements require C^1 continuous shape functions (Sander (1969); Debongnie (2003)). Mindlin-Reissner plates take shear effects into account. An advantage of the Mindlin-Reissner model over the biharmonic plate model is that the energy involves only first derivatives of the unknowns and so conforming finite element approximations require only the use of C^0 shape functions instead of the required C^1 shape functions for the biharmonic model. However, Mindlin-Reissner plate elements exhibit a phenomenon called shear locking when the thickness of the plate tends to zero. Shear locking results in incorrect transverse forces under bending. When linear finite element shape functions are used, the shear angle is linear within an element while the contribution of the displacement is only constant. The linear contribution of the rotation cannot be "balanced" by a contribution from the displacement. Hence, the Kirchhoff constraint $w_{,x} + \beta_y = 0$, $w_{,y} + \beta_x = 0$ is not fulfilled in the entire element any more. Typically, when shear locking occurs, there are large oscillating shear/transverse forces and hence a simple smoothing procedure can drastically improve the results. In order to avoid this drawback, various improvements of formulations as well as numerical techniques have been used, such as the reduced and selective integration elements (Hughes *et al.* (1977, 1978); Zienkiewicz *et al.* (1971)), equilibrium elements (Fraeijs de Veubeke & Sander (1968); Fraeijs De Veubeke *et al.* (1972); Sander (1969); Beckers (1972)), mixed formulation/hybrid elements by Lee & Pian (1978); Lee & Wong (1982); Nguyen & Nguyen-Dang (2006); Nguyen-Dang (1980b); Nguyen-Dang & Tran (2004); Pian & Tong (1969), the Assumed Natural Strain (ANS) method (Bathe & Dvorkin (1985, 1986); Dvorkin & Bathe (1994); Hughes & Tezduyar (1981)) and Enhanced Assumed Strain

(EAS) method (Andelfinger & Ramm (1993); Simo & Rifai (1990)). Many improved versions of plate elements have been developed and can be found in the textbooks (Bathe (1996); Zienkiewicz & Taylor (2000)). Alternative methods of stabilization approach such as given in Gruttmann & Wagner (2004), Kouhia (2007). Of course the references mentioned above are by no means exhaustive.

In this chapter, improved plate elements based on the MITC4 element in which the smoothing curvature technique (Chen *et al.* (2001)) is combined are presented. An introduction of a strain smoothing operation to the finite elements also has obtained by Liu *et al.* (2007a). It will be shown by numerical experiments that present method is faster and more accurate than the original MITC4 element, at least for all examples tested. Moreover, due to the integration technique, the element promises to be more accurate especially for distorted meshes. Also present element is free of shear locking in limitation of thin plate.

5.2   Meshfree methods and integration constraints

In mesh-free methods based on nodal integration for Mindlin–Reissner plates, convergence requires fulfilling bending exactness (BE) and thus requires the following bending integration constraint (IC) to be satisfied, see Wang & Chen (2004)

$$\int_\Omega \mathbf{B}_I^b(\mathbf{x})d\Omega = \int_\Gamma \mathbf{E}_I(\mathbf{x})d\Gamma \tag{5.1}$$

where $\mathbf{B}_I$ is the standard gradient matrix

$$\mathbf{B}_I^b = \begin{bmatrix} 0 & 0 & N_{I,x} \\ 0 & -N_{I,y} & 0 \\ 0 & -N_{I,x} & N_{I,y} \end{bmatrix}, \quad \mathbf{E}_I = \begin{bmatrix} 0 & 0 & N_I n_x \\ 0 & -N_I n_y & 0 \\ 0 & -N_I n_x & N_I n_y \end{bmatrix} \tag{5.2}$$

The IC criterion comes from the equilibrium of the internal and external forces of the Galerkin approximation assuming pure bending. This is similar to the consistency with the pure bending deformation in the constant moment patch test in FEM.

The basic idea is to couple the MITC element with the curvature smoothing method (CSM). Therefore, smoothing cells are constructed that do not necessarily have to be coincident with the finite elements. The integration is carried out either on the elements themselves, or over the smoothing cells that form a partition of the elements. The CSM is employed on each smoothing cell to normalize the local curvature and to calculate the bending stiffness matrix. The shear strains are obtained with independent interpolation functions as in the MITC element. Result of this work is given by Nguyen-Xuan *et al.* (2008b) in detail.

5.3 A formulation for four-node plate element

Introducing Equation (2.70) for the curvature of the plate and applying the divergence theorem, we obtain

$$\tilde{\boldsymbol{\kappa}}_{ij}^h(\mathbf{x}_C) = \frac{1}{2A_C} \int_{\Omega_C} \left(\frac{\partial \theta_i^h}{\partial x_j} + \frac{\partial \theta_j^h}{\partial x_i} \right) d\Omega = \frac{1}{2A_C} \int_{\Gamma_C} (\theta_i^h n_j + \theta_j^h n_i) d\Gamma \qquad (5.3)$$

Next, we consider an arbitrary smoothing cell, Ω_C illustrated in Figure 3.1 with boundary $\Gamma_C = \bigcup_{b=1}^{nb} \Gamma_C^b$, where Γ_C^b is the boundary segment of Ω_C, and nb is the total number of edges of each smoothing cell. The relationship between the smoothed curvature field and the nodal displacement is written by

$$\tilde{\boldsymbol{\kappa}}^h = \tilde{\mathbf{B}}_C^b \mathbf{q} \qquad (5.4)$$

The smoothed element bending stiffness matrix is obtained by

$$\tilde{\mathbf{K}}^b = \int_{\Omega^e} (\tilde{\mathbf{B}}_C^b)^T \mathbf{D}^b \tilde{\mathbf{B}}_C^b d\Omega = \sum_{C=1}^{nc} (\tilde{\mathbf{B}}_C^b)^T(\mathbf{x}_C) \mathbf{D}^b \tilde{\mathbf{B}}_C^b(\mathbf{x}_C) A_C \qquad (5.5)$$

where nc is the number of smoothing cells of the element, see Figure 3.2.
Here, the integrands are constant over each Ω_C and the non-local curvature displacement matrix reads

$$\tilde{B}_{CI}^b(\mathbf{x}_C) = \frac{1}{A_C} \int_{\Gamma_C} \begin{pmatrix} 0 & 0 & N_I n_x \\ 0 & -N_I n_y & 0 \\ 0 & -N_I n_x & N_I n_y \end{pmatrix} d\Gamma \qquad (5.6)$$

We use Gauss quadrature to evaluate (5.6) with one integration point over each line segment Γ_C^b:

$$\tilde{B}_{CI}^b(\mathbf{x}_C) = \frac{1}{A_C} \sum_{b=1}^{nb} \begin{pmatrix} 0 & 0 & N_I(\mathbf{x}_b^G) n_x \\ 0 & -N_I(\mathbf{x}_b^G) n_y & 0 \\ 0 & -N_I(\mathbf{x}_b^G) n_x & N_I(\mathbf{x}_b^G) n_y \end{pmatrix} l_b^C \qquad (5.7)$$

where $\mathbf{x}_b^G$ and l_b^C are the midpoint (Gauss point) and the length of Γ_b^C, respectively.
The smoothed curvatures lead to high flexibility such as arbitrary polygonal elements (Dai *et al.* (2007)), and a slight reduction in computational cost. The element is subdivided into nc non-overlapping sub-domains also called smoothing cells (Liu *et al.* (2007a)). Figure 3.2 illustrates different smoothing cells for nc = 1, 2, 3 and 4 corresponding to 1-subcell, 2-subcell, 3-subcell and 4-subcell methods. The curvature is smoothed over each sub-cell. The values of the shape functions are indicated at the corner nodes in Figure 3.2 in the format (N_1, N_2, N_3, N_4). The values of the non-mapped shape functions at the integration nodes are determined based on the linear interpolation of shape functions along boundaries of the element or the smoothing cells, e.g. Liu *et al.* (2007a).

Therefore the element stiffness matrix in (2.21) can be modified as follows:

$$\tilde{\mathbf{K}} = \tilde{\mathbf{K}}^b + \mathbf{K}^s = \sum_{C=1}^{nc} (\tilde{\mathbf{B}}_C^b)^T \mathbf{D}^b \tilde{\mathbf{B}}_C^b A_C + \int_{\Omega^e} (\mathbf{B}^s)^T \mathbf{D}^s \mathbf{B}^s d\Omega \tag{5.8}$$

It can be seen that a reduced integration on the shear term $\mathbf{K}^s$ is necessary to avoid shear locking as the thickness of the plate tends to zero. We will denote these elements by SC1Q4, SC2Q4, SC3Q4 and SC4Q4 corresponding to subdivision into $nc =$1, 2, 3 and 4 smoothing cells, Figure 3.2. However, we will show that these elements fail the patch test and they exhibit an instability due to rank deficiency. Therefore, we employ a mixed interpolation as in the MITC4 element and use independent interpolation fields in the natural coordinate system (Bathe & Dvorkin (1985)) for the approximation of the shear strains:

$$\begin{bmatrix} \gamma_x \\ \gamma_y \end{bmatrix} = \mathbf{J}^{-1} \begin{bmatrix} \gamma_\xi \\ \gamma_\eta \end{bmatrix} \tag{5.9}$$

where

$$\gamma_\xi = \frac{1}{2}[(1-\eta)\gamma_\xi^B + (1+\eta)\gamma_\xi^D], \ \gamma_\eta = \frac{1}{2}[(1-\xi)\gamma_\eta^A + (1+\xi)\gamma_\eta^C] \tag{5.10}$$

where $\mathbf{J}$ is the Jacobian matrix and the midside nodes A, B, C, D are shown in Figure 2.2. Presenting $\gamma_\xi^B, \gamma_\xi^D$ and $\gamma_\eta^A, \gamma_\eta^C$ based on the discretized fields u^h, we obtain the shear matrix:

$$\mathbf{B}_I^s = \mathbf{J}^{-1} \begin{bmatrix} N_{I,\xi} & -b_I^{12} N_{I,\xi} & b_I^{11} N_{I,\xi} \\ N_{I,\eta} & -b_I^{22} N_{I,\eta} & b_I^{21} N_{I,\eta} \end{bmatrix} \tag{5.11}$$

where

$$b_I^{11} = \xi_I x_{,\xi}^M, \ b_I^{12} = \xi_I y_{,\xi}^M, \ b_I^{21} = \eta_I x_{,\eta}^L, \ b_I^{22} = \eta_I y_{,\eta}^L \tag{5.12}$$

with $\xi_I \in \{-1, 1, 1, -1\}$, $\eta_I \in \{-1, -1, 1, 1\}$ and $(I, M, L) \in \{(1, B, A); (2, B, C); (3, D, C); (4, D, A)\}$. Note that the shear term $\mathbf{K}^s$ is still computed by 2×2 Gauss quadrature while the element bending stiffness $\mathbf{K}^b$ in Equation (2.44) is replaced by the smoothed curvature technique on each smoothing cell of the element.

5.4 Numerical results

We will test our new element for different numbers of smoothing cells and call our element MISCk (Mixed Interpolation and Smoothed Curvatures) with k $\in \{1, 2, 3, 4\}$ smoothing cells for the bending terms. For instance, the MISC1 element is the element with only one smoothing cell to integrate the bending part of the element stiffness matrix. We will compare our results to the results obtained with the reduced/selective integrated quadrilateral element (Q4-R), the MITC4 element and with several other 4-node elements in the literatures such as

CRB1 and CRB2 – The coupled resultants bending associated with the incompatible modes in mixed plate bending formulation by Weissman & Taylor (1990).

S4R – The element is commercially available by Abaqus (2004).

DKQ – The Discrete Kirchhoff Quadrilateral element developed by Batoz & Tahar (1982).

G/W – A stabilized one-point integrated quadrilateral Reissner-Mindlin plate element presented by Gruttmann & Wagner (2004).

5.4.1 Patch test

The patch test was introduced by Bruce Irons and Bazeley (see Bazeley *et al.* (1965)) to check the convergence of finite elements. It is checked if the element is able to reproduce a constant distribution of all quantities for arbitrary meshes. It is important that one element is completely surrounded by neighboring elements in order to test if a rigid body motion is modelled correctly, Figure 5.1. The boundary deflection is assumed to be $w = \frac{1}{2}(1+x+2y+x^2+xy+y^2)$ (Chen & Cheung (2000)). The results are shown in Table 5.1. While the MITC4 element and the MISCk elements pass the patch test, the Q4-R element and the SC1Q4, SC2Q4, SC3Q4, SC4Q4 elements fail the patch test. Note that also the fully integrated Q4 element (on both the bending and the shear terms) does not pass the patch test.

Node	coordinates	
1	0.0	0.0
2	0.24	0.0
3	0.24	0.12
4	0.0	0.12
5	0.04	0.02
6	0.18	0.03
7	0.16	0.08
8	0.08	0.08
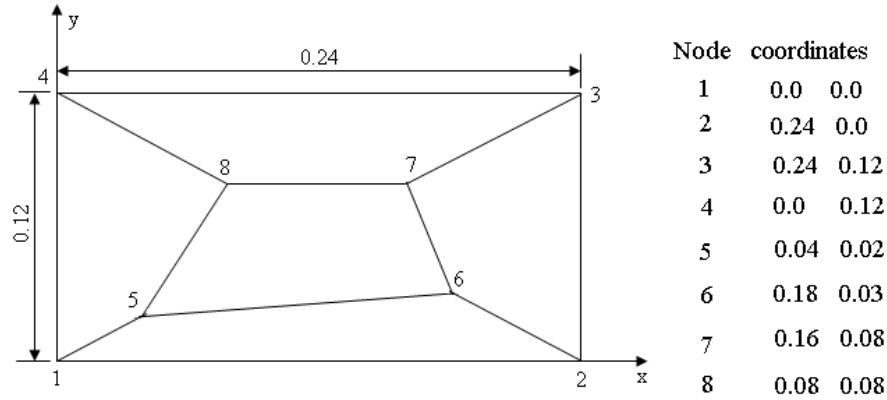
Figure 5.1: Patch test of elements

5.4.2 Sensitivity to mesh distortion

Consider a clamped square plate subjected to a center point F or uniform load p shown in Figure 5.2. The geometry parameters and the Poisson's ratio are: length L, thickness t, and $\nu = 0.3$. Due to its symmetry, only a quarter (lower – left) of the plate is modelled with a mesh of 8×8 elements. To study the effect of mesh distortion on the results, interior nodes are moved by an irregularity factor s. The coordinates of interior nodes is

Table 5.1: Patch test

Element	w_5	θ_{x5}	θ_{y5}	m_{x5}	m_{y5}	m_{xy5}
Q4-R	0.5440	1.0358	-0.676	—	—	—
SC1Q4	0.5431	1.0568	-0.7314	—	—	—
SC2Q4	0.5439	1.0404	-0.6767	—	—	—
SC3Q4	0.5440	1.0396	-0.6784	—	—	—
SC4Q4	0.5439	1.0390	-0.6804	—	—	—
MITC4	0.5414	1.04	-0.55	-0.01111	-0.01111	-0.00333
MISC1	0.5414	1.04	-0.55	-0.01111	-0.01111	-0.00333
MISC2	0.5414	1.04	-0.55	-0.01111	-0.01111	-0.00333
MISC3	0.5414	1.04	-0.55	-0.01111	-0.01111	-0.00333
MISC4	0.5414	1.04	-0.55	-0.01111	-0.01111	-0.00333
Exact	0.5414	1.04	-0.55	-0.01111	-0.01111	-0.00333

— no constant moments

perturbed as follows (Liu *et al.* (2007a)):

$$x' = x + r_c s \Delta x$$
$$y' = y + r_c s \Delta y \tag{5.13}$$

where r_c is a generated random number given values between -1.0 and 1.0, $s \in [0, 0.5]$ is used to control the *s*hapes of the distorted elements and $\Delta x, \Delta y$ are initial regular element sizes in the x–and y–directions, respectively.

For the concentrated center point load F, the influence of the mesh distortion on the center deflection is given in Figure 5.3 for a thickness ratio of ($t/L = 0.01$ and 0.001). The results of our presented method are more accurate than those of the Q4-R element and the MITC4 element, especially for extremely distorted meshes. Here, the MISC1 element gives the best result. However, this element contains two zero-energy modes. In simple problems, these hourglass modes can be automatically eliminated by the boundary conditions. However, this is not in general the case. Otherwise, the MISC2, MISC3 and MISC4 elements retain a sufficient rank of the element stiffness matrix and give excellent results.

Let us consider a thin plate with ($t/L = 0.001$) under uniform load as shown Figure 5.2a. The numerical results of the central deflections are shown in Table 5.2 and Figure 5.4 and compared to other elements. Overall, it can be seen that the MISCk elements give more accurate results than the other elements, especially for distorted meshes.

5.4.3 Square plate subjected to a uniform load or a point load

Figure 5.2a and Figure 5.5 are the model of a square plate with clamped and simply supported boundary conditions, respectively, subjected to a uniform load $p = 1$ or a

78
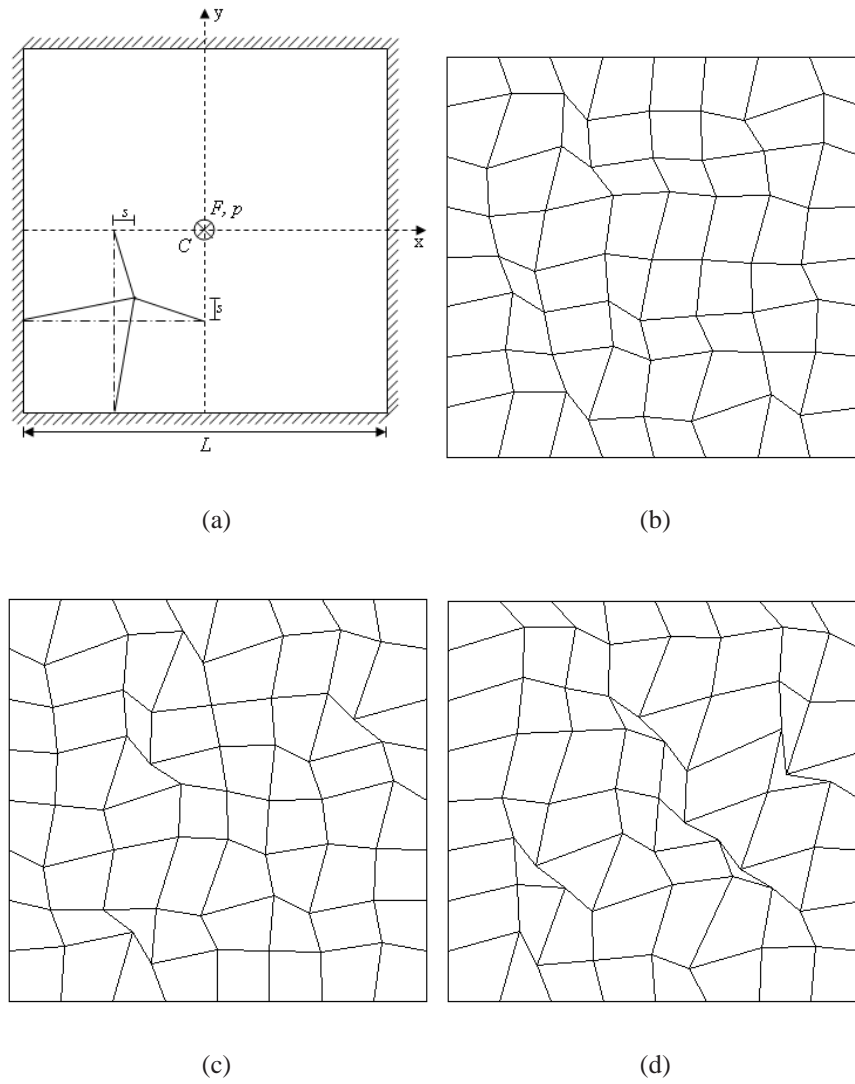
Figure 5.2: Effect of mesh distortion for a clamped square plate: (a) clamped plate model; (b) $s = 0.3$; (c) $s = 0.4$; and (d) $s = 0.5$

(a)   (b)
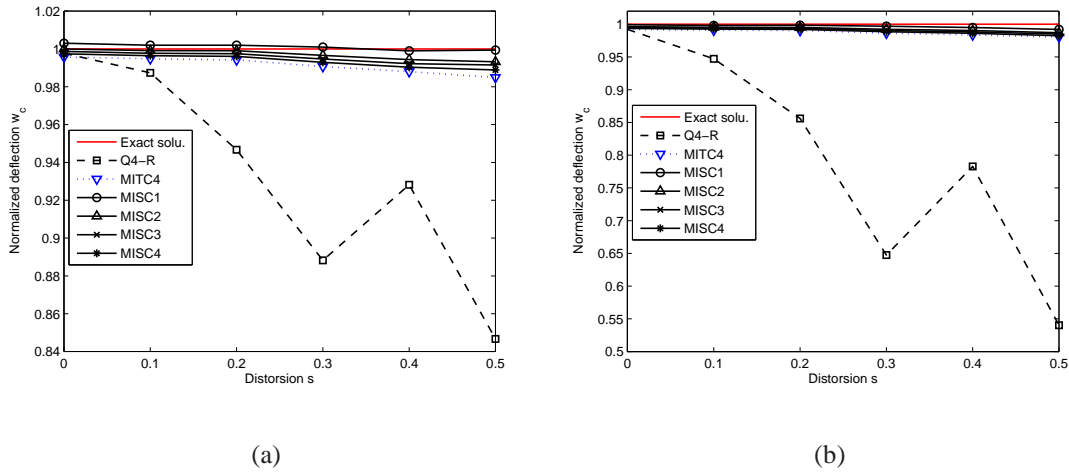
Figure 5.3: The normalized center deflection with influence of mesh distortion for a clamped square plate subjected to a concentrated load: a) t/L=0.01, b) t/L=0.001
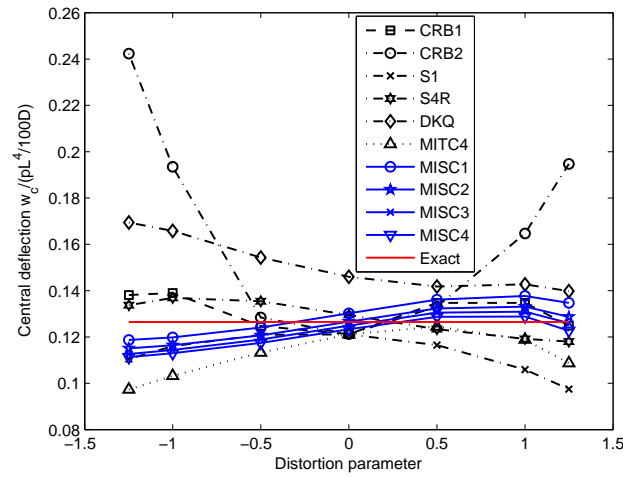
Figure 5.4: Comparison of other elements through the center deflection with mesh distortion

80

Table 5.2: The central deflection $w_c/(pL^4/100D), D = Et^3/12(1 - \nu^2)$ with mesh distortion for thin clamped plate subjected to uniform load p

s	-1.249	-1.00	-0.5	0.00	0.5	1.00	1.249
CRB1	0.1381	0.1390	0.1247	0.1212	0.1347	0.1347	0.1249
CRB2	0.2423	0.1935	0.1284	0.1212	0.1331	0.1647	0.1947
Q4-R	0.1105	0.1160	0.1209	0.1211	0.1165	0.1059	0.0975
S4R	0.1337	0.1369	0.1354	0.1295	0.1234	0.1192	0.1180
DKQ	0.1694	0.1658	0.1543	0.1460	0.1418	0.1427	0.1398
MITC4	0.0973	0.1032	0.1133	0.1211	0.1245	0.1189	0.1087
MISC1	0.1187	0.1198	0.1241	0.1302	0.1361	0.1377	0.1347
MISC2	0.1151	0.1164	0.1207	0.1266	0.1323	0.1331	0.1287
MISC3	0.1126	0.1144	0.1189	0.1249	0.1305	0.1309	0.1260
MISC4	0.1113	0.1130	0.1174	0.1233	0.1287	0.1288	0.1227
Exact solu.	0.1265	0.1265	0.1265	0.1265	0.1265	0.1265	0.1265
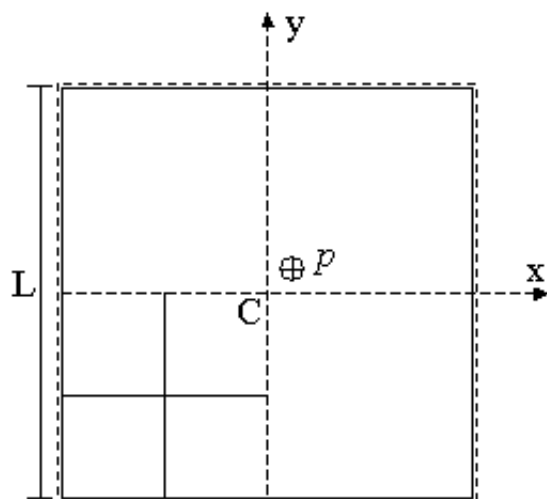
Figure 5.5: A simply supported square plate subjected to a point load or a uniform load

central load $F = 16.3527$. The material parameters are given by Young's modulus $E = 1092000$ and Poisson's ratio $\nu = 0.3$. Uniform meshes with $N = 2, 4, 8, 16, 32$ are used and symmetry conditions are exploited. For a clamped case, Figure 5.6 illustrates the convergence of the normalized deflection and the normalized moment at the center versus the mesh density N for a relation $t/L = 0.01$. Even for very coarse meshes, the deflection tends to the exact solution. For the finest mesh, the displacement slightly (.06%) exceeds the value of the exact solution. The bending moment converges to the analytical value. The rate of convergence in the energy norm is presented in Figure 5.7 and is for all elements equal to 1.1 but the MISCk elements are more accurate than the MITC4 element.

(a)	(b)
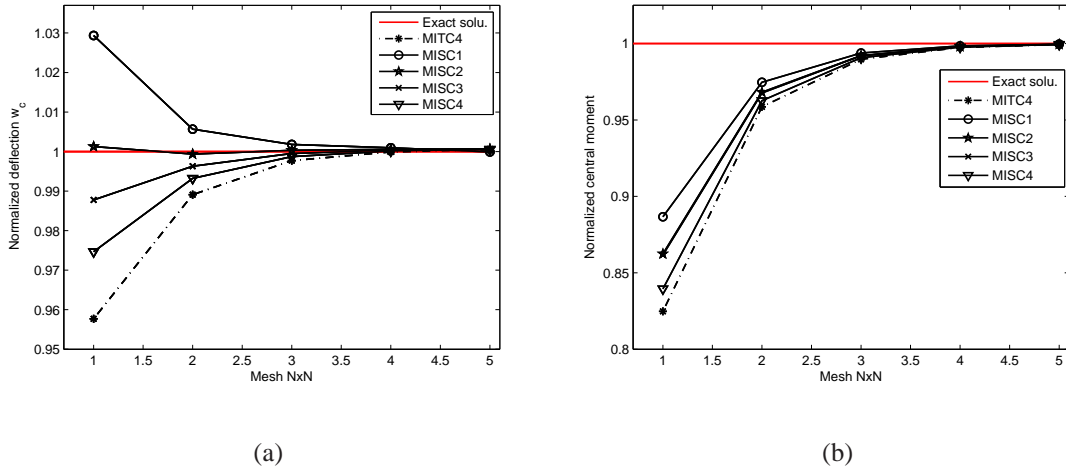
Figure 5.6: Normalized deflection and moment at center of clamped square plate subjected to uniform load

Tables 5.3–5.4 show the performance of the plate element compared the exact solution[1] for different thickness ratios, $t/L = 10^{-1} \sim 10^{-5}$. No shear locking is observed.

Next we consider a sequence of distorted meshes with 25, 81, 289 and 1089 nodes as shown in Figure 5.8. The numerical results in terms of the error in the central displacement and the strain energy are illustrated in Figure 5.9. All proposed elements give stable and accurate results. Especially for coarse meshes, the MISCk elements are more accurate than the MITC4 element; a reason for this may be that for our finest meshes, fewer elements are distorted in comparison to coarse meshes.

Now we will test the computing time for the clamped plate analyzed above. The program is compiled by a personal computer with Pentium(R)4, CPU-3.2GHz and RAM-512MB. The computational cost to set up the global stiffness matrix and to solve the algebraic equations is illustrated in Figure 5.10. The MISCk elements and the MITC4

---

[1]The exact value is cited from Taylor & Auricchio (1993)

Table 5.3: Central deflections $w_c/(pL^4/100D)$ for the clamped plate subjected to uniform load

L/t	elements	Mesh					Exact
		2	4	8	16	32	
	MITC4	0.1431	0.1488	0.1500	0.1504	0.1504	
	MISC1	0.1517	0.1507	0.1505	0.1505	0.1505	
10	MISC2	0.1483	0.1500	0.1503	0.1504	0.1505	0.1499
	MISC3	0.1467	0.1496	0.1502	0.1504	0.1504	
	MISC4	0.1451	0.1493	0.1502	0.1504	0.1504	
	MITC4	0.1213	0.1253	0.1264	0.1267	0.1268	
	MISC1	0.1304	0.1274	0.1269	0.1268	0.1268	
10^2	MISC2	0.1269	0.1266	0.1267	0.1268	0.1268	0.1267
	MISC3	0.1252	0.1262	0.1266	0.1267	0.1268	
	MISC4	0.1235	0.1258	0.1265	0.1267	0.1268	
	MITC4	0.1211	0.1251	0.1262	0.1264	0.1265	
	MISC1	0.1302	0.1272	0.1267	0.1266	0.1265	
10^3	MISC2	0.1266	0.1264	0.1265	0.1265	0.1265	0.1265
	MISC3	0.1249	0.1260	0.1264	0.1265	0.1265	
	MISC4	0.1233	0.1256	0.1263	0.1265	0.1265	
	MITC4	0.1211	0.1251	0.1262	0.1264	0.1265	
	MISC1	0.1302	0.1272	0.1267	0.1266	0.1265	
10^4	MISC2	0.1266	0.1264	0.1265	0.1265	0.1265	0.1265
	MISC3	0.1249	0.1260	0.1264	0.1265	0.1265	
	MISC4	0.1233	0.1256	0.1263	0.1265	0.1265	
	MITC4	0.1211	0.1251	0.1262	0.1264	0.1265	
	MISC1	0.1302	0.1272	0.1267	0.1266	0.1265	
10^5	MISC2	0.1266	0.1264	0.1265	0.1265	0.1265	0.1265
	MISC3	0.1249	0.1260	0.1264	0.1265	0.1265	
	MISC4	0.1233	0.1256	0.1263	0.1265	0.1265	

Table 5.4: Central moments $M_c/(pL^2/10)$ for the clamped plate subjected to uniform load

L/t	elements	Mesh					Exact
		2	4	8	16	32	
	MITC4	0.1898	0.2219	0.2295	0.2314	0.2318	
	MISC1	0.2031	0.2254	0.2304	0.2316	0.2319	
10	MISC2	0.1982	0.2241	0.2300	0.2315	0.2319	0.231
	MISC3	0.1974	0.2239	0.2300	0.2315	0.2319	
	MISC4	0.1930	0.2228	0.2297	0.2314	0.2319	
	MITC4	0.1890	0.2196	0.2267	0.2285	0.2289	
	MISC1	0.2031	0.2233	0.2277	0.2287	0.2290	
10^2	MISC2	0.1976	0.2218	0.2273	0.2286	0.2290	0.2291
	MISC3	0.1974	0.2217	0.2273	0.2286	0.2290	
	MISC4	0.1923	0.2205	0.2270	0.2286	0.2290	
	MITC4	0.1890	0.2196	0.2267	0.2285	0.2289	
	MISC1	0.2031	0.2233	0.2276	0.2287	0.2290	
10^3	MISC2	0.1976	0.2218	0.2273	0.2286	0.2289	0.2291
	MISC3	0.1974	0.2217	0.2272	0.2286	0.2289	
	MISC4	0.1923	0.2205	0.2269	0.2285	0.2289	
	MITC4	0.1890	0.2196	0.2267	0.2285	0.2289	
	MISC1	0.2031	0.2233	0.2276	0.2287	0.2290	
10^4	MISC2	0.1976	0.2218	0.2273	0.2286	0.2289	0.2291
	MISC3	0.1974	0.2217	0.2272	0.2286	0.2289	
	MISC4	0.1923	0.2205	0.2269	0.2285	0.2289	
	MITC4	0.1890	0.2196	0.2267	0.2285	0.2289	
	MISC1	0.2031	0.2233	0.2276	0.2287	0.2290	
10^5	MISC2	0.1976	0.2218	0.2273	0.2286	0.2289	0.2291
	MISC3	0.1974	0.2217	0.2272	0.2286	0.2289	
	MISC4	0.1923	0.2205	0.2269	0.2285	0.2289	

Figure 5.7: Rate of convergence in energy norm versus with number of nodes for clamped square plate subjected to uniform load

element give nearly the same CPU time for coarse meshes where the MISCk elements are more accurate. From the plots, we can conjecture that, in the limit where the numbers of degrees of freedom tends to infinity, the MITC4 element is computationally more expensive than the MISCk element, and the MISCk elements are generally more accurate. The lower computational cost comes from the fact that no computation of the Jacobian matrix is necessary for the MISCk elements while the MITC4 element needs to determine the Jacobian determinant, the inverse of the Jacobian matrix (transformation of two coordinates; global coordinate and local coordinate) and then the stiffness matrix is calculated by 2×2 Gauss points. Previously, the same tendency was observed for the standard (Q4 element).

For a simply supported plate subjected to central concentrate load, the same tendencies as described above are observed. Exemplarily, we will show the results of the normalized deflection in Figure 5.11a for the uniform meshes and in Figure 5.11b for the distorted meshes illustrated in Figure 5.8.

The numerical results for a simply supported plate subjected to a uniform load are presented in Tables 5.5–5.6 and Figures 5.12 – 5.13 for a regular mesh. We note that the MISCk elements are more accurate than the MITC4 element but show the same convergence rate. We also see that no shear locking occurs with decreasing thickness. Also, for all elements presented, the displacement results do not seem to be influenced by the value of the thickness ratio, at least in the range $t/L \in [10^{-3}, 10^{-5}]$. The moments remain accurate throughout the range of thickness ratios that we considered.

(a)

(b)

(c)

(d)
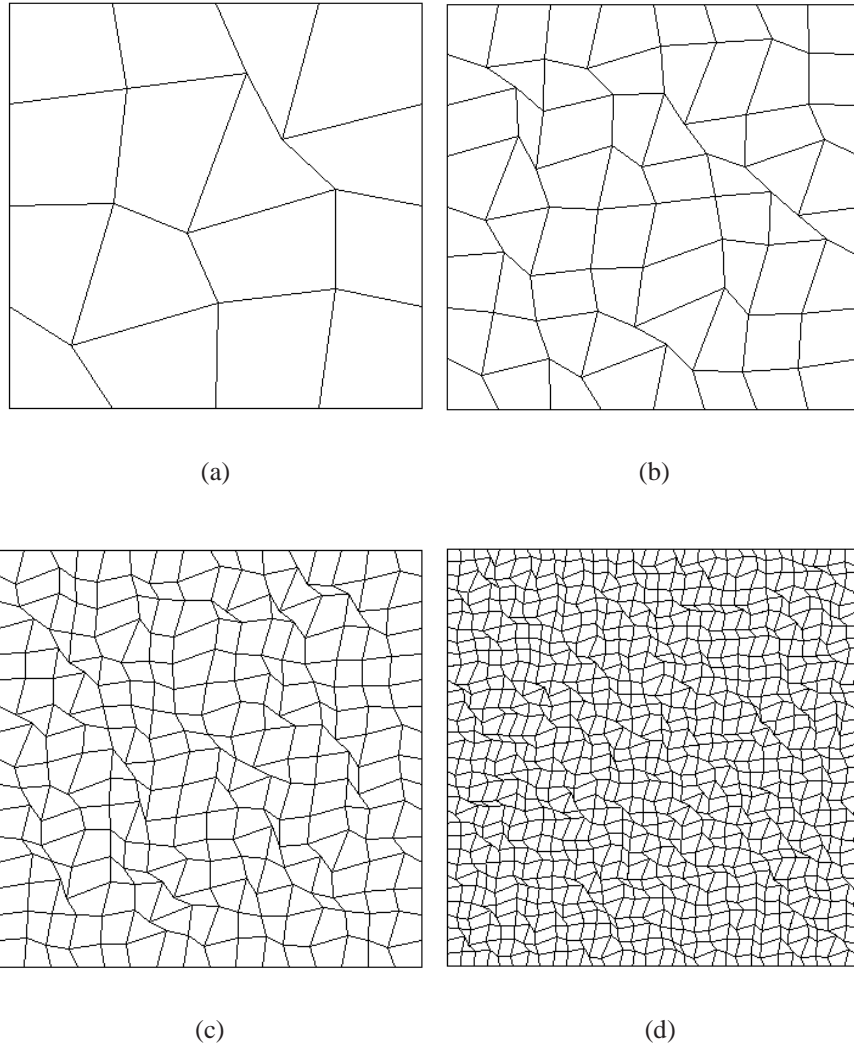
Figure 5.8: Analysis of clamped plate with irregular elements: (a) 25; (b) 64; (c) 256; and (d) 1024

(a)   (b)
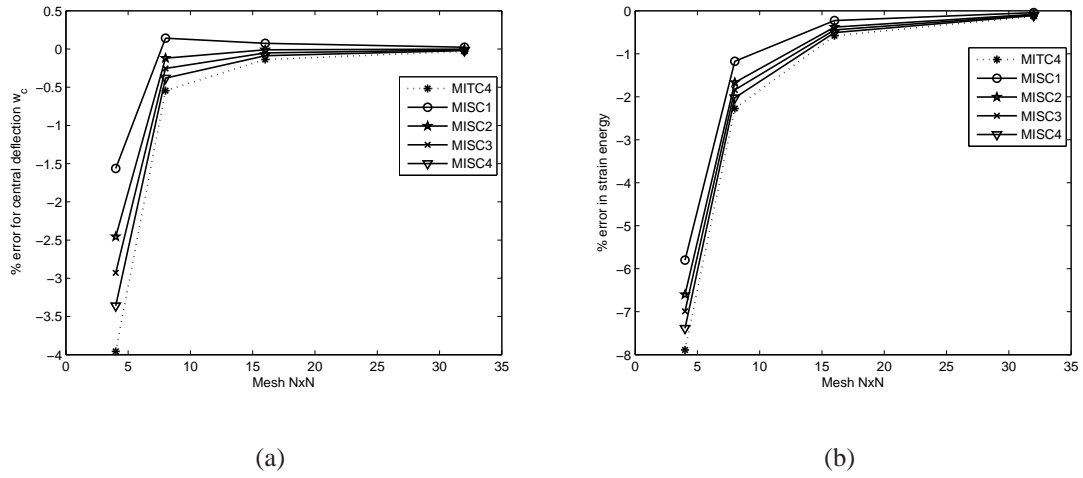
Figure 5.9: The convergence test of thin clamped plate (t/L=0.001) (with irregular elements: (a) the deflection; (b) the strain energy
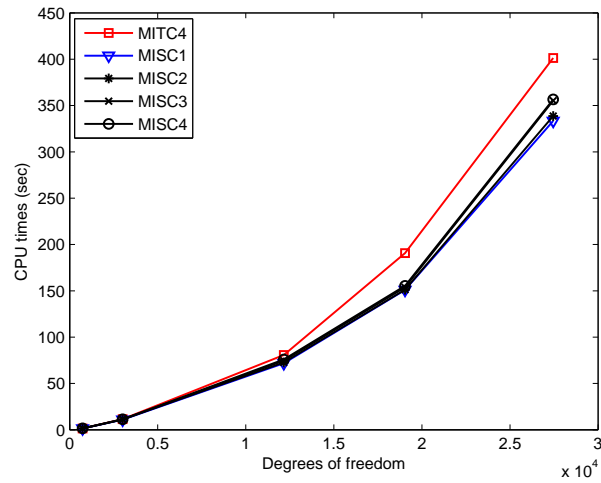
Figure 5.10: Computational cost for establishing the global stiffness matrix and solving system equations of clamped plate subjected to a uniform load

87

(a) regular mesh (b) distorted mesh
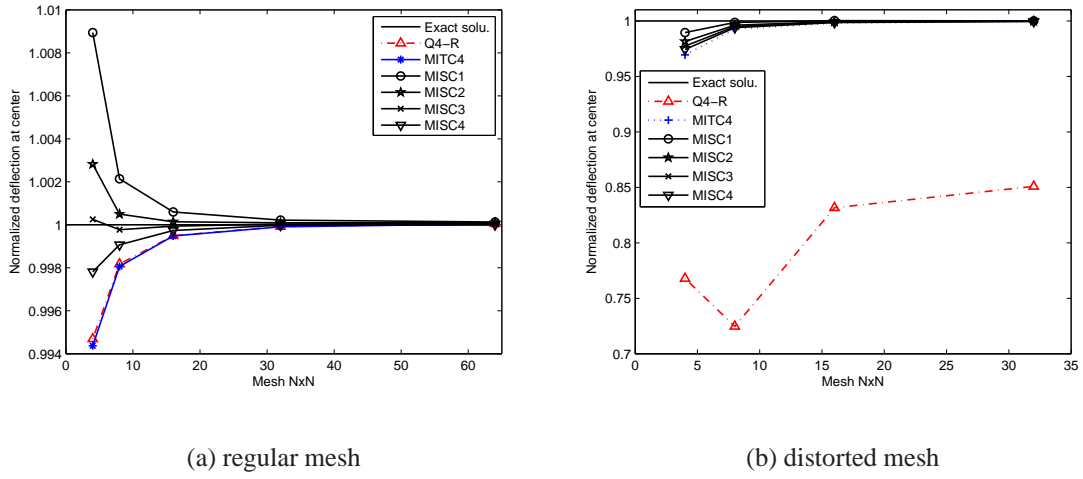
Figure 5.11: Normalized deflection at the centre of the simply supported square plate subjected to a center load

(a) (b)
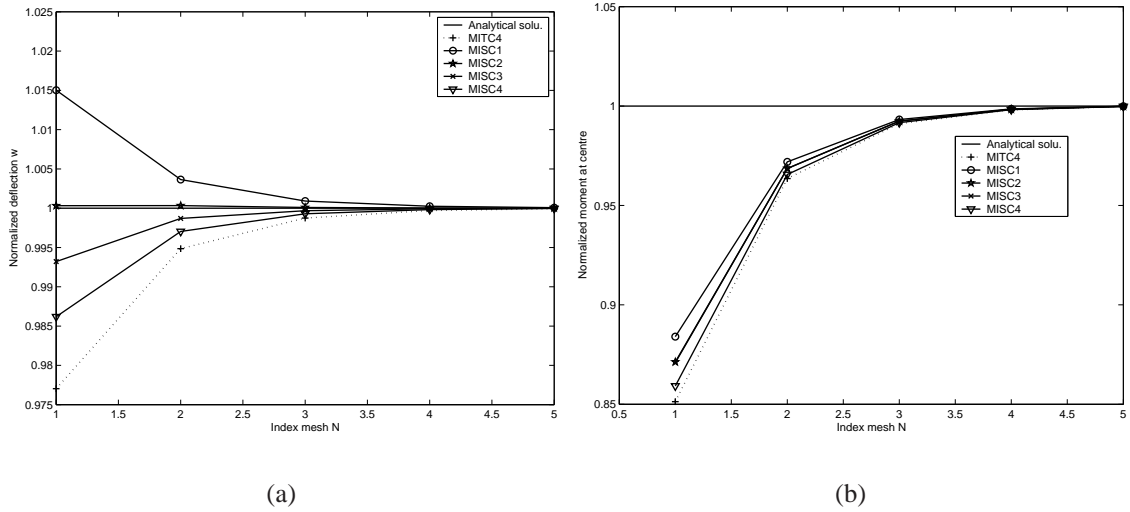
Figure 5.12: Normalized deflection and moment at center of simply support square plate subjected to uniform load

Table 5.5: Central deflections $w_c/(pL^4/100D)$ for the simply supported plate subjected to uniform load

L/t	elements	Mesh					Exact
		2	4	8	16	32	
	MITC4	0.4190	0.4255	0.4268	0.4272	0.4273	
	MISC1	0.4344	0.4290	0.4277	0.4274	0.4273	
10	MISC2	0.4285	0.4277	0.4274	0.4273	0.4273	0.4273
	MISC3	0.4256	0.4270	0.4272	0.4273	0.4273	
	MISC4	0.4227	0.4263	0.4271	0.4272	0.4273	
	MITC4	0.3971	0.4044	0.4059	0.4063	0.4064	
	MISC1	0.4125	0.4079	0.4068	0.4065	0.4065	
10^2	MISC2	0.4066	0.4066	0.4065	0.4065	0.4064	0.4064
	MISC3	0.4037	0.4059	0.4063	0.4064	0.4064	
	MISC4	0.4008	0.4052	0.4062	0.4064	0.4064	
	MITC4	0.3969	0.4041	0.4057	0.4061	0.4062	
	MISC1	0.4123	0.4077	0.4066	0.4063	0.4063	
10^3	MISC2	0.4064	0.4064	0.4063	0.4062	0.4062	0.4062
	MISC3	0.4035	0.4057	0.4061	0.4062	0.4062	
	MISC4	0.4006	0.4050	0.4059	0.4062	0.4062	
	MITC4	0.3969	0.4041	0.4057	0.4061	0.4062	
	MISC1	0.4123	0.4077	0.4066	0.4063	0.4063	
10^4	MISC2	0.4064	0.4064	0.4063	0.4062	0.4062	0.4062
	MISC3	0.4035	0.4057	0.4061	0.4062	0.4062	
	MISC4	0.4006	0.4050	0.4059	0.4062	0.4062	
	MITC4	0.3969	0.4041	0.4057	0.4061	0.4062	
	MISC1	0.4123	0.4077	0.4066	0.4063	0.4063	
10^5	MISC2	0.4064	0.4064	0.4063	0.4062	0.4062	0.4062
	MISC3	0.4035	0.4057	0.4061	0.4062	0.4062	
	MISC4	0.4006	0.4050	0.4059	0.4062	0.4062	

Table 5.6: Central moments $M_c/(pL^2/10)$ for the simply supported plate subjected to uniform load

L/t	elements	Mesh					Exact
		2	4	8	16	32	
	MITC4	0.4075	0.4612	0.4745	0.4778	0.4786	
	MISC1	0.4232	0.4652	0.4755	0.4780	0.4787	
10	MISC2	0.4172	0.4637	0.4751	0.4779	0.4786	
	MISC3	0.4169	0.4637	0.4751	0.4779	0.4786	
	MISC4	0.4113	0.4622	0.4747	0.4778	0.4786	
	MITC4	0.4075	0.4612	0.4745	0.4778	0.4786	
	MISC1	0.4232	0.4652	0.4755	0.4780	0.4787	
10^2	MISC2	0.4171	0.4637	0.4751	0.4779	0.4786	
	MISC3	0.4169	0.4636	0.4751	0.4779	0.4786	
	MISC4	0.4113	0.4622	0.4747	0.4778	0.4786	
							0.4789
	MITC4	0.4075	0.4612	0.4745	0.4778	0.4786	
	MISC1	0.4232	0.4652	0.4755	0.4780	0.4787	
10^3	MISC2	0.4171	0.4637	0.4751	0.4779	0.4786	
	MISC3	0.4169	0.4636	0.4751	0.4779	0.4786	
	MISC4	0.4113	0.4622	0.4747	0.4778	0.4786	
	MITC4	0.4075	0.4612	0.4745	0.4778	0.4786	
	MISC1	0.4232	0.4652	0.4755	0.4780	0.4787	
10^4	MISC2	0.4171	0.4637	0.4751	0.4779	0.4786	
	MISC3	0.4169	0.4636	0.4751	0.4779	0.4786	
	MISC4	0.4113	0.4622	0.4747	0.4778	0.4786	
	MITC4	0.4075	0.4612	0.4745	0.4778	0.4786	
	MISC1	0.4232	0.4652	0.4755	0.4780	0.4786	
10^5	MISC2	0.4171	0.4637	0.4751	0.4779	0.4786	
	MISC3	0.4169	0.4636	0.4751	0.4779	0.4786	
	MISC4	0.4113	0.4622	0.4747	0.4778	0.4786	

Figure 5.13: Rate of convergence in energy norm for simply supported square plate subjected to uniform load

5.4.4 Skew plate subjected to a uniform load

5.4.4.1 Razzaque's skew plate model.

Let us consider a rhombic plate subjected to a uniform load $p = 1$ as shown in Figure 5.14a. This plate was originally studied by Razzaque (1973). Dimensions and boundary conditions are specified in Figure 5.14a, too. Geometry and material parameters are length $L = 100$, thickness $t = 0.1$, Young's modulus $E = 1092000$ and Poisson's ratio $\nu = 0.3$. The results in Table 5.7 show that the accuracy of the presented method is always better than that of the MITC4 element. Figure 5.15 illustrates the contribution of the von Mises stresses and the level lines for Razzaque's skew plate with our MISC4 element.

5.4.4.2 Morley's skew plate model.

The set-up of a skew plate is shown in Figure 5.14b. This example was first studied by Morley (1963). The geometry and material parameters are length $L = 100$, thickness t, Young's modulus $E = 1092000$, Poisson's ratio $\nu = 0.3$ and a uniform load $p = 1$. The values of the deflection at the central point are given in Figure 5.17 for different plate thickness. The MISCk elements show remarkably good results compared the MITC4 element. The distribution of the von Mises stresses and the level lines are illustrated in Figure 5.16. It is evident that this problem has the corner singularity. An adaptive approach might be useful for computational reasons.

(a)

(b)
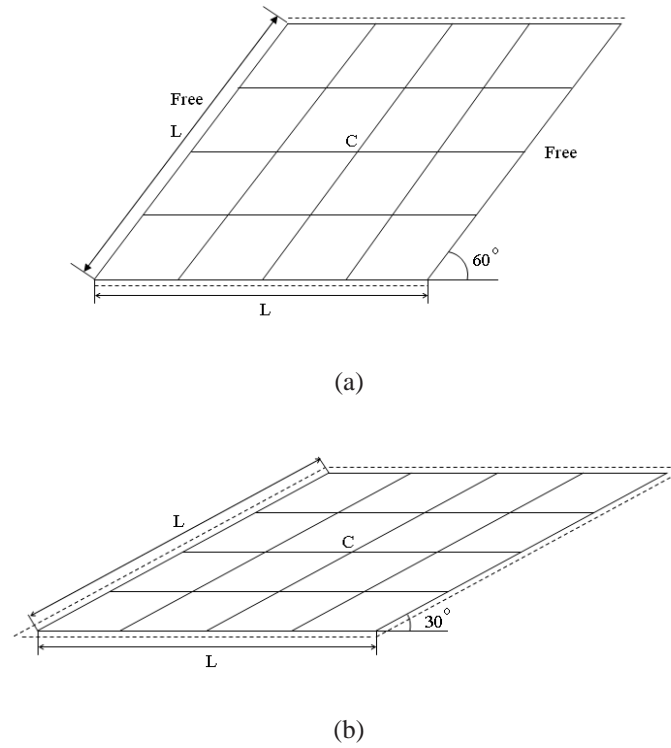
Figure 5.14: A simply supported skew plate subjected to a uniform load

(a)   (b)
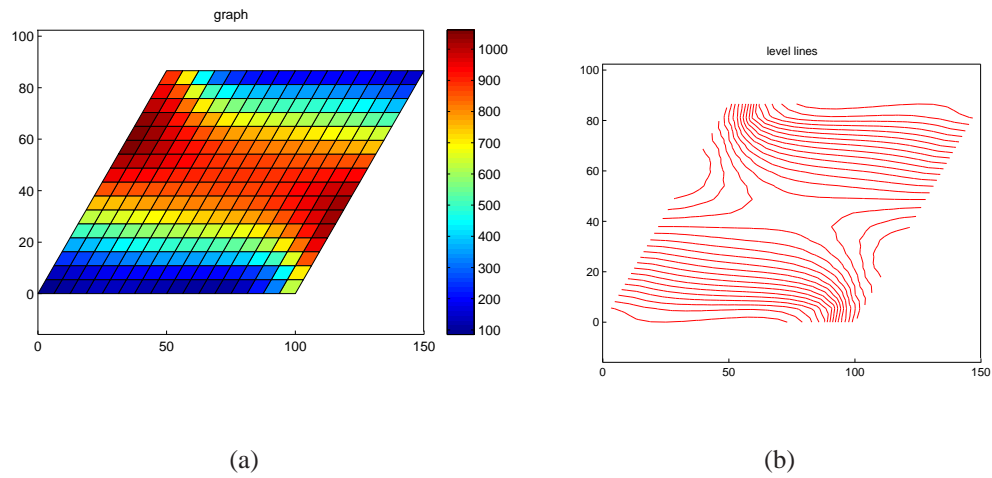
Figure 5.15: A distribution of von Mises stress and level lines for Razzaque's skew plate using MISC4 element

92

Table 5.7: Central defection and moment of the Razzaque's skew plate

Mesh	MITC4	MISC1	MISC2	MISC3	MISC4
(a) Central deflection $w_c/10^4$					
2×2	0.3856	0.3648	0.3741	0.3781	0.3816
4×4	0.6723	0.6702	0.6725	0.6725	0.6724
6×6	0.7357	0.7377	0.7377	0.7370	0.7364
8×8	0.7592	0.7615	0.7610	0.7604	0.7598
12×12	0.7765	0.7781	0.7776	0.7772	0.7769
16×16	0.7827	0.7838	0.7834	0.7832	0.7830
32×32	0.7888	0.7892	0.7891	0.7890	0.7889
Razzaque (1973)					0.7945
(b) Central moment $M_y/10^3$					
2×2	0.4688	0.4688	0.4688	0.4688	0.4688
4×4	0.8256	0.8321	0.8301	0.8284	0.8269
6×6	0.8976	0.9020	0.9005	0.8994	0.8984
8×8	0.9242	0.9272	0.9260	0.9254	0.9245
12×12	0.9439	0.9454	0.9448	0.9445	0.9442
16×16	0.9510	0.9518	0.9515	0.9513	0.9511
32×32	0.9577	0.9580	0.9579	0.9578	0.9578
Razzaque (1973)					0.9589

(a)   (b)
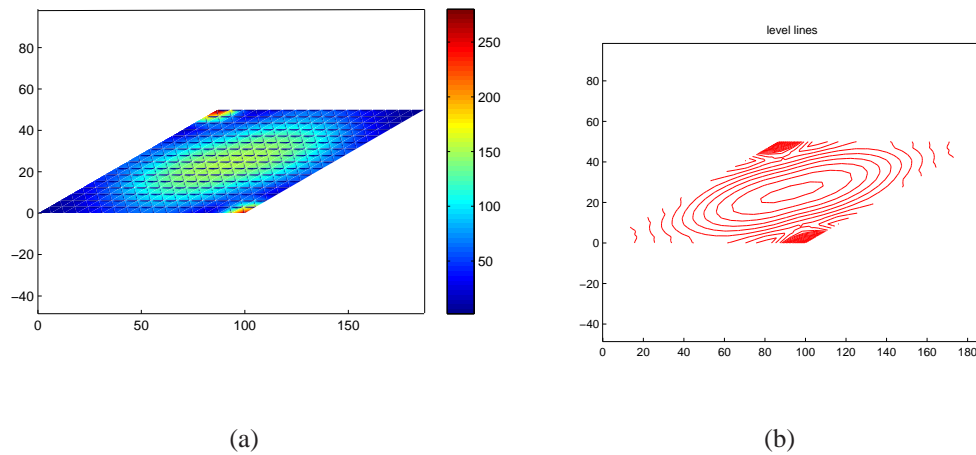
Figure 5.16: A distribution of von Mises and level lines for Morley's skew plate using MISC2 element

(a)   (b)
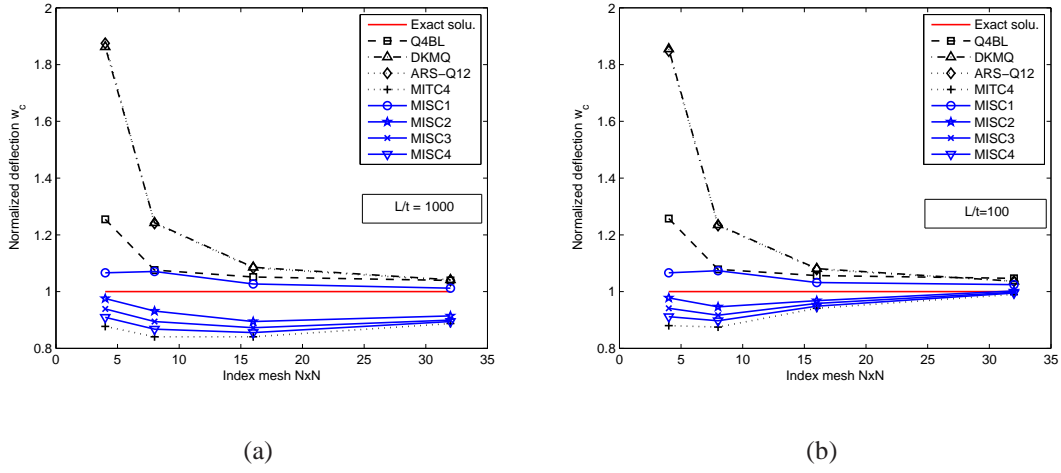
Figure 5.17: The convergence of the central deflection w_c for Morley plate with different thickness/span ratio

5.4.5 Corner supported square plate

Consider a corner supported plate subjected to a uniform load $p = 0.03125$ with edge length $L = 24$ and thickness $t = 0.375$. This example is often studied to test the existence of spurious energy modes. The material parameters are Young's modulus $E = 430000$ and Poisson's ratio $\nu = 0.38$. The shear correction factor was set to a value of $k = 1000$. A symmetric model with an initial mesh of 8×8 elements is shown in Figure 5.18. Table 5.8 shows the convergence of the center deflection. We note that even our rank-deficient MISC1 element gives stable and very accurate results.

We have also carried out a frequency analysis. The mass density is chosen to be $\rho = 0.001$ and the normalized frequencies are $\bar{\omega} = \omega L^2 (D/t\rho)^{-1/2}$. The results are illustrated in Table 5.9 for two mesh densities (6×6 and 32×32). It can be seen that all proposed elements give stable and accurate solutions.

5.4.6 Clamped circular plate subjected to a concentrated load

Let us consider a clamped circular plate with radius $R = 5$ subjected to a point load $F = 1$ at the center. The material and geometric parameters are Young's modulus $E = 10.92$, Poisson's ratio $\nu = 0.3$ and the thickness of the plate is 1. The analytical deflection for this problem is

$$w(r) = \frac{FR^2}{16\pi D}\left(1 - \frac{r^2}{R^2} + \frac{2r^2}{R^2}ln\frac{r}{R} - \frac{8D}{kGtR^2}ln\frac{r}{R}\right) \qquad (5.14)$$

A discretization of this problem with 48 elements is illustrated in Figure 5.19. We exploited the symmetry of the plate and modelled only one quarter. Because of the singular-

94
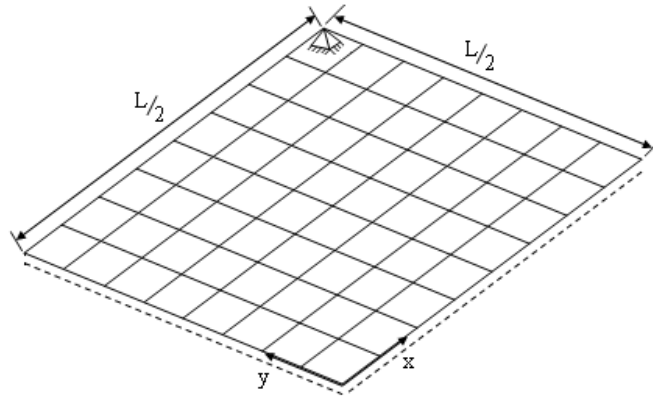
Figure 5.18: Corner supported plate subjected to uniform load

Table 5.8: The convergence of center defection for corner supported plate

Elem. per side	8	16	24	48	96
DKQ	0.11914	0.11960	0.11969	0.11974	0.11975
G/W	0.11862	0.11947	0.11963	0.11973	0.11975
MITC4	0.11856	0.11946	0.11963	0.11973	0.11975
MISC1	0.11873	0.11950	0.11965	0.11973	0.11975
MISC2	0.11867	0.11949	0.11964	0.11973	0.11975
MISC3	0.11864	0.11948	0.11963	0.11973	0.11975
MISC4	0.11861	0.11947	0.11963	0.11973	0.11975
Theory					0.12253

Table 5.9: Three lowest frequencies for corner supported plate

Element	6×6 mesh			32×32 mesh		
	$\bar\omega_1$	$\bar\omega_2$	$\bar\omega_3$	$\bar\omega_1$	$\bar\omega_2$	$\bar\omega_3$
DKQ	7.117	18.750	43.998	–	–	–
G/W	7.144	18.800	44.105	–	–	–
MITC4	7.135	18.795	44.010	7.036	18.652	43.163
MISC1	7.136	18.799	44.011	7.075	18.661	43.553
MISC2	7.141	18.800	44.065	7.075	18.661	43.555
MISC3	7.143	18.800	44.092	7.075	18.661	43.556
MISC4	7.145	18.800	44.119	7.076	18.661	43.557
Leissa (1969)				7.120	19.600	44.400

ity at the center, the normalized central deflection is evaluated at the radius $r = 10^{-3}R$. The numerical results are summarized in Table 5.10 and Figure 5.20. The MITC4 and MISCk elements converge to the exact value with refined meshes. However, the convergence in the central deflection is slow due to the singularity at the center. To increase the convergence rate of the problem, an adaptive local refinement procedure should be considered in the future. If the ratio r/R is large enough, the numerical results are very close to the analytical solution.
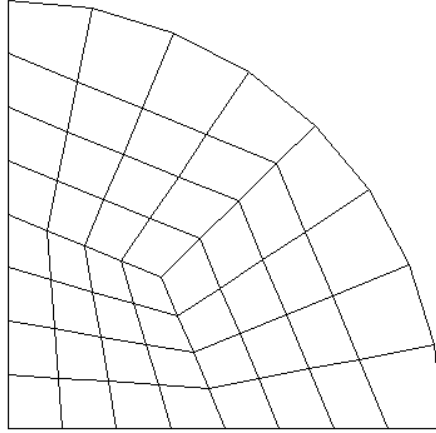
Figure 5.19: Clamped circular plate subjected to concentrated load

Table 5.10: The normalized defection at center for circular plate

Mesh	2	4	8	16	32
MITC4	0.7817	0.8427	0.8874	0.9278	0.9671
MISC1	0.8011	0.8492	0.8893	0.9284	0.9673
MISC2	0.7910	0.8457	0.8883	0.9281	0.9672
MISC3	0.7880	0.8448	0.8880	0.9280	0.9672
MISC4	0.7854	0.8439	0.8877	0.9279	0.9672

5.5 Concluding remarks

A quadrilateral plate element based on a mixed interpolation with smoothed curvatures has been proposed. Except for the MISC1 element that exhibits two zero energy modes, the MISC2, MISC3 and MISC4 elements maintain a sufficient rank and no zero energy modes are present. Moreover, all proposed elements do not exhibit shear locking in the limit to thin plates. It is also shown that the MISCk element passes the patch test. In
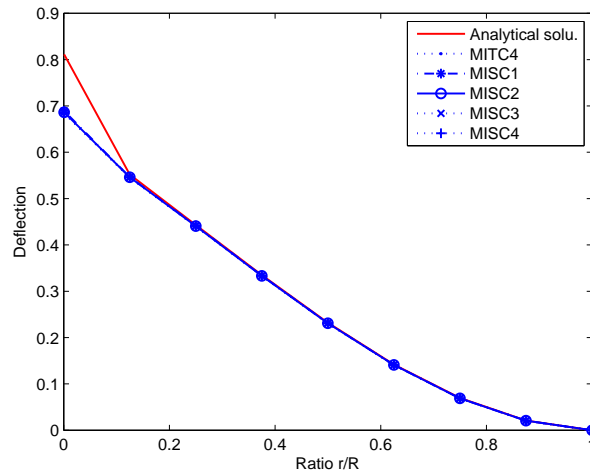
Figure 5.20: Clamped circular plate subjected to concentrated load

comparison to the well known MITC4 element, the proposed elements are more accurate[1] for regular and especially for irregular meshes or coarse meshes while their computational cost is lower.

The element with the best performance is the MISC1 element but it exhibits two zero energy modes. However, for the examples tested here, no instabilities were observed. The elimination of the zero-energy modes of our MISC1 elements will be investigated in the future. The MISC2 element is almost of the same accuracy as the MISC1 element and it is stable but it is also slower.

Another study will concern the shear term. By replacing 2×2 Gauss integration on the shear term with a reduced integration with stabilization, we expect the element to be even better suited to handle arbitrary mesh distortions.

---

[1]for all examples tested

Chapter 6

A stabilized smoothed finite element method for free vibration analysis of Mindlin–Reissner plates

6.1 Introduction

The free vibration analysis of plate structures plays an important role in engineering applications. Due to limitations of the analytical methods for practical applications, numerical methods have become the most widely used computational tool for plate structures. One of the most popular numerical approaches for analyzing vibration characteristics of the plates is the well-known Finite Element Method (FEM).

Although the finite element method provides a general and systematic technique for constructing basis functions, a number of difficulties have still existed in the development of plate elements based on shear deformation theories. One of which is the shear locking phenomena as the plate thickness decreases. In order to avoid this drawback, various improvements of formulations as well as numerical techniques have been used, such as the reduced and selective integration elements (Zienkiewicz *et al.* (1971); Hughes *et al.* (1977); Hughes *et al.* (1978)), mixed formulation/hybrid elements by Pian & Tong (1969); Lee & Pian (1978); Lee & Wong (1982), the Assumed Natural Strain (ANS) method (Hughes & Tezduyar (1981); Bathe & Dvorkin (1985, 1986); Dvorkin & Bathe (1994)) and Enhanced Assumed Strain (EAS) method (Simo & Rifai (1990)). Many improved versions of plate elements have been developed and can be found in the textbooks (Bathe (1996); Zienkiewicz & Taylor (2000)). In the other front of element's technology development, Liu *et al.* (2007a) have recently proposed a smoothed finite element method (SFEM) by introducing a strain smoothing operation (Chen *et al.* (2001)) into the finite element formulation for two dimensional problems. Based on the idea of the SFEM, Nguyen-Xuan *et al.* (2008b) formulated a plate element so-called the MISCk elements by incorporating the curvature smoothing operation (the strain smoothing method) with the original MITC4 element in Bathe & Dvorkin (1985). The properties of the SFEM

are studied in detail by Liu *et al.* (2007b); Nguyen *et al.* (2007b); Nguyen-Xuan *et al.* (2007b). The SFEM has also been applied to dynamic problems for 2D solids (Dai & Liu (2007)).

The objective of this chapter is to further extend the MISCk elements to the free vibration analysis of plates of various shapes, see e. g. Nguyen-Xuan & Nguyen (2008). 4-node quadrilateral elements are considered and each is subdivided into $k \in \{1, 2, 4\}$ smoothing cells in the calculation of bending stiffness matrix. Shear strains are interpolated from the values of the covariant components of the transverse shear strains at four mid-side points of the quadrilateral element. To improve the convergence of the elements, the issue of shear strain stabilization is also studied. The evaluation of the shear stiffness matrix is done using 2×2 Gauss quadrature points. Several numerical examples are presented to show the accuracy, stability and effectiveness of the present elements. We will show by numerical experiments that the present method is faster and more accurate than the original MITC4 element, at least for all examples tested. Moreover, due to the integration technique, the element promises to be more accurate especially for distorted meshes. Also the present element is free of shear locking in thin plate limit.

6.2   A formulation for stabilized elements

The application of the SFEM to plate analysis by Nguyen-Xuan *et al.* (2008b) has resulted in the MISCk elements that use $k \in \{1, 2, 4\}$ smoothing cells as shown in Figure 3.2 for the bending strains and an independent interpolation for shear strains. The smoothing cells are created by subdividing the element.
A smoothed curvature operation is recalled as

$$\tilde{\boldsymbol{\kappa}}^h(\mathbf{x}_C) = \int_{\Omega^h} \boldsymbol{\kappa}^h(\mathbf{x}) \Phi(\mathbf{x} - \mathbf{x}_C) d\Omega \tag{6.1}$$

where Φ is assumed to be a step function defined by

$$\Phi(\mathbf{x} - \mathbf{x}_C) = \begin{cases} 1/A_C, \mathbf{x} \in \Omega_C \\ 0, \mathbf{x} \notin \Omega_C \end{cases} \tag{6.2}$$

where A_C is the area of the smoothing cell, $\Omega_C \subset \Omega^e \subset \Omega^h$.
Substituting Equation (6.2) into Equation (6.1), and applying the divergence theorem, we obtain

$$\tilde{\boldsymbol{\kappa}}_{ij}^h(\mathbf{x}_C) = \frac{1}{2A_C} \int_{\Omega_C} \left(\nabla \otimes \boldsymbol{\beta}^h + \boldsymbol{\beta}^h \otimes \nabla\right)_{ij} d\Omega = \frac{1}{2A_C} \int_{\Gamma_C} (\beta_i^h n_j + \beta_j^h n_i) d\Gamma \tag{6.3}$$

where Γ_C is the boundary of the smoothing cell and n_i, n_j are the components of the normal vector of the boundary.
The discretized solutions of the problem associated with the smoothed operator are : find

$\omega^h \in \mathbb{R}^+$ and $\mathbf{0} \neq (w^h, \boldsymbol{\beta}^h) \in \mathcal{V}^h$ such as

$$\begin{aligned} \tilde{a}(\boldsymbol{\beta}^h, \boldsymbol{\eta}) + \lambda t(\nabla w^h - \mathbf{R}_h \boldsymbol{\beta}^h, \nabla v - \mathbf{R}_h \boldsymbol{\eta}) + k(w^h, v) = (\omega^h)^2 \{\rho t(w^h, v) \\ + \frac{1}{12} \rho t^3 (\boldsymbol{\beta}^h, \boldsymbol{\eta})\}, \forall (v, \boldsymbol{\eta}) \in \mathcal{V}_0^h \end{aligned} \tag{6.4}$$

where $\tilde{a}(., .)$ is a "smoothed" bilinear form:

$$\tilde{a}(\boldsymbol{\beta}^h, \boldsymbol{\eta}) = \sum_{e=1}^{ne} \sum_{ic=1}^{nc} \int_{\Omega_{ic}^e} \tilde{\boldsymbol{\kappa}}_{ic}(\boldsymbol{\beta}^h) : \mathbf{D}^b : \tilde{\boldsymbol{\kappa}}_{ic}(\boldsymbol{\eta}) d\Omega_{ic}^e \tag{6.5}$$

and

$$\tilde{\boldsymbol{\kappa}}_{ic} = \frac{1}{A_{ic}} \int_{\Omega_{ic}^e} \boldsymbol{\kappa}(\mathbf{x}) d\Omega_{ic}^e \text{ and } A^e = \sum_{ic=1}^{nc} A_{ic} \tag{6.6}$$

with A_{ic} is the area of the ic^{th} smoothing cell of the element, $\Omega_{ic}^e \equiv \Omega_C$.
We thus point out a modified method on the bending terms by the smoothed operator while the shear terms are enforced by the reduced operator. As resulted in previous chapter, the MISCk element passes the patch test. Except for the MISC1 element that exhibits two zero energy modes, the MISC2 and MISC4 elements have a sufficient rank and no zero energy modes. It was also shown that the MISC2 element gives the best performance. In comparison to the well known MITC4 element, the MISCk elements are more accurate[1] for regular and especially for irregular meshes or coarse meshes while their computational cost does not increase.
Although the MISCk elements showed that it performed better compared to the MITC4 element, it may suffer from a decreased accuracy and lead to low convergence as the plate thickness is reduced. This drawback is inherited from the original MITC4 element. To overcome this drawback, we adopt a well-known stabilization technique of Stenberg's group in (Kouhia (2007); Lyly *et al.* (1993)) for the shear terms of the MISCk elements to give the so-called SMISCk elements (Nguyen-Xuan & Nguyen (2008)).
The shear term in (6.4) is hence modified as follows

$$\sum_{e=1}^{ne} \frac{\lambda t^3}{t^2 + \alpha h_e^2} \int_{\Omega^e} (\nabla w^h - \mathbf{R}_h \boldsymbol{\beta}^h) : (\nabla v - \mathbf{R}_h \boldsymbol{\eta}) d\Omega \tag{6.7}$$

where h_e is the longest length of the edges of the element $\Omega^e \in \Omega^h$, $\alpha \geq 0$ is a positive constant fixed at 0.1, see e.g. Lyly *et al.* (1993).
Remark. It can seen that the smoothed curvature field, $\tilde{\boldsymbol{\kappa}}^h$ does not satisfy the compatibility equations with the displacement field at any point within the cell. Therefore, $\tilde{\boldsymbol{\kappa}}^h$ can be considered as an assumed curvature field. The weak form needs to be derived using the Hu–Washizu principle (Washizu (1982)) and the Simo–Hughes orthogonality condition (Simo & Hughes (1986)). More details of the variational formulation for the SFEM can find in Liu *et al.* (2007b); Nguyen-Xuan *et al.* (2008b).

---

[1] for all examples tested

6.3   Numerical results

In this section, we examine the numerical accuracy and efficiency of the SMISCk elements (Nguyen-Xuan & Nguyen (2008)) in solving the free vibration problem of plates for natural frequencies. The plates may have free (F), simply (S) supported or clamped (C) edges including square, cantilever, rhombic, stepped cantilever plates, and square plates partially resting on a Winkler elastic foundation. The results of the present method are compared with existing results from published sources. For convenience, the natural frequencies were calculated in a non-dimensional parameter ϖ as defined by authors.

6.3.1   Locking test and sensitivity to mesh distortion

In this subsection, the performance of the element for very thin plates and the sensitivity of the element to mesh distortion is analyzed. We first consider a square plate of width a and thickness t subjected to a uniform load p. The material parameters are Young's modulus $E = 2 \times 10^{11}$ and Poisson's ratio $\nu = 0.3$. Owing to symmetry, only one quadrant of simply supported (SSSS) and fully clamped (CCCC) plates is modelled and illustrated in Figure 6.1. Figures 6.2–6.5 plot the convergence of normalized central deflection and

(a)   (b)
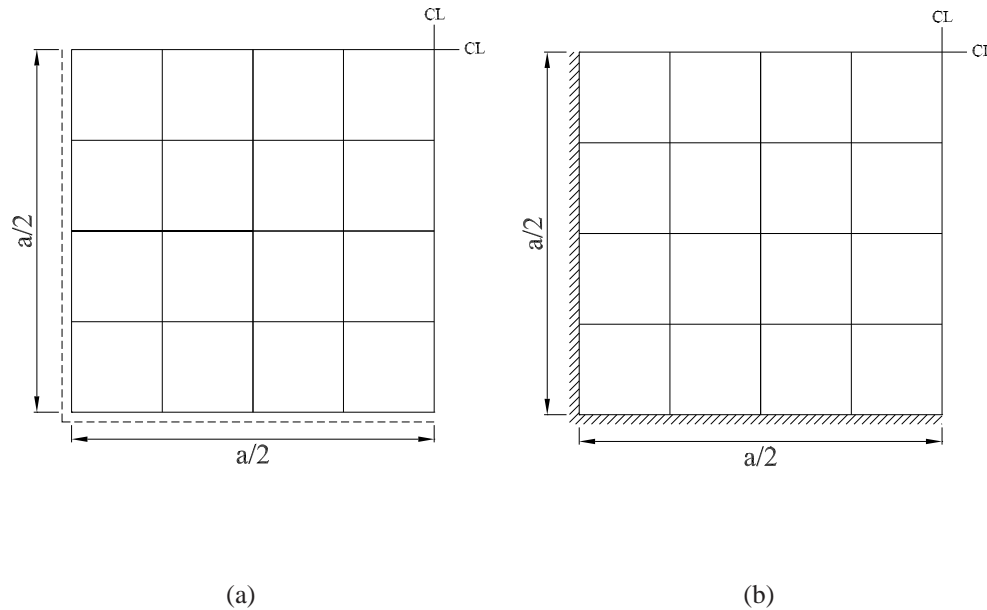
Figure 6.1: Quarter model of plates with uniform mesh (*N*=4): (a) simply supported plate, (b) clamped plate

normalized central moment of the simply supported and clamped plates for varying thicknesses. It is found that all elements give a good agreement with the analytical solution.

In comparison with the results of the original elements without stabilization, the MISCk elements are better about 1.02% to 2.34% for the displacement and 0.8% to 3.28% for the moment (depending on the choice of k- smoothing cells) when coarse meshes are exploited. Additionally, as proved numerically by Liu *et al.* (2007a) that the SFEM and the FEM based on four-node quadrilateral element(Q4) give nearly the same computational cost for coarse meshes where the SFEM gains the better accuracy. However, for finer meshes, the standard FEM is computationally more expensive than the SFEM, and the accuracy of SFEM solution is still maintained. Consequently, the MISCk elements also inherit the effectively computational cost from the SFEM, also see Nguyen-Xuan *et al.* (2008b) for details. With the stabilization technique, the moments of the SMISCk elements converge slightly faster than those of the STAB element[1] while the deflection of the STAB element is better than the SMISCk elements about 0.91% to 3.79%. This reason may come from the fact that the stiffness matrix of SMISCk elements becomes softer after combining with the stabilization issue.

To test the sensitivity to mesh distortion, a sequence of meshes modelling a very thin plate ($a/t = 10^9$) is used as shown in Figure 6.6. The results given in Figures 6.7–6.8 show that the SMISCk elements are relatively insensitive to mesh distortion for this problem.

6.3.2 Square plates

Square plates of width a and thickness t are considered. The material parameters are Young's modulus $E = 2 \times 10^{11}$, Poisson's ratio $\nu = 0.3$ and the density $\rho = 8000$. The plate is modelled with uniform meshes of 4, 8, 16 and 32 elements per each side.

The first problem considered is a SSSS thin plate, as shown in Figure 6.9a. Tables 6.1 and 6.3 give the convergence of the eight lowest modes corresponding to total numbers of d.o.f of 39, 175, 735 and 3007. It can be seen that the MISCk elements agree well with the analytical results and converge slightly faster than the original MITC4 element. The highest frequency of the MISCk is better than the MITC4 about 1.5% to 11.06%. With the stabilization technique, the results given in Tables 6.2 and 6.4 show that the SMISCk elements are slightly more accuracy than the STAB element**?**). The highest frequency of the SMISCk is better than the STAB about 0.93% to 6%.

The second problem is a CCCC square thin plate shown in Figure 6.9b. The convergence of eight lowest modes is summarized in Tables 6.5–6.8 corresponding to total numbers of d.o.f of 27, 147, 675 and 2883. Compare to the STAB elements, the SMISCk elements give the better results about 0.5% to 3%.

6.3.3 Cantilever plates

Consider thin and thick cantilever (CFFF) plates with various shape geometries, see Figures 6.10a–6.10b. A total number of degree of freedom of 816 is used to analyze the

---

[1]the abbreviation of the stabilized MITC4 element resulted in Lyly *et al.* (1993)

(a)

(b)

(c)
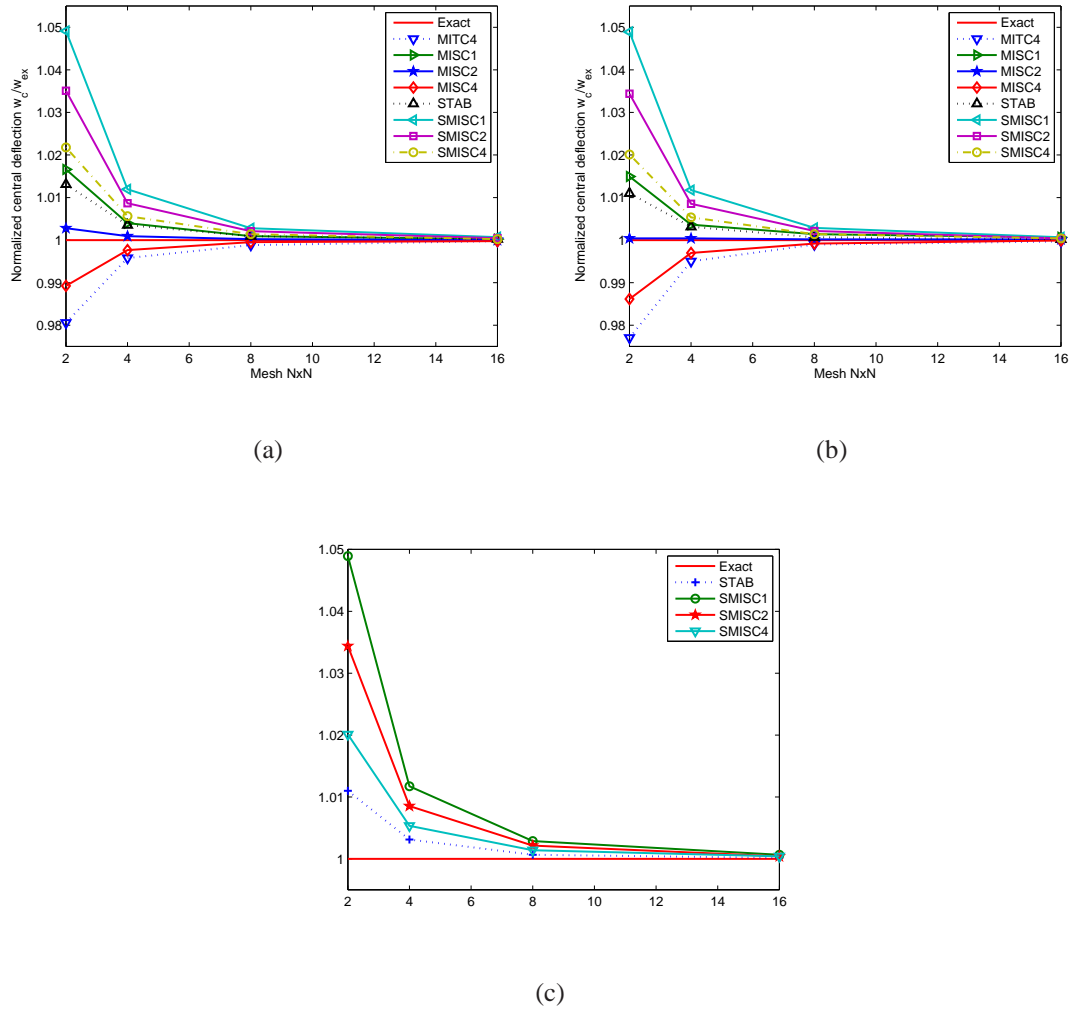
Figure 6.2: Convergence of central deflection of simply supported plate: a) $a/t = 10$, b) $a/t = 10^6$, c) $a/t = 10^9$

(a)

(b)

(c)
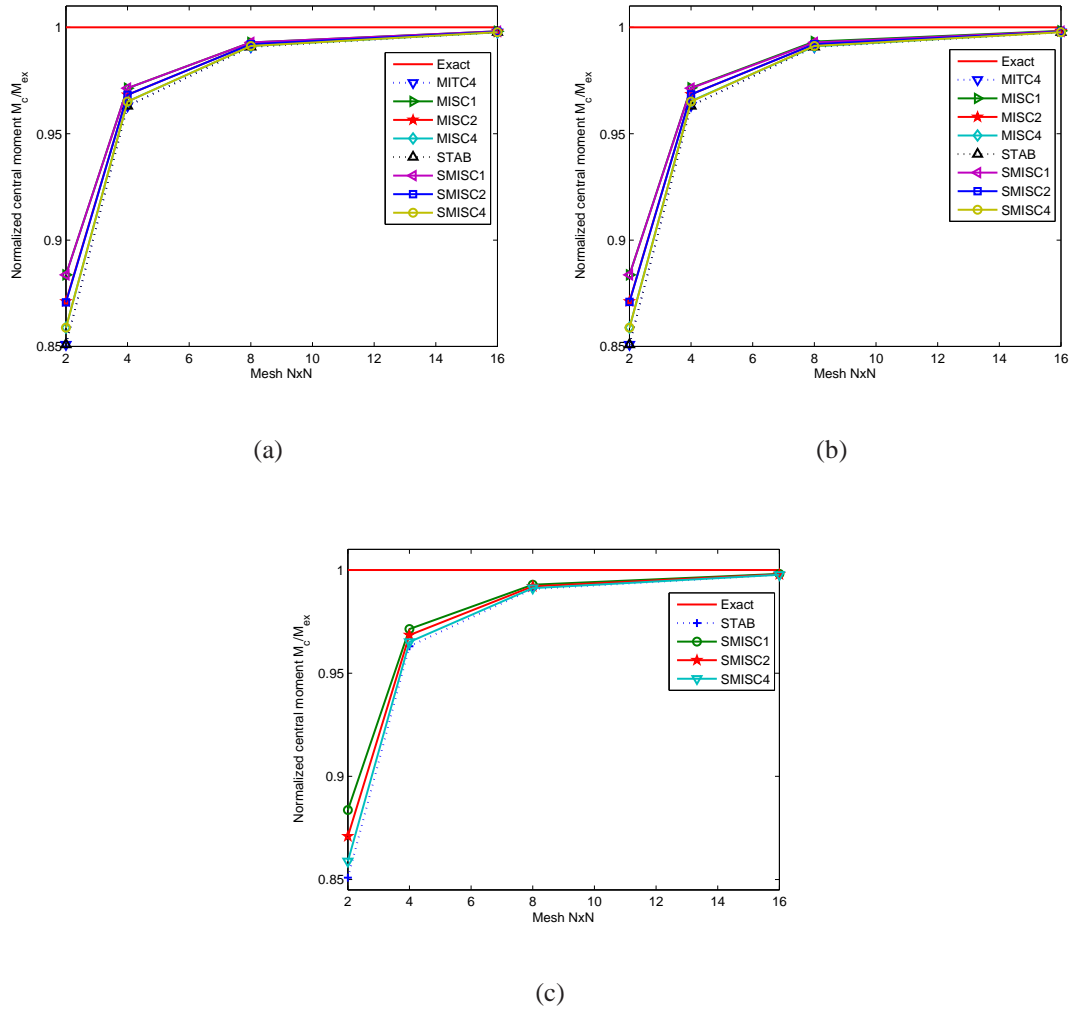
Figure 6.3: Convergence of central moment of simply supported plate: a) $a/t = 10$, b) $a/t = 10^6$, c) $a/t = 10^9$

(a)

(b)

(c)
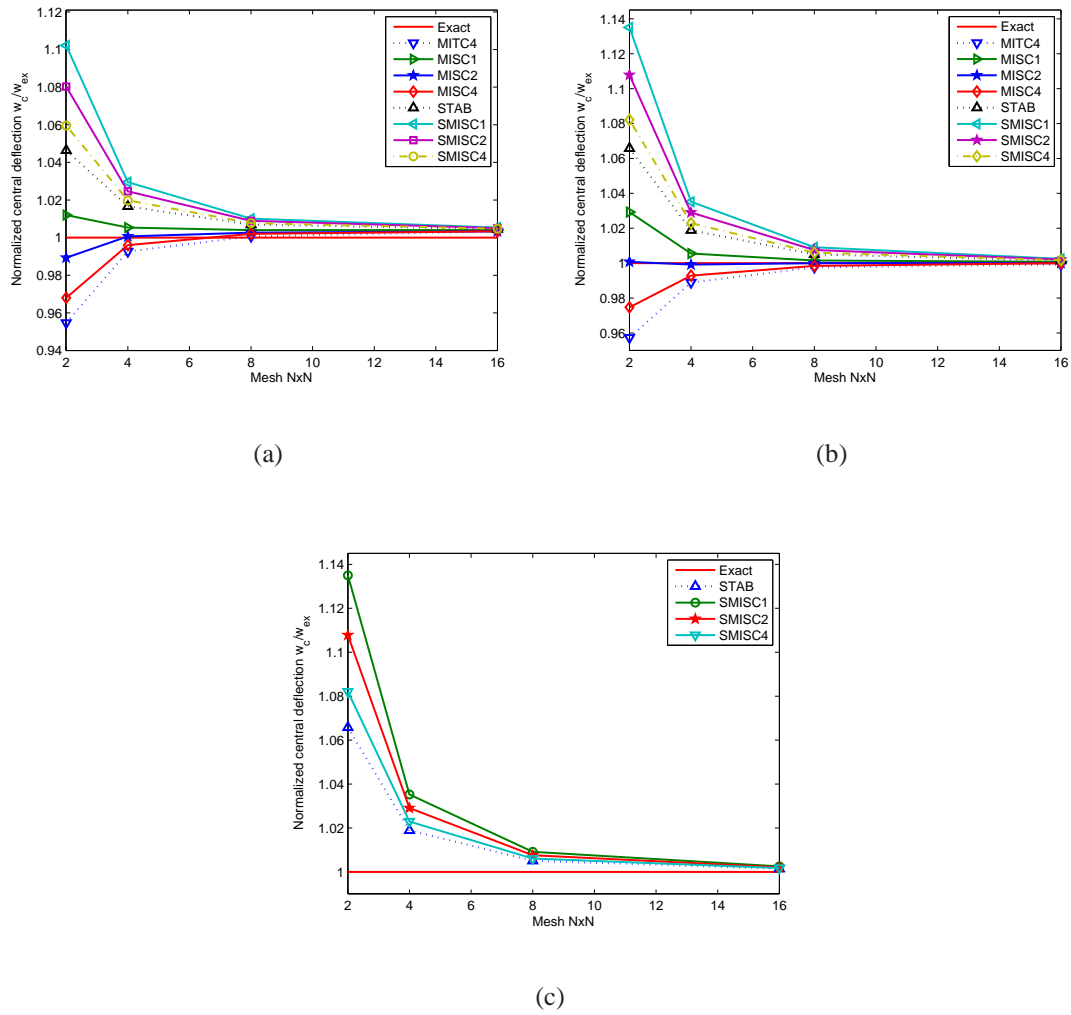
Figure 6.4: Convergence of central deflections of clamped square plate: a) $a/t = 10$, b) $a/t = 10^6$, c) $a/t = 10^9$

(a)   (b)

(c)
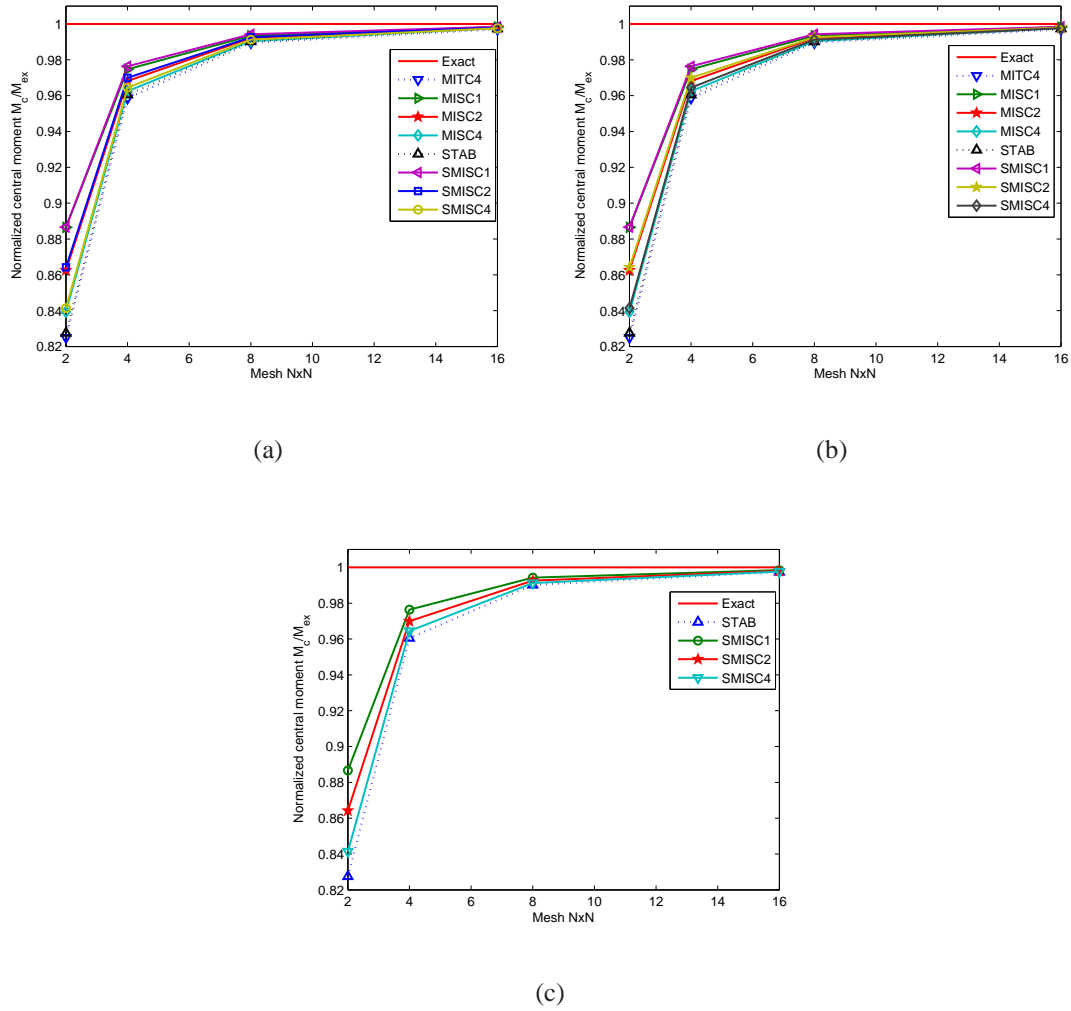
Figure 6.5: Convergence of central moment of square clamped plate: a) $a/t = 10$, b) $a/t = 10^6$, c) $a/t = 10^9$

(a)

(b)

(c)

(d)
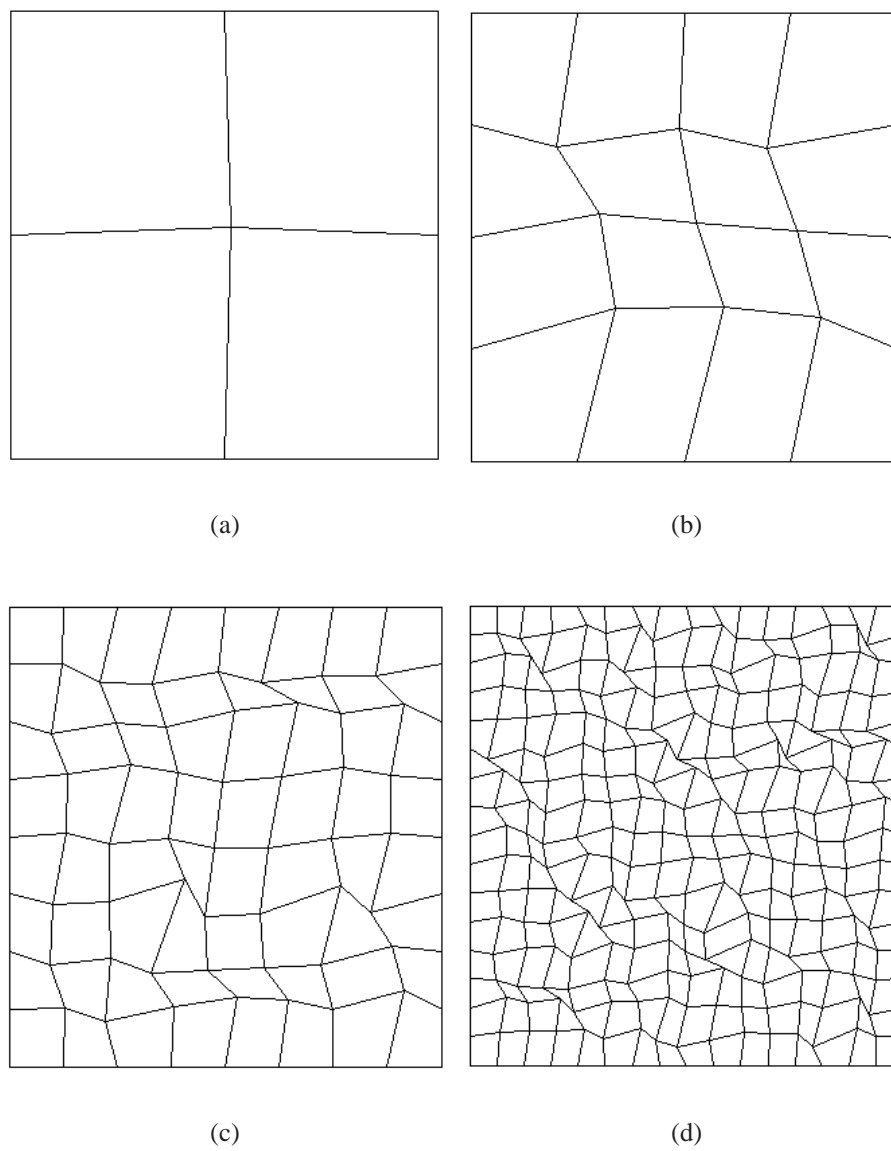
Figure 6.6: Distorted meshes

(a)   (b)
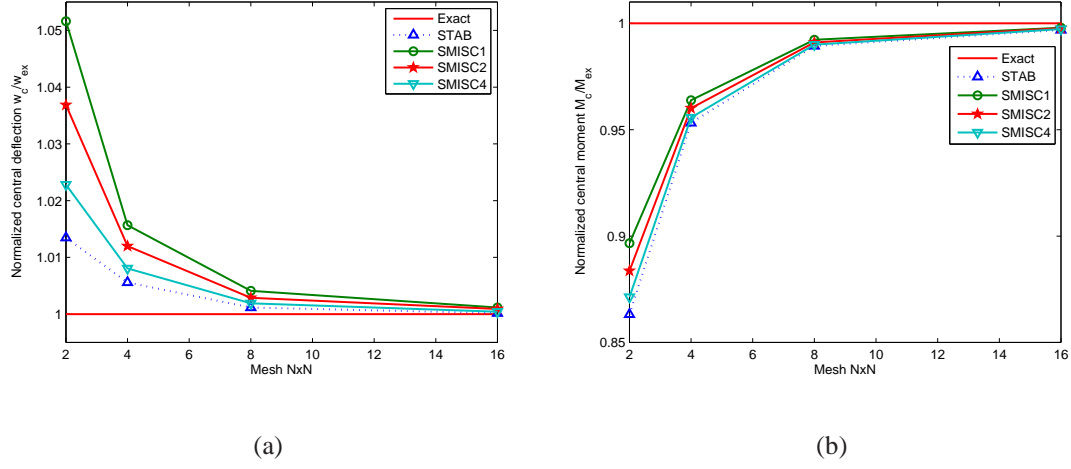
Figure 6.7: Convergence of central deflection and moment of simply supported plate with distorted meshes ($a/t = 10^9$)

(a)   (b)
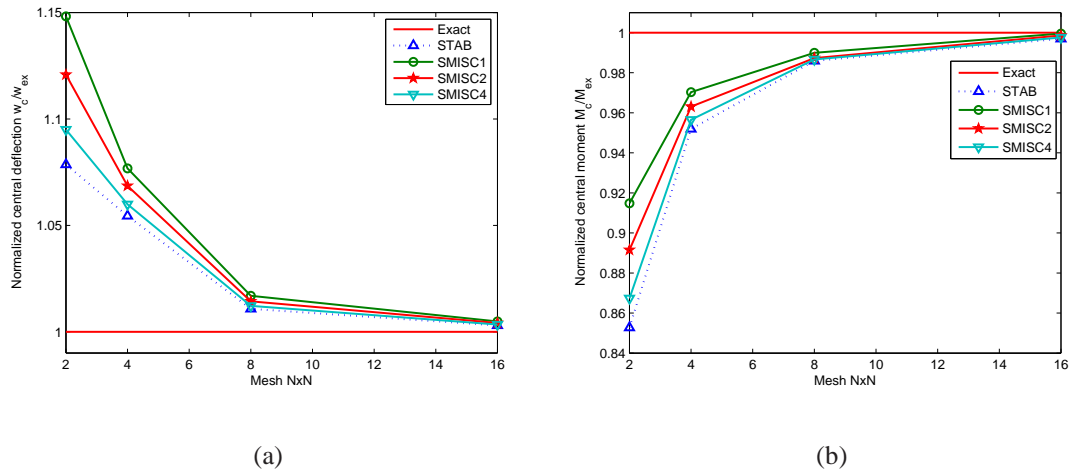
Figure 6.8: Convergence of central deflection and moment of clamped plate with distorted meshes ($a/t = 10^9$)
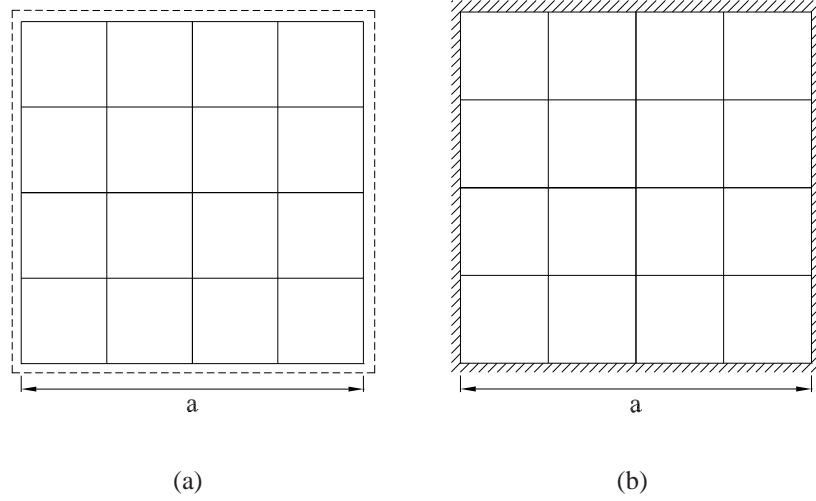
Figure 6.9: plates and initial mesh: (a) supported plate; (b) clamped plate

Table 6.1: A non-dimensional frequency parameter $\varpi = (\omega^2 \rho t a^4 / D)^{1/4}$ of a SSSS thin plate ($t/a = 0.005$), where $D = Et^3/[12(1 - \nu^2)]$ is the flexural rigidity of the plate

modes	1	2	3	4	5	6	7	8
MITC4	4.6009	8.0734	8.0734	10.3050	15.0109	15.0109	16.0952	16.0952
	4.4812	7.2519	7.2519	9.2004	10.7796	10.7796	12.1412	12.1412
	4.4522	7.0792	7.0792	8.9611	10.1285	10.1285	11.5149	11.5149
	4.4451	7.0377	7.0377	8.9033	9.9805	9.9805	11.3708	11.3708
MISC1	4.5576	7.9457	7.9457	9.7956	14.7426	14.7426	14.8420	14.8420
	4.4713	7.2259	7.2259	9.1138	10.7360	10.7360	11.9778	11.9778
	4.4498	7.0730	7.0730	8.9413	10.1185	10.1185	11.4794	11.4794
	4.4445	7.0362	7.0362	8.8984	9.9780	9.9780	11.3622	11.3622
MISC2	4.5739	7.9779	8.0107	9.9959	14.7987	14.8907	15.1820	15.5099
	4.4750	7.2327	7.2386	9.1466	10.7458	10.7590	12.0266	12.0530
	4.4507	7.0746	7.0760	8.9488	10.1208	10.1237	11.4902	11.4953
	4.4447	7.0366	7.0369	8.9002	9.9786	9.9793	11.3649	11.36607
MISC4	4.5902	8.0420	8.0420	10.1847	14.9451	14.9452	15.8092	15.8092
	4.4787	7.2454	7.2454	9.1790	10.7688	10.7688	12.1010	12.1010
	4.4516	7.0776	7.0776	8.9562	10.1260	10.1260	11.5060	11.5060
	4.4449	7.0373	7.0373	8.9021	9.9799	9.9799	11.3687	11.3687
Exact	4.443	7.025	7.025	8.886	9.935	9.935	11.327	11.327

The exact value is cited from Abbassian *et al.* (1987)

Table 6.2: A non-dimensional frequency parameter $\varpi = (\omega^2 \rho t a^4 / D)^{1/4}$ of a SSSS thin plate ($t/a = 0.005$) using the stabilized method

modes	1	2	3	4	5	6	7	8
STAB	4.5576	7.8291	7.8291	9.8260	13.1854	13.1854	14.0314	14.0314
	4.4712	7.2091	7.2091	9.1140	10.6360	10.6360	11.9408	11.9408
	4.4498	7.0693	7.0693	8.9411	10.0994	10.0994	11.4723	11.4723
	4.4445	7.0353	7.0353	8.8984	9.9735	9.9735	11.3606	11.3606
SMISC1	4.5162	7.7191	7.7191	9.4161	13.0420	13.0420	13.3398	13.3398
	4.4614	7.1838	7.1838	9.0312	10.5952	10.5952	11.7901	11.7901
	4.4474	7.0631	7.0631	8.9215	10.0896	10.0896	11.4374	11.4374
	4.4439	7.0337	7.0337	8.8935	9.9711	9.9711	11.3520	11.3520
SMISC2	4.5319	7.7472	7.7749	9.5787	13.0736	13.1204	13.5587	13.6972
	4.4650	7.1905	7.1962	9.0626	10.6044	10.6167	11.8353	11.8594
	4.4441	7.0648	7.0661	8.9289	10.0918	10.0947	11.4480	11.4531
	4.4441	7.0341	7.0345	8.8953	9.9717	9.9724	11.3547	11.3558
SMISC4	4.5474	7.8022	7.8022	9.7307	13.1507	13.1507	13.8825	13.8825
	4.4687	7.2028	7.2028	9.0935	10.6259	10.6259	11.9037	11.9037
	4.4492	7.0677	7.0677	8.9362	10.0969	10.0969	11.4636	11.4636
	4.4443	7.0349	7.0349	8.8971	9.9729	9.9729	11.3584	11.3584
Exact	4.443	7.025	7.025	8.886	9.935	9.935	11.327	11.327

The exact value is cited from Abbassian *et al.* (1987)

Table 6.3: A non-dimensional frequency parameter $\varpi = (\omega^2 \rho t a^4/D)^{1/4}$ of a SSSS thick plate ($t/a = 0.1$)

modes	1	2	3	4	5	6	7	8
MITC4	4.5146	7.6192	7.6192	9.4471	12.2574	12.2574	13.0033	13.0033
	4.4025	6.9402	6.9402	8.6082	9.8582	9.8582	10.9111	10.9111
	4.3753	6.7918	6.7918	8.4166	9.3728	9.3728	10.4685	10.4685
	4.3686	6.7559	6.7559	8.3698	9.2589	9.2589	10.3633	10.3633
MISC1	4.4744	7.5171	7.5171	9.0739	12.1321	12.1321	12.3836	12.3836
	4.3933	6.9184	6.9184	8.5414	9.8275	9.8275	10.8026	10.8026
	4.3731	6.7866	6.7866	8.4012	9.3655	9.3655	10.4440	10.4440
	4.3680	6.7547	6.7547	8.3660	9.2571	9.2571	10.3574	10.3574
MISC2	4.4896	7.5433	7.5688	9.2223	12.1604	12.2002	12.5879	12.6975
	4.3968	6.9242	6.9291	8.5667	9.8345	9.8437	10.8357	10.8523
	4.3739	6.7880	6.7891	8.4070	9.3672	9.3693	10.4515	10.4550
	4.3682	6.7550	6.7553	8.3674	9.2575	9.2580	10.3592	10.3600
MISC4	4.5047	7.5943	7.5943	9.3608	12.2272	12.2272	12.8713	12.8713
	4.4002	6.9348	6.9348	8.5917	9.8506	9.8506	10.8846	10.8846
	4.3748	6.7905	6.7905	8.4128	9.3710	9.3710	10.4624	10.4624
	4.3684	6.7556	6.7556	8.3689	9.2585	9.2585	10.3618	10.3618
Exact	4.37	6.74	6.74	8.35	9.22	9.22	10.32	10.32

The exact value is cited from Abbassian *et al.* (1987)

Table 6.4: A non-dimensional frequency parameter $\varpi = (\omega^2 \rho t a^4 / D)^{1/4}$ of a SSSS thick plate ($t/a = 0.1$) with stabilized technique

modes	1	2	3	4	5	6	7	8
STAB	4.4758	7.4402	7.4402	9.1415	11.5180	11.5180	12.2134	12.2134
	4.3935	6.9069	6.9069	8.5486	9.7703	9.7703	10.7989	10.7989
	4.3731	6.7840	6.7840	8.4026	9.3540	9.3540	10.4434	10.4434
	4.3680	6.7540	6.7540	8.3663	9.2544	9.2544	10.3573	10.3573
SMISC1	4.4372	7.3495	7.3495	8.8226	11.4278	11.4278	11.7529	11.7529
	4.3843	6.8856	6.8856	8.4841	9.7409	9.7409	10.6960	10.6960
	4.3708	6.7788	6.7788	8.3872	9.3467	9.3467	10.4193	10.4193
	4.3675	6.7527	6.7527	8.3626	9.2526	9.2526	10.3513	10.3513
SMISC2	4.4518	7.3729	7.3953	8.9499	11.4492	11.4761	11.9188	11.9764
	4.3878	6.8912	6.8960	8.5086	9.7477	9.7564	10.7274	10.7431
	4.3717	6.7802	6.7813	8.3930	9.3484	9.3505	10.4267	10.4301
	4.3677	6.7531	6.7534	8.3640	9.2530	9.2535	10.3531	10.3540
SMISC4	4.4663	7.4181	7.4181	9.0684	11.4964	11.4964	12.1175	12.1175
	4.3912	6.9016	6.9016	8.5327	9.7630	9.7630	10.7738	10.7738
	4.3725	6.7827	6.7827	8.3988	9.3522	9.3522	10.4374	10.4374
	4.3679	6.7537	6.7537	8.3654	9.2539	9.2539	11.3578	11.3578
Exact	4.37	6.74	6.74	8.35	9.22	9.22	10.32	10.32

The exact value is cited from Abbassian *et al.* (1987)

Table 6.5: A non-dimensional frequency parameter $\varpi = (\omega^2 \rho t a^4 / D)^{1/4}$ of a CCCC square thin plate ($t/a = 0.005$)

modes	1	2	3	4	5	6	7	8
MITC4	6.5638	11.5231	11.5231	13.9504	62.6046	62.6054	62.6222	62.6222
	6.1234	9.0602	9.0602	11.0186	12.9981	13.0263	14.2733	14.2733
	6.0284	8.6801	8.6801	10.5442	11.7989	11.8266	13.1537	13.1537
	6.0055	8.5931	8.5931	10.4346	11.5466	11.5740	12.9150	12.9150
MISC1	6.4463	11.2616	11.2616	12.8858	62.6040	62.6045	62.6081	62.6081
	6.0974	9.0088	9.0088	10.8586	12.9231	12.9583	14.0023	14.0023
	6.0222	8.6680	8.6680	10.5091	11.7818	11.8108	13.0970	13.0970
	6.0039	8.5901	8.5901	10.4261	11.5424	11.5701	12.9014	12.9014
MISC2	6.4911	11.3299	11.3934	13.3155	62.6042	62.6049	62.6110	62.6158
	6.1072	9.0249	9.0315	10.9195	12.9495	12.9857	14.0887	14.1229
	6.0245	8.6719	8.6732	10.5223	11.7881	11.8168	13.1157	13.1211
	6.0045	8.5911	8.5914	10.4293	11.5440	11.5716	12.9059	12.9072
MISC4	6.5350	11.4594	11.4594	13.7071	62.6044	62.6052	62.6187	62.6187
	6.1170	9.0475	9.0475	10.9793	12.9794	13.0094	14.2071	14.2071
	6.0269	8.6771	8.6771	10.5355	11.7946	11.8227	13.1396	13.1396
	6.0051	8.5924	8.5924	10.4325	11.5456	11.5730	12.9116	12.9116
Exact	5.999	8.568	8.568	10.407	11.472	11.498	–	–

The exact solution is cited from Robert (1979)

Table 6.6: A non-dimensional frequency parameter $\varpi = (\omega^2 \rho t a^4/D)^{1/4}$ of a CCCC thin plate ($t/a = 0.005$) with the stabilization

modes	1	2	3	4	5	6	7	8
STAB	6.3137	10.1693	10.1693	12.0678	15.8569	15.8906	16.4953	16.4953
	6.0711	8.9120	8.9120	10.7746	12.5865	12.6206	13.7708	13.7708
	6.0157	8.6478	8.6478	10.4897	11.7257	11.7547	13.0561	13.0561
	6.0023	8.5852	8.5852	10.4212	11.5296	11.5572	12.8917	12.8917
SMISC1	6.2216	10.0205	10.0205	11.5181	15.8293	15.8532	16.1768	16.1768
	6.0467	8.8657	8.8657	10.6352	12.5239	12.5634	13.5493	13.5493
	6.0095	8.6359	8.6359	10.4557	11.7073	11.7396	13.0020	13.0020
	6.0007	8.5823	8.5823	10.4128	11.5254	11.5534	12.8783	12.8783
SMISC2	6.2570	10.0674	10.0904	11.7482	15.8393	15.8688	16.2655	16.3777
	6.0559	8.8802	8.8861	10.6884	12.5465	12.5861	13.6212	13.6474
	6.0119	8.6397	8.6410	10.4685	11.7154	11.7453	13.0197	13.0249
	6.0013	8.5832	8.5835	10.4160	11.5270	11.5549	12.8827	12.8839
SMISC4	6.2913	10.1343	10.1343	11.9500	15.8504	15.8819	16.4363	16.4363
	6.0650	8.9005	8.9005	10.7405	12.5710	12.6064	13.7170	13.7170
	6.0142	8.6448	8.6448	10.4813	11.7216	11.7509	13.0426	13.0426
	6.0019	8.5845	8.5845	10.4191	11.5285	11.5285	12.8884	12.8884
Exact	5.999	8.568	8.568	10.407	11.472	11.498	–	–

The exact solution is cited from Robert (1979)

Table 6.7: A non-dimensional frequency parameter $\varpi = (\omega^2 \rho t a^4/D)^{1/4}$ of a CCCC thick plate ($t/a = 0.1$)

modes	1	2	3	4	5	6	7	8
MITC4	6.1612	9.5753	9.5753	11.2543	14.0893	14.1377	14.7229	14.7229
	5.8079	8.2257	8.2257	9.7310	10.9921	11.0457	11.9161	11.9161
	5.7288	7.9601	7.9601	9.4230	10.3257	10.3752	11.3168	11.3168
	5.7094	7.8972	7.8972	9.3491	10.1714	10.2199	11.1766	11.1766
MISC1	6.0789	9.4501	9.4501	10.8003	14.0489	14.0852	14.3067	14.3067
	5.7892	8.1944	8.1944	9.6447	10.9575	11.0124	11.7964	11.7964
	5.7243	7.9525	7.9525	9.4029	10.3168	10.3168	11.2889	11.2889
	5.7083	7.8953	7.8953	9.3441	10.1692	10.2178	11.1698	11.1698
MISC2	6.1105	9.4923	9.5065	10.9918	14.0641	14.1076	14.4373	14.5842
	5.7963	8.2046	8.2079	9.6777	10.9704	11.0252	11.8376	11.8475
	5.7260	7.9550	7.9557	9.4105	10.3202	10.3699	11.2982	11.3006
	5.7087	7.8959	7.8961	9.3460	10.1700	10.2186	11.1721	11.1726
MISC4	6.1412	9.5459	9.5459	11.1586	14.0802	14.1261	14.6558	14.6558
	5.8032	8.2179	8.2179	9.7100	10.9836	11.0374	11.8873	11.8873
	5.7277	7.9582	7.9582	9.4180	10.3235	10.3731	11.3099	11.3099
	5.7092	7.8967	7.8967	9.3478	10.1708	10.2194	11.1749	11.1749
Ref[*]	5.71	7.88	7.88	9.33	10.13	10.18	11.14	11.14

(*) The solution is cited from Liu (2002)

Table 6.8: A non-dimensional frequency parameter $\varpi = (\omega^2 \rho t a^4 / D)^{1/4}$ of a CCCC thick plate ($t/a = 0.1$) with the stabilization

modes	1	2	3	4	5	6	7	8
STAB	5.9821	8.9828	8.9828	10.5032	12.5564	12.6050	13.2327	13.2327
	5.7700	8.1376	8.1376	9.6084	10.8160	10.8706	11.7213	11.7213
	5.7197	7.9404	7.9404	9.3950	10.2901	10.3399	11.2752	11.2752
	5.7072	7.8924	7.8924	9.3422	10.1629	10.2115	11.1666	11.1666
SMISC1	5.9121	8.8866	8.8866	9.5277	12.5120	12.5527	12.9001	12.9001
	5.7520	8.1080	8.1080	9.5277	10.7840	10.8397	11.6112	11.6112
	5.7152	7.9328	7.9328	9.3753	10.2813	10.3315	11.2479	11.2479
	5.7060	7.8905	7.8905	9.3373	10.1607	10.20937	11.1598	11.1598
SMISC2	5.9389	8.9218	8.9271	10.3211	12.5292	12.5757	13.0150	13.1271
	5.7588	8.1177	8.1207	9.5585	10.7960	10.8515	11.6494	11.6579
	5.7169	7.9353	7.9360	9.3827	10.2846	10.3347	11.2570	11.2593
	5.7065	7.8911	7.8913	9.3392	10.1615	10.2102	11.1621	11.1626
SMISC4	5.9651	8.9602	8.9602	10.4377	12.5467	12.5940	13.1837	13.1837
	5.7655	8.1303	8.1303	9.5887	10.8081	10.8630	11.6948	11.6948
	5.7186	7.9385	7.9385	9.3901	10.2879	10.3378	11.2684	11.2684
	5.7069	7.8919	7.8919	9.3410	10.1624	10.2110	11.1649	11.1649
Ref[*]	5.71	7.88	7.88	9.33	10.13	10.18	11.14	11.14

(*) The solution is cited from Liu (2002)

convergence for modes.

For square cantilever and rhombic plates, it is shown in Table 6.9 that the MISCk elements are in close agreement with results of the pb-2 Ritz method and 9–node quadrilateral element proposed by Karunasena *et al.* (1996) for the same unknowns (d.o.f). Note that the computational cost of the proposed elements is almost lower than that of the 9–node quadrilateral element because of Gauss quadrature points up to 3×3 in terms of the 9–node quadrilateral element. An improved version using stabilization technique is also listed in Table 6.10.

Table 6.9: A frequency parameter $\varpi = (\omega a^2/\pi^2)\sqrt{\rho t/D}$ of a cantilever plates

Case	elements	t/a	Mode sequence number					
			1	2	3	4	5	6
i	MITC4	0.001	0.3520	0.8632	2.1764	2.7733	3.1619	5.5444
	MISC1	0.001	0.3518	0.8623	2.1755	2.7709	3.1564	5.5246
	MISC2	0.001	0.3519	0.8626	2.1759	2.7718	3.1579	5.5311
	MISC4	0.001	0.3519	0.8630	2.1762	2.7727	3.1606	5.5396
	Ref$^{(*)}$	0.001	0.352	0.862	2.157	2.754	3.137	5.481
	MITC4	0.2	0.3387	0.7472	1.7941	2.2912	2.4401	3.9214
	MISC1	0.2	0.3386	0.7467	1.7935	2.2899	2.4374	3.6957
	MISC2	0.2	0.3386	0.7468	1.7938	2.2905	2.4382	3.9166
	MISC4	0.2	0.3386	0.7471	1.7939	2.2909	2.4395	3.9194
	Ref	0.2	0.338	0.745	1.781	2.277	2.421	3.887
ii	MITC4	0.001	0.3986	0.9567	2.5907	2.6504	4.2414	5.2105
	MISC1	0.001	0.3981	0.9542	2.5838	2.6433	4.2304	5.1873
	MISC2	0.001	0.3983	0.9550	2.5863	2.6456	4.2340	5.1953
	MISC4	0.001	0.3985	0.9556	2.5878	2.6472	4.2365	5.2001
	Ref.	0.001	0.398	0.954	2.564	2.627	4.189	5.131
	MITC4	0.2	0.3781	0.8208	1.9999	2.1831	3.1395	3.8069
	MISC1	0.2	0.3769	0.8201	1.9966	2.1798	3.1345	3.7942
	MISC2	0.2	0.3777	0.8204	1.9985	2.1812	3.1366	3.8008
	MISC4	0.2	0.3779	0.8206	1.9993	2.1823	3.1383	3.8045
	Ref	0.2	0.377	0.817	1.981	2.166	3.104	3.760

Case i: square plate   Case ii: rhombic plate, $\alpha = 60^0$

(*) the solution is cited from Karunasena *et al.* (1996)

For the stepped cantilever plate shown in Figure 6.10c, the plate thickness ratio a/t is equal to 24 for the thickest segment. The plate thickness ratio of the two remaining segments equals 32 and 48, respectively. The solutions given in Table 6.11 are compared to the results of Gorman & Singhal (2002). It can be seen that the computed frequencies of our elements converge to Gorman and Singhal's experimentally measured frequencies with refined meshes. Figure 6.11 also illustrates eight mode shapes of free vibration of the stepped cantilever plate.

(a)   (b)

(c)
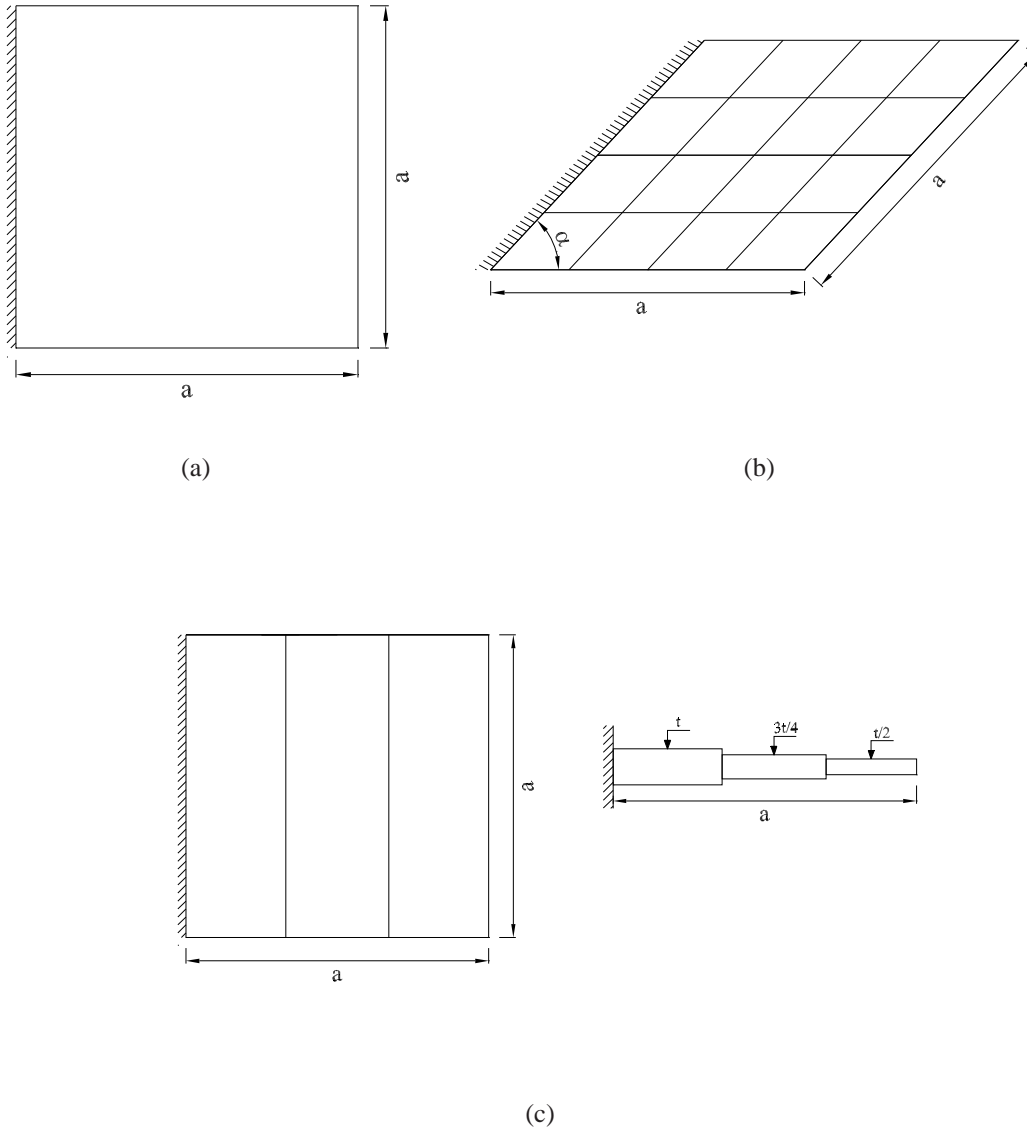
Figure 6.10: A cantilever plate: (a) rectangular plate; (b) rhombic plate; (c) square cantilever plate of three steps of equal width with different thickness

Table 6.10: A frequency parameter $\varpi = (\omega a^2/\pi^2)\sqrt{\rho t/D}$ of a cantilever plates (816 d.o.f) with stabilized method

Case	elements	t/a	Mode sequence number					
			1	2	3	4	5	6
i	STAB	0.001	0.3518	0.8609	2.1720	2.7669	3.1494	5.5131
	SMISC1	0.001	0.3517	0.8601	2.1712	2.7646	3.1442	5.4942
	SMISC2	0.001	0.3517	0.8603	2.1715	2.7654	3.1456	5.5005
	SMISC4	0.001	0.3517	0.8607	2.1718	2.7663	3.1482	5.5085
	Ref$^{(*)}$	0.001	0.352	0.862	2.157	2.754	3.137	5.481
	STAB	0.2	0.3386	0.7465	1.7920	2.2893	2.4368	3.9154
	SMISC1	0.2	0.3385	0.7460	1.7914	2.2880	2.4341	3.6922
	SMISC2	0.2	0.3385	0.7462	1.7917	2.2886	2.4348	3.9106
	SMISC4	0.2	0.3386	0.7465	1.7919	2.2890	2.4361	3.9134
	Ref	0.2	0.338	0.745	1.781	2.277	2.421	3.887
ii	STAB	0.001	0.3982	0.9537	2.5827	2.6433	4.2219	5.1869
	SMISC1	0.001	0.3977	0.9514	2.5756	2.6363	4.2117	5.1647
	SMISC2	0.001	0.3979	0.9527	2.5793	2.6396	4.2167	5.1741
	SMISC4	0.001	0.3981	0.9532	2.5813	2.6417	4.2196	5.1815
	Ref	0.001	0.398	0.954	2.564	2.627	4.189	5.131
	STAB	0.2	0.3780	0.8202	1.9971	2.1810	3.1352	3.8013
	SMISC1	0.2	0.3768	0.8194	1.9938	2.1777	3.1303	3.7887
	SMISC2	0.2	0.3776	0.8198	1.9958	2.1791	3.1324	3.7952
	SMISC4	0.2	0.3778	0.8200	1.9965	2.1802	3.1340	3.7989
	Ref	0.2	0.377	0.817	1.981	2.166	3.104	3.760

Case i: square plate   Case ii: rhombic plate, $\alpha = 60^0$
(*) the solution is cited from Karunasena *et al.* (1996)

Table 6.11: A square plate with two step discontinuities in thickness $\varpi = \omega a^2 \sqrt{\rho t/D}$ with aspect ratio $a/t = 24$ (2970 d.o.f) with the stabilized technique

modes	Gorman & Singhal (2002)	STAB	SMISCk		
			SMISC1	SMISC2	SMISC4
1	4.132	4.1391	4.1389	4.1390	4.1391
2	7.597	7.6681	7.6657	7.6665	7.66755
3	16.510	16.5991	16.5960	16.5975	16.5984
4	18.760	18.7734	18.7659	18.7689	18.7716
5	—	21.9651	21.9528	21.9565	21.9621
6	—	36.8331	36.7950	36.8078	36.8238
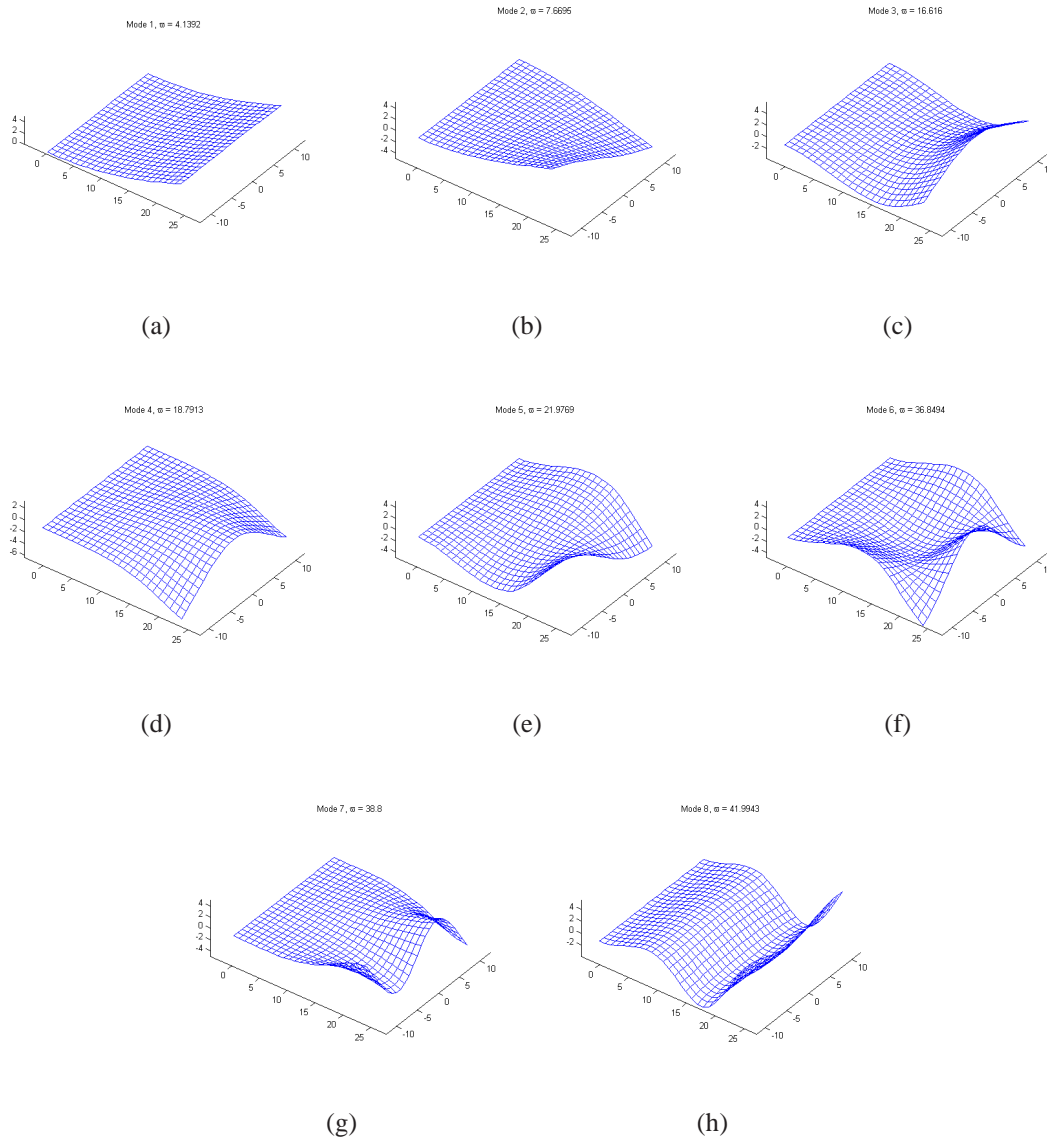
Figure 6.11: The eight shape modes of two step discontinuities cantilever plate using the SMISC2 element

6.3.4 Square plates partially resting on a Winkler elastic foundation

We consider a square plate partially resting on an elastic foundation ($R_1 \neq 0, R_2 = 0$, see Figure 6.12) introduced in Xiang (2003). Two parallel edges are prescribed by a simply supported condition and the two remaining edges may be associated by simply, clamped or free conditions. The foundation stiffness k_i for the ith segment (i=1,2) is described in terms of a non-dimensional foundation stiffness parameter $R_i = k_i a^4/(\pi^4 D)$. For comparison, the foundation length b/a is assigned to 0.5 and the foundation stiffness parameter R_1 is assumed to be 10, 100, 1000, 10000, respectively. The exact solution is cited from Xiang (2003). Results of present elements are given in Tables 6.12–6.15 using the discretized mesh of 625 nodes. It is observed that the frequency parameters λ increase with the corresponding increase of the foundation stiffness R_1. Moreover, the frequency parameters of the SS plate are most identical to those of the CS plate as the foundation stiffness R_1 is large enough. The FF, SF and CF plates also have the same conclusion. The frequency parameters of the presented element approach to an exact value with refined meshes. It is seen that the results of the SMISCk elements give a good agreement with the analytical solution for all cases.
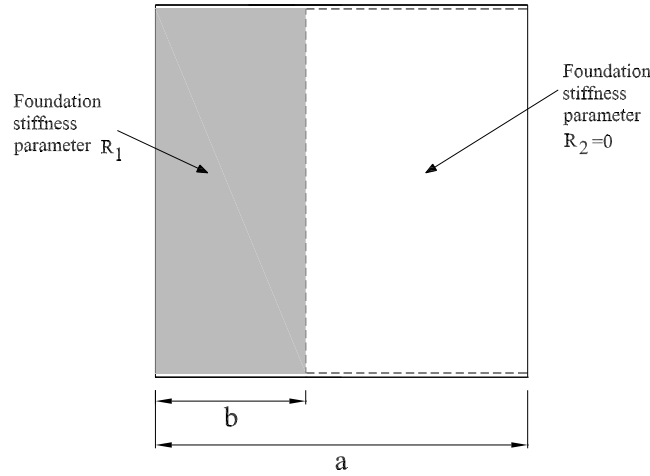
Figure 6.12: A square plate partially resting on elastic foundation under a simply supported condition at two parallel edges

6.4 Concluding remarks

A free vibration of plates using the MISCk elements with stabilization technique, SMISCk, has been studied. Several numerical benchmark tests are verified and the obtained results

Table 6.12: A frequency parameter $\varpi = (\omega a^2/\pi^2)\sqrt{\rho t/D}$ for thick square plates partially resting on a Winkler elastic foundation with the stabilized method ($t/a = 0.1$, $R_1 = 10$)

Cases	elements	Mode sequence number					
		1	2	3	4	5	6
SS plate	STAB	2.7791	5.0721	5.2080	7.4691	8.9725	8.9942
	SMISC1	2.7782	5.0690	5.2053	7.4583	8.9665	8.9883
	SMISC2	2.7785	5.0705	5.2060	7.4624	8.9696	8.9896
	SMISC4	2.7789	5.0713	5.2074	7.4664	8.9710	8.9927
	Exact	2.7752	5.0494	5.1872	7.4348	8.8659	8.8879
CC plate	STAB	3.4196	5.4243	6.4705	8.3469	9.1520	10.6553
	SMISC1	3.4181	5.4196	6.4669	8.3335	9.1441	10.6492
	SMISC2	3.4185	5.4214	6.4678	8.3379	9.1476	10.6506
	SMISC4	3.4192	5.4231	6.4696	8.3435	9.1500	10.6538
	Exact	3.4131	5.4021	6.4277	8.3007	9.0478	10.5016
FF plate	STAB	1.4171	3.2456	4.0133	4.1089	5.1168	6.6913
	SMISC1	1.4167	3.2452	4.0121	4.1071	5.1146	6.6824
	SMISC2	1.4169	3.2454	4.0127	4.1077	5.1157	6.6865
	SMISC4	1.4170	3.2455	4.0130	4.1084	5.1162	6.6891
	Exact	1.4141	3.2431	3.9862	4.0995	5.0933	6.6571
CS plate	STAB	2.8741	5.1597	5.8372	7.8973	9.0302	9.8195
	SMISC1	2.8729	5.1559	5.8340	7.8852	9.0233	9.8134
	SMISC2	2.8733	5.1575	5.8348	7.8894	9.0266	9.8148
	SMISC4	2.8738	5.1587	5.8364	7.8943	9.0285	9.8180
	Exact	2.8693	5.1370	5.8063	7.8579	8.9243	9.6897
CF plate	STAB	1.4272	3.7426	4.0405	6.1075	6.7886	8.1319
	SMISC1	1.4268	3.7409	4.0389	6.1007	6.7845	8.1284
	SMISC2	1.4270	3.7415	4.0396	6.1037	6.7855	8.1299
	SMISC4	1.4271	3.7422	4.0401	6.1058	6.7876	8.1310
	Exact	1.4243	3.7342	4.0132	6.0798	6.7439	8.0135
SF plate	STAB	1.4213	3.5258	4.0295	5.9163	6.0714	8.1240
	SMISC1	1.4209	3.5247	4.0281	5.9105	6.0677	8.1207
	SMISC2	1.4211	3.5251	4.0288	5.9133	6.0687	8.1221
	SMISC4	1.4212	3.5255	4.0292	5.9148	6.0704	8.1231
	Exact	1.4183	3.5199	4.0022	5.8898	6.0384	8.0055

Table 6.13: A frequency parameter $\varpi = (\omega a^2/\pi^2)\sqrt{\rho t/D}$ for thick square plates partially resting on a Winkler elastic foundation with the stabilized method ($t/a = 0.1$, $R_1 = 100$)

Cases	elements	Mode sequence number					
		1	2	3	4	5	6
SS plate	STAB	4.0557	6.2292	9.3539	9.8971	10.7820	11.4449
	SMISC1	4.0537	6.2226	9.3510	9.8860	10.7728	11.4413
	SMISC2	4.0542	6.2252	9.3517	9.8912	10.7759	11.4421
	SMISC4	4.0552	6.2276	9.3532	9.8944	10.7797	11.4440
	Exact	4.0340	6.1991	9.2958	9.7930	10.7375	11.3785
CC plate	STAB	5.0603	6.8109	10.1162	10.1883	11.3586	12.6584
	SMISC1	5.0579	6.8031	10.1136	10.1755	11.3487	12.6537
	SMISC2	5.0585	6.8057	10.1143	10.1808	11.3519	12.6548
	SMISC4	5.0597	6.8089	10.1156	10.1851	11.3561	12.6573
	Exact	5.0313	6.7778	10.0609	10.0862	11.3112	12.5362
FF plate	STAB	1.6618	4.2491	5.5098	7.8368	8.2960	9.9915
	SMISC1	1.6611	4.2465	5.5070	7.8269	8.2907	9.9911
	SMISC2	1.6614	4.2477	5.5078	7.8310	8.2931	9.9912
	SMISC4	1.6616	4.2484	5.5091	7.8344	8.2947	9.9914
	Exact	1.6568	4.2203	5.4796	7.7932	8.1772	9.9851
CS plate	STAB	4.0565	6.2293	9.3970	9.8983	10.8796	12.1289
	SMISC1	4.0545	6.2227	9.3937	9.8872	10.8687	12.1248
	SMISC2	4.0550	6.2253	9.3945	9.8924	10.8723	12.1257
	SMISC4	4.0560	6.2276	9.3961	9.8955	10.8769	12.1279
	Exact	4.0366	6.1992	9.3336	9.7942	10.8291	12.0389
CF plate	STAB	1.6624	4.2492	5.5137	7.8389	8.2961	10.4224
	SMISC1	1.6617	4.2466	5.5110	7.8290	8.2908	10.4195
	SMISC2	1.6620	4.2479	5.5117	7.8330	8.2932	10.4202
	SMISC4	1.6622	4.2485	5.5130	7.8364	8.2948	10.4216
	Exact	1.6573	4.2204	5.4834	7.7953	8.1772	10.3795
SF plate	STAB	1.6619	4.2492	5.5134	7.8376	8.2960	10.2191
	SMISC1	1.6612	4.2466	5.5107	7.8277	8.2908	10.2170
	SMISC2	1.6615	4.2478	5.5114	7.8317	8.2932	10.2175
	SMISC4	1.6618	4.2485	5.5127	7.8351	8.2947	10.2186
	Exact	1.6569	4.2204	5.4831	7.7940	8.1772	10.1900

Table 6.14: A frequency parameter $\varpi = (\omega a^2/\pi^2)\sqrt{\rho t/D}$ for thick square plates partially resting on a Winkler elastic foundation ($t/a = 0.1$, $R_1 = 1000$) with stabilized method

Cases	elements	Mode sequence number					
		1	2	3	4	5	6
SS plate	STAB	4.8727	7.0329	10.6551	12.7649	14.4912	15.4124
	SMISC1	4.8698	7.0230	10.6370	12.7580	14.4654	15.3865
	SMISC2	4.8706	7.0266	10.6448	12.7595	14.4725	15.3988
	SMISC4	4.8720	7.0305	10.6506	12.7632	14.4848	15.4059
	Exact	4.8241	6.9800	10.5372	12.4980	14.2491	15.1195
CC plate	STAB	6.1756	7.8732	11.1256	14.2389	15.6724	15.6812
	SMISC1	6.1722	7.8614	11.1044	14.2325	15.6432	15.6563
	SMISC2	6.1730	7.8651	11.1126	14.2339	15.6560	15.6632
	SMISC4	6.1748	7.8702	11.1203	14.2373	15.6652	15.6750
	Exact	6.1042	7.8068	11.0046	13.9260	15.3817	15.4000
FF plate	STAB	1.8290	4.4032	6.7313	8.4340	9.1464	12.7596
	SMISC1	1.8282	4.3998	6.7273	8.4269	9.1311	12.7276
	SMISC2	1.8285	4.4014	6.7283	8.4302	9.1366	12.7414
	SMISC4	1.8288	4.4024	6.7303	8.4322	9.1426	12.7516
	Exact	1.8194	4.3709	6.6558	8.3129	9.0586	12.0694
CS plate	STAB	4.8727	7.0329	10.6551	12.7649	14.4912	15.4124
	SMISC1	4.8698	7.0230	10.6370	12.7580	14.4654	15.3865
	SMISC2	4.8706	7.0266	10.6448	12.7595	14.4725	15.3988
	SMISC4	4.8720	7.0305	10.6506	12.7632	14.4848	15.4059
	Exact	4.8241	6.9800	10.5372	12.4980	14.2491	15.1195
CF plate	STAB	1.8290	4.4032	6.7313	8.4340	9.1464	12.7596
	SMISC1	1.8282	4.3998	6.7273	8.4269	9.1311	12.7276
	SMISC2	1.8285	4.4014	6.7283	8.4302	9.1366	12.7414
	SMISC4	1.8288	4.4024	6.7303	8.4322	9.1426	12.7516
	Exact	1.8194	4.3709	6.6558	8.3129	9.0586	12.0694
SF plate	STAB	1.8290	4.4032	6.7313	8.4340	9.1464	12.7596
	SMISC1	1.8282	4.3998	6.7273	8.4269	9.1311	12.7276
	SMISC2	1.8285	4.4014	6.7283	8.4302	9.1366	12.7414
	SMISC4	1.8288	4.4024	6.7303	8.4322	9.1426	12.7516
	Exact	1.8194	4.3709	6.6558	8.3129	9.0586	12.0694

Table 6.15: A frequency parameter $\varpi = (\omega a^2/\pi^2)\sqrt{\rho t/D}$ for thick square plates partially resting on a Winkler elastic foundation ($t/a = 0.1$, $R_1 = 10000$) with stabilized method

Cases	elements	Mode sequence number					
		1	2	3	4	5	6
SS plate	STAB	5.3136	7.4455	11.0250	14.1533	15.7395	15.8556
	SMISC1	5.3104	7.4341	11.0036	14.1454	15.7087	15.8258
	SMISC2	5.3112	7.4381	11.0126	14.1471	15.7229	15.8337
	MISC4	5.3128	7.4427	11.0197	14.1513	15.7318	15.8482
	Exact	5.2270	7.3589	10.8802	13.7198	15.4271	15.4547
CC plate	STAB	6.7553	8.4060	11.5803	15.7518	16.0536	17.1701
	SMISC1	6.7515	8.3925	11.5554	15.7445	16.0186	17.1417
	SMISC2	6.7524	8.3966	11.5648	15.7461	16.0336	17.1494
	SMISC4	6.7543	8.4027	11.5741	15.7500	16.0449	17.1630
	Exact	6.6318	8.2943	11.4250	15.2522	15.7395	16.7107
FF plate	STAB	1.9260	4.4870	7.3556	8.5057	9.7647	13.3665
	SMISC1	1.9250	4.4832	7.3510	8.4978	9.7473	13.3297
	SMISC2	1.9254	4.4850	7.3521	8.5015	9.7533	13.3450
	SMISC4	1.9258	4.4861	7.3544	8.5037	9.7604	13.3574
	Exact	1.9093	4.4486	7.2238	8.3798	9.6227	13.1661
CS plate	STAB	5.3136	7.4455	11.0250	14.1533	15.7395	15.8556
	SMISC1	5.3104	7.4341	11.0036	14.1454	15.7087	15.8258
	SMISC2	5.3112	7.4381	11.0126	14.1471	15.7229	15.8337
	SMISC4	5.3128	7.4427	11.0197	14.1513	15.7318	15.8482
	Exact	5.2270	7.3589	10.8802	13.7198	15.4271	15.4547
CF plate	STAB	1.9260	4.4870	7.3556	8.5057	9.7647	13.3665
	SMISC1	1.9250	4.4832	7.3510	8.4978	9.7473	13.3297
	SMISC2	1.9254	4.4850	7.3521	8.5015	9.7533	13.3450
	SMISC4	1.9258	4.4861	7.3544	8.5037	9.7604	13.3574
	Exact	1.9093	4.4486	7.2238	8.3798	9.6227	13.1661
SF plate	STAB	1.9260	4.4870	7.3556	8.5057	9.7647	13.3665
	SMISC1	1.9250	4.4832	7.3510	8.4978	9.7473	13.3297
	SMISC2	1.9254	4.4850	7.3521	8.5015	9.7533	13.3450
	SMISC4	1.9258	4.4861	7.3544	8.5037	9.7604	13.3574
	Exact	1.9093	4.4486	7.2238	8.3798	9.6227	13.1661

are a good agreement with the analytical solution and published sources. All present elements are free of shear locking in the limit of thin plates. It is found that the MISCk and SMISCk elements gain slightly more accurate than the MITC4 and STAB elements, respectively, for the analysis of natural frequencies. In addition, the present method computes directly the bending stiffness matrix in physical coordinates instead of using the iso-parametric mapping as in the MITC4 and STAB elements. The accuracy, therefore, can be maintained even when coarse or distorted meshes are employed.

Chapter 7

A smoothed finite element method for shell analysis

7.1 Introduction

Shell elements are especially useful when the behavior of large structures is of interest. Shell element formulations can be classified into three categories: (1) Curved shell elements based on general shell theory; (2) Degenerated shell elements, that are derived from the three dimensional solid theory; and (3) Flat shell elements, that are formulated by combining a membrane element for plane elasticity and a bending element for plate theory. Since it avoids complex shell formulations, the flat shell element is the simplest one. Therefore, and due to their low computational cost, the flat shell elements are more popular.

Shell elements can also be classified according to the thickness of the shell and the curvature of the mid-surface. Depending on the thickness, shell elements can be separated into thin shell elements (Idelsohn (1974); Nguyen-Dang *et al.* (1979); Debongnie (1986, 2003); Zhang *et al.* (2000); Areias *et al.* (2005); Wu *et al.* (2005)) and thick shell elements (Bathe *et al.* (2000); Bletzinger *et al.* (2000); Sá *et al.* (2002); Cardoso *et al.* (2006, 2007)). Thin shell elements are based on the Kirchoff-Love theory in which transverse shear deformations are neglected. They require C^1 displacement continuity. Thick shell elements are based on the Mindlin theory which includes transverse shear deformations.

Especially the development of Mindlin–Reissner type shell elements suffer from one intrinsic difficulty: locking, i.e. the presence of artificial stresses. It is well known that low-order finite elements lock and that locking can be alleviated by higher order finite elements. There are basically four types of locking:

1. Transverse shear locking, that occurs due to uncorrect transverse forces under bending. It refers to the most important locking phenomenon for plate and shell elements in bending.

2. In-plane shear locking in plates and shells, that is only important under in-plane

loading. For example, the four-node quadrilateral element develops artificial shear stresses under pure bending whereas the eight-node quadrilateral element does not.

3. Membrane locking is often well-known for low-order plane elements and also occurs in shell elements. For examples bilinear elements exhibit membrane locking types; a) membrane locking dominated by a bending response, b) membrane locking caused by mesh distortion.

4. Volumetric locking that occurs when the Poisson ratio ν approaches a value of 0.5.

Methods such as the reduced and selective integration elements, mixed formulation/hybrid elements, the Enhanced Assumed Strain (EAS) method, the Assumed Natural Strain (ANS) method, etc, tried to overcome the locking phenomenon can be found in the textbooks by Hughes (1987); Batoz & Dhatt (1990); Bathe (1996); Zienkiewicz & Taylor (2000).

Among the methods applied to overcome transverse shear locking of Mindlin-Reissner type plate and shell elements, we concern on the Assumed Natural Strain (ANS) method, namely MITC4, in Bathe & Dvorkin (1985, 1986) because the ANS elements are simple and effective. Consequently, the ANS method is widely used in commercial software such as ANSYS, ADINA, NASTRAN, etc.

The objective of this chapter is to present a method to improve the performance of the ANS element based on incorporating the stabiled conforming nodal integration (SCNI) into the MITC4 element. The smoothing procedure was originally developed for meshfree methods to stabilize the rank-deficient nodal integration. Based on the SFEM formula for plate elements in Nguyen-Xuan *et al.* (2008b), Nguyen *et al.* (2007a) have extended the SFEM to analyze shell structures. Herein a quadrilateral shell element with smoothed curvatures that is based on the flat shell concept is presented. It is a combination of the quadrilateral membrane element and the quadrilateral bending Mindlin–Reissner plate element. The inclusion of drilling degrees of freedom summarized in Zienkiewicz & Taylor (2000) is considered in order to avoid a singularity in the local stiffness matrix in cases where all the elements are coplanar.

The way to constitute the element stiffness matrix for the flat shell element is given in Section 2.3.

Membrane strains and bending strains are normalized by a smoothing operator which results in computing membrane and bending stiffness matrices on the boundary of the element while shear strains are approximated by independent interpolation in natural coordinates.

As we will show by several numerical examples, the proposed shell element is especially useful for distorted meshes which often causes membrane locking in shell elements. It is also verified that the original MITC4 element does not perform well with irregular elements.

128

7.2 A formulation for four-node flat shell elements

Based on the previous chapters, the smoothed strain field of a flat shell element may be expressed as

$$\tilde{\varepsilon}^h = \left\{ \begin{array}{c} \tilde{\boldsymbol{\kappa}}^h \\ \tilde{\varepsilon}^m \end{array} \right\} \tag{7.1}$$

where

$$\begin{aligned} \tilde{\boldsymbol{\kappa}} &= \tilde{\mathbf{B}}_C^b \mathbf{q} \\ \tilde{\varepsilon}^m &= \tilde{\mathbf{B}}_C^m \mathbf{q} \end{aligned} \tag{7.2}$$

The smoothed element membrane and bending stiffness matrix in the local coordinate is obtained by

$$\tilde{\mathbf{k}}^m = \int_{\Omega^e} (\tilde{\mathbf{B}}_C^m)^T \mathbf{D}^m \tilde{\mathbf{B}}_C^m d\Omega = \sum_{C=1}^{nc} (\tilde{\mathbf{B}}_C^m)^T \mathbf{D}^m \tilde{\mathbf{B}}_C^m A_C \tag{7.3}$$

$$\tilde{\mathbf{k}}^b = \int_{\Omega^e} (\tilde{\mathbf{B}}_C^b)^T \mathbf{D}^b \tilde{\mathbf{B}}_C^b d\Omega = \sum_{C=1}^{nc} (\tilde{\mathbf{B}}_C^b)^T \mathbf{D}^b \tilde{\mathbf{B}}_C^b A_C \tag{7.4}$$

where nc is the number of smoothing cells of the element, see Figure 3.2. By analyzing the eigenvalue of the stiffness matrix, it is noted that for $nc = 1$, the MIST1 element which will be given in a numerical part contains two zero-energy modes resulted in rank deficiency. The rank of the MIST1 element stiffness matrix is equal to twelve instead of the sufficient rank that would be fourteen.

The integrands are constant over each Ω_C and the non-local strain displacement matrix reads

$$\tilde{\mathbf{B}}_{C_I}^m = \frac{1}{A_C} \int_{\Gamma_C} \begin{pmatrix} N_I n_{\bar{x}} & 0 & 0 & 0 & 0 & 0 \\ 0 & N_I n_{\bar{y}} & 0 & 0 & 0 & 0 \\ N_I n_{\bar{y}} & N_I n_{\bar{x}} & 0 & 0 & 0 & 0 \end{pmatrix} d\Gamma \tag{7.5}$$

$$\tilde{\mathbf{B}}_{CI}^b = \frac{1}{A_C} \int_{\Gamma_C} \begin{pmatrix} 0 & 0 & 0 & 0 & N_I n_{\bar{x}} & 0 \\ 0 & 0 & 0 & -N_I n_{\bar{y}} & 0 & 0 \\ 0 & 0 & 0 & -N_I n_{\bar{x}} & N_I n_{\bar{y}} & 0 \end{pmatrix} d\Gamma \tag{7.6}$$

From Equation (7.6), we can use Gauss points for line integration along each segment of Γ_C^b. If the shape functions are linear on each segment of a cell's boundary, one Gauss point is sufficient for an exact integration:

$$\tilde{\mathbf{B}}_{C_I}^m = \frac{1}{A_C} \sum_{b=1}^{nb} \begin{pmatrix} N_I\left(\bar{\mathbf{x}}_m^G\right) n_{\bar{x}} & 0 & 0 & 0 & 0 & 0 \\ 0 & N_I\left(\bar{\mathbf{x}}_m^G\right) n_{\bar{y}} & 0 & 0 & 0 & 0 \\ N_I\left(\bar{\mathbf{x}}_m^G\right) n_{\bar{y}} & N_I\left(\bar{\mathbf{x}}_m^G\right) n_{\bar{x}} & 0 & 0 & 0 & 0 \end{pmatrix} l_m^C \tag{7.7}$$

$$\tilde{\mathbf{B}}_{CI}^b = \frac{1}{A_C} \sum_{b=1}^{nb} \begin{pmatrix} 0 & 0 & 0 & 0 & N_I(\bar{\mathbf{x}}_b^G) n_{\bar{x}} & 0 \\ 0 & 0 & 0 & -N_I(\bar{\mathbf{x}}_b^G) n_{\bar{y}} & 0 & 0 \\ 0 & 0 & 0 & -N_I(\bar{\mathbf{x}}_b^G) n_{\bar{x}} & N_I(\bar{\mathbf{x}}_b^G) n_{\bar{y}} & 0 \end{pmatrix} l_b^C \tag{7.8}$$

where $\bar{\mathbf{x}}_b^G$ and l_b^C are the midpoint (Gauss point) and the length of Γ_b^C, respectively. The smoothed membrane and curvatures lead to high flexibility such as distorted elements, and a slight reduction in computational cost. The membrane and curvature are smoothed over each sub-cell as shown in Figure 3.2.

Therefore the shell element stiffness matrix can be modified as follows:

$$
\begin{aligned}
\tilde{\mathbf{k}}^e = \tilde{\mathbf{k}}_b^e + \tilde{\mathbf{k}}_m^e + \mathbf{k}_s^e &= \sum_{C=1}^{nc} (\tilde{\mathbf{B}}_C^b)^T \mathbf{D}^b \tilde{\mathbf{B}}_C^b A_C \\
&+ \sum_{C=1}^{nc} (\tilde{\mathbf{B}}_C^m)^T \mathbf{D}^m \tilde{\mathbf{B}}_C^m A_C + \sum_{i=1}^{2} \sum_{i=1}^{2} w_i w_j \mathbf{B}_s^T \mathbf{D}_s \mathbf{B}_s \, |\mathbf{J}| \, d\xi d\eta
\end{aligned}
\tag{7.9}
$$

The transformation of the element stiffness matrix from the local to the global coordinate system is given by

$$
\tilde{\mathbf{K}} = \mathbf{T}^T \tilde{\mathbf{k}}^e \mathbf{T}
\tag{7.10}
$$

As well known, shear locking can appear as the thickness of the shell tends to zero. In order to improve these elements, the so-called assumed natural strain (ANS) method is used to approximate the shear strains (Bathe & Dvorkin (1985)). This work is similar to the plate formulations.

Note that the shear term $\mathbf{k}^s$ is still computed by 2×2 Gauss quadrature while the element membrane and bending stiffness $\mathbf{k}^m$, $\mathbf{k}^b$ in Equation (2.57) is replaced by the smoothed membrane and curvature techniques on each smoothing cell of the element.

7.3 Numerical results

We name our element MISTk (Mixed Interpolation with Smoothing Technique with $k \in \{1, 2, 4\}$ related to number of smoothing cells as given by Figure 3.2). For several numerical examples, we will now compare the MISTk elements to the widely used MITC4 elements. One major advantage of our element is that it is especially accurate for distorted meshes. The distortion meshes are created by the formulations used in Chapter 2.

7.3.1 Scordelis - Lo roof

Consider a cylindrical concrete shell roof where two curved edges are supported by rigid diaphragms, and the other two edges are free, see Figure 7.1. This example was first modeled by MacNeal & Harder (1985). The theoretical midside vertical displacement given by Scordelis & Lo (1964) is 0.3024.

Regular and irregular meshes of $N \times N$ elements are studied for the MITC4 element and the MISTk elements. Typical meshes are shown in Figure 7.2. The results for the uniform meshes are summarized in Table 7.1 and Table 7.2. SFEM elements are also compared to the mixed element by Simo *et al.* (1989), the 4-node physical stabilization shell (QPH) element by Belytschko *et al.* (1994) and the reduced and selective integration (SRI) element in Hughes & Liu (1981).
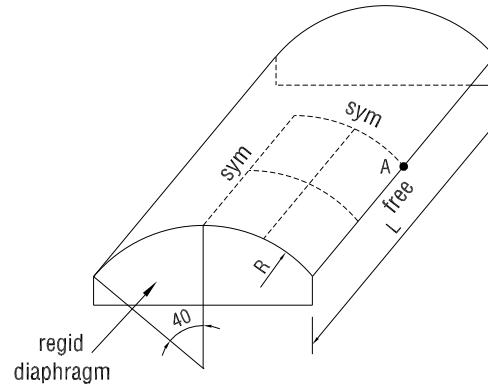
Figure 7.1: Scordelis-Lo roof (R = 25; L = 50; t = 0.25; E = 4.32x10^8; self-weight 90/area; $\nu = 0.0$)

(a) Regular meshes   (b) Irregular meshes

Figure 7.2: Regular and irregular meshes used for the analysis

Table 7.1: Normalized displacement at the point A for a regular mesh

Mesh	MITC4	Mixed	QPH	SRI	MISTk elements		
					MIST1	MIST2	MIST4
4×4	0.9284	1.083	0.940	0.964	1.168	1.060	0.977
6×6	0.9465	-	-	-	1.062	1.014	0.972
8×8	0.9609	1.015	0.980	0.984	1.028	1.001	0.976
10×10	0.9706	-	-	-	1.014	0.997	0.981
12×12	0.9781	-	-	-	1.009	0.997	0.985
14×14	0.9846	-	-	-	1.007	0.998	0.990
16×16	0.9908	1.000	1.010	0.999	1.008	1.001	0.995

131

Table 7.2: The strain energy for a regular mesh

Mesh N^o	MITC4	MISTk elements		
		MIST1	MIST2	MIST4
4×4	1.1247e3	1.4456e3	1.3002e3	1.1888e3
6×6	1.1589e3	1.3126e3	1.2488e3	1.1934e3
8×8	1.1808e3	1.2700e3	1.2342e3	1.2017e3
10×10	1.1942e3	1.2524e3	1.2294e3	1.2082e3
12×12	1.2037e3	1.2446e3	1.2286e3	1.2136e3
14×14	1.2113e3	1.2416e3	1.2299e3	1.2187e3
16×16	1.2180e3	1.2415e3	1.2324e3	1.2238e3

Figure 7.3 plots the convergence of deflection at point A and the strain energy , respectively, for uniform meshes. Especially for coarse meshes, the MISTk elements are more accurate than MITC4 element and show a better convergence rate to the exact solution.

(a)   (b)
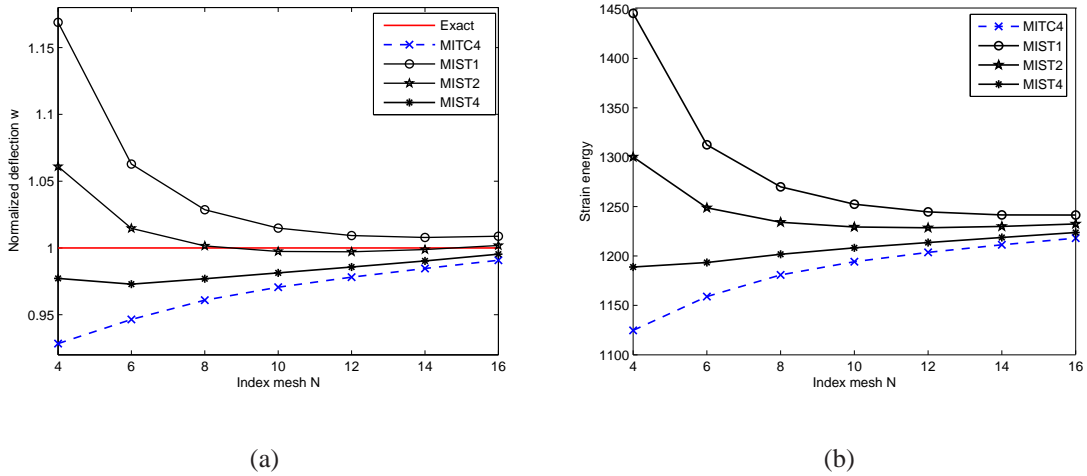
Figure 7.3: Convergence of Scordelis-Lo roof with regular meshes: (a) Deflection at point A; (b) Strain energy

Figure 7.4 depicts the numerical results of the deflections at point A and the strain energy, respectively, for distorted meshes. We note that the MISTk elements are always slightly more accurate compared to the MITC4 element. Simultaneously, they are computationally cheaper.

However, the most remarkable feature of the results appear for highly distorted meshes where the performance of the MISTk elements are vastly superior to the MITC4 element, which fails to converge. when increasing curvature and distortion of the mesh, the effect of membrane locking becomes more pronounced. The MISTk-element are free of membrane and shear locking while the MITC4 element is only free of shear locking. We also
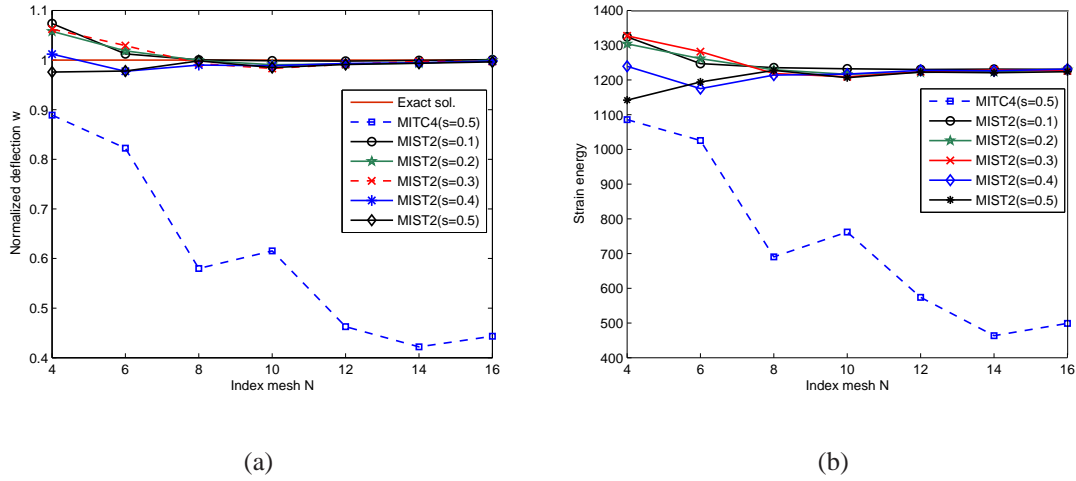
Figure 7.4: Convergence of Scordelis-Lo roof with irregular meshes: (a) Deflection at point A; (b) Strain energy

would like to note that inter alia Lyly *et al.* (1993) found shear force oscillations for the MITC4 element especially for distorted meshes. They proposed a stabilization procedure which is not incorporated in our formulation here. This effect may contribute to the error accumulation in the example tested as well.

In Figure 7.4, we have described the results of our best element, the MIST2 element, for different degrees of mesh distortion s and compared it to the MITC4 element. Though our element is based on flat shell theory, it provides relatively accurate results for non-flat structures.

7.3.2 Pinched cylinder with diaphragm

Consider a cylindrical shell with rigid end diaphragm subjected to a point load at the center of the cylindrical surface. Due to symmetry, only one eighth of the cylinder shown in Figure 7.5 is modeled. The expected deflection under a concentrated load is 1.8245×10^{-5}, see e.g. Taylor & Kasperm (2000).

The problem is described with $N \times N$ MITC4 or MISTk elements in regular and irregular configurations. The meshes used are shown in Figure 7.6.
Figure 7.7 illustrates the convergence of the displacement under the center load point and the strain energy, respectively, for the MITC4 element and our MISTk elements using regular meshes. Our element is slightly more accurate than the MITC4 element for structured meshes. In Table 7.3, we have compared the normalized displacement at the center point of our element to the MITC4 element. The strain energy is summarized in Table 7.4.

The advantage of our element becomes more relevant for distorted meshes, see Fig-
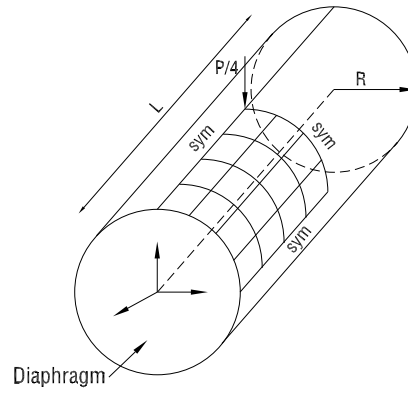
Figure 7.5: Pinched cylinder with diaphragms boundary conditions (P = 1; R = 300; L = 600; t = 3; $v = 0.3$; E = 3×10^7)

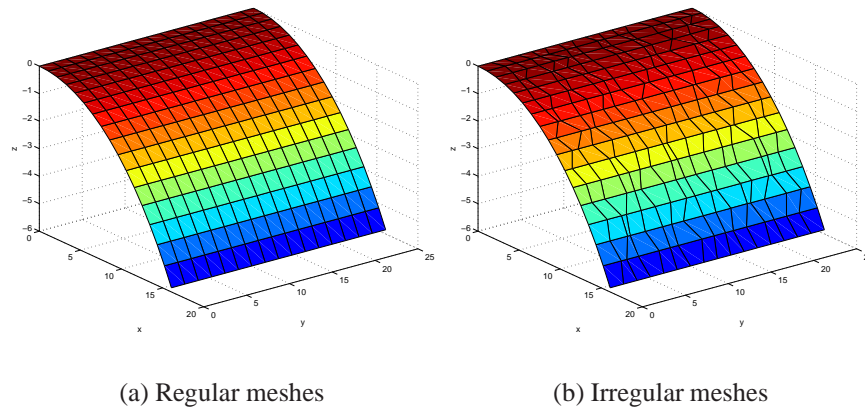(a) Regular meshes
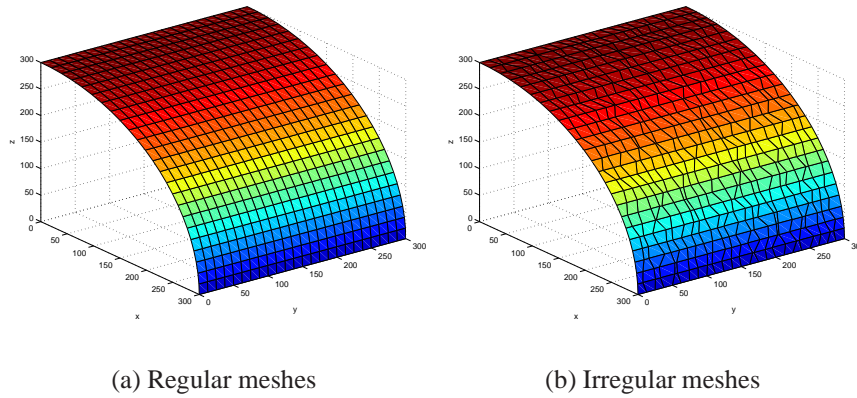
(b) Irregular meshes

Figure 7.6: Regular and irregular meshes used for the analysis

Table 7.3: Normal displacement under the load for a regular mesh

Mesh	MITC4	Mixed	QPH	SRI	MISTk elements		
					MIST1	MIST2	MIST4
4×4	0.3712	0.399	0.370	0.373	0.4751	0.4418	0.3875
8×8	0.7434	0.763	0.740	0.747	0.8094	0.7878	0.7554
12×12	0.8740	-	-	-	0.9159	0.9022	0.8820
16×16	0.9292	0.935	0.930	0.935	0.9574	0.9483	0.9347
20×20	0.9573	-	-	-	0.9774	0.9709	0.9612
24×24	0.9737	-	-	-	0.9889	0.9840	0.9767

Table 7.4: The strain energy for a regular mesh

Mesh N^o	MITC4	MISTk elements		
		MIST1	MIST2	MIST4
4×4	8.4675e-7	1.0837e-6	1.0078e-6	8.8394e-7
8×8	1.6958e-6	1.8462e-6	1.7970e-6	1.7230e-6
12×12	1.9937e-6	2.0891e-6	2.0579e-6	2.0118e-6
16×16	2.1196e-6	2.1837e-6	2.1630e-6	2.1320e-6
20×20	2.1836e-6	2.2296e-6	2.2147e-6	2.1926e-6
24×24	2.2210e-6	2.2556e-6	2.2444e-6	2.2278e-6

(a) (b)
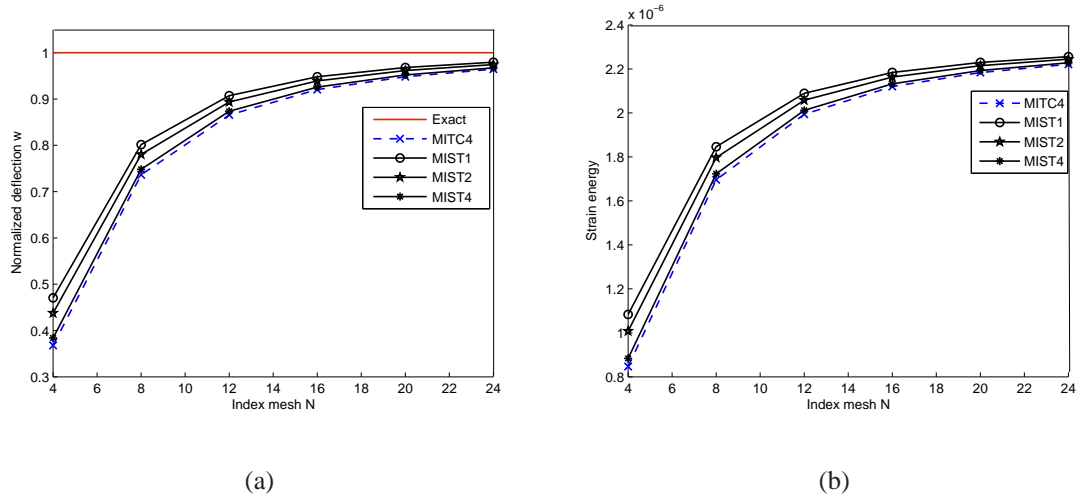
Figure 7.7: Convergence of pinched cylinder with regular meshes: (a) Deflection at point A; (b) Strain energy

135
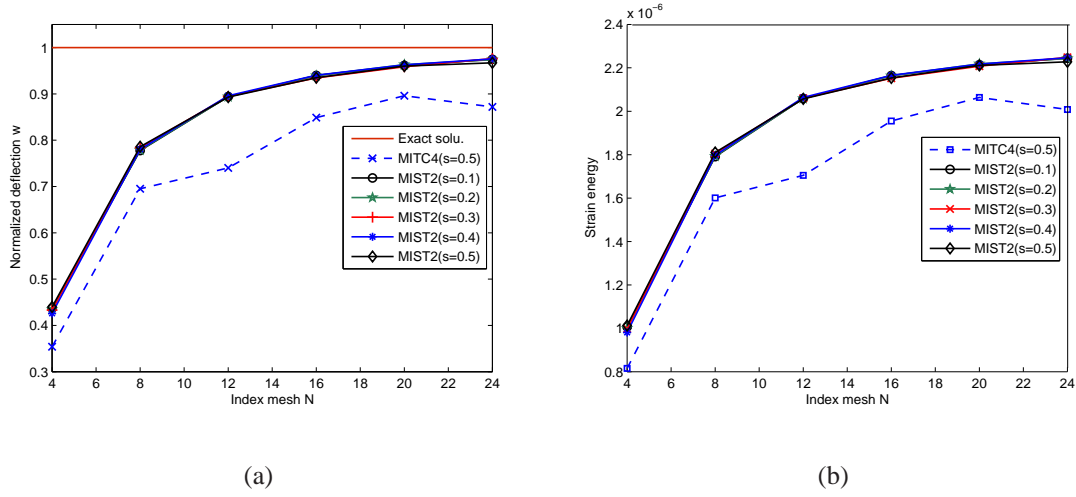
Figure 7.8: Convergence of pinched cylinder with irregular meshes: (a) Deflection at point A; (b) Strain energy

ures 7.8. For the same reasons as outlined in the previous section, the MISTk elements are significantly more accurate as compared to the MITC4-element with increasing mesh distortion.

7.3.3 Hyperbolic paraboloid

A hyperbolic paraboloid shell are restrained the boundary the deflections z direction. Furthermore the boundary conditions are considered $u(-L/2, 0) = u(L/2, 0)$ and $v(0, -L/2) = v(0, L/2)$, respectively. The shell is subjected to a normal pressure loading of $5kN/m^2$. It has a length of $20m$, a height of $L/32m$, and a thickness of $0.2m$. The material has an elastic modulus of $10^8 kN/m^2$ and a Poisson's ratio of 0. An analytical solution has been derived by Duddeck (1962).

The model problem is described in Figure 7.9. Both the MITC4 element and the MISTk elements are tested for a series of meshes with $N \times N$ elements. This problem was chosen in order to study the effect of membrane locking. The meshes are illustrated in Figure 7.10. Figures 7.11 presents the convergence of deflection at point A and the strain energy for regular meshes. In Table 7.5, we have compared the normalized displacement at the center point of our element to other elements in the literature. Knowing that present element is based on flat shell theory, our results are reasonably good. We note that the MISTk elements are always more accurate compared to the MITC4 element. The strain energy is summarized in Table 7.6. The results for distorted meshes are shown in Figures 7.12. We note again that the results of the MITC4 element do not converge since it is not free of membrane locking.

136
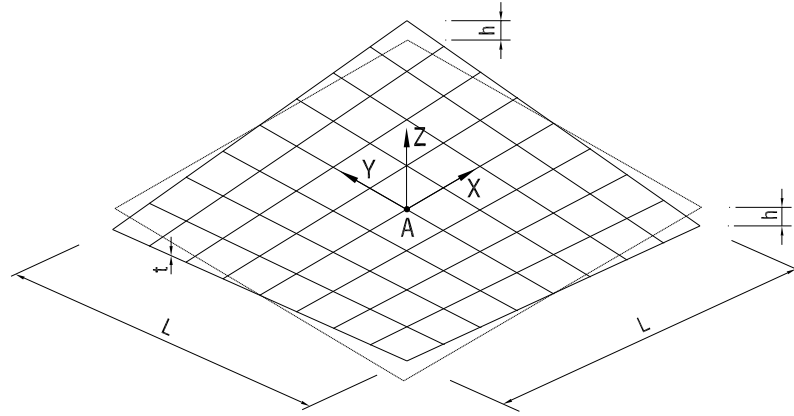
Figure 7.9: Hyperbolic paraboloid ($p = -5kN/m^2$; $L = 20m$; $h = L/32m$; $t = 0.2m$; $\nu = 0$; $E = 10^8 kN/m^2$)

Table 7.5: The displacement at point A for a regular mesh

Mesh	MITC4	Taylor (1988)	Sauer (1998)	G/W	MISTk elements		
					MIST1	MIST2	MIST4
8×8	3.7311	4.51	4.51	4.52	4.5029	4.2315	3.9031
16×16	4.2955	4.55	4.56	4.56	4.5190	4.4468	4.3507
32×32	4.4694	4.56	4.58	4.58	4.5282	4.5089	4.4841
40×40	4.4937	-	-	-	4.5319	4.5195	4.5034
48×48	4.5089	-	-	-	4.5351	4.5259	4.5154
56×56	4.5186	-	-	-	4.5384	4.5315	4.5236
64×64	4.5259	4.57	4.57	4.60	4.5412	4.5362	4.5297

G/W – A linear quadrilateral shell element proposed by Gruttmann & Wagner (2005)

Table 7.6: The strain energy for a regular mesh

Mesh N^o	MITC4	MISTk elements		
		MIST1	MIST2	MIST4
8×8	1.5946e4	2.1015e4	1.8237e4	1.6705e4
16×16	1.8617e4	1.9920e4	1.9289e4	1.8858e4
32×32	1.9440e4	1.9790e4	1.9620e4	1.9504e4
40×40	1.9558e4	1.9791e4	1.9679e4	1.9599e4
48×48	1.9630e4	1.9799e4	1.9705e4	1.9658e4
56×56	1.9678e4	1.9809e4	1.9827e4	1.9699e4
64×64	1.9714e4	1.9842e4	1.9820e4	1.9730e4

(a) Regular meshes   (b) Irregular meshes
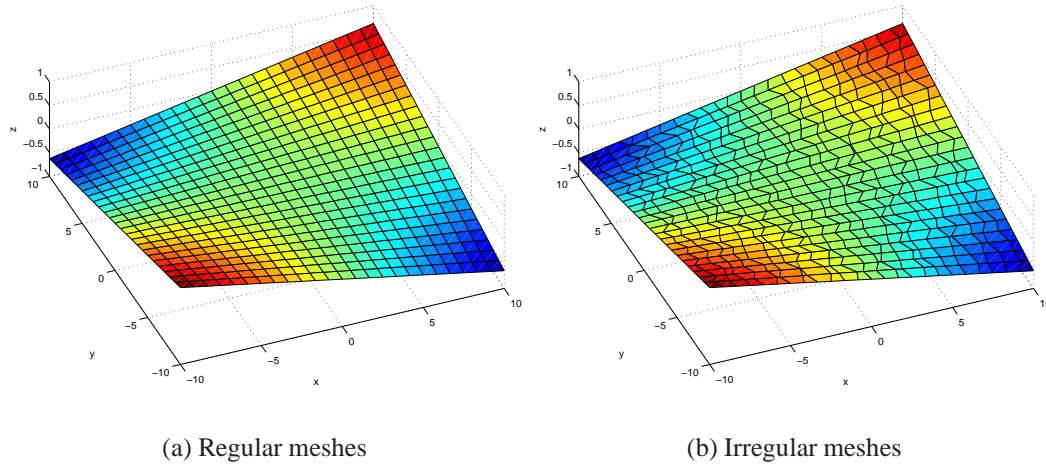
Figure 7.10: Regular and irregular meshes used for the analysis

(a)   (b)
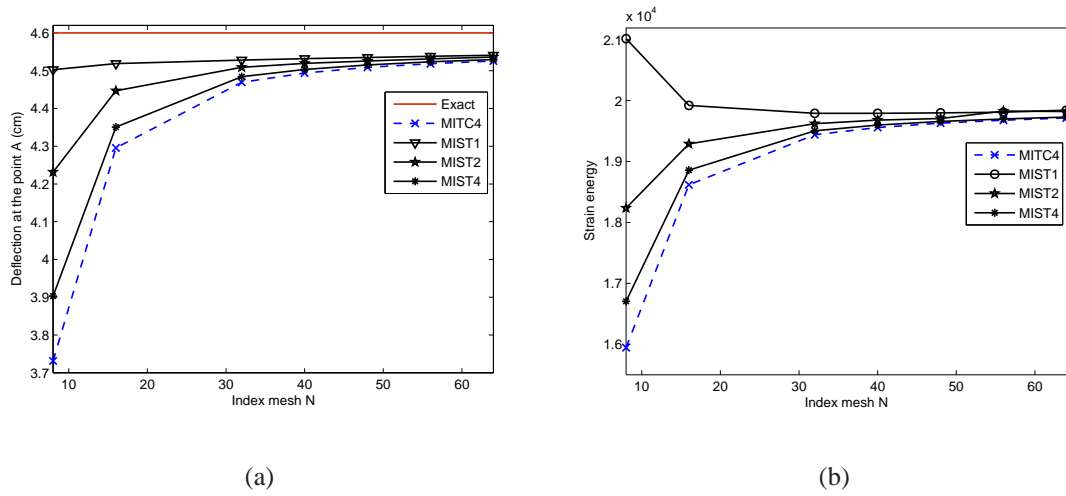
Figure 7.11: Convergence of hyper shell with regular meshes: (a) Deflection at point A; (b) Strain energy
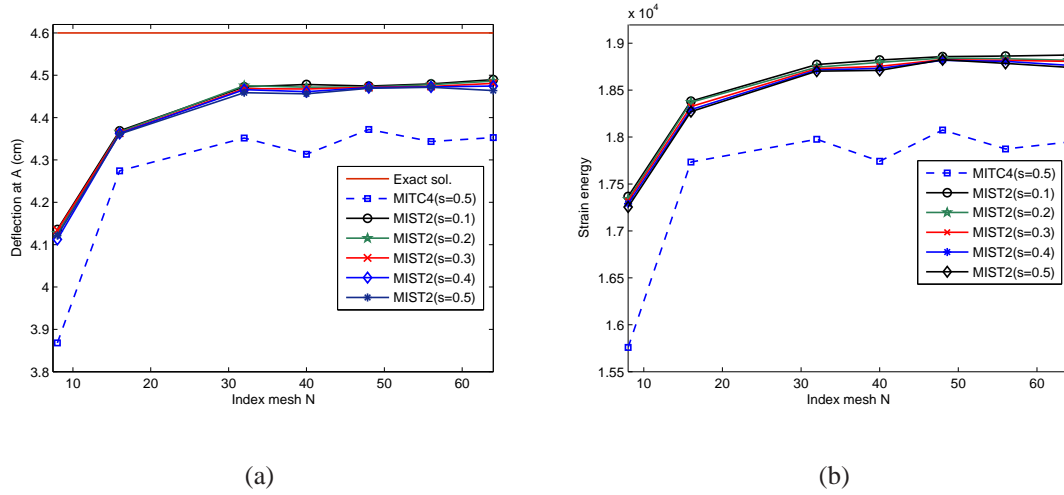
Figure 7.12: Convergence of hyper shell with irregular meshes: (a) Deflection at point A; (b) Strain energy

7.3.4 Partly clamped hyperbolic paraboloid

We consider the partly clamped hyperbolic paraboloid shell structure, loaded by self-weight and clamped along one side. The geometric, material and load data are given in Figure 7.13, and only one half of the surface needs to be considered in the analysis.
For this problem there is no analytical solution, and reference values for the total strain energy E and vertical displacement present in Table 7.7, previously obtained by Bathe *et al.* (2000).

Table 7.7: The reference values for the total strain energy E and vertical displacement w at point B $(x = L/2, y = 0)$

t/L	Strain energy $E(N.m)$	Displacement $w(m)$
1/1000	1.1013×10^{-2}	-6.3941×10^{-3}
1/10000	8.9867×10^{-2}	-5.2988×10^{-1}

Figures 7.15 –7.16 exhibit the convergence of deflection at point B and the strain energy error for a regular mesh with ratio t/L=1000, t/L=1/10000, respectively. In Tables 7.8–7.11 we have compared the displacement at at point B for a regular mesh of our element to other elements in the literature. We note that the MISTk elements are always more accurate compared to the elements compared with. The strain energy is summarized in Tables 7.9 – 7.11. The illustration of the results for the distorted meshes is displayed on Figure 7.17. It largely confirms that the MISTk elements perform well with very distorted meshes.
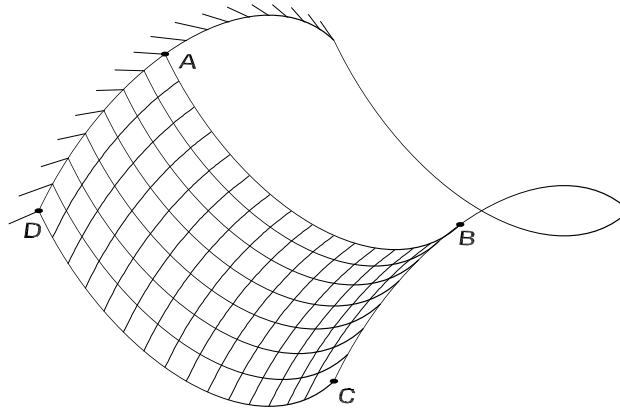
Figure 7.13: Partly clamped hyperbolic paraboloid ($L = 1m$, $E = 2 \times 10^{11} N/m^2$, $\nu = 0.3$, $\rho = 8000 kg/m^3$, $z = x^2 - y^2$, $x \in [-0.5, 0.5]$, $y \in [-0.5, 0.5]$)

(a) Regular meshes
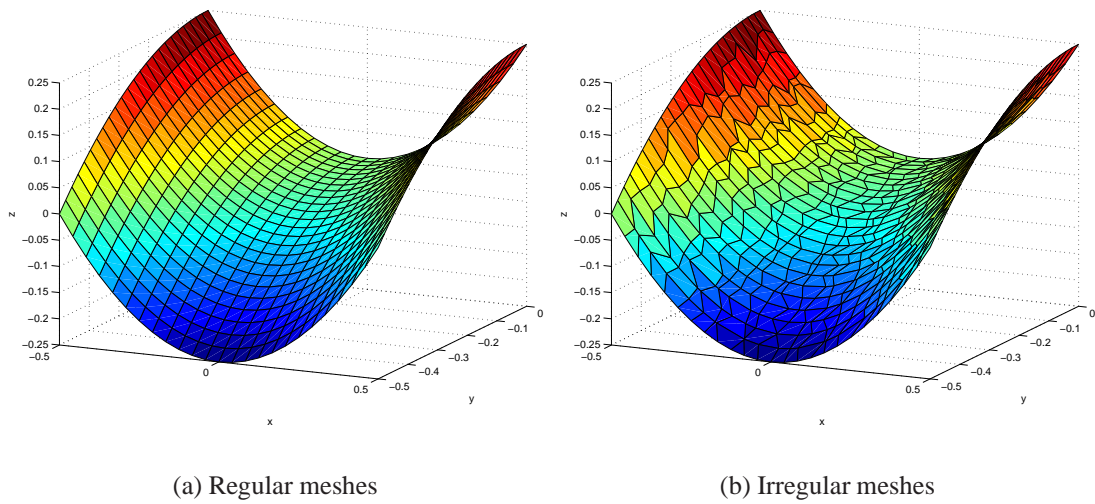
(b) Irregular meshes

Figure 7.14: Regular and irregular meshes used for the analysis

Table 7.8: Deflection at point B for a regular mesh(t/L=1/1000)

Mesh N^o	MITC4	MITC16	MISTk elements		
			MIST1	MIST2	MIST4
8×4	4.7581e-3	-	5.5858e-3	4.9663e-3	4.8473e-3
16×8	5.8077e-3	-	6.1900e-3	5.9294e-3	5.8624e-3
32×16	6.1904e-3	-	6.3470e-3	6.2487e-3	6.2180e-3
40×20	6.2539e-3	-	6.3691e-3	6.2982e-3	6.2751e-3
48×24	6.2939e-3	6.3941e-3	6.3829e-3	6.3287e-3	6.3108e-3

Table 7.9: Convergence in strain energy for a regular mesh (t/L=1/1000)

Mesh N^o	MITC4	MITC16	MISTk elements		
			MIST1	MIST2	MIST4
8×4	0.8016e-2	-	0.9499e-2	0.8384e-2	0.8172e-2
16×8	0.9918e-2	-	1.0623e-2	1.0141e-2	1.0018e-2
32×16	1.0629e-2	-	1.0921e-2	1.0737e-2	1.0668e-2
40×20	1.0741e-2	-	1.0963e-2	1.0831e-2	1.0795e-2
48×24	1.0821e-2	1.1013e-2	1.0989e-2	1.0885e-2	1.0845e-2

Table 7.10: Deflection at point B for a regular mesh(t/L=1/10000)

Mesh N^o	MITC4	MITC16	MISTk elements		
			MIST1	MIST2	MIST4
8×4	0.2851	-	0.3398	0.2959	0.2899
16×8	0.4360	-	0.4789	0.4453	0.4401
32×16	0.4967	-	0.5169	0.5021	0.4991
40×20	0.5063	-	0.5214	0.5106	0.5085
48×24	0.5121	0.5298	0.5240	0.5157	0.5137

Table 7.11: Convergence in strain energy for a regular mesh(t/L=1/10000)

| Mesh N^o	MITC4	MITC16	MISTk elements		
			MIST1	MIST2	MIST4
8×4	0.0471	-	0.0562	0.0488	0.0478
16×8	0.0731	-	0.0806	0.0747	0.0738
32×16	0.0839	-	0.0875	0.0848	0.0844
40×20	0.0856	-	0.0883	0.0865	0.0858
48×24	0.0869	0.0898	0.0892	0.0881	0.0874
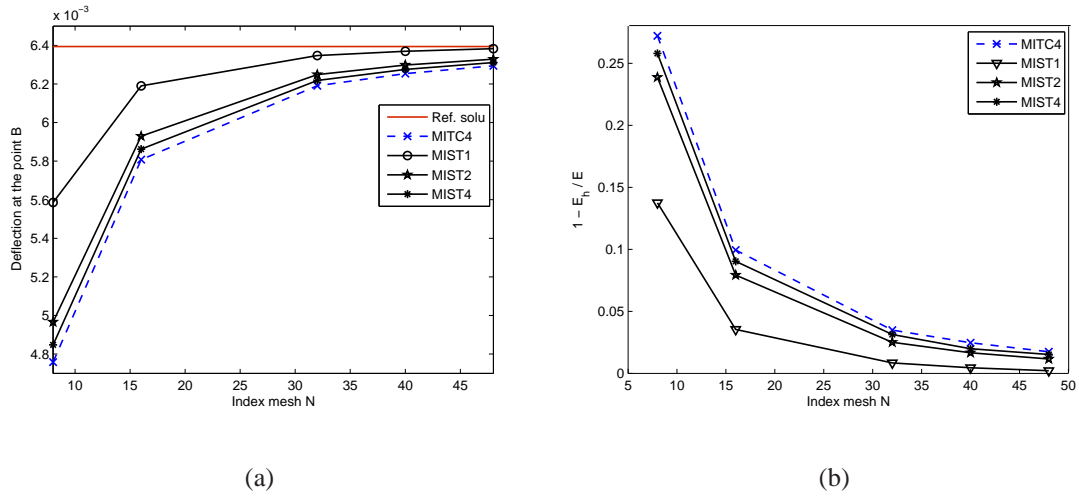
Figure 7.15: Convergence of hyper shell with regular meshes (t/L=1/1000): (a) Deflection at point B; (b) Strain energy error
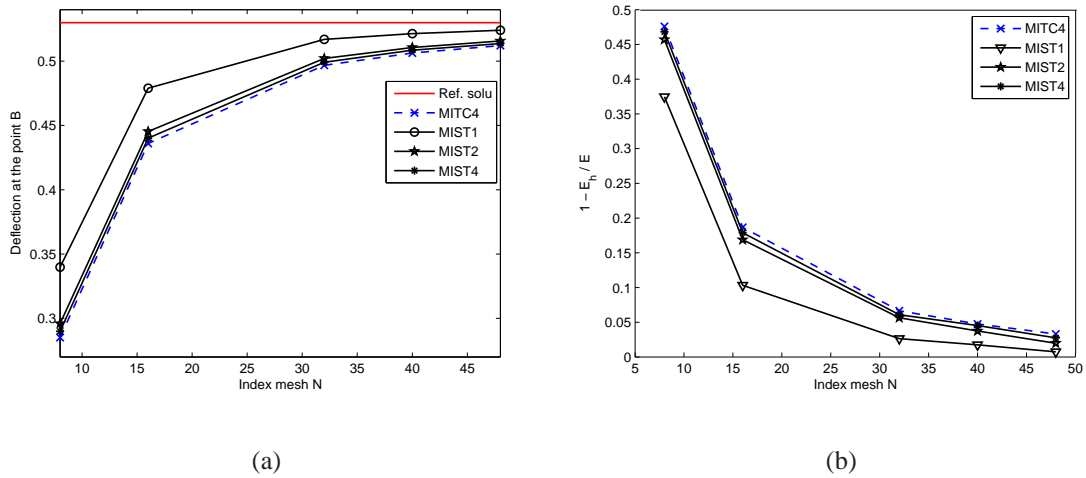
Figure 7.16: Convergence of hyper shell with regular meshes(t/L=1/10000): (a) Deflection at point B; (b) Strain energy error

142
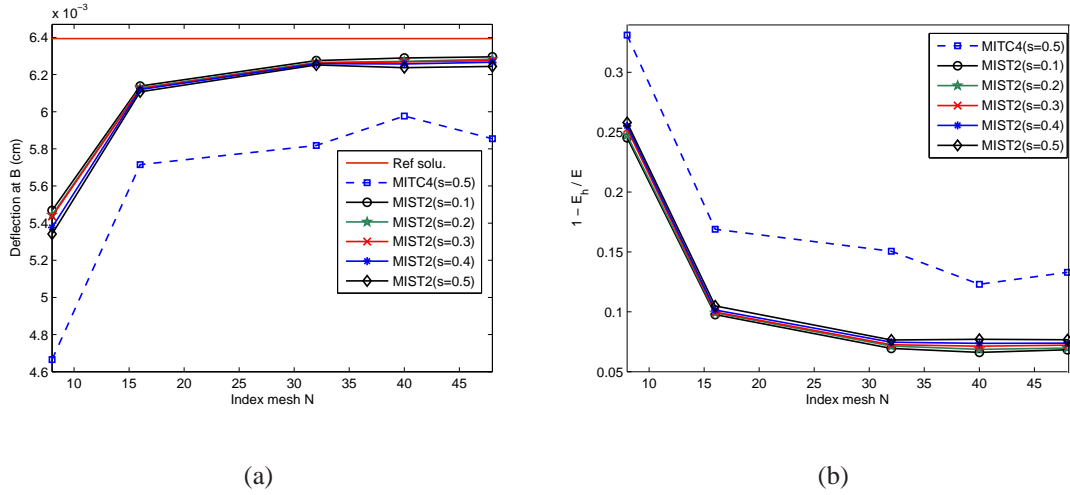
Figure 7.17: Convergence of hyper shell with irregular meshes (t/L=1/1000): (a) Deflection at point B; (b) Strain energy error

7.4 Concluding Remarks

A family of quadrilateral shell elements based on mixed interpolation with smoothed membrane strain and bending strains is proposed. The element is based on the flat element concept though we also tested several problems involving curved structures. Except for the MIST1 element which exhibits two zero energy modes, the MIST2 and the MIST4 elements maintain a sufficient rank. Moreover, these elements do not exhibit membrane locking nor shear locking in the thin shell limit, and they pass the patch test.

The MIST1 element gave the best results for several problems studied. However, this element contains two hourglass modes. In simple cases, the hourglass modes can be automatically eliminated by the boundary conditions, but are still undesirable in more general settings. Therefore, the most reliable element is the MIST2 that retains both a sufficient rank and accuracy.

The major advantage of the method, emanating from the fact that the membrane and bending stiffness matrix are evaluated on element boundaries instead of on their interiors is that the proposed formulation gives very accurate and convergent results for distorted meshes.

In addition to the above points, the author believes that the strain smoothing technique herein is seamlessly extendable to complex shell problems such as non-linear material and geometric non-linearities, problems where large mesh-distortion play a major role.

Chapter 8

A node-based smoothed finite element method: an alternative mixed approach

8.1 Introduction

It is known that a stabilized conforming nodal integration technique has been applied by Chen *et al.* (2001) for stabilizing the solutions in the context of meshfree methods and later applied in the natural-element method (Yoo *et al.* (2004); Yvonnet *et al.* (2004); Cescotto & Li (2007)). Liu *et al* have applied this technique to formulate the linear conforming point interpolation method (LC-PIM) (Liu *et al.* (2006b); Zhang *et al.* (2007)), the linearly conforming radial point interpolation method (LC-RPIM) (Liu *et al.* (2006a)), and the element-based smoothed finite element method (elemental SFEM) (Liu *et al.* (2007a)). Then Liu & Zhang (2007) have explained intuitively and showed numerically that the LC-PIM yields an upper bound in the strain energy when a reasonably fine mesh is employed. Recently, Liu *et al.* (2007c) proposed a node-based smoothed finite element method (N-SFEM) for solid mechanics problems. In the N-SFEM, the domain discretization is still based on elements but the calculation of the system stiffness matrix is performed on cells each of which is associated with a single node, and the strain smoothing technique (Chen *et al.* (2001)) is used. The numerical results demonstrated that the N-SFEM possesses the following properties: 1) it gives an upper bound (in the case of homogeneous essential boundary conditions) in the strain energy of the exact solution when meshes are sufficiently fine; 2) it is relatively immune from volumetric locking; 3) it allows the use of polygonal elements with an arbitrary number of sides; 4) no mapping or coordinate transformation is involved in the N-SFEM and its element is allowed to be of arbitrary shape. The problem domain can be discretized in more flexible ways, and even severely distorted elements can be used. All these features have been demonstrated in detail in Liu *et al.* (2007c) using many numerical examples and elements of complex shapes including polygon with an arbitrary number of sides, extremely distorted quadrilateral elements. However, the related theory has not been set up fully to provide more general theoretical explanation for the N-SFEM.

The aim of this chapter is to elucidate the properties of the N-SFEM and establish the nodal strain smoothing based on the Hellinger-Reissner principle, and formulate a four - node quadrilateral element node quadrilateral element in the setting of N-SFEM termed as NSQ4(Liu *et al.* (2007c)). In the present N-SFEM with NSQ4 elements, the domain discretization is the same as that of the standard FEM and the bilinear interpolation functions of the original displacement FEM model are still used. A quasi-equilibrium quadrilateral element based on the following properties of the NSQ4 is obtained: 1) As long as the external forces are non-zero, strain energy is an upper bound of the exact solution when the used mesh is reasonably fine; 2) volumetric locking is eliminated naturally. Moreover the accuracy and convergence of the present N-SFEM will be proved by a rigorous mathematical proofs on which affirms the reliability of present method theoretically. Finally, all these theories will be confirmed numerically.

8.2 The N-SFEM based on four-node quadrilateral elements (NSQ4)

Assumed that the problem domain Ω is divided into smoothing cells (Liu *et al.* (2007c)) associated with nodes such that $\Omega = \Omega^{(1)} \cup \Omega^{(2)} \cup .... \cup \Omega^{(N_n)}$ and $\Omega^{(i)} \cap \Omega^{(j)} = \emptyset, \ i \neq j$ in which N_n is the total number of field nodes located in the entire problem domain. For four-node quadrilateral elements, the cell $\Omega^{(k)}$ associated with the node k is created by connecting sequentially the mid-edge-point to the intersection of two bi-medians of the surrounding four-node quadrilateral elements as shown in Figure 8.1. As a result, each four-node quadrilateral element will be subdivided into four sub-domains and each sub-domain is attached with the nearest field node, e.g. Liu *et al.* (2007c). The cell $\Omega^{(k)}$ associated with the node k is then created by combination of each nearest sub-domain of all elements around the node k, $\Omega^{(k)} = \Omega_1^{(k)} \cup \Omega_2^{(k)} \cup \Omega_2^{(k)} \cup \Omega_4^{(k)}$. The areas $A^{(k)}$ of the nodal smoothing cells are computed by

$$A^{(k)} = \sum_{c \in T^{(k)}} A^c \tag{8.1}$$

where $T^{(k)}$ is the set of subcells c associated with node k and A^c is the area of the subcells. Introducing now the node-based strain smoothing operation,

$$\tilde{\varepsilon}_{ij}^k(\mathbf{u}^h) = \frac{1}{A^{(k)}} \sum_{c \in T^{(k)}} A^c \tilde{\varepsilon}_{ij}^c(\mathbf{u}^h) \tag{8.2}$$

where

$$\tilde{\varepsilon}_{ij}^c(\mathbf{u}^h) = \frac{1}{A^c} \int_{\Omega_c^{(k)}} \varepsilon_{ij}(\mathbf{x}) d\Omega = \frac{1}{2A^c} \int_{\partial\Omega_c^{(k)}} (u_i^h n_j + u_j^h n_i) d\Gamma \tag{8.3}$$

and $A^c = \int_{\Omega_c^{(k)}} d\Omega$ is the area of the subcell $\Omega_c^{(k)}$.
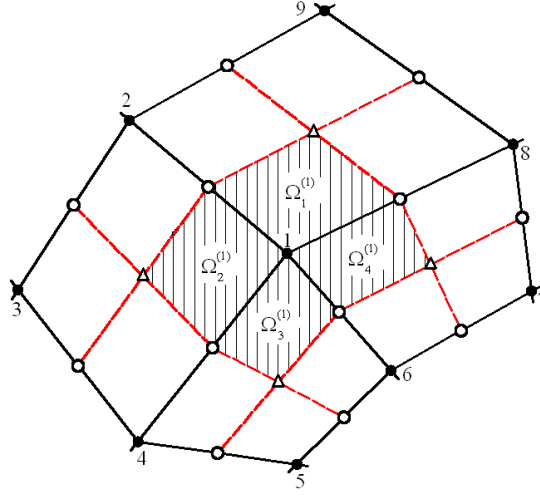
Figure 8.1: Example of the node associated with subcells: The symbols (●), (○) and (△) denote the nodal field, the mid-edge point and the intersection point of two bi-medians of Q4 element, respectively

Inserting Equation (8.3) to Equation (8.2) and rearranging in the reduced form, one obtains the smoothed strain field (Liu *et al.* (2007c)) defined as

$$\tilde{\varepsilon}_{ij}^k(\mathbf{u}^h) = \frac{1}{A^{(k)}} \int_{\Gamma^{(k)}} (n_i u_j + n_j u_i) d\Gamma \tag{8.4}$$

Substituting Equation (2.18) into Equation (8.4), the smoothed strain at the node k can be formulated by the following matrix form based on nodal displacements

$$\tilde{\varepsilon}^k = \sum_{I \in N^{(k)}} \tilde{\mathbf{B}}_I(\mathbf{x}_k)\mathbf{q}_I \equiv \tilde{\mathbf{B}}\mathbf{q} \tag{8.5}$$

where $N^{(k)}$ is the number of nodes that are directly connected to node k and $\tilde{\mathbf{B}}_I(\mathbf{x}_k)$ is termed as the smoothed strain gradient matrix on the cell $\Omega^{(k)}$ and is calculated numerically by

$$\tilde{\mathbf{B}}_I(\mathbf{x}_k) = \frac{1}{A^{(k)}} \int_{\Gamma^{(k)}} N_I \mathbf{n}^{(k)}(\mathbf{x}) d\Gamma \tag{8.6}$$

When a linear compatible displacement field along the boundary $\Gamma^{(k)}$ is used, one Gaussian point is sufficient for line integration along each segment of boundary $\Gamma_b^{(k)}$ of $\Omega^{(k)}$, Equation (8.6) can be expressed as

$$\tilde{\mathbf{B}}_I(\mathbf{x}_k) = \frac{1}{A^{(k)}} \sum_{b=1}^{nb} N_I(\mathbf{x}_b^G)\mathbf{n}^{(k)}(\mathbf{x}_b^G)l_b^{(k)} \tag{8.7}$$

where nb is the total number of edges of $\Gamma^{(k)}$, $\mathbf{x}_b^G$ is the midpoint (Gaussian point) of the boundary segment of $\Gamma_b^{(k)}$, whose length and outward unit normal matrix are denoted as

$l_b^{(k)}$ and $\mathbf{n}^{(k)}(\mathbf{x}_b^G)$, respectively. The stiffness matrix $\tilde{\mathbf{K}}$ of the system is then assembled by a similar process as in the FEM

$$\tilde{\mathbf{K}} = \sum_{k=1}^{N_n} \tilde{\mathbf{K}}^{(k)} \tag{8.8}$$

where $\tilde{\mathbf{K}}^{(k)}$ is the stiffness matrix associated with node k and is calculated by

$$\tilde{\mathbf{K}}^{(k)} = \int_{\Omega^{(k)}} \tilde{\mathbf{B}}^T \mathbf{D} \tilde{\mathbf{B}} d\Omega = \tilde{\mathbf{B}}^T \mathbf{D} \tilde{\mathbf{B}} A^{(k)} = \frac{1}{A^{(k)}} \left(\int_{\Gamma^{(k)}} \mathbf{n}^{(k)} \mathbf{N} d\Gamma \right)^T \mathbf{D} \left(\int_{\Gamma^{(k)}} \mathbf{n}^{(k)} \mathbf{N} d\Gamma \right) \tag{8.9}$$

Equation (8.9) implies that in the NSQ4, the shape function itself is used to evaluate the stiffness matrix and no derivative of the shape function is needed. Because of using the bilinear shape functions for four-node quadrilateral elements, the displacement field along the boundaries $\Gamma_b^{(k)}$ of the domain $\Omega^{(k)}$ is linear and compatible. Hence one Gauss point is sufficient to compute exactly the integrations of Equation (8.6). The purpose of this section is to recall briefly theoretical basis of the N-SFEM. More details can be found in Liu *et al.* (2007c).

8.3 A quasi-equilibrium element via the 4-node N-SFEM element

The purpose of this section is to show some common properties of the NSQ4 and the pure equilibrium quadrilateral element (EQ4) given in Appendix A, and to establish a variational form derived from the Hellinger-Reissner principle.

8.3.1 Stress equilibrium inside the element and traction equilibrium on the edge of element

Without loss of generality, we assume that the problem domain is first divided into four quadrilateral elements as shown in Figure 8.2. it is then re-partitioned into the cells $\Omega^{(k)}$ associated with nodes, $k = 1, ..., 9$ such that $\Omega^{(i)} \cap \Omega^{(j)} = \emptyset, i \neq j$. Let $\boldsymbol{\sigma}_e^{(k)}$ be the stress vector of sub-domain in the element "e" belonging to the cell $\Omega^{(k)}$. Assume that the finite element solutions of problem have already obtained. The stress vector at a node k can be computed through the smoothed strain at the node k as

$$\boldsymbol{\sigma}^{(k)} = \mathbf{D} \tilde{\boldsymbol{\varepsilon}}^k \tag{8.10}$$

Based on Equation (8.2), the stress $\boldsymbol{\sigma}^{(k)}$ in Equation (8.10) is termed as the smoothed stress on the cell $\Omega^{(k)}$. Hence, the stresses in all the sub-domains from adjacent elements in the cell $\Omega^{(k)}$ have the same values,

$$\boldsymbol{\sigma}_{e_1}^{(k)} = \boldsymbol{\sigma}_{e_2}^{(k)} = \boldsymbol{\sigma}^{(k)} \tag{8.11}$$
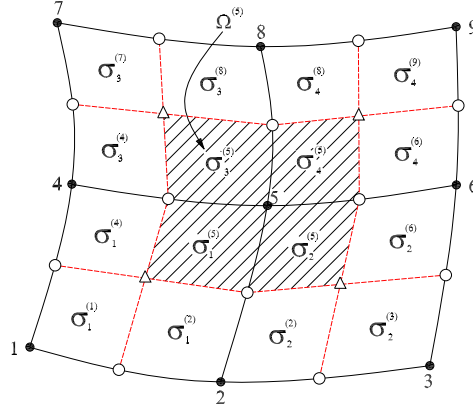
Figure 8.2: Stresses of background four-node quadrilateral cells and of the element:The symbols (●), (○) and (△) denote the nodal field, the mid-edge point and the intersection point of two bi-medians of Q4 element, respectively

For details, we illustrate the contribution of the stress as shown in Figure 8.2.

$$
\begin{aligned}
\text{For node } 1 &: \boldsymbol{\sigma}_1^{(1)} = \boldsymbol{\sigma}^{(1)} \\
2 &: \boldsymbol{\sigma}_1^{(2)} = \boldsymbol{\sigma}_2^{(2)} = \boldsymbol{\sigma}^{(2)} \\
3 &: \boldsymbol{\sigma}_2^{(3)} = \boldsymbol{\sigma}^{(3)} \\
4 &: \boldsymbol{\sigma}_1^{(4)} = \boldsymbol{\sigma}_3^{(4)} = \boldsymbol{\sigma}^{(4)} \\
5 &: \boldsymbol{\sigma}_1^{(5)} = \boldsymbol{\sigma}_2^{(5)} = \boldsymbol{\sigma}_3^{(5)} = \boldsymbol{\sigma}_4^{(5)} = \boldsymbol{\sigma}^{(5)} \\
6 &: \boldsymbol{\sigma}_2^{(6)} = \boldsymbol{\sigma}_4^{(6)} = \boldsymbol{\sigma}^{(6)} \\
&\ etc...
\end{aligned}
\tag{8.12}
$$

For element e connected with four nodes; k_1, k_2, k_3, k_4, the "element" stress can be reconstructed by averaging the nodal stresses:

$$
\boldsymbol{\sigma}_e = \frac{\boldsymbol{\sigma}_e^{(k_1)} + \boldsymbol{\sigma}_e^{(k_2)} + \boldsymbol{\sigma}_e^{(k_3)} + \boldsymbol{\sigma}_e^{(k_4)}}{4}
\tag{8.13}
$$

The traction on edge ij connecting node i and j of element "e" can be constructed by

$$
\mathbf{t}_{ij}^e = \mathbf{n}_{ij} \left(\boldsymbol{\sigma}_e^{(i)} + \boldsymbol{\sigma}_e^{(j)} \right) / 2
\tag{8.14}
$$

where $\mathbf{n}_{ij}$ is the matrix of outward normals on edge ij. By the above construction, equilibrating tractions on the common side of adjacent elements are always ensured. It is clear that in the present NSQ4, the equilibrium is satisfied strongly inside the element and on boundary of the element. However, the tractions along interfaces of the cell are not in equilibrium, and exists a stress gap. Based on numerical experiences below, the NSQ4 model can be considered as a quasi-equilibrium model that does not seek equilibrium for every point in the whole domain, but constitutes equilibrium status only in node-based

smoothing domains resulting in a sufficient softening in the discretized model. As a result, it can provide an upper bound to the exact solution in the energy norm for elasticity problems.

8.3.2 The variational form of the NSQ4

We start with the Hellinger–Reissner variational principle, e.g. Pian & Wu (2006), where the arbitrary stress $\boldsymbol{\sigma}$ and the displacement $\mathbf{u}$ are considered as independent field variables. Two 2-field variational principles result:

$$\Pi_{HR}(\boldsymbol{\sigma}, \mathbf{u}) = \int_{\Omega} \left(-\frac{1}{2}\sigma_{ij}D_{ijkl}^{-1}\sigma_{kl} + \sigma_{ij}\frac{1}{2}(u_{i,j} + u_{j,i}) - b_i u_i \right) d\Omega - \int_{\Gamma_t} \bar{t}_i u_i d\Gamma \quad (8.15)$$

Equation (8.15) can be expressed through the smoothing cells as follows

$$\Pi_{HR} = \sum_{k=1}^{N_n} \left(\int_{\Omega^{(k)}} [-\frac{1}{2}\sigma_{ij}D_{ijkl}^{-1}\sigma_{kl} + \sigma_{ij}\frac{1}{2}(u_{i,j} + u_{j,i}) - b_i u_i] d\Omega - \int_{\Gamma_t^{(k)}} \bar{t}_i u_i d\Gamma \right)$$
$$(8.16)$$

where $\Gamma^{(k)}$ is the entire boundary of the cell and $\Gamma_t^{(k)}$ is the portion of the element boundary over which the prescribed surface tractions $\bar{\mathbf{t}}$ are applied.

An integration part of the second term in the right hand side of Equation (8.16) becomes

$$\int_{\Omega^{(k)}} \sigma_{ij}\frac{1}{2}(u_{i,j} + u_{j,i})d\Omega = \int_{\Gamma^{(k)}} \sigma_{ij}\frac{1}{2}(n_i u_j + n_j u_i)d\Gamma - \int_{\Omega^{(k)}} u_i \sigma_{ij,j} d\Omega \quad (8.17)$$

Assuming that a constant stress $\boldsymbol{\sigma}$ is chosen, and inserting Equation (8.17) back Equation (8.16), one has
$\Pi_{HR} =$

$$\sum_{k=1}^{N_n} \left(-\frac{1}{2}\sigma_{ij}D_{ijkl}^{-1}\sigma_{kl}A^{(k)} + \sigma_{ij}\frac{1}{2}\int_{\Gamma^{(k)}}(n_i u_j + n_j u_i)d\Gamma - \int_{\Omega^{(k)}} b_i u_i d\Omega - \int_{\Gamma_t^{(k)}} \bar{t}_i u_i d\Gamma \right)$$
$$(8.18)$$

In this principle, the variation of stress field leads to

$$D_{ijkl}^{-1}\sigma_{kl}A^{(k)} = \frac{1}{2}\int_{\Gamma^{(k)}}(n_i u_j + n_j u_i)d\Gamma \quad (8.19)$$

This implies that there exists the strain field $\tilde{\varepsilon}_{ij} = D_{ijkl}^{-1}\sigma_{kl}$ such that

$$\tilde{\varepsilon}_{ij} = \frac{1}{2A^{(k)}}\int_{\Gamma^{(k)}}(n_i u_j + n_j u_i)d\Gamma \quad (8.20)$$

This shows that the smoothed strain in Equation (8.4) that used in the N-SFEM can derived from the Hellinger-Reissner variational justification. Therefore, we obtain the variational principles of two fields based on the smoothed strain $\tilde{\varepsilon}$ and the displacement $\mathbf{u}$ as

$$\Pi_{HR}(\tilde{\varepsilon}, \mathbf{u}) = \frac{1}{2} \sum_{k=1}^{N_n} \left(\tilde{\varepsilon}_{ij} D_{ijkl} \tilde{\varepsilon}_{ij} A^{(k)} - \int_{\Omega^{(k)}} b_i u_i d\Omega - \int_{\Gamma_t^{(k)}} \bar{t}_i u_i d\Gamma \right) \tag{8.21}$$

which is identical to the often used mixed approach. This means that the NSQ4 has a foundation on the Hellinger-Reissner variational principle.

8.4 Accuracy of the present method

Here it will be shown in energy form that the work of the present N-SFEM is larger than that of the displacement approach. Or in other words, the stiffness matrix of the NSQ4 element is softer than that of the Q4 element and therefore the present model is more accurate than the displacement model.

8.4.1 Exact and finite element formulations

Based on the Hellinger-Reissner variational principle, the weak form is to find the solution $(\boldsymbol{\sigma}, \mathbf{u})$ such that the functional

$$\Pi_{HR}(\boldsymbol{\sigma}, \mathbf{u}) = (\boldsymbol{\sigma}, \partial \mathbf{u}) - \frac{1}{2}(\boldsymbol{\sigma}, \mathbf{D}^{-1}\boldsymbol{\sigma}) - f(\mathbf{u}) \tag{8.22}$$

is maximum for all stress fields $\boldsymbol{\sigma} \in \mathcal{S}$ and minimum for all displacement fields $\mathbf{u} \in \mathcal{V}$. Hence we have the following weak statement

$$\begin{aligned} (\boldsymbol{\tau}, \partial \mathbf{u}) &= (\boldsymbol{\tau}, \mathbf{D}^{-1}\boldsymbol{\sigma}), \quad \forall \boldsymbol{\tau} \in \mathcal{S} \\ (\boldsymbol{\sigma}, \partial \mathbf{v}) &= f(\mathbf{v}), \quad \forall \mathbf{v} \in \mathcal{V}_0 \end{aligned} \tag{8.23}$$

Let $\mathcal{V}^h \subset \mathcal{V}$ and $\mathcal{S}^h \subset \mathcal{S}$ be a finite element space. The weak form for the approximated solution becomes: Find $(\boldsymbol{\sigma}^h, \mathbf{u}^h) \in \mathcal{S}^h \times \mathcal{V}^h$ such that

$$\begin{aligned} (\boldsymbol{\tau}, \partial \mathbf{u}^h) &= (\boldsymbol{\tau}, \mathbf{D}^{-1}\boldsymbol{\sigma}^h), \quad \forall \boldsymbol{\tau} \in \mathcal{S}^h \\ (\boldsymbol{\sigma}^h, \partial \mathbf{v}^h) &= f(\mathbf{v}^h), \quad \forall \mathbf{v}^h \in \mathcal{V}_0^h \end{aligned} \tag{8.24}$$

Equation $(8.24)_1$ means that $\mathbf{D}^{-1}\boldsymbol{\sigma}^h$ is a result of the projection of the element $\partial \mathbf{u}^h$ of $\mathcal{S}$ into $\mathcal{S}^h$. Therefore there exists ae projection operator P_h from $\mathcal{S}$ to $\mathcal{S}^h$ such that

$$\mathbf{D}^{-1}\boldsymbol{\sigma}^h = P_h \partial \mathbf{u}^h \quad \text{or} \quad \boldsymbol{\sigma}^h = \mathbf{D}P_h \partial \mathbf{u}^h \tag{8.25}$$

Using P_h, we have

$$(\boldsymbol{\sigma}^h, \partial \mathbf{v}^h) = (\boldsymbol{\sigma}^h, P_h \partial \mathbf{v}^h) \tag{8.26}$$

Using Equations (8.25) and (8.26), Equation $(8.24)_2$ becomes

$$(\mathbf{D}P_h \partial \mathbf{u}^h, P_h \partial \mathbf{v}) = f(\mathbf{v}), \quad \forall \mathbf{v} \in \mathcal{V}_0^h \tag{8.27}$$

which is a displacement-like formulation. When P_h is an identity operator, the conventional displacement approach is recovered.

8.4.2 Comparison with the classical displacement approach

For simplicity, we assume $\mathcal{V}^h = \mathcal{V}_0^h$. Let $\mathbf{w}^h$ be the solution of the classical displacement model. It verifies

$$(\mathbf{D}\boldsymbol{\partial}\mathbf{w}^h, \boldsymbol{\partial}\mathbf{v}^h) = f(\mathbf{v}^h), \ \ \forall \mathbf{v}^h \in \mathcal{V}^h \tag{8.28}$$

Setting $\mathbf{w}^h = \mathbf{v}^h$ and using the definition of energy norm in Chapter 2, one sets

$$\left\|\mathbf{w}^h\right\|_E^2 = f(\mathbf{w}^h) \tag{8.29}$$

Thereby, from (8.27), we reach the following inequality
$$f(\mathbf{w}^h) = (\mathbf{D}P_h\boldsymbol{\partial}\mathbf{u}^h, P_h\boldsymbol{\partial}\mathbf{w}^h) = (\mathbf{D}P_h\boldsymbol{\partial}\mathbf{u}^h, \boldsymbol{\partial}\mathbf{w}^h) = \left(P_h\boldsymbol{\partial}\mathbf{u}^h, \boldsymbol{\partial}\mathbf{w}^h\right)_E$$

$$\leq \left\|P_h\boldsymbol{\partial}\mathbf{u}^h\right\|_E \left\|\boldsymbol{\partial}\mathbf{w}^h\right\|_E = \sqrt{f(\mathbf{u}^h)}\sqrt{f(\mathbf{w}^h)} \Leftrightarrow f(\mathbf{w}^h) \leq f(\mathbf{u}^h) \tag{8.30}$$

This proves that the work of the solution of the presented approach (the mixed approach) is always greater than that of the solution of the classical displacement approach.

8.5 Convergence of the present method

The objective of this section is to establish a priori error estimation which ensures the convergence of proposed approach.

8.5.1 Exact and approximate formulations

Let $a(\boldsymbol{\sigma}, \boldsymbol{\tau}) = (\mathbf{D}^{-1}\boldsymbol{\sigma}, \boldsymbol{\tau})$ be the bilinear form and the norm in L^2 is denoted by $\|\cdot\|$. The exact formulation is to find $\boldsymbol{\sigma} \in \mathcal{S}$ and $\mathbf{u} \in \mathcal{V}$ such that

$$\begin{aligned} a(\boldsymbol{\sigma}, \boldsymbol{\tau}) &= (\boldsymbol{\tau}, \boldsymbol{\partial}\mathbf{u}), \ \ \forall \boldsymbol{\tau} \in \mathcal{S} \\ (\boldsymbol{\sigma}, \boldsymbol{\partial}\mathbf{v}) &= f(\mathbf{v}), \ \ \forall \mathbf{v} \in \mathcal{V}_0 \end{aligned} \tag{8.31}$$

Hence the following properties of the bilinear form $a(.;.)$ are satisfied:

$$\begin{aligned} \exists \alpha > 0 : a(\boldsymbol{\sigma}, \boldsymbol{\sigma}) &\geq \alpha \|\boldsymbol{\sigma}\|^2, \ \ \forall \boldsymbol{\sigma} \in \mathcal{S} \\ \exists M > 0 : a(\boldsymbol{\sigma}, \boldsymbol{\tau}) &\leq M \|\boldsymbol{\sigma}\| \|\boldsymbol{\tau}\|, \ \ \forall \boldsymbol{\tau} \in \mathcal{S} \end{aligned} \tag{8.32}$$

and on continuity condition, one has

$$(\boldsymbol{\sigma}, \boldsymbol{\partial}\mathbf{v}) \leq \|\boldsymbol{\sigma}\| \|\boldsymbol{\partial}\mathbf{v}\| \tag{8.33}$$

Moreover, Brezzi's condition is fulfilled as

$$\sup_{\boldsymbol{\sigma} \in \mathcal{S}} \frac{(\boldsymbol{\sigma}, \boldsymbol{\partial}\mathbf{u})}{\|\boldsymbol{\sigma}\|} \geq \frac{(\boldsymbol{\partial}\mathbf{u}, \boldsymbol{\partial}\mathbf{u})}{\|\boldsymbol{\partial}\mathbf{u}\|} = \|\boldsymbol{\partial}\mathbf{u}\|, (\text{constant } \beta = 1) \tag{8.34}$$

So, there exists a unique solution to the problem.

Let us now define the Z-space as $Z = \{\boldsymbol{\sigma} \in \mathcal{S} \mid \forall \mathbf{v} \in \mathcal{V}, (\boldsymbol{\sigma}, \boldsymbol{\partial}\mathbf{v}) = 0\}$ and $Z(f) = \{\boldsymbol{\sigma} \in \mathcal{S} \mid \forall \mathbf{v} \in \mathcal{V}, (\boldsymbol{\sigma}, \boldsymbol{\partial}\mathbf{v}) = f(\mathbf{v})\}$. The approximate spaces for Z and $Z(f)$ are denoted as $Z^h = \{\boldsymbol{\sigma}^h \in \mathcal{S}^h \mid \forall \mathbf{v}^h \in \mathcal{V}^h, (\boldsymbol{\sigma}^h, \boldsymbol{\partial}\mathbf{v}^h) = 0\}$ and $Z^h(f) = \{\boldsymbol{\sigma}^h \in \mathcal{S}^h \mid \forall \mathbf{v}^h \in \mathcal{V}^h, (\boldsymbol{\sigma}^h, \boldsymbol{\partial}\mathbf{v}^h) = f(\mathbf{v}^h)\}$. Again for simplicity, it is assumed that $\mathcal{V}^h = \mathcal{V}_0^h$

The finite element solution for the problem is to find $(\boldsymbol{\sigma}^h, \mathbf{u}^h) \in \mathcal{S}^h \times \mathcal{V}^h$ such that

$$
\begin{aligned}
a(\boldsymbol{\sigma}^h, \boldsymbol{\tau}^h) &= (\boldsymbol{\tau}^h, \boldsymbol{\partial}\mathbf{u}^h), \quad \forall \boldsymbol{\tau}^h \in \mathcal{S}^h \\
(\boldsymbol{\sigma}^h, \boldsymbol{\partial}\mathbf{v}^h) &= f(\mathbf{v}^h), \quad \forall \mathbf{v}^h \in \mathcal{V}^h
\end{aligned}
\tag{8.35}
$$

Assume that the present element is stable and convergent, hence there exists a constant $\beta_h > 0$ such that

$$
\sup_{\boldsymbol{\sigma}^h \in \mathcal{S}^h} \frac{(\boldsymbol{\sigma}^h, \boldsymbol{\partial}\mathbf{u}^h)}{\|\boldsymbol{\sigma}^h\|} \geq \beta_h \|\boldsymbol{\partial}\mathbf{u}^h\|
\tag{8.36}
$$

The condition (8.36) plays a fundamental role in the convergence analysis of mixed finite element methods, e.g. Brezzi & Fortin (1991).

8.5.2 A priori error on the stress

Let $\boldsymbol{\sigma}^h$ be the approximated solution and $\boldsymbol{\tau}^h$ be another element of $Z^h(f)$, i.e, $\boldsymbol{\sigma}^h - \boldsymbol{\tau}^h \in Z^h$. One has

$$
\begin{aligned}
a(\boldsymbol{\sigma}^h - \boldsymbol{\tau}^h, \boldsymbol{\sigma} - \boldsymbol{\sigma}^h) &= (\boldsymbol{\sigma}^h - \boldsymbol{\tau}^h, \boldsymbol{\partial}\mathbf{u}) - (\boldsymbol{\sigma}^h - \boldsymbol{\tau}^h, \boldsymbol{\partial}\mathbf{u}^h) = (\boldsymbol{\sigma}^h - \boldsymbol{\tau}^h, \boldsymbol{\partial}\mathbf{u}) + 0 \\
&= (\boldsymbol{\sigma}^h - \boldsymbol{\tau}^h, \boldsymbol{\partial}\mathbf{u} - \boldsymbol{\partial}\mathbf{v}^h) \leq \|\boldsymbol{\sigma}^h - \boldsymbol{\tau}^h\| \|\boldsymbol{\partial}\mathbf{u} - \boldsymbol{\partial}\mathbf{v}^h\|, \quad \forall \mathbf{v}^h \in \mathcal{V}^h
\end{aligned}
\tag{8.37}
$$

and of course

$$
a(\boldsymbol{\sigma}^h - \boldsymbol{\tau}^h, \boldsymbol{\sigma} - \boldsymbol{\tau}^h) \leq M \|\boldsymbol{\sigma}^h - \boldsymbol{\tau}^h\| \|\boldsymbol{\sigma} - \boldsymbol{\tau}^h\|
\tag{8.38}
$$

From Equations (8.32),(8.37)-(8.38), it results that

$$
\begin{aligned}
\alpha \|\boldsymbol{\sigma}^h - \boldsymbol{\tau}^h\|^2 &\leq a(\boldsymbol{\sigma}^h - \boldsymbol{\tau}^h, \boldsymbol{\sigma}^h - \boldsymbol{\tau}^h) \\
&\leq \|\boldsymbol{\sigma}^h - \boldsymbol{\tau}^h\| \|\boldsymbol{\partial}\mathbf{u} - \boldsymbol{\partial}\mathbf{v}^h\| + M \|\boldsymbol{\sigma}^h - \boldsymbol{\tau}^h\| \|\boldsymbol{\sigma} - \boldsymbol{\tau}^h\|
\end{aligned}
\tag{8.39}
$$

Hence

$$
\|\boldsymbol{\sigma}^h - \boldsymbol{\tau}^h\| \leq \frac{1}{\alpha} \|\boldsymbol{\partial}\mathbf{u} - \boldsymbol{\partial}\mathbf{v}^h\| + \frac{M}{\alpha} \|\boldsymbol{\sigma} - \boldsymbol{\tau}^h\|
\tag{8.40}
$$

Now,

$$
\|\boldsymbol{\sigma} - \boldsymbol{\sigma}^h\| \leq \|\boldsymbol{\sigma} - \boldsymbol{\tau}^h\| + \|\boldsymbol{\sigma}^h - \boldsymbol{\tau}^h\| \leq \frac{1}{\alpha} \|\boldsymbol{\partial}\mathbf{u} - \boldsymbol{\partial}\mathbf{v}^h\| + (1 + \frac{M}{\alpha}) \|\boldsymbol{\sigma} - \boldsymbol{\tau}^h\|
\tag{8.41}
$$

and as it is true for any $\mathbf{v}^h \in \mathcal{V}^h$ and for any $\boldsymbol{\tau}^h \in Z^h(f)$, one obtains

$$
\|\boldsymbol{\sigma} - \boldsymbol{\sigma}^h\| \leq \frac{1}{\alpha} \inf_{\mathbf{v}^h \in \mathcal{V}^h} \|\boldsymbol{\partial}\mathbf{u} - \boldsymbol{\partial}\mathbf{v}^h\| + (1 + \frac{M}{\alpha}) \inf_{\boldsymbol{\tau}^h \in Z^h(f)} \|\boldsymbol{\sigma} - \boldsymbol{\tau}^h\|
\tag{8.42}
$$

It is noted that the last term is embarrassing as the infinum has to be taken on a sub-space of $\mathcal{S}^h$. However, considering a stress field $\varsigma^h \in \mathcal{S}^h$, one knows that there exits a $\boldsymbol{\theta}^h \in Z_\perp^h$ such that

$$(\boldsymbol{\theta}^h, \boldsymbol{\partial}\mathbf{v}^h) = (\boldsymbol{\sigma} - \varsigma^h, \boldsymbol{\partial}\mathbf{v}^h) = f(\mathbf{v}^h) - (\varsigma^h, \boldsymbol{\partial}\mathbf{v}^h), \ \ \forall \mathbf{v}^h \in \mathcal{V}^h \tag{8.43}$$

Now we have

$$\left\|\boldsymbol{\theta}^h\right\| \leq \frac{1}{\beta_h} \sup_{\mathbf{v}^h \in \mathcal{V}^h} \frac{(\boldsymbol{\theta}^h, \boldsymbol{\partial}\mathbf{v}^h)}{\left\|\boldsymbol{\partial}\mathbf{v}^h\right\|} \leq \frac{1}{\beta_h} \sup_{\mathbf{v}^h \in \mathcal{V}^h} \frac{\left\|\boldsymbol{\sigma} - \varsigma^h\right\| \left\|\boldsymbol{\partial}\mathbf{v}^h\right\|}{\left\|\boldsymbol{\partial}\mathbf{v}^h\right\|} = \frac{1}{\beta_h} \left\|\boldsymbol{\sigma} - \varsigma^h\right\| \tag{8.44}$$

By choosing $\boldsymbol{\chi}^h = \boldsymbol{\theta}^h + \varsigma^h \Rightarrow \boldsymbol{\chi}^h \in Z^h(f)$ as $(\boldsymbol{\theta}^h + \varsigma^h, \boldsymbol{\partial}\mathbf{v}^h) = (\boldsymbol{\sigma}, \boldsymbol{\partial}\mathbf{v}^h) = f(\mathbf{v}^h), \ \forall \mathbf{v}^h \in \mathcal{V}^h$ and noting $\left\|\boldsymbol{\sigma} - \boldsymbol{\chi}^h\right\| \leq \left\|\boldsymbol{\sigma} - \varsigma^h\right\| + \left\|\boldsymbol{\theta}^h\right\| = (1 + \frac{1}{\beta_h}) \left\|\boldsymbol{\sigma} - \varsigma^h\right\|$, the following estimation is achieved:

$$\left\|\boldsymbol{\sigma} - \boldsymbol{\chi}^h\right\| \leq (1 + \frac{1}{\beta_h}) \inf_{\varsigma^h \in \mathcal{S}^h} \left\|\boldsymbol{\sigma} - \varsigma^h\right\| \tag{8.45}$$

And therefore one obtains

$$\inf_{\boldsymbol{\tau}^h \in Z^h(f)} \left\|\boldsymbol{\sigma} - \boldsymbol{\tau}^h\right\| \leq (1 + \frac{1}{\beta_h}) \inf_{\varsigma^h \in \mathcal{S}^h} \left\|\boldsymbol{\sigma} - \varsigma^h\right\| \tag{8.46}$$

Finally, assembling (8.46) to (8.42), a priori error on the stress is obtained as

$$\left\|\boldsymbol{\sigma} - \boldsymbol{\sigma}^h\right\| \leq \frac{1}{\alpha} \inf_{\mathbf{v}^h \in \mathcal{V}^h} \left\|\boldsymbol{\partial}\mathbf{u} - \boldsymbol{\partial}\mathbf{v}^h\right\| + (1 + \frac{M}{\alpha})(1 + \frac{1}{\beta_h}) \inf_{\varsigma^h \in \mathcal{S}^h} \left\|\boldsymbol{\sigma} - \varsigma^h\right\| \tag{8.47}$$

Note that in pure displacement model the first term of (8.47) is present and in pure equilibrium model the second term is present. The convergence will disappear if $\beta_h = O(h)$ and $\left\|\boldsymbol{\sigma} - \varsigma^h\right\| \leq Ch$. That is the well-known drawback of mixed approaches.

8.5.3 A priori error on the displacement

Let $\mathbf{u}^h$ be the approximate solution and another value $\mathbf{v}^h \in \mathcal{V}^h$. It satisfies

$$\left\|\boldsymbol{\partial}\mathbf{u}^h - \boldsymbol{\partial}\mathbf{v}^h\right\| \leq \frac{1}{\beta_h} \sup_{\boldsymbol{\tau}^h \in \mathcal{S}^h} \frac{(\boldsymbol{\tau}^h, \boldsymbol{\partial}\mathbf{u}^h - \boldsymbol{\partial}\mathbf{v}^h)}{\left\|\boldsymbol{\tau}^h\right\|} \tag{8.48}$$

and

$$\begin{aligned} (\boldsymbol{\tau}^h, \boldsymbol{\partial}\mathbf{u}^h - \boldsymbol{\partial}\mathbf{v}^h) &= (\boldsymbol{\tau}^h, \boldsymbol{\partial}\mathbf{u}^h - \boldsymbol{\partial}\mathbf{u}) + (\boldsymbol{\tau}^h, \boldsymbol{\partial}\mathbf{u} - \boldsymbol{\partial}\mathbf{v}^h) \\ &= a(\boldsymbol{\tau}^h, \boldsymbol{\sigma} - \boldsymbol{\sigma}^h) + (\boldsymbol{\tau}^h, \boldsymbol{\partial}\mathbf{u} - \boldsymbol{\partial}\mathbf{v}^h) \\ &\leq M \left\|\boldsymbol{\tau}^h\right\| \left\|\boldsymbol{\sigma} - \boldsymbol{\sigma}^h\right\| + \left\|\boldsymbol{\tau}^h\right\| \left\|\boldsymbol{\partial}\mathbf{u} - \boldsymbol{\partial}\mathbf{v}^h\right\| \end{aligned} \tag{8.49}$$

Hence

$$\left\|\boldsymbol{\partial}\mathbf{u}^h - \boldsymbol{\partial}\mathbf{v}^h\right\| \leq \frac{M}{\beta_h} \left\|\boldsymbol{\sigma} - \boldsymbol{\sigma}^h\right\| + \frac{1}{\beta_h} \left\|\boldsymbol{\partial}\mathbf{u} - \boldsymbol{\partial}\mathbf{v}^h\right\| \tag{8.50}$$

153

By the triangle inequality

$$\left\|\boldsymbol{\partial}\mathbf{u} - \boldsymbol{\partial}\mathbf{u}^h\right\| \leq \left\|\boldsymbol{\partial}\mathbf{u} - \boldsymbol{\partial}\mathbf{v}^h\right\| + \left\|\boldsymbol{\partial}\mathbf{u}^h - \boldsymbol{\partial}\mathbf{v}^h\right\| \leq \frac{M}{\beta_h}\left\|\boldsymbol{\sigma} - \boldsymbol{\sigma}^h\right\| + (1 + \frac{1}{\beta_h})\left\|\boldsymbol{\partial}\mathbf{u} - \boldsymbol{\partial}\mathbf{v}^h\right\| \tag{8.51}$$

for any $\mathbf{v}^h \in \mathcal{V}^h$, a priori error on the displacement is accomplished as

$$\left\|\boldsymbol{\partial}\mathbf{u} - \boldsymbol{\partial}\mathbf{u}^h\right\| \leq \frac{M}{\beta_h}\left\|\boldsymbol{\sigma} - \boldsymbol{\sigma}^h\right\| + (1 + \frac{1}{\beta_h})\inf_{\mathbf{v}^h \in \mathcal{V}^h}\left\|\boldsymbol{\partial}\mathbf{u} - \boldsymbol{\partial}\mathbf{v}^h\right\| \tag{8.52}$$

in which $\left\|\boldsymbol{\sigma} - \boldsymbol{\sigma}^h\right\|$ derived from Equation (8.47). It is clear that $\left\|\boldsymbol{\partial}\mathbf{u} - \boldsymbol{\partial}\mathbf{u}^h\right\|$ contains a factor $\frac{1}{\beta_h^2}$. So a "bad" β_h will cause that the displacements are worse than the stresses.

Thus the formulations on a priori error on the stress and displacement fields were established. The convergence of the presented method is ensured and conducted by the satisfaction Brezzi's condition.

8.6 Numerical tests

As discussed in Section 8.3 and Section 8.4, the NSQ4 possesses advantage characteristics of pure equilibrium element and mixed element; 1) the equilibrium stresses inside and the continuity of stress resultants across interface of the element are ensured strongly but may not be satisfy along interfaces of cell, and 2) its connectors are still at the corner nodes as the displacement model used. Therefore, the NSQ4 element is considered as the incorporation of pure equilibrium approach and mixed model, and is proposed to be a quasi-equilibrium approach. All theoretical proofs will be confirmed with numerically following tests again. In order to make comparison with the NSQ4 element, the formulations of the pure equilibrium quadrilateral element (EQ4) are given in Appendix A.

8.6.1 Cantilever loaded at the end

A cantilever with length $L = 8$ and height $D = 4$ is studied as a benchmark here, which is subjected to a parabolic traction at the free end as shown in Chapter 3. The cantilever is assumed to have a unit thickness so that plane stress condition is valid. The analytical solution is available and can be found in a textbook by Timoshenko & Goodier (1987).

The related parameters are taken as in Chapter 3. In the computations, the nodes on the left boundary are constrained using the exact displacements obtained from Timoshenko & Goodier (1987) and the loading on the right boundary is a distributed parabolic shear stress.

To assess the convergence rate, the same as Puso & Solberg (2006), the error in energy

norm for node-based smoothed finite elements is defined by

$$\left\| u - u^h \right\|_E = \left(\sum_{k=1}^{N_n} \left(\boldsymbol{\varepsilon}(\mathbf{x}_k) - \tilde{\boldsymbol{\varepsilon}}^k(\mathbf{x}_k) \right) : \mathbf{D} : \left(\boldsymbol{\varepsilon}(\mathbf{x}_k) - \tilde{\boldsymbol{\varepsilon}}^k(\mathbf{x}_k) \right) A^{(k)} \right)^{1/2} \qquad (8.53)$$
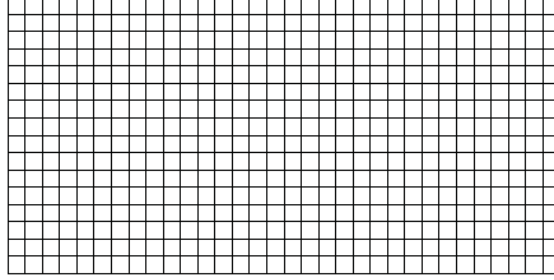

Figure 8.3: Uniform mesh with 512 quadrilateral elements for the cantilever beam

The domain discretization for uniform meshes of quadrilateral elements is shown in Figure 8.3. Herein, the connectors of the Q4 and NSQ4 elements are established at the corner nodes of quadrilateral element while those of the (EQ4) element are at the middle points along the element edges.

Figure 8.4 depicts graphically the strain energy obtained against number of elements and, also, the rate of convergence. It can be seen that the NSQ4 overestimates the strain energy compared to the pure equilibrium element (EQ4) while the Q4 underestimates the strain energy. Moreover, in this problem, the NSQ4 element is more accurate than EQ4 element with coarse mesh. As resulted in the error of energy norm, solutions of

(a)   (b)
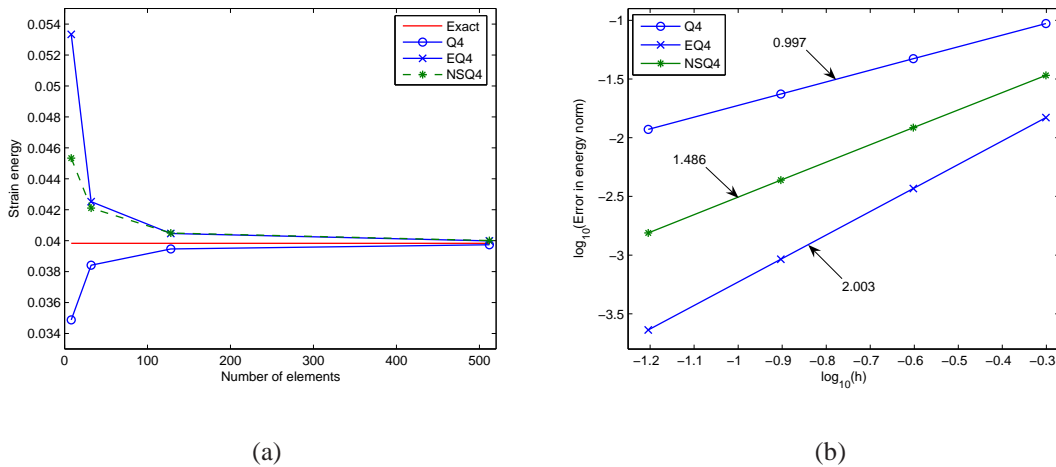
Figure 8.4: The convergence of cantilever: (a) Strain energy ; (b) The convergence rate

the SNQ4 are more accurate and achieve a higher convergence rate than FEM-Q4. It is known that if the conforming model(Q4) is exploited, the convergence rate in energy norm should be mathematically equal to 1.0, and if a pure equilibrium model (EQ4) is used, the convergence rate in energy norm should equal mathematically 2.0, see e.g. Johnson & Mercier (1979). It is clear that the equilibrium model gains the superconvergence rate in the energy norm which was demonstrated theoretically. For the NSQ4, the rate of convergence in energy norm shown in Figure 8.4b is 1.486 and is higher than that of the Q4. As discussed in previous sections of this chapter, the equilibrium for the SNQ4 is ensured strongly in the elements and inside the smoothing cells while on all the interfaces of the smoothing cells equilibrating tractions may not be ensured and only the continuity of displacements is satisfied. Therefore, the rate of convergence in energy norm for many problems may be, theoretically, between 1.0 and 2.0, also see e.g. Liu & Zhang (2007). And in several cases the rate of convergence may be larger than 2.0. Thus the optimal value will depend on another forms of structure.

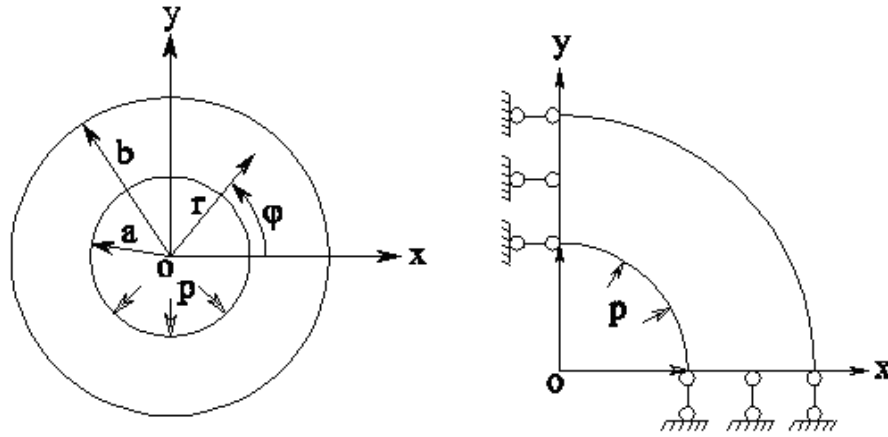### 8.6.2 A cylindrical pipe subjected to an inner pressure

Figure 8.5 shows a thick cylindrical pipe, with internal radius $a = 0.1m$, external radius $b = 0.2m$, subjected to an internal pressure $p = 6kN/m^2$. Because of the symmetric characteristic of the problem, we only calculate one quarter of cylinder as shown in Figure 8.5. The discretization of the domain uses 4-node quadrilateral elements. Plane strain condition is considered and Young's modulus $E = 21000kN/m^2$, Poisson's ratio $\nu = 0.3$. Symmetric conditions are imposed on the left and bottom edges, and outer boundary is traction free. The exact solution is given in Timoshenko & Goodier (1987). Again, Figure 8.6a shows that the NSQ4 maintains the upper bound property of the strain energy. However, the EQ4 element is more accurate than the NSQ4 element. The EQ4 element exhibits a superconvergence in the energy norm while the NSQ4 provides the rate of convergence between 1.0 and 2.0 (as depicted by Figure 8.6b).

### 8.6.3 Infinite plate with a circular hole

Figure 8.7 represents a plate with a central circular hole of radius $a = 1m$, subjected to a unidirectional tensile load of $\sigma = 1.0N/m$ at infinity in the x-direction. Due to its symmetry, only the upper right quadrant of the plate is modeled. Plane strain condition is considered and $E = 1.0 \times 10^3 N/m^2, \nu = 0.3$. Symmetric conditions are imposed on the left and bottom edges, and the inner boundary of the hole is traction free. The exact solution for the stress is (Timoshenko & Goodier (1987))

$$\begin{aligned}
\sigma_{11}(r,\theta) &= 1 - \frac{a^2}{r^2}\left[\frac{3}{2}\cos 2\theta + \cos 4\theta\right] + \frac{3a^4}{2r^4}\cos 4\theta \\
\sigma_{22}(r,\theta) &= -\frac{a^2}{r^2}\left[\frac{1}{2}\cos 2\theta - \cos 4\theta\right] - \frac{3a^4}{2r^4}\cos 4\theta \\
\tau_{12}(r,\theta) &= -\frac{a^2}{r^2}\left[\frac{1}{2}\sin 2\theta + \sin 4\theta\right] + \frac{3a^4}{2r^4}\sin 4\theta
\end{aligned} \tag{8.54}$$

where (r,θ) are the polar coordinates and θ is measured counterclockwise from the positive x-axis. Traction boundary conditions are imposed on the right $(x = 5.0)$ and top

(a)
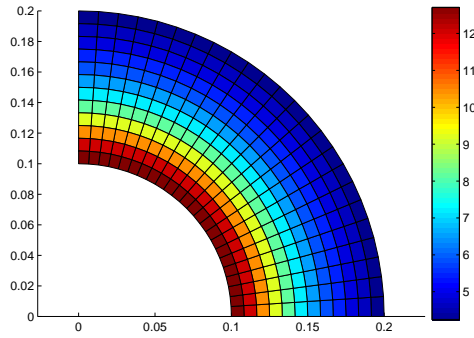
(b)

Figure 8.5: (a) A thick cylindrical pipe subjected to an inner pressure and its quarter model; (b) A sample discretization of 1024 quadrilateral elements and distribution of von Mises stresses
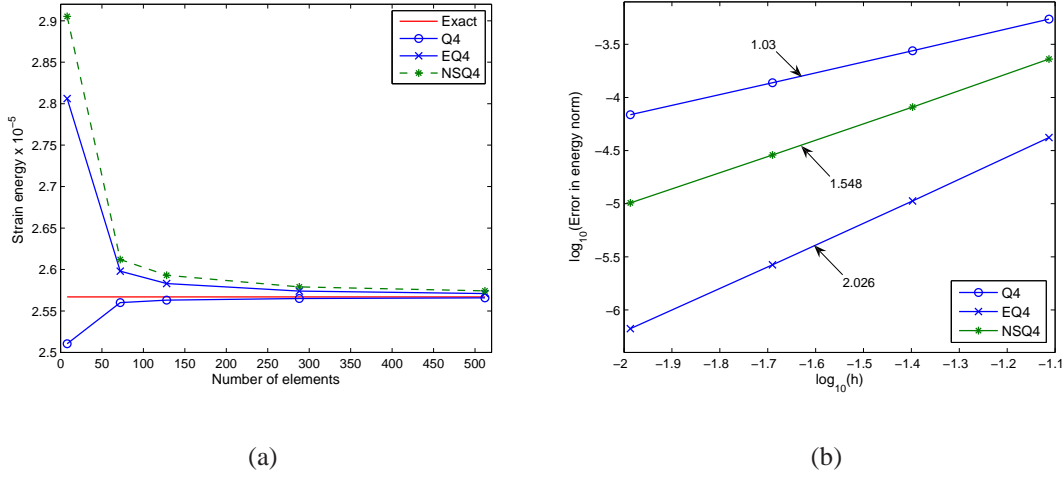
(a)   (b)

Figure 8.6: The convergence in energy of the cylindrical pipe: (a) Strain energy ; (b) The convergence rate

$(y = 5.0)$ edges based on the exact solution Equation (8.54). The displacement components corresponding to the stresses are

$$
\begin{aligned}
u_1(r,\theta) &= \frac{a}{8\mu}\left[\frac{r}{a}\left(\kappa+1\right)\cos\theta + 2\frac{a}{r}\left(\left(1+\kappa\right)\cos\theta + \cos 3\theta\right) - 2\frac{a^3}{r^3}\cos 3\theta\right] \\
u_2(r,\theta) &= \frac{a}{8\mu}\left[\frac{r}{a}\left(\kappa-1\right)\sin\theta + 2\frac{a}{r}\left(\left(1-\kappa\right)\sin\theta + \sin 3\theta\right) - 2\frac{a^3}{r^3}\sin 3\theta\right]
\end{aligned}
\tag{8.55}
$$

where $\mu = E/\left(2\left(1+\nu\right)\right)$, κ is defined in terms of Poisson's ratio by $\kappa = 3-4\nu$ for plane strain cases. Figure 8.7 gives the discretization of the domain using 4-node quadrilateral elements. Figure 8.8a shows the upper bound property of the strain energy of the NSQ4 with fine enough meshes, while the Q4 give the lower bound of strain energy. As plotted in Figure 8.8b, the superconvergent results in energy norm are obtained for the EQ4 and NSQ4 elements.

For nearly incompressible case $(\nu = 0.4999999)$, Figure 8.9 plots the computed stresses obtained by the EQ4 element and the NSQ4 element. It is shown that both these elements are in good agreement with the analytical solutions. Figure 8.10 depicts the behaviour of error in the energy norm as Poissons ratio tends to 0.5. It is observed that insensitivity to locking is evident for both EQ4 and NSQ4 whereas the FEM-Q4 is obviously subjected to volumetric locking. Therefore the NSQ4 element possesses the advantage of being relatively immune from volumetric locking as the pure equilibrium element (EQ4).

8.6.4   Cook's membrane

The benchmark problem studied in Chapter 3 and this model is recalled in Figure 8.11. Under plane stress conditions, the reference value of the vertical displacement at the cen-
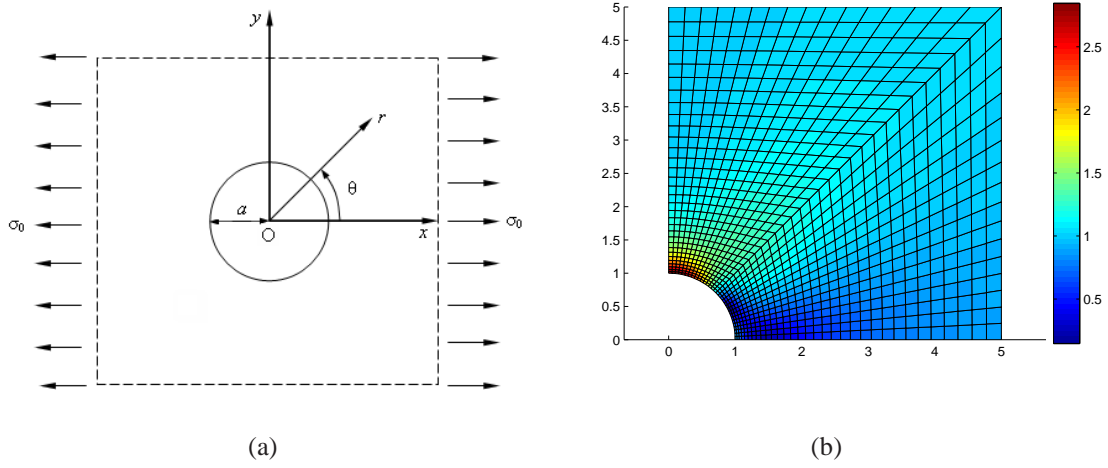
(a)   (b)

Figure 8.7: (a) Infinite plate with a circular hole subjected to uniform tensile load σ_0; (b) A sample discretization of 1024 quadrilateral elements and distribution of von Mises stresses
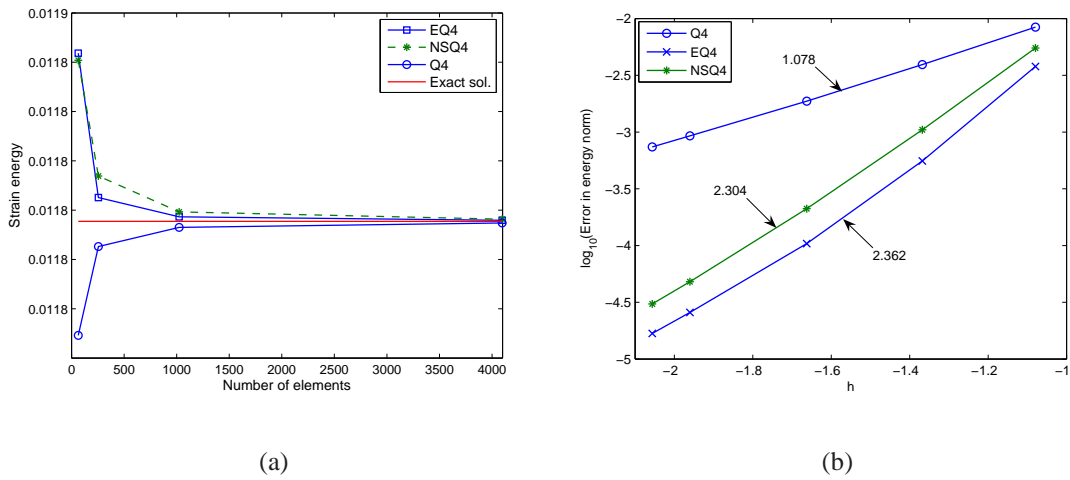

(a)   (b)

Figure 8.8: The convergence of the infinite plate a circular hole problem: (a) Strain energy ; (b) The convergence rate

159

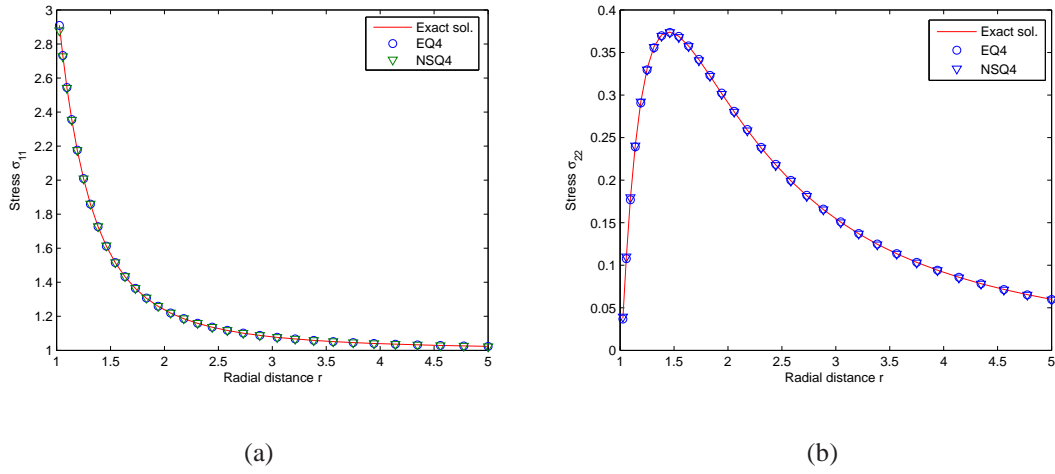(a)   (b)

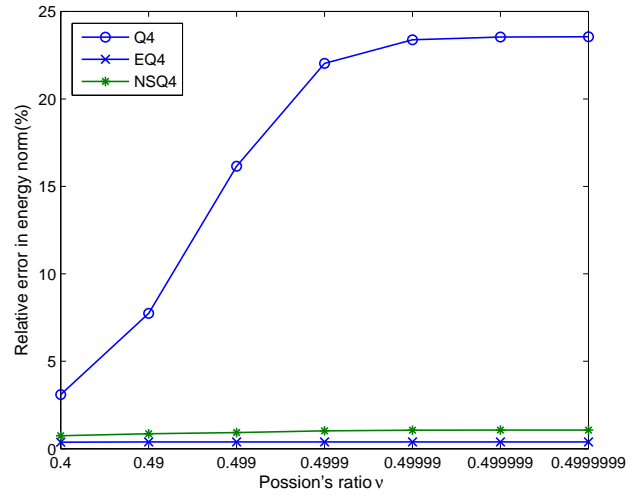Figure 8.9: Stresses of hole plate for incompressibility

Figure 8.10: Relative error in energy norm of hole plate using 256 elements with different Poissons ratios

ter of the tip section (C) in Fredriksson & Ottosen (2004) is 23.9642 and the reference value of the strain energy given by Mijuca & Berković (1998) is 12.015.

Here, the SNQ4 is compared with other elements listed in Table 8.1: Allman's membrane triangle (AT) (Allman (1984)), assumed stress hybrid methods such as P-S element (Pian & Sumihara (1984)), Xie-Zhou's element (ECQ4/LQ6)(Xie & Zhou (2004)), Zhou-Nie's element (CH(0-1)) (Zhou & Nie (2001)) and HQM/HQ4 element (Xie (2005)), finite element primal-mixed approach (FEMIXHB) introduced by Mijuca & Berković (1998). It is found that the SNQ4 solution overestimates the best reference solution while the other hybrid stress elements converge to this exact solution from below.

In addition to the results shown in Table 8.1, the values obtained for the energy estimation and the displacement at the tip are presented in Figure 8.12. It can be seen that the proposed element provides an improved solution in strain energy compared to the equilibrium element (EQ4). However the rate of convergence in the strain energy for the EQ4 and NSQ4 is lower than the Q4 for this case. When we estimate the convergence of displacement, the very good behavior of the NSQ4 element is obvious for compressible and nearly incompressible materials. Further, the present element is compared to the stabilization elements by Belytschko & Bachrach (1986) and Belytschko & Bindeman (1991) and is good agreement with these elements.

Table 8.1: Results of displacement tip (at C) and strain energy for Cook's problem

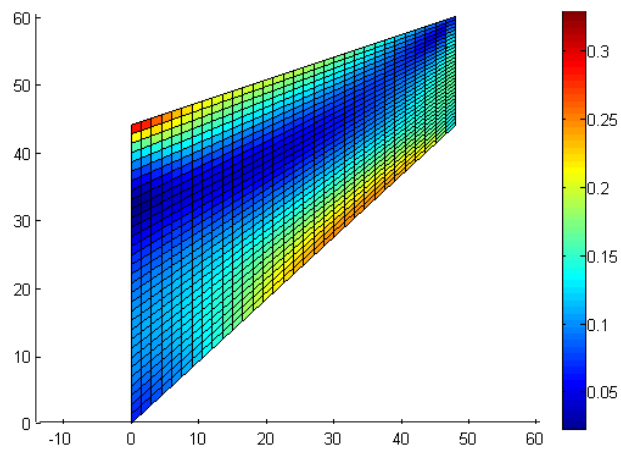| Node	Displacement tip			Strain energy		
	2×2	4×4	8×8	2×2	4×4	8×8
AT	19.67(27)[*]	22.41(75)	23.45(243)	9.84	11.22	11.75
P-S	21.13(18)	23.02(50)	23.69(162)	10.50	11.51	11.85
CH(0-1)	23.01(18)	23.48(50)	23.81(162)	11.47	11.75	11.91
ECQ4/LQ6	23.05(18)	23.48(50)	23.81(162)	11.48	11.75	11.91
HMQ/HQ4	21.35(18)	23.04(50)	23.69(162)	10.61	11.52	11.85
FEMIXHB	22.81(35)	23.52(135)	23.92(527)	11.27	11.79	11.97
NSQ4	24.69(18)	25.38(50)	24.51(162)	12.29	12.70	12.27
Ref	23.9642	23.9642	23.9642	12.015	12.015	12.015

(*) Number of degrees of freedom denoted in parenthesis

8.6.5 Crack problem in linear elasticity

A crack problem with data of the structure is considered as in Chapter 3. Only half of domain is modeled with uniform meshes with the same aspect ratio and a distribution of von Mises stress is illustrated by Figure 8.13. Note that, the solution of the crack problem includes the strong singularity (namely a $r^{-1/2}$ in stress) at the crack tip. In the present study, we only estimate the results based on the global strain energy of entire domain. Hence discontinuity fields such as displacements and stresses along crack path should be further considered by incorporating the present method into the extended finite element
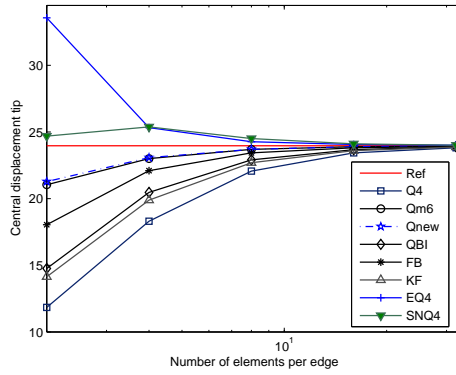
161
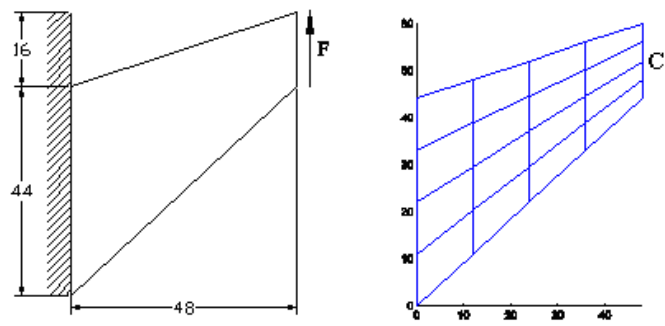
(a)
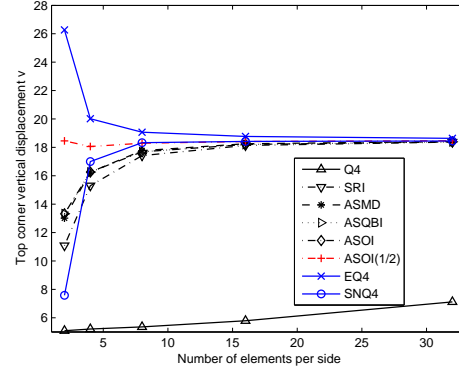

(b)
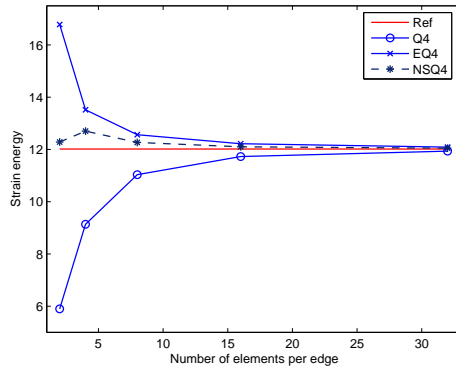
Figure 8.11: Cook's membrane and a distribution of von Mises stress using 1024 elements
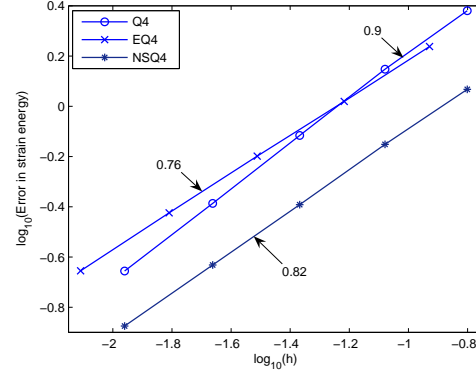
Figure 8.12: Convergence in strain energy and the central displacement for the Cook membrane: (a) Displacement at C ($\nu = 1/3$), plane stress ; (b) Displacement at C ($\nu = 0.4999$), plane strain; and (c) Strain energy ($\nu = 1/3$); (d) Convergence rate in strain energy ($\nu = 1/3$)

method (XFEM) (Moës *et al.* (1999)) which has been recently proved to be advantageous to solve crack problems.
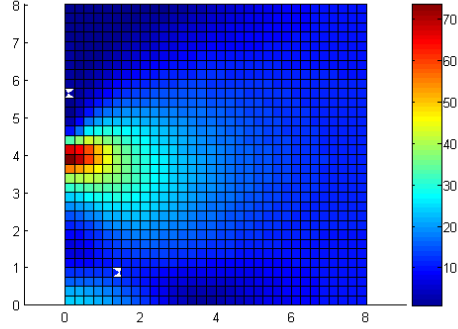
Figure 8.13: A distribution of von Mises stress for crack using the SNQ4 element

(a)   (b)
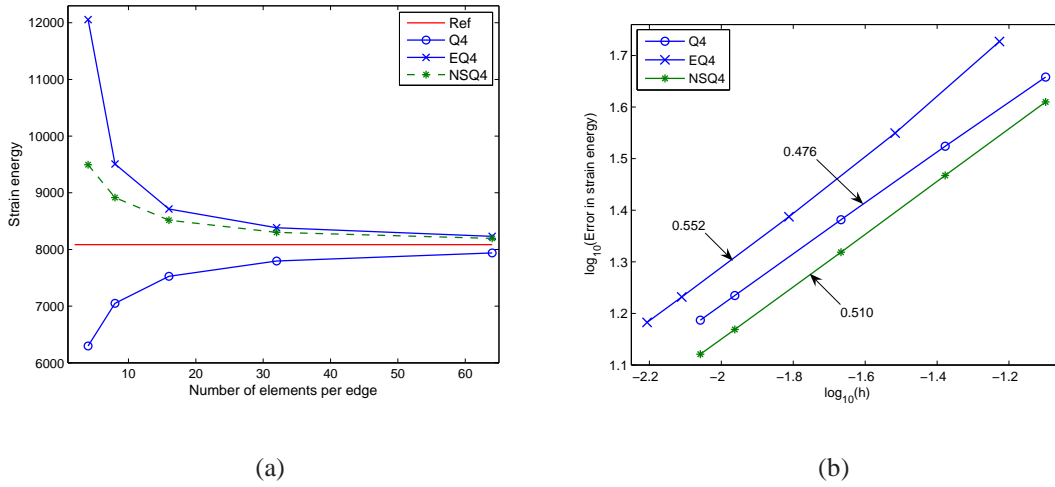
Figure 8.14: Convergence in energy for the crack problem:(a) Strain energy ; (b) The convergence rate

The convergence of strain energy for the NSQ4 and EQ4 elements is illustrated in Figure 8.14. As a result, the upper bound property of the NSQ4 on the strain energy is obtained for meshes that are not too coarse. The NSQ4 element provides the better solution in strain energy compared to the EQ4 element for this problem and does not converge monotonically.

164

8.6.6 The dam problem

A 2D dam under hydrostatic loads and its geometry data (Cugnon (2000) and Nguyen (2006)) are shown in Figure 8.15. Plane strain conditions are assumed and numerical parameters are: thickness = 1, hydrostatic load p = 103, Young's modulus $E = 2 \times 10^{12}$, Poisson's ratio $\nu = 0.3$. An illustration of 972 quadrilateral elements and a distribution of von Mises stress shown in Figure 8.16. We can realize a singularity in stress at the left and right corners of dam. Hence, an adaptive approach might be useful. Figure 8.17a gives the energy convergence of the Q4 and the NSQ4. Because an exact solution of this problem is not available, an estimated solution may be obtained by mean of two extrapolated energy values; one is of the Q4 element and the other is the NSQ4 element. The estimated strain energy is 0.52733×10^{-4}. The rate of convergence in strain energy is also exhibited by Figure 8.17b. The good convergence of the NSQ4 is observed.
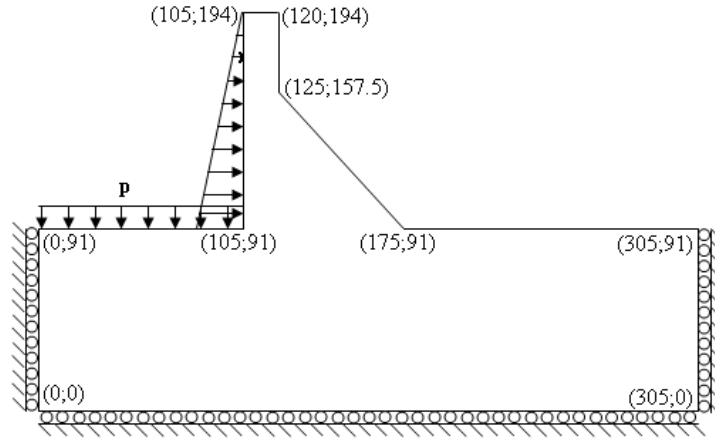
Figure 8.15: A 2D dam problem

8.6.7 Plate with holes

We consider a three-hole plate under plane strain conditions. This problem was investigated by Paulino *et al.* (1999) for self-adaptive procedures. Numerical parameters are: thickness = 1, a uniform load p = 1.0, Young's modulus $E = 2 \times 10^5$, Poisson's ratio $\nu = 0.3$. The geometry and boundary conditions of problem are shown in Figure 8.18.

Figure 8.19 gives an illustration of quadrilateral element meshes and a distribution of von Mises stress. We can realize the regions of stress concentration as shown in Figure 8.19b. Figure 8.20a plots the strain energy of the Q4 and the NSQ4. An exact solution of this problem is unknown and the extrapolated energy value is hence exploited. The estimated strain energy is 1.59196. Figure 8.17b gives the rate of convergence in strain energy corresponding to dimensionless length $h = 1/\sqrt{N}$, where $N = [316 \quad 762 \quad 2262 \quad 8774 \quad 19094]$ is the number of degrees of freedom (D.O.F) re-

Figure 8.16: Example of 972 quadrilateral elements and a distribution of von Mises stress

(a)   (b)

Figure 8.17: Convergence in energy for the dam problem:(a) Strain energy ; (b) The convergence rate

Figure 8.18: A 2D plate with holes

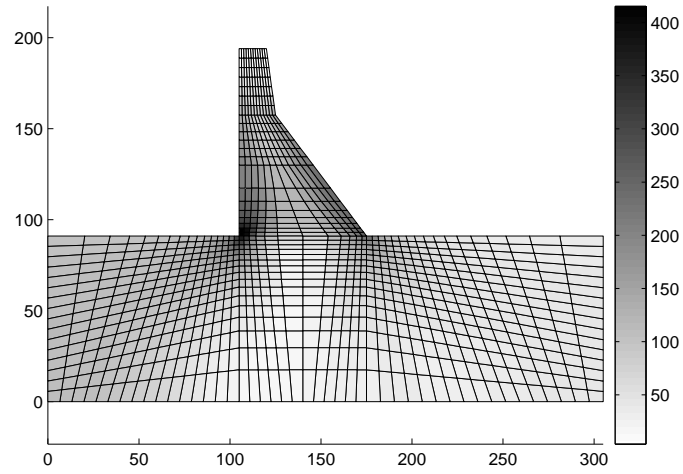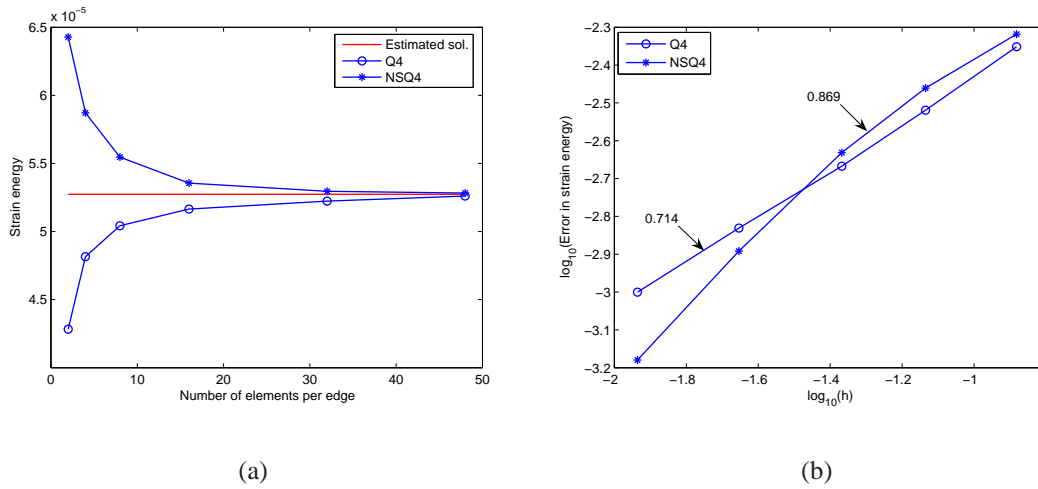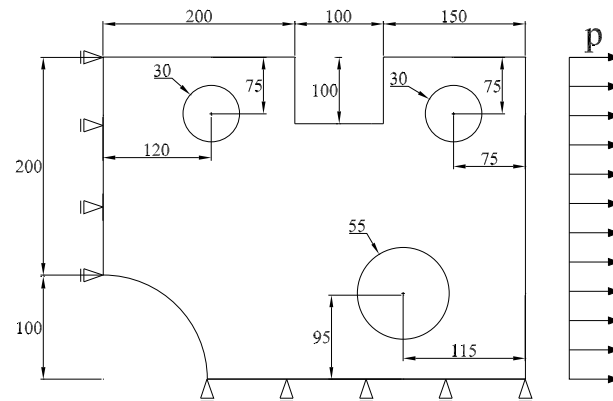(a)   (b)
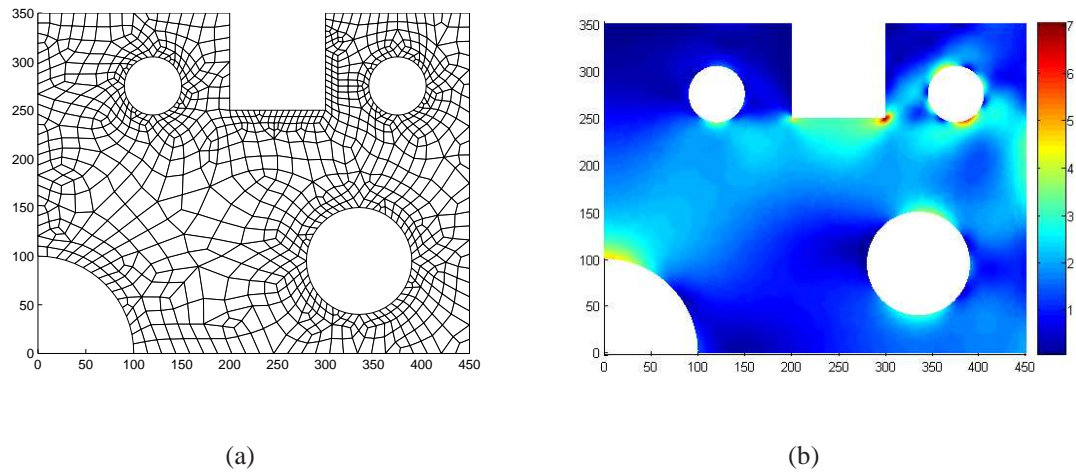
Figure 8.19: Example of 1022 quadrilateral elements and a distribution of von Mises stress using the NSQ4

167
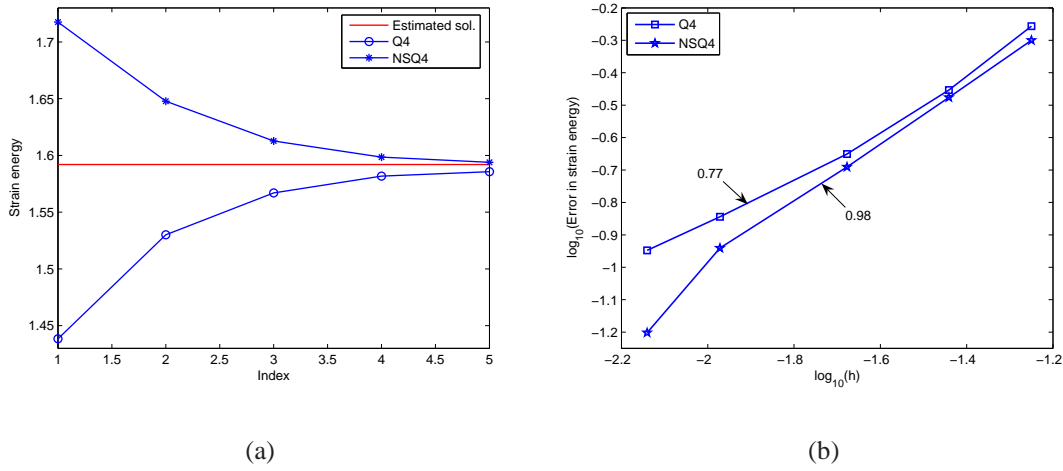
Figure 8.20: Convergence in energy for the plate with holes:(a) Strain energy ; (b) The convergence rate

maining after imposing boundary conditions. The NSQ4 converges monotonically from above and is more accurate than the Q4.

8.7 Concluding remarks

In this chapter, the NSQ4 is compared to a variety of four-node quadrilateral elements from the literature. Based on formulations and numerical examples, the following conclusions are remarked:

- The stress field is a statically admissible within the element (equilibrated inside the element and transmitted continuously over adjacent elements). This property is well-known in the equilibrium finite models. Additionally, the displacement field is continuous through element boundaries while the equilibrium models are defined by average displacements. When smoothing cells are used, the equilibrium of stresses is satisfied inside the cells but reciprocity between tractions across their boundaries may not be ensured. In this context, the nodally strain smoothing is also obtained from the justification of a mixed approach. Therefore, the NSQ4 can be seen as a quasi - equilibrium approach of pure equilibrium model. As a result, when homogeneous displacements are prescribed, the NSQ4 always achieves an overestimation of the true energy when the mesh is sufficiently fine.

- The accuracy and convergence of the NSQ4 have been proved theoretically in the framework of functional analysis.

- For all examples tested, the NSQ4 is in good agreement with the analytical solution. The accuracy of the NSQ4 is also compared with other elements.

- In an analogous manner to that advocated for the EQ4, the NSQ4 overcomes relatively volumetric locking.

- Moreover, in the NSQ4, field gradients are computed directly only using shape functions themselves and no derivative of shape function is needed. The shape functions are created in a trivial, simple and explicit manner. Unlike the conventional FEM using isoparametric elements, as no coordinate transformation or mapping is performed in the NSQ4, no limitation is imposed on the shape of elements used herein. Even severely distorted elements are allowed. Hence domain discretization is more flexible than FEM.

- Last but not least, the NSQ4 is more convenient to compute directly the nodal stresses while the standard displacement models often use post-processing procedure to recover these stresses. Therefore, the NSQ4 is very promising to obtain a simple and practical procedure for the stress analysis of the FEM using four-noded quadrilateral elements.

Chapter 9

Conclusions

The method exploited here originated from mesh-free research. The main aim of smoothing strain fields is to eliminate the instability of direct nodal integration techniques in the mesh-free methods when the shape function derivatives at nodes vanish. The direct nodal integration (NI) often causes large oscillations in the solution because it violates integration constraints (IC) that any meshless method needs to pass similarly to the patch test as in FEM. Although the stabilized conforming nodal integration (SCNI) using the strain smoothing method avoids instability of the NI and obtains good accuracy and high convergence rates, the non-polynomial or usually complex approximation space increases the computational cost of numerical integration.

The objective of this thesis is therefore to present numerous applications of the strain smoothing method to finite elements, namely SFEM, for analyzing static and dynamic structures of two and three dimensional solids, plates, shells, etc. In finite elements, the strain smoothing technique is similar to stabilized conforming nodal integration for meshfree methods. Except some special cases of three-dimensional solids where standard interior integration is used, the stiffness matrix is computed by boundary integration instead of the standard interior integration of the traditional FEM. This permits to utilize distorted meshes. In all the numerical examples tested, it is observed that the present method is more accurate than the standard FEM element for a lower computational cost.

This thesis has shown the following results:

- Based on a Taylor series, the strain smoothing field is considered as an alternative form of the enhanced assumed strain method. The smoothed strains are sum of two terms; one is the compatible strains and the other is the enhanced strains. A rigorous variational framework based on the Hu – Washizu assumed strain variational form was shown to be suitable. It is found that solutions yielded by the SFEM are in a space bounded by the standard, finite element solution (infinite number of smoothing cells) and a quasi-equilibrium finite element solution (a single cell). The benchmark problems of compressible and incompressible two and three dimensional elasticity have adequately chosen and analyzed in detail. It is shown that the SFEM always achieves higher accuracy and convergence rates than the standard finite element method, especially in the presence

of incompressibility, singularities or distorted meshes, for a smaller computational cost.

- New 8 noded hexahedral elements based on the smoothed finite element method (SFEM) with various numbers of smoothing cells were proposed. It was observed that low numbers of smoothing cells lead to higher stress accuracy but instabilities; high numbers yield lower stress accuracy but are always stable. Hence a stabilization procedure is formulated which is based on the linear combination of the one subcell element and the four or eight subcell element. As a result, zero energy modes are suppressed and the stabilized elements are free of volumetric locking and obtain higher accuracy than the eight-node hexahedral brick element.

- A quadrilateral Mindlin - Reissner plate element with smoothed curvatures, the so-called MISCk element, was proposed. The curvature at each point is smoothed via a spatial averaging. The smoothed curvatures are also considered as the enhanced assumed curvatures while the approximation of the shear strains follows the assumed natural strain (ANS) method. The reliability of the proposed element is confirmed through numerical tests. It is seen that the present method is robust, computationally inexpensive and simultaneously very accurate and free of locking. The most promising feature of the present elements is their insensitivity to mesh distortion.

- A further extension of the MISCk element combined with a stabilization technique, namely SMISCk element, to the free vibration analysis of Mindlin – Reissner plates was investigated. It was also remarked that the present elements are free of shear locking for very thin plates and give a good agreement with analytical solutions and published results. From frequency analysis, the MISCk elements exhibit higher accuracy than the MITC4 element for all examples tested. Moreover, if associated with the stabilization technique, the SMISCk elements are always superior in terms of convergence to the STAB element.

- A family of quadrilateral shell elements based on the incorporation of smoothed membrane - bending strains and assumed natural shear strains was devised. The flat element concept is available for solving several benchmark problems involving curved structures. These elements are insensitive to membrane locking caused by distorted meshes and free of shear locking in the thin shell limit. Several numerical examples were used to demonstrate the good performance of the present element. Additionally, this element works well with distorted meshes while the MITC4 element seems to lead to large oscillations in the solution.

- Based on obtained results of the recent investigation of the node-based smoothed finite element method (N-SFEM) in Liu *et al.* (2007c), it was shown that the N-SFEM justified the Reissner mixed variational principle. The accuracy and convergence of the N-SFEM are demonstrated both theoretically and numerically. A quasi-equilibrium element which gives a new link between the N-SFEM and an equilibrium finite element model is then proposed. The convergence properties of the quasi-equilibrium element are also confirmed by numerical results. It is found that the quasi-equilibrium element (or the N-SFEM) exhibits following properties: 1) it gives an upper bound in the strain energy in limit when meshes are not too coarse; 2) it can eliminate volumetric locking relatively; 3) the element works well with distorted elements; 4) The convergence rate in the energy

tested for most problems is between 1.0 and 2.0. In addition the N-SFEM gives a way to compute directly the nodal stresses while the standard displacement models often need a post-processing procedure to recovery these stresses. The N-SFEM is therefore very promising to obtain a simple and practical procedure for stress analysis.

Although the present method has shown to be effective for structural analysis, further investigations need to be considered for general engineering applications. Thus as an extension of the present work, the following points will open forthcoming research:

- The strain smoothing technique presented herein for continuum finite elements in two dimensional elasto-statics problems are seamlessly extendable to non-linear material and geometric problems: the volumetric-locking insensitivity provides the SFEM with an important advantage when treating plasticity problems and its ability to yield accurate results on distorted meshes may help in solving large deformation problems with minimal remeshing. Large strain plasticity problems, for instance would certainly be elegantly treated by the present method which would provide a mid-way between FEM and mesh-free methods.

-Coupling boundary integration with partition of unity methods such as the extended finite element method provides an alternate integration scheme for discontinuous approximations. Indeed, our first results in the smoothed extended finite element method (FleXFEM) (Bordas *et al.* (2008a)) show improvements in the solution of LEFM fracture mechanics problems both accuracy and robustness. The FleXFEM is thus very promising to enhance the effective computation of the classically extended finite element method for practical applications.

- We believe that the present method is especially useful for certain types of problems where locally large deformations or strains occur, e.g. ductile cracking where crack initiation and propagation occurs under large strains and large deformation. It is important to retain accuracy in a local region before cracking happens in order to obtain the correct crack path (Bordas *et al.* (2008b); Rabczuk *et al.* (2007c, 2008)). This will be investigated in the future using open source XFEM libraries (Bordas *et al.* (2007b); Dunant *et al.* (2007)).

-It may be useful to combine the present method and $h-$ adaptivity procedure for computing and simulating complex industrial structures in Bordas & Moran (2006); Bordas *et al.* (2007a) and, later, Wyart *et al.* (2007).

-An interesting topic is how to construct the 2D N-SFEM such that an upper bound is always ensured. So, the the N-SFEM is then very promising to give a simple and practical procedure in determining an upper bound of the global error estimation based on the concept of dual analysis, e.g. (Beckers (2008); Debongnie *et al.* (1995, 2006)), dual limit analysis (Le *et al.* (2005). Also, the N-SFEM will be extended to three dimensional solid problems.

-Finally, it may also be helpful to incorporate the N-SFEM and the XFEM for the estimation of the lower and upper bounds of path integrals in fracture mechanics, e.g. Wu *et al.* (1998); Li *et al.* (2005); Wu & Xiao (2005).

Appendix A

Quadrilateral statically admissible stress element (EQ4)

The equilibrium models are obtained from the principle of minimum complementary potential energy which may be expressed as:

$$\Psi(\boldsymbol{\sigma}) = \frac{1}{2} \int_{\Omega} \boldsymbol{\sigma} : \mathbf{D}^{-1} : \boldsymbol{\sigma} d\Omega - \int_{\Gamma_{\mathbf{u}}} \mathbf{t}.\bar{\mathbf{u}} d\Gamma \qquad (A.1)$$

where $\boldsymbol{\sigma}$ is the statically stress field satisfied homogeneous equilibrium equations a priori. In matrix form, the stresses vector expressed as

$$\boldsymbol{\sigma} = \mathbf{Sb} \qquad (A.2)$$

where $\mathbf{b}^T = \{\beta_1...\beta_m\}$, the parameters β_i i of the equilibrium stress field are arbitrary and independent in the principle.
The conjugate boundary displacements $\bar{q}_i$ with generalized boundary loads $\bar{\mathbf{g}}$ are obtained from the virtual work equation

$$\int_{\Gamma_{\mathbf{u}}} \mathbf{t}.\bar{\mathbf{u}} d\Gamma = \bar{\mathbf{q}}^T \bar{\mathbf{g}} \quad \text{along each boundary} \qquad (A.3)$$

with $\bar{\mathbf{q}}^T = \{\bar{q}_1........\bar{q}_n\}$ is the conjugate displacement vector of the generalized forces $\bar{\mathbf{g}}$. From this appropriated definitions the generalized loads $\bar{\mathbf{g}}$ may always be expressed in terms of the field parameters by a matrix form

$$\bar{\mathbf{g}} = \mathbf{Cb} \qquad (A.4)$$

173

where $\mathbf{C}$ is load connection matrices. Substituting Equation (A.2), Equation (A.3) to Equation (A.1), we write the principle of minimum total complementary energy into the following discrete form:

$$\Psi(\mathbf{b}) = \left(\frac{1}{2} \mathbf{b}^T \mathbf{F} \mathbf{b} - \bar{\mathbf{q}}^T \mathbf{C} \mathbf{b} \right) \tag{A.5}$$

with a sort of flexibility matrices $\mathbf{F} = \int_\Omega \mathbf{S}^T \mathbf{D}^{-1} \mathbf{S} d\Omega$ The stationary conditions with respect to variations of $\mathbf{b}$ lead to the two systems of linear equations:

$$\mathbf{F} \mathbf{b} = \mathbf{C}^T \bar{\mathbf{q}} \Rightarrow \mathbf{b} = \mathbf{F}^{-1} \mathbf{C}^T \bar{\mathbf{q}} \tag{A.6}$$

By eliminating the parameters $\mathbf{b}$, the stationary conditions can be rewritten in the form

$$\mathbf{K}^{eq} \bar{\mathbf{q}} = \bar{\mathbf{g}} \tag{A.7}$$

where $\mathbf{K}^{eq} = \mathbf{C} \mathbf{F}^{-1} \mathbf{C}^T$ is called the stiffness matrix.
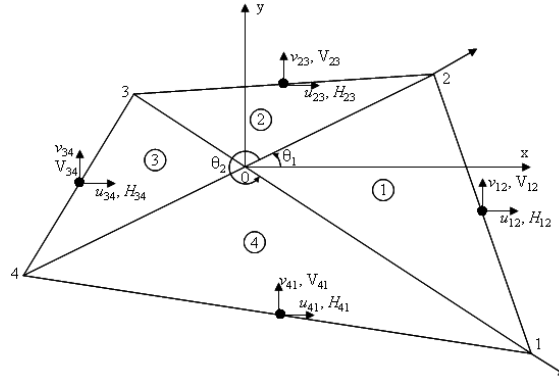
Figure A.1: Quadrilateral element with equilibrium composite triangle

Now we consider a quadrilateral element subdivided into four triangular equilibrium elements of the constant stress as shown in Figure A.1. The stress field on each sub-triangle is defined as Fraeijs De Veubeke (1965):

$$\boldsymbol{\sigma}^i = \mathbf{S}_i \boldsymbol{\beta}, \quad \forall i = 1, 2, 3, 4 \tag{A.8}$$

where

$$\boldsymbol{\beta} = \begin{bmatrix} \beta_1 & \beta_2 & \beta_3 & \beta_4 & \beta_5 \end{bmatrix}^T \tag{A.9}$$

$$\mathbf{S}_1 = \begin{bmatrix} 1 & 0 & 0 & 0 & c_2^2 \\ 0 & 1 & 0 & 0 & s_2^2 \\ 0 & 0 & 1 & 0 & c_2 s_2 \end{bmatrix}, \quad \mathbf{S}_2 = \begin{bmatrix} 1 & 0 & 0 & c_1^2 & c_2^2 \\ 0 & 1 & 0 & s_1^2 & s_2^2 \\ 0 & 0 & 1 & c_1 s_1 & c_2 s_2 \end{bmatrix}$$

$$\mathbf{S}_3 = \begin{bmatrix} 1 & 0 & 0 & c_1^2 & 0 \\ 0 & 1 & 0 & s_1^2 & 0 \\ 0 & 0 & 1 & c_1 s_1 & 0 \end{bmatrix}, \quad \mathbf{S}_4 = \begin{bmatrix} 1 & 0 & 0 & 0 & 0 \\ 0 & 1 & 0 & 0 & 0 \\ 0 & 0 & 1 & 0 & 0 \end{bmatrix} \tag{A.10}$$

with $c_1 = cos\theta_1$, $c_2 = cos\theta_2$, $s_1 = sin\theta_1$, $s_2 = sin\theta_2$. The generalized loads and generalized displacements must be defined on the edges of element to ensure completely the reciprocity between generalized loads across the common boundary of the adjacent elements. The generalized loads have the following form

$$H_{ij} = \left(n_x^{ij} \sigma_x + n_y^{ij} \tau_{xy} \right) l_{ij}, \quad V_{ij} = \left(n_x^{ij} \tau_{xy} + n_y^{ij} \sigma_y \right) l_{ij} \tag{A.11}$$

For the cyclic index permutations on i, j. The generalized loads and generalized displacements can be rewritten in matrix form

$$\bar{\mathbf{g}} = \begin{bmatrix} H_{12} & V_{12} & H_{23} & V_{23} & H_{34} & V_{34} & H_{41} & V_{41} \end{bmatrix}^T = \mathbf{C}\boldsymbol{\beta} \tag{A.12}$$

$$\bar{\mathbf{q}}^T = \left\{ u_{12} \quad v_{12} \quad u_{23} \quad v_{23} \quad u_{34} \quad v_{34} \quad u_{41} \quad v_{41} \right\} \tag{A.13}$$

The results of the connection matrix $\mathbf{C}$ and the flexibility matrix $\mathbf{F}$ are given by

$$\mathbf{C} = \begin{bmatrix} y_{21} & 0 & x_{12} & 0 & y_{21}c_2^2 + x_{12}c_2 s_2 \\ 0 & x_{12} & y_{21} & 0 & x_{12}s_2^2 + y_{12}s_2 c_2 \\ y_{32} & 0 & x_{23} & y_{32}c_1^2 + x_{23}s_1 c_1 & y_{32}c_2^2 + x_{23}s_2 c_2 \\ 0 & x_{23} & y_{32} & x_{23}s_1^2 + y_{23}s_1 c_1 & x_{23}s_2^2 + y_{32}s_2 c_2 \\ y_{43} & 0 & x_{34} & y_{43}c_1^2 + x_{34}s_1 c_1 & 0 \\ 0 & x_{34} & y_{43} & x_{34}s_1^2 + y_{43}s_1 c_1 & 0 \\ y_{14} & 0 & x_{41} & 0 & 0 \\ 0 & x_{41} & y_{14} & 0 & 0 \end{bmatrix} \tag{A.14}$$

$$\mathbf{F} = \sum_{i=1}^{4} \mathbf{S}_i^T \mathbf{D}^{-1} \mathbf{S}_i A_i \tag{A.15}$$

where A_i is the area of the triangle i, $x_{ij} = x_i - x_j, y_{ij} = y_i - y_j$

By substituting Equation (A.8), Equation (A.9) and Equation (A.10) to complementary potential energy (Fraeijs De Veubeke (1965)) with minimization, we obtain the system equations as in Equation (A.7). It was proven that the stiffness matrix of quadrilateral equilibrium element has sufficient rank. The application of this element is largely performed by Nguyen-Dang (1980a, 1985) and his collaborators during two decades: elastic, plastic analysis of structures, limit and shakedown analysis and solids in contact. This element was also proven to give the good result for nearly incompressible material, see e.g. Nguyen-Dang (1985).

Appendix B

An extension of Kelly's work on an equilibrium finite model

In displacement-based finite element methods, the compatibility equations are verified a priori, since the unknowns are displacements. The solution of the problem then leads to a weak form of the equilibrium equations. Equilibrium finite elements are a family of elements dual to displacement finite elements. In these elements, an equilibrated stress field is used, the computation results in a weak enforcement of the compatibility equations. The advantage of the equilibrium approach for practical design purposes lies in the fact that the stresses are more accurate than those obtained by the displacement formulation. In the equilibrium approach, the degrees of freedom of the equilibrium element are mean displacements on the edges instead of generalized nodal displacements as in the displacement model. In this work, we transform the connectors at the middle points along the element edges of the equilibrium element to the connectors at the corner nodes as in a displacement element. Performing this transformation, we obtain a quasi-equilibrium element (QE) and notice that we recover exactly the one-subcell element (the SC1Q4 element or 4-node quadrilateral element with one-point quadrature) pointed in Chapter 3. This can be seen as follows: the mean generalized displacements are mapped to the corner nodes displacements as follows

$$\bar{\mathbf{q}} = \mathbf{L}\mathbf{q} \tag{B.1}$$

where

$$\mathbf{L} = \frac{1}{2} \begin{bmatrix} 1 & 0 & 1 & 0 & 0 & 0 & 0 & 0 \\ 0 & 1 & 0 & 1 & 0 & 0 & 0 & 0 \\ 0 & 0 & 1 & 0 & 1 & 0 & 0 & 0 \\ 0 & 0 & 0 & 1 & 0 & 1 & 0 & 0 \\ 0 & 0 & 0 & 0 & 1 & 0 & 1 & 0 \\ 0 & 0 & 0 & 0 & 0 & 1 & 0 & 1 \\ 1 & 0 & 0 & 0 & 0 & 0 & 1 & 0 \\ 0 & 1 & 0 & 0 & 0 & 0 & 0 & 1 \end{bmatrix} \tag{B.2}$$

Permuting the entries in vector $\mathbf{q}$ and stiffness matrix $\mathbf{K}^{eq}$ with permutation matrix $\mathbf{L}$, we obtain the system of equations

$$\mathbf{L}^T \mathbf{K}^{eq} \mathbf{L} \bar{\mathbf{q}} = \mathbf{L}^T \bar{\mathbf{g}} \tag{B.3}$$

Based on a numerical examination, see below, it is found that the new, permuted, stiffness $\mathbf{L}^T \mathbf{K}^{eq} \mathbf{L}$ is identical to the SC1Q4 element stiffness matrix denoted by $\widetilde{\mathbf{K}}$

$$\widetilde{\mathbf{K}} = \mathbf{L}^T \mathbf{K}^{eq} \mathbf{L}, \ \mathbf{g} = \mathbf{L}^T \bar{\mathbf{g}} \tag{B.4}$$

The conclusion is that by mapping the mean displacements to the nodal displacements of the equilibrium element, we recover the SC1Q4[1]. Now, consider the example of a quadrilateral element with degrees of freedom $\mathbf{q}$ formulated using one-cell smoothing. The constant strain displacement matrix is

$$\widetilde{\mathbf{B}}_I = \frac{1}{A^e} \begin{bmatrix} \frac{1}{2}(n_x^i l_i + n_x^j l_j) & 0 \\ 0 & \frac{1}{2}(n_y^i l_i + n_y^j l_j) \\ \frac{1}{2}(n_y^i l_i + n_y^j l_j) & \frac{1}{2}(n_x^i l_i + n_x^j l_j) \end{bmatrix} \tag{B.5}$$

where the indices i, j are defined by the recursive rule, $ij = 14, 21, 32, 43$ and (n_x^i, n_y^i) is the normal vector on edge l_i. The smoothed strain fields on the element can then be rearranged and expressed in the form

$$\widetilde{\varepsilon}^h = \widetilde{\bar{\mathbf{B}}} \bar{\mathbf{q}} \tag{B.6}$$

where

$$\widetilde{\bar{B}}_I = \frac{1}{A^e} \begin{bmatrix} n_x^i l_i & 0 \\ 0 & n_y^i l_i \\ n_y^i l_i & n_x^i l_i \end{bmatrix} \tag{B.7}$$

The smoothed strain fields now are written in terms of $\widetilde{\bar{\mathbf{B}}}$ and the mean generalized displacement (the conjugate displacements) at the mid-sides of the element. Each of the conjugate displacements must be linked with an equivalent surface load at the mid-sides shown in Figure A.1. The work of these equivalent external loads at the mid-sides of the

---

[1]stabilized conforming nodal integration with one subcell of the four-node quadrilateral

element is then computed. By transforming the generalized displacements at the nodes to the mean displacements at the mid-points of the edges of the element, we obtain the pseudo-equilibrium element with the same connectors as the FEM quadrilateral equilibrium element using constant stress fields. The weak form with no body force is

$$\int_{\Omega^e} \delta\widetilde{\boldsymbol{\varepsilon}}^h : \mathbf{D} : \widetilde{\boldsymbol{\varepsilon}}^h d\Omega - \delta\bar{\mathbf{q}}^T \bar{\mathbf{g}} = 0 \tag{B.8}$$

Substituting Equation (B.6) into Equation (B.8) leads to

$$\widetilde{\mathbf{K}}\bar{\mathbf{q}} = \bar{\mathbf{g}} \tag{B.9}$$

where

$$\widetilde{\mathbf{K}} = \int_{\Omega^e} \widetilde{\mathbf{B}}^T \mathbf{D}\widetilde{\mathbf{B}} d\Omega \tag{B.10}$$

Based on the relation between $\bar{\mathbf{q}}$ and $\mathbf{q}$ in Equation (B.1) and assuming that $\mathbf{q}$ is known through the strain smoothing method, the external loads at the mid-sides of the element $\bar{\mathbf{g}}$ in Equation (B.9) can be computed. It is also remarkable that $\widetilde{\mathbf{K}}$ has five (5) zero eigenvalues and hence two spurious zero energy kinematic modes exit. These modes still appear after an assembly process and an enforcement of boundary conditions. Special care must therefore be taken upon imposing boundary conditions for equilibrium models (Fraeijs De Veubeke (1965); Kelly (1979, 1980)). Our work on the transformation of the connectors at the middle points along the element edges of the equilibrium element to the connectors at the corner nodes as in a displacement element is completely identical to the way of D.W. Kelly. In Kelly (1979, 1980), he showed the equivalence between equilibrium models and the displacement models using a reduced integration via the transformation of the connectors. However, his method is only true with the rectangular elements. It fails to work with the quadrilateral elements. In order to extend investigation's Kelly for the arbitrarily quadrilateral elements, above our method is more suitable to perform the formulation for all cases.

For more detail, we will redo a work of Kelly as proven in Kelly (1979, 1980). In Kelly (1979), a square element was chosen to compute the stiffness matrix of the Q4 element using a reduced integration with one Gauss point and this square element was subdivided into two triangles in order to construct the stiffness matrix of equilibrium model using two de Veubeke equilibrium triangles (Fraeijs De Veubeke (1965)). However, we further consider a rectangular element with corner coordinates given in Figure B.1a for one element and it is partitioned to two triangles for establishing the stiffness matrix of equilibrium elements. We will compare the stiffness matrix of equilibrium model using two de Veubeke equilibrium triangles and that of smoothed finite element using one cell (the SC1Q4). For simplify, Young's Modulus, Poisson's coefficient, thickness are chosen to be $1.0, 0, 1.0$ respectively.
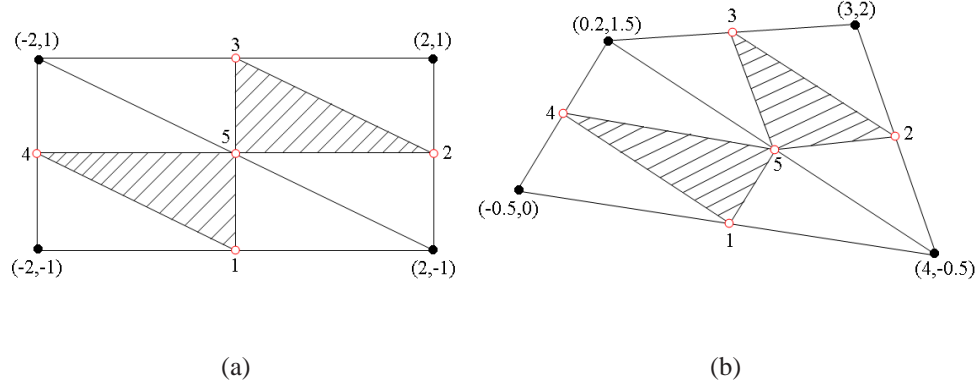
(a)   (b)

Figure B.1: Assembly of equilibrium triangular elements: (a) rectangular domain; (b) quadrilateral domain

The stiffness matrix of the SC1Q4 is

$$\tilde{\mathbf{K}} = \frac{1}{8} \begin{bmatrix} 3 & 1 & 1 & -1 & -3 & -1 & -1 & 1 \\ 1 & 4.5 & 1 & 3.5 & -1 & -4.5 & -1 & -3.5 \\ 1 & 1 & 3 & -1 & -1 & -1 & -3 & 1 \\ -1 & 3.5 & -1 & 4.5 & 1 & -3.5 & 1 & -4.5 \\ -3 & -1 & -1 & 1 & 3 & 1 & 1 & -1 \\ -1 & -4.5 & -1 & -3.5 & 1 & 4.5 & 1 & 3.5 \\ -1 & -1 & -3 & 1 & 1 & 1 & 3 & -1 \\ 1 & -3.5 & 1 & -4.5 & -1 & 3.5 & -1 & 4.5 \end{bmatrix} \tag{B.11}$$

After assembling equilibrium model using two triangular de Veubeke elements, one gives

$$\mathbf{K}^* \mathbf{q}^* = \mathbf{g}^* \tag{B.12}$$

where

$$\mathbf{K}^* = \begin{bmatrix} 2 & 0 & 0 & 0 & 0 & 0 & 0 & 1 & -2 & -1 \\ & 4 & 0 & 0 & 0 & 0 & 0 & 0 & 0 & -4 \\ & & 1 & 0 & 0 & 0 & 0 & 0 & -1 & 0 \\ & & & 0.5 & 1 & 0 & 0 & 0 & -1 & -0.5 \\ & & & & 2 & 0 & 0 & 0 & -2 & -1 \\ & & & & & 4 & 0 & 0 & 0 & -4 \\ & & sym & & & & 1 & 0 & -1 & 0 \\ & & & & & & & 0.5 & -1 & -0.5 \\ & & & & & & & & 6 & 2 \\ & & & & & & & & & 9 \end{bmatrix} \tag{B.13}$$

$\mathbf{q}^*, \mathbf{g}^*$ are the conjugate displacements and generalized boundary loads, respectively. In equilibrium model, the equilibrium conditions of the surface tractions at the interelement

boundary must be maintained. Therefore, two end terms contained in $\mathbf{g}^*$ are equal to zeros due to two triangular elements with common connectors at node 5 shown in Figure B.1a. By transforming connectors at the midpoints to the corner nodes, yielding the stiffness matrices:

$$\mathbf{K}' = \mathbf{L}'^T \mathbf{K}^* \mathbf{L}' = \frac{1}{4}
\begin{bmatrix}
3 & 1 & -1 & -1 & 0 & 0 & -2 & 0 \\
1 & 4.5 & 0 & -0.5 & 0 & 0 & -1 & -4 \\
-1 & 0 & 3 & 0 & -2 & -1 & 0 & 1 \\
-1 & -0.5 & 0 & 4.5 & 0 & -4 & 1 & 0 \\
0 & 0 & -2 & 0 & 3 & 1 & -1 & -1 \\
0 & 0 & -1 & -4 & 1 & 4.5 & 0 & -0.5 \\
-2 & -1 & 0 & 1 & -1 & 0 & 3 & 0 \\
0 & -4 & 1 & 0 & -1 & -0.5 & 0 & 4.5
\end{bmatrix} \tag{B.14}$$

where $\mathbf{L}'$ is defined by

$$\mathbf{L}' = \frac{1}{2}
\begin{bmatrix}
1 & 0 & 1 & 0 & 0 & 0 & 0 & 0 \\
0 & 1 & 0 & 1 & 0 & 0 & 0 & 0 \\
0 & 0 & 1 & 0 & 1 & 0 & 0 & 0 \\
0 & 0 & 0 & 1 & 0 & 1 & 0 & 0 \\
0 & 0 & 0 & 0 & 1 & 0 & 1 & 0 \\
0 & 0 & 0 & 0 & 0 & 1 & 0 & 1 \\
1 & 0 & 0 & 0 & 0 & 0 & 1 & 0 \\
0 & 1 & 0 & 0 & 0 & 0 & 0 & 1 \\
0 & 0 & 1 & 0 & 0 & 0 & 1 & 0 \\
0 & 0 & 0 & 1 & 0 & 0 & 0 & 1
\end{bmatrix} \tag{B.15}$$

and load vector:

$$\mathbf{g}' = \mathbf{L}'^T \mathbf{g}^* \tag{B.16}$$

with $\mathbf{g}^*$ is now redefined to be the generalized boundary loads which do not contain zero load terms at common node.

By combining the row operations of the stiffness equations of the assembly equilibrium triangular elements as shown in Kelly (1979, 1980),

$$\text{row}_{I+4} = \frac{1}{2}(\text{row}_{I+4} - \text{row}_I) \text{ and } \text{row}_I = \frac{1}{2}(\text{row}_I - \text{row}_{I+4}) \quad I = 1, 2, 3, 4 \tag{B.17}$$

we obtain completely the stiffness matrix $\tilde{K}$ of the one cell, and reducing to the relation between $\bar{\mathbf{g}}$ and $\mathbf{g}^*$ as follows

$$\bar{\mathbf{g}} = \mathbf{H}\mathbf{g}^* \tag{B.18}$$

180

where

$$\mathbf{H} = \frac{1}{2} \begin{bmatrix} 1 & 0 & 0 & 0 & -1 & 0 & 0 & 0 \\ & 1 & 0 & 0 & 0 & -1 & 0 & 0 \\ & & 1 & 0 & 0 & 0 & -1 & 0 \\ & & & 1 & 0 & 0 & 0 & -1 \\ & & & & 1 & 0 & 0 & 0 \\ & & sym & & & 1 & 0 & 0 \\ & & & & & & 1 & 0 \\ & & & & & & & 1 \end{bmatrix} \tag{B.19}$$

The above equivalence demonstration is the same way as a transformation from a displacement approach to a stress equilibrium model based on reduced integration(Kelly (1979)). Now we consider the quadrilateral element contained two equilibrium triangular elements as shown in Figure B.1b. The stiffness matrix of SFEM using one cell results in

$$\tilde{\mathbf{K}} = \begin{bmatrix} 0.3842 & 0.1301 & 0.0908 & -0.1301 & -0.3842 & -0.1301 & -0.0908 & 0.1301 \\ 0.1301 & 0.5630 & 0.1199 & 0.3870 & -0.1301 & -0.5630 & -0.1199 & -0.3870 \\ 0.0908 & 0.1199 & 0.3467 & -0.1199 & -0.0908 & -0.1199 & -0.3467 & 0.1199 \\ -0.1301 & 0.3870 & -0.1199 & 0.4880 & 0.1301 & -0.3870 & 0.1199 & -0.4880 \\ -0.3842 & -0.1301 & -0.0908 & 0.1301 & 0.3842 & 0.1301 & 0.0908 & -0.1301 \\ -0.1301 & -0.5630 & -0.1199 & -0.3870 & 0.1301 & 0.5630 & 0.1199 & 0.3870 \\ -0.0908 & -0.1199 & -0.3467 & 0.1199 & 0.0908 & 0.1199 & 0.3467 & -0.1199 \\ 0.1301 & -0.3870 & 0.1199 & -0.4880 & -0.1301 & 0.3870 & -0.1199 & 0.4880 \end{bmatrix} \tag{B.20}$$

The stiffness matrix of two equilibrium triangular elements after assembling and transforming connectors at the midpoints to the corner nodes is

$$\mathbf{K}' = \begin{bmatrix} 0.7480 & 0.2533 & -0.4600 & -0.3167 & 0 & 0 & -0.2880 & 0.0633 \\ 0.2533 & 1.0960 & -0.0667 & -0.4200 & 0 & 0 & -0.1867 & -0.6760 \\ -0.4600 & -0.0667 & 1.1806 & 0.1626 & -0.6725 & -0.3169 & -0.0481 & 0.2210 \\ -0.3167 & -0.4200 & 0.1626 & 1.7099 & -0.0669 & -1.2394 & 0.2210 & -0.0504 \\ 0 & 0 & -0.6725 & -0.0669 & 0.7901 & 0.2676 & -0.1176 & -0.2007 \\ 0 & 0 & -0.3169 & -1.2394 & 0.2676 & 1.1577 & 0.0493 & 0.0817 \\ -0.2880 & -0.1867 & -0.0481 & 0.2210 & -0.1176 & 0.0493 & 0.4537 & -0.0836 \\ 0.0633 & -0.6760 & 0.2210 & -0.0504 & -0.2007 & 0.0817 & -0.0836 & 0.6447 \end{bmatrix} \tag{B.21}$$

It is clear that, by combining the row, even at column, operations using (B.17), we can not gain the stiffness matrix of SFEM method as in (B.20). Therefore, work of Kelly is only used for the rectangle elements. However, this limitation is always overcomed by our method. In our work, the equilibrium quadrilateral element is used. Hence the

equilibrium element stiffness matrix is

$$
\mathbf{K}^{eq} =
\begin{bmatrix}
1.9940 & 0.1414 & -1.0522 & -0.7578 & -0.2560 & 0.1414 & -0.6858 & 0.4751 \\
0.1414 & 2.9628 & -0.0215 & -0.8737 & -0.1086 & -1.5372 & -0.0112 & -0.5518 \\
-1.0522 & -0.0215 & 1.4974 & 0.1585 & -0.5522 & -0.0215 & 0.1070 & -0.1155 \\
-0.7578 & -0.8737 & 0.1585 & 0.7368 & 0.4922 & 0.1263 & 0.1071 & 0.0107 \\
-0.2560 & -0.1086 & -0.5522 & 0.4922 & 1.1440 & -0.1086 & -0.3358 & -0.2749 \\
0.1414 & -1.5372 & -0.0215 & 0.1263 & -0.1086 & 1.2628 & -0.0112 & 0.1482 \\
-0.6858 & -0.0112 & 0.1070 & 0.1071 & -0.3358 & -0.0112 & 0.9146 & -0.0847 \\
0.4751 & -0.5518 & -0.1155 & 0.0107 & -0.2749 & 0.1482 & -0.0847 & 0.3929
\end{bmatrix}
$$

$$(B.22)$$

Using permutation matrix $\mathbf{L}$ of (B.2) and the formulation $\mathbf{L}^T \mathbf{K}^{eq} \mathbf{L}$ of (B.4), we obtain the stiffness matrix that is always identical to the SC1Q4 stiffness matrix $\widetilde{\mathbf{K}}$.

Appendix C

Finite element formulation for the eight-node hexahedral element

We consider a trilinear form for the eight-node hexahedral element (H8)in physical coordinates as

$$
\begin{aligned}
u\left(x, y, z\right) &= a_1 + a_2 x + a_3 y + a_4 z + a_5 xy + a_6 yz + a_7 zx + a_8 xyz \\
v\left(x, y, z\right) &= a_9 + a_{10} x + a_{11} y + a_{12} z + a_{13} xy + a_{14} yz + a_{15} zx + a_{16} xyz \\
w\left(x, y, z\right) &= a_{17} + a_{18} x + a_{19} y + a_{20} z + a_{21} xy + a_{22} yz + a_{23} zx + a_{24} xyz
\end{aligned} \qquad \text{(C.1)}
$$

or a matrix formula is of the form

$$
\mathbf{u} = \mathbf{M}\mathbf{a} \qquad \text{(C.2)}
$$

where

$$
\mathbf{u} = \left\{\ u \quad v \quad w\ \right\}^T \qquad \text{(C.3)}
$$

$$
\mathbf{M} = \begin{bmatrix} \mathbf{P}\left(x, y, z\right) & 0 & 0 \\ 0 & \mathbf{P}\left(x, y, z\right) & 0 \\ 0 & 0 & \mathbf{P}\left(x, y, z\right) \end{bmatrix} \qquad \text{(C.4)}
$$

$$
\mathbf{P}\left(x, y, z\right) = \left\{\ 1 \quad x \quad y \quad z \quad xy \quad yz \quad zx \quad xyz\ \right\} \qquad \text{(C.5)}
$$

$$
\mathbf{a} = \left\{\ a_1 \quad a_2 \quad a_3 \quad \ldots \quad a_{24}\ \right\}^T \qquad \text{(C.6)}
$$

183

Generalized displacements are determined by substituting the x, y, z values at each point of the element as

$$
\mathbf{q} \equiv
\begin{Bmatrix}
u_1 \\
v_1 \\
w_1 \\
\vdots \\
u_8 \\
v_8 \\
w_8
\end{Bmatrix}
=
\begin{bmatrix}
\mathbf{P}_1 & 0 & 0 \\
0 & \mathbf{P}_1 & 0 \\
0 & 0 & \mathbf{P}_1 \\
\vdots & \vdots & \vdots \\
\mathbf{P}_8 & 0 & 0 \\
0 & \mathbf{P}_8 & 0 \\
0 & 0 & \mathbf{P}_8
\end{bmatrix}
\begin{Bmatrix}
a_1 \\
a_2 \\
a_3 \\
\vdots \\
a_{22} \\
a_{23} \\
a_{24}
\end{Bmatrix}
\tag{C.7}
$$

or

$$
\mathbf{q} = \mathbf{Ca} \tag{C.8}
$$

leading to

$$
\mathbf{a} = \mathbf{C}^{-1}\mathbf{q} \tag{C.9}
$$

Substituting Equation (C.9) into Equation (C.2) one obtains

$$
\mathbf{u} = \mathbf{MC}^{-1}\mathbf{q} \tag{C.10}
$$

or

$$
\mathbf{u} = \mathbf{Nq} \tag{C.11}
$$

where $\mathbf{N} = \mathbf{MC}^{-1}$ is called matrix of shape functions. For the eight-node hexahedral element, the functions are trilinear and the matrix form is

$$
\mathbf{N} =
\begin{bmatrix}
N_1 & 0 & 0 & \dots & N_8 & 0 & 0 \\
0 & N_1 & 0 & \dots & 0 & N_8 & 0 \\
0 & 0 & N_1 & \dots & 0 & 0 & N_8
\end{bmatrix}
\tag{C.12}
$$

The displacement components of H8 is therefore formulated as

$$
\begin{aligned}
u\,(x, y, z) &= \sum_{I=1}^{8} N_I\,(x, y, z)\,u_I \\
v\,(x, y, z) &= \sum_{I=1}^{8} N_I\,(x, y, z)\,v_I \\
w\,(x, y, z) &= \sum_{I=1}^{8} N_I\,(x, y, z)\,w_I
\end{aligned}
\tag{C.13}
$$

The strain-displacement matrix writes

$$\mathbf{B} = \partial\mathbf{N} = \begin{bmatrix} \dfrac{\partial}{\partial x} & 0 & 0 \\ 0 & \dfrac{\partial}{\partial y} & 0 \\ 0 & 0 & \dfrac{\partial}{\partial z} \\ \dfrac{\partial}{\partial y} & \dfrac{\partial}{\partial x} & 0 \\ 0 & \dfrac{\partial}{\partial z} & \dfrac{\partial}{\partial y} \\ \dfrac{\partial}{\partial z} & 0 & \dfrac{\partial}{\partial x} \end{bmatrix} \begin{bmatrix} N_1 & 0 & 0 & N_2 & 0 & 0 & \dots & N_8 & 0 & 0 \\ 0 & N_1 & 0 & 0 & N_2 & 0 & \dots & 0 & N_8 & 0 \\ 0 & 0 & N_1 & 0 & 0 & N_2 & \dots & 0 & 0 & N_8 \end{bmatrix}$$

(C.14)

Then stiffness matrix, strain and stress of element can be written as

$$\mathbf{K}^e = \int_{\Omega^e} \mathbf{B}^T \mathbf{D} \mathbf{B} d\Omega$$

(C.15)

where size of the stiffness matrix is 24×24. The strain and stress are vectors that have 6 components

$$\boldsymbol{\varepsilon} = \{\varepsilon_x \quad \varepsilon_y \quad \varepsilon_z \quad \varepsilon_{xy} \quad \varepsilon_{yz} \quad \varepsilon_{zx}\}^T$$

(C.16)

$$\boldsymbol{\sigma} = \{\sigma_x \quad \sigma_y \quad \sigma_z \quad \sigma_{xy} \quad \sigma_{yz} \quad \sigma_{zx}\}^T$$

(C.17)

$\mathbf{D}$ is the material property matrix for 3D solid problem

$$\mathbf{D} = \begin{bmatrix} \lambda + 2\mu & \lambda & \lambda & 0 & 0 & 0 \\ \lambda & \lambda + 2\mu & \lambda & 0 & 0 & 0 \\ \lambda & \lambda & \lambda + 2\mu & 0 & 0 & 0 \\ 0 & 0 & 0 & \mu & 0 & 0 \\ 0 & 0 & 0 & 0 & \mu & 0 \\ 0 & 0 & 0 & 0 & 0 & \mu \end{bmatrix}$$

(C.18)

where $\lambda = \nu E/((1+\nu)(1-2\nu))$ and $\mu = E/(2(1+\nu))$. To develop the isoparamatric eight node brick element, the parent element must be defined in the natural coordinate system (ξ, η, ζ) as shown in Figure C.1 The geometry of the eight node brick element can be defined using Lagrange interpolating functions

$$x(\xi, \eta, \zeta) = \sum_{I=1}^{8} N_I(\xi, \eta, \zeta) x_I$$
$$y(\xi, \eta, \zeta) = \sum_{I=1}^{8} N_I(\xi, \eta, \zeta) y_I$$
$$z(\xi, \eta, \zeta) = \sum_{I=1}^{8} N_I(\xi, \eta, \zeta) z_I$$
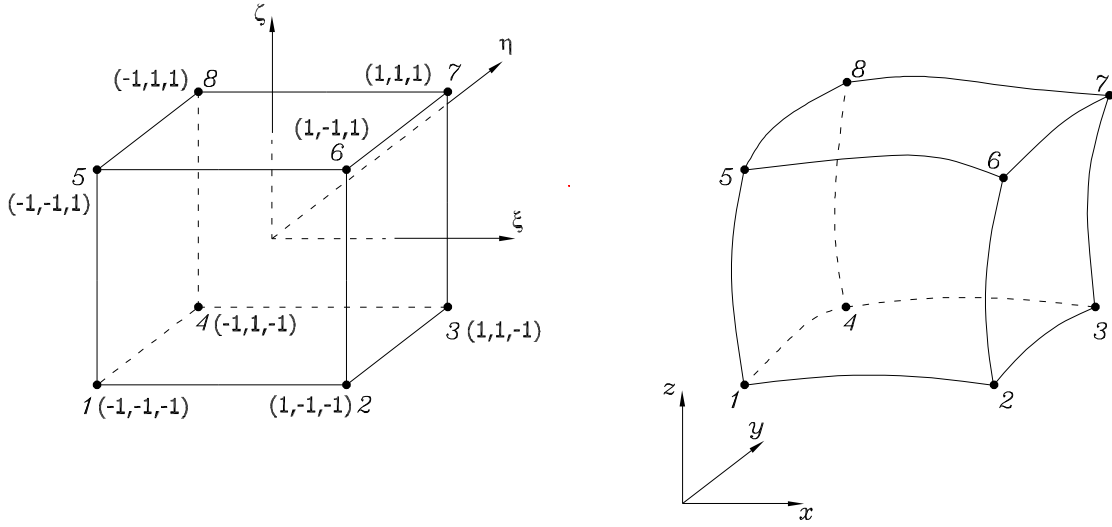
(C.19)

185

Figure C.1: Eight node brick element

Similarly, the relationship between displacements in the natural coordinate system and the nodal displacements can be written in the following manner

$$
\begin{aligned}
u\left(\xi, \eta, \zeta\right) &= \sum_{I=1}^{8} N_I\left(\xi, \eta, \zeta\right) u_I \\
v\left(\xi, \eta, \zeta\right) &= \sum_{I=1}^{8} N_I\left(\xi, \eta, \zeta\right) v_I \\
w\left(\xi, \eta, \zeta\right) &= \sum_{I=1}^{8} N_I\left(\xi, \eta, \zeta\right) w_I
\end{aligned}
\tag{C.20}
$$

where $N_I, \forall I \in \{1, .., 8\}$ are the shape functions for the eight-node hexahedral element in the natural coordinate system. The shape functions are

$$
N_I = \frac{1}{8}\left(1 + \xi_I \xi\right)\left(1 + \eta_I \eta\right)\left(1 + \zeta_I \zeta\right)
\tag{C.21}
$$

where the normalized coordinates at node I given by $\xi_I \in \{-1, 1, 1, -1, -1, 1, 1, -1\}$, $\eta_I \in \{-1, -1, 1, 1, -1, -1, 1, 1\}$, $\zeta_I \in \{-1, -1, -1, -1, 1, 1, 1, 1\}$.
From Equation (C.21), the partial derivatives of the field variable with respect to the

natural coordinates are expressed as

$$
\begin{aligned}
\frac{\partial N_I}{\partial \xi} &= \frac{\partial N_I}{\partial x}\frac{\partial x}{\partial \xi} + \frac{\partial N_I}{\partial y}\frac{\partial y}{\partial \xi} + \frac{\partial N_I}{\partial z}\frac{\partial z}{\partial \xi} \\
\frac{\partial N_I}{\partial \eta} &= \frac{\partial N_I}{\partial x}\frac{\partial x}{\partial \eta} + \frac{\partial N_I}{\partial y}\frac{\partial y}{\partial \eta} + \frac{\partial N_I}{\partial z}\frac{\partial z}{\partial \eta} \\
\frac{\partial N_I}{\partial \zeta} &= \frac{\partial N_I}{\partial x}\frac{\partial x}{\partial \zeta} + \frac{\partial N_I}{\partial y}\frac{\partial y}{\partial \zeta} + \frac{\partial N_I}{\partial z}\frac{\partial z}{\partial \zeta}
\end{aligned}
\tag{C.22}
$$

or in matrix form,

$$
\left\{ \begin{array}{c} \frac{\partial N_I}{\partial \xi} \\ \frac{\partial N_I}{\partial \eta} \\ \frac{\partial N_I}{\partial \zeta} \end{array} \right\} = \mathbf{J} \left\{ \begin{array}{c} \frac{\partial N_I}{\partial x} \\ \frac{\partial N_I}{\partial y} \\ \frac{\partial N_I}{\partial z} \end{array} \right\}
\tag{C.23}
$$

where $\mathbf{J}$ is called the *Jacobian* matrix,

$$
\mathbf{J} = \left[\begin{array}{ccc} \frac{\partial x}{\partial \xi} & \frac{\partial y}{\partial \xi} & \frac{\partial z}{\partial \xi} \\ \frac{\partial x}{\partial \eta} & \frac{\partial y}{\partial \eta} & \frac{\partial z}{\partial \eta} \\ \frac{\partial x}{\partial \zeta} & \frac{\partial y}{\partial \zeta} & \frac{\partial z}{\partial \zeta} \end{array} \right]
\tag{C.24}
$$

Substituting Equation (C.19) into Equation (C.24) we obtain

$$
\mathbf{J} = \left[\begin{array}{ccc} \sum_{I=1}^{8} \frac{\partial N_I}{\partial \xi} x_I & \sum_{I=1}^{8} \frac{\partial N_I}{\partial \xi} y_I & \sum_{I=1}^{8} \frac{\partial N_I}{\partial \xi} z_I \\ \sum_{I=1}^{8} \frac{\partial N_I}{\partial \eta} x_I & \sum_{I=1}^{8} \frac{\partial N_I}{\partial \eta} y_I & \sum_{I=1}^{8} \frac{\partial N_I}{\partial \eta} z_I \\ \sum_{I=1}^{8} \frac{\partial N_I}{\partial \zeta} x_I & \sum_{I=1}^{8} \frac{\partial N_I}{\partial \zeta} y_I & \sum_{I=1}^{8} \frac{\partial N_I}{\partial \zeta} z_I \end{array} \right]
\tag{C.25}
$$

Assumed there exist the inverse of the Jacobian matrix, the partial derivatives of the shape functions with respect to the global coordinates in Equation (C.23) are completely determined by

$$
\left\{ \begin{array}{c} \frac{\partial N_I}{\partial x} \\ \frac{\partial N_I}{\partial y} \\ \frac{\partial N_I}{\partial z} \end{array} \right\} = \mathbf{J}^{-1} \left\{ \begin{array}{c} \frac{\partial N_I}{\partial \xi} \\ \frac{\partial N_I}{\partial \eta} \\ \frac{\partial N_I}{\partial \zeta} \end{array} \right\}
\tag{C.26}
$$

Therefore, Equation (C.15) can be rewritten as,

$$
\mathbf{K}^e = \int_{-1}^{1} \int_{-1}^{1} \int_{-1}^{1} \mathbf{B}^T \mathbf{D} \mathbf{B} \, |\mathbf{J}| d\xi d\eta d\zeta
\tag{C.27}
$$

The element stiffness matrix can be then obtained by using $2 \times 2 \times 2$ Gauss quadrature and has the form,

$$\mathbf{K}^e = \sum_{j=1}^{2}\sum_{k=1}^{2}\sum_{l=1}^{2} \mathbf{B}^T\mathbf{D}\mathbf{B} \, |\mathbf{J}| \, w_j w_k w_l \tag{C.28}$$

The strain and stress of each element can average over Gauss quadrature points.

$$\varepsilon = \frac{1}{8}\sum_{j=1}^{2}\sum_{k=1}^{2}\sum_{l=1}^{2} \mathbf{B}\mathbf{q} \tag{C.29}$$

$$\sigma = \frac{1}{8}\sum_{j=1}^{2}\sum_{k=1}^{2}\sum_{l=1}^{2} \mathbf{D}\mathbf{B}\mathbf{q} \tag{C.30}$$

References

ABAQUS (2004). *ABAQUS/Standard User's Manual,Version 6.4*. Hibbitt, Karlsson and Sorensen, Inc.: Rawtucket, Rhode Island. 77

ABBASSIAN, F., DAWSWELL, D.J. & KNOWLES, N.C. (1987). Free vibration benchmarks. Tech. rep., Softback, 40 Pages, Atkins Engineering Sciences,Glasgow. 109, 110, 111, 112

ALEMEIDA, J.P.M. (2008). Hybrid equilibrium hexahedral elements and super-elements. *Communications in Numerical Methods in Engineering*, **24**, 157–165. 3

ALEMEIDA, J.P.M. & FREITAS, J.A.T. (1991). Alternative approach to the formulation of hybrid equilibrium finite elements. *Computers and Structures*, **40**, 1043–1047. 3

ALLMAN, D.J. (1984). A compatible triangular element including vertex rotations for plane elasticity analysis. *Computers and Structures*, **19**, 1–8. 161

ANDELFINGER, U. & RAMM, E. (1993). EAS-elements for two-dimensional, three-dimensional, plate and shells and their equivalence to HR-elements. *International Journal for Numerical Methods in Engineering*, **36**, 1413–1449. 3, 74

AREIAS, P.M.A., SONG, J.H. & BELYTSCHKO, T. (2005). A simple finite-strain quadrilateral shell element part i: Elasticity. *International Journal for Numerical Methods in Engineering*, **64**, 1166 – 1206. 127

ARMERO, F. (2007). Assumed strain finite element methods for conserving temporal integrations in non-linear solid dynamics. *International Journal for Numerical Methods in Engineering*, DOI: 10.1002/nme.2233, in press. 3

ATLURI, S.N. & SHEN, S.P. (2002). The meshless local Petrov-Galerkin (MLPG) method: a simple and less-costly alternative to the finite element and boundary element methods. *Computer Modeling in Engineering and Sciences*, **3**, 11–51. 4

BABUŠKA, I. & MELENK, J.M. (1997). The partition of unity method. *International Journal for Numerical Methods in Engineering*, **40**, 727–758. 48

189

BATHE, K.J. (1996). *Finite element procedures*. Englewood Cliffs, NJ: Prentice-Hall, Masetchuset(MIT). 13, 74, 98, 128

BATHE, K.J. & DVORKIN, E.N. (1985). A four-node plate bending element based on Mindlin/Reissener plate theory and a mixed interpolation. *International Journal for Numerical Methods in Engineering*, **21**, 367–383. 3, 13, 18, 73, 76, 98, 128, 130

BATHE, K.J. & DVORKIN, E.N. (1986). A formulation of general shell elements. the use of mixed interpolation of tensorial components. *International Journal for Numerical Methods in Engineering*, **22**, 697–722. 3, 7, 73, 98, 128

BATHE, K.J., IOSILEVICH, A. & CHAPELLE, D. (2000). An evaluation of the MITC shell elements. *Computers and Structures*, **75**, 1–30. 127, 139

BATOZ, J.L. & DHATT, G. (1990). *Modélisation des structures par éléments finis, Vol.2, poutres et plaques*. Hermès. 13, 128

BATOZ, J.L. & TAHAR, M.B. (1982). Evaluation of a new quadrilateral thin plate bending element. *International Journal for Numerical Methods in Engineering*, **18**, 1655–1677. 77

BAZELEY, G.P., CHEUNG, Y.K., IRONS, B.M. & ZIENKIEWICZ, O.C. (1965). Triangular elements in plate bending. In *Proc. First Conf. on Matrix Methods in Stuctural Mechanics, Wright-Patterson AFB, Ohio*. 77

BECKERS, P. (1972). *Les fonctions de tension dans la méthod des éléments finis*. Ph.D. thesis, LTAS, Faculté des Sciences Appliquées, Université de Liège. 2, 5, 73

BECKERS, P. (2008). Extension of dual analysis to 3-D problems: evaluation of its advantages in error estimation. *Computational Mechanics*, **41**, 421–427. 2, 5, 172

BECKERS, P., ZHONG, H.G. & MAUNDER, E. (1993). Numerical comparison of several a posteriori error estimators for 2D stress analysis. *European Journal of Finite Element Method*, **2**. 44, 46

BEISSEL, S. & BELYTSCHKO, T. (1996). Nodal integration of the element-free Galerkin method. *Computer Methods in Applied Mechanics and Engineering*, **139**, 49–74. 4

BELYTSCHKO, T. & BACHRACH, W.E. (1986). Efficient implementation of quadrilaterals with high coarse-mesh accuracy. *Computer Methods in Applied Mechanics and Engineering*, **54**, 279–301. 2, 30, 161

BELYTSCHKO, T. & BINDEMAN, L.P. (1991). Assumed strain stabilization of the 4-node quadrilateral with l-point quadrature for nonlinear problems. *Computer Methods in Applied Mechanics and Engineering*, **88**, 311–340. 2, 44, 161

BELYTSCHKO, T. & BINDEMAN, L.P. (1993). Assumed strain stabilization of the eight node hexahedral element. *Computer Methods in Applied Mechanics and Engineering*, **105**, 225–260. 2, 55, 63

BELYTSCHKO, T. & BLACK, T. (1999). Elastic crack growth in finite elements with minimal remeshing. *International Journal for Numerical Methods in Engineering*, **45**, 601–620. 45

BELYTSCHKO, T. & LEVIATHAN, I. (1994). Physical stabilization of the 4-node shell element with one-point quadrature. *Computer Methods in Applied Mechanics and Engineering*, **113**, 321–350. 2

BELYTSCHKO, T. & TSAY, C.S. (1983). A stabilization procedure for the quadrilateral plate element with one-point quadrature. *International Journal for Numerical Methods in Engineering*, **19**, 405–419. 2

BELYTSCHKO, T., TSAY, C.S. & LIU, W.K. (1981). A stabilixation matrix for the bilinear Mindlin plate element. *Computer Methods in Applied Mechanics and Engineering*, **29**, 313–327. 2

BELYTSCHKO, T., ONG, J.S.J., LIU, W.K. & KENNEDY, J.M. (1985). Houglass control in linear and nonlinear problems. *Computer Methods in Applied Mechanics and Engineering*, **43**, 251–276. 2

BELYTSCHKO, T., LU, Y.Y. & GU, L. (1994). Element-free Galerkin methods. *International Journal for Numerical Methods in Engineering*, **37**, 229–256. 4, 130

BELYTSCHKO, T., MOËS, N., USUI, S. & PARIMI, C. (2001). Arbitrary discontinuities in finite elements. *Internation Journal of Numerical Methods in Engineering*, **50**. 45

BISCHOFF, M., RAMM, E. & BRAESS, D. (1999). A class equivalent enhanced assumed strain and hybrid stress finite elements. *Computational Mechanics*, **22**, 44–449. 3

BLETZINGER, K.U., BISCHOFF, M. & RAMM, E. (2000). A unified approach for shear-locking-free triangular and rectangular shell finite elements. *Computers and Structures*, **75**, 321–334. 3, 127

BONET, J. & KULASEGARAM, S. (1999). Correction and stabilization of smooth particle hydrodynamics methods with applications in metal forming simulation. *International Journal for Numerical Methods in Engineering*, **47**, 1189–1214. 4

BORDAS, S. & MORAN, B. (2006). Enriched finite elements and level sets for damage tolerance assessment of complex structures. *Engineering Fracture Mechanics*, **73**, 1176–1201. 172

BORDAS, S., CONLEY, J.G., MORAN, B., GRAY, J. & NICHOLS, E. (2007a). A simulation based on design paradigm for complex cast components. *Engineering Computation*, **23**, 25–37. 172

BORDAS, S., NGUYEN, V.P., DUNANT, C., NGUYEN-DANG, H. & GUIDOUMM, A. (2007b). An extended finite element library. *International Journal for Numerical Methods in Engineering*, **71**, 703 – 732. 172

BORDAS, S., RABCZUK, T., NGUYEN-XUAN, H., NGUYEN-VINH, P., SUNDARARAJAN, N., TINO, B., DO-MINH, Q. & NGUYEN-VINH, H. (2008a). Strain smoothing in fem and xfem. *Computers and Structures*, DOI: 10.1016/j.compstruc.2008.07.006, in press. 6, 52, 72, 172

BORDAS, S., RABCZUK, T. & ZI, G. (2008b). Three-dimensional crack initiation, propagation, branching and junction in non-linear materials by an extended meshfree method without asymptotic enrichment. *Engineering Fracture Mechanics*, **75**, 943–960. 5, 172

BREZZI, F. & FORTIN, M. (1991). *Mixed and Hybrid finite element methods*. Springer-Verlag, New York. 1, 7, 152

CARDOSO, R.P.R., YOON, J.W. & VALENTE, R.A.F. (2006). A new approach to reduce membrane and transverse shear locking for one-point quadrature shell elements: linear formulation. *International Journal for Numerical Methods in Engineering*, **66**, 214–249. 3, 127

CARDOSO, R.P.R., YOON, J.W., MAHARDIKA, M., CHOUDHRY, S., SOUSA, R.J.A. & VALENTE, R.A.F. (2007). Enhanced assumed strain (EAS) and assumed natural strain (ANS) methods for one-point quadrature solid-shell elements. *International Journal for Numerical Methods in Engineering*, DOI: 10.1002/nme.2250, in press. 3, 127

CESCOTTO, S. & LI, X. (2007). A natural neighbour method for linear elastic problems based on fraeijs de veubeke variational principle. *International Journal for Numerical Methods in Engineering*, **71**, 1081–1101. 4, 5, 144

CHEN, J.S., WU, C.T., YOON, S. & YOU, Y. (2001). A stabilized conforming nodal integration for Galerkin mesh-free methods. *International Journal for Numerical Methods in Engineering*, **50**, 435–466. 4, 18, 19, 20, 21, 74, 98, 144

CHEN, W. & CHEUNG, Y.K. (2000). Refined quadrilateral element based on Mindlin/Reissner plate theory. *International Journal for Numerical Methods in Engineering*, **47**, 605–627. 77

CLOUGH, R.W. (1960). The finite element method in plane stress analysis. In *Proceedings of the Second ASCE Conference on Electronic Computation*, Pittsburgh, PA. 1

COOK, R.D. (1974). Improved two-dimensional finite element. *Journal of Engineering Mechanics Division, ASCE*, **100**, 1851–1863. 43

COOK, R.D., MALKUS, D.S., PLESHA, M.E. & WITT, R.J. (2001). *Concepts and Applications of Finite Element Analysis*. 4th Edition, John Wiley and Sons. 17

CUGNON, F. (2000). *Automatisation des calculs éléments finis dans le cadre de la méthode-p*. Ph.D. thesis, LTAS, Faculté des Sciences Appliquées, Université de Liège. 66, 165

DAI, K.Y. & LIU, G.R. (2007). Free and forced vibration analysis using the smoothed finite element method (sfem). *Journal of Sound and Vibration*, **301**, 803–820. 5, 99

DAI, K.Y., LIU, G.R. & NGUYEN, T.T. (2007). An n-sided polygonal smoothed finite element method (nsfem) for solid mechanics. *Finite Elements in Analysis and Design*, **43**, 847–860. 26, 75

DE-SAXCE, G. & CHI-HANG, K. (1992a). Application of the hybrid mongrel displacement finite element method to the computation of stress intensity factors in anisotropic materials. *Engineering Fracture Mechanics*, **41**, 71–83. 3

DE-SAXCE, G. & CHI-HANG, K. (1992b). Computation of stress intensity factors for plate bending problem in fracture mechanics by hybrid mongrel finite element. *Computers and Structures*, **42**, 581–589. 3

DE-SAXCE, G. & NGUYEN-DANG, H. (1984). Dual analysis of frictionless problems by displacement and equilibrium finite elements. *Engineering Structures*, **6**, 26–32. 5

DEBONGNIE, J.F. (1977). A new look at Herman's formulation of incompressibility. In *Proceedings of the symposium on applications of computer methods in engineering*, University of Southern California, Los Angeles, USA. 1

DEBONGNIE, J.F. (1978). *Modélisation de problèmes hydro-élastiques par éléments finis. Application aux lanceurs aérospatiaux*. Ph.D. thesis, LTAS, Faculté des Sciences Appliquées, Université de Liège. 1

DEBONGNIE, J.F. (1986). Convergent thin-shell models using cartesian components of the displacements. **24**, 353–365. 127

DEBONGNIE, J.F. (2001). Some aspects of the finite element errors. Report LMF/D42, Université de Liège. 9

DEBONGNIE, J.F. (2003). *Fundamentials of finite elements*. Les Éditions de l'Université, 31, Boulevard Frère-Orban 4000 Liège. 73, 127

DEBONGNIE, J.F., ZHONG, H.G. & BECKERS, P. (1995). Dual analysis with general boundary conditions. *Computer Methods in Applied Mechanics and Engineering*, **122**, 183–192. 5, 45, 172

DEBONGNIE, J.F., NGUYEN-XUAN, H. & NGUYEN, H.C. (2006). Dual analysis for finite element solutions of plate bending. In *Proceedings of the Eighth International Conference on Computational Structures Technology*, Civil-Comp Press, Stirlingshire, Scotland. 5, 172

DOLBOW, J. & BELYTSCHKO, T. (1999). Numerical integration of Galerkin weak form in meshfree methods. *Computational Mechanics*, **23**, 219–230. 4

DUDDECK, H. (1962). Die biegetheorie der flachen hyperbolischen paraboloidschale z=cxy. *Ing. Archiv*, **31**, 44–78. 136

DUFLOT, M. (2006). A meshless method with enriched weight functions for three-dimensional crack propagation. *International Journal for Numerical Methods in Engineering*, **65**, 1970–2006. 4, 5

DUNANT, C., NGUYEN, V.P., BELGASMIA, M., BORDAS, S., GUIDOUM, A. & NGUYEN-DANG, H. (2007). Architecture trade-offs of including a mesher in an object-oriented extended finite element code. *Europian Journal of Mechanics*, **16**, 237–258. 172

DVORKIN, E.N. & BATHE, K.J. (1984). A continuum mechanics based four-node shell element for general nonlinear analysis. *Engineering Computation*, **1**, 77–88. 3

DVORKIN, E.N. & BATHE, K.J. (1994). A continuum mechanics based four-node shell element for general nonlinear analysis. *Engineering Computations*, **1**, 77–88. 3, 73, 98

FELIPPA, C.A. (1995). Parametric unification of matrix structural analysis: classical formulation and d-connected mixed elements. *Finite Elements in Analysis and Design*, **21**, 45–74. 1

FELIPPA, C.A. (2000). On the original publication of the general canonical functional of linear elasticity. *ASME Journal of Applied Mechanics*, **67**, 217–219. 1

FELIPPA, C.A. (2001). A historical outline of matrix structural analysis: A play in three acts. *Computers and Structures*, **79**, 1313–1324. 1

FLANAGAN, D. & BELYTSCHKO, T. (1981). A uniform strain hexahedron and quadrilateral with orthogonal hourglass control. *International Journal for Numerical Methods in Engineering*, **17**, 679–706. 2

FRAEIJS DE VEUBEKE, B. (1965). Displacement and equilibrium models in the finite element Method. In "Stress analysis", Zienkiewicz OC, Holister G (eds). John Wiley

and Sons, 1965: chapter 9, 145-197. *Reprinted in International Journal for Numerical Methods in Engineering*, **52**, 287–342(2001). 1, 2, 5, 45, 58, 174, 175, 178

FRAEIJS DE VEUBEKE, B. & SANDER, G. (1968). An equilibrium model for plate bending. *International Journal of Solids and Structures*, **4**, 447–468. 73

FRAEIJS DE VEUBEKE, B., SANDER, G. & BECKERS, P. (1972). Dual analysis by finite elements linear and non-linear applications. Final scientific report, LTAS, Faculté des Sciences Appliquées, Université de Liège. 2, 5, 73

FREDRIKSSON, M. & OTTOSEN, N.S. (2004). Fast and accurate 4-node quadrilateral. *International Journal for Numerical Methods in Engineering*, **61**, 1809–1834. 63, 161

FREDRIKSSON, M. & OTTOSEN, N.S. (2007). Accurate eight-node hexahedral element. *International Journal for Numerical Methods in Engineering*, **72**, 631–657. 55, 59

GERADIN, M. (1972). *Analyse dynamique duale des structures par la méthod des éléments finis*. Ph.D. thesis, LTAS, Faculté des Sciences Appliquées, Université de Liège. 2

GORMAN, D.J. & SINGHAL, R. (2002). Free vibration analysis of cantilever plates with step discontinuities in properties by the method of superposition. *Journal Sound and Vibration*, **253**, 631–652. 117, 119

GRUTTMANN, F. & WAGNER, W. (2004). A stabilized one-point integrated quadrilateral Reissener-Mindlin plate element. *International Journal for Numerical Methods in Engineering*, **61**, 2273 – 2295. 74, 77

GRUTTMANN, F. & WAGNER, W. (2005). A linear quadrilateral shell element with fast stiffness computation. *Computer Methods in Applied Mechanics and Engineering*, **194**, 4279–4300. 137

HERRMANN, L.R. (1965). Elasticity equations for incompressible and nearly incompressible materials by a variational theorem. *AIAA Journal*, **3**, 1896 –1900. 1

HUGHES, T.J.R. (1980). Generalization of selective integration procedures to antisotropic and nonlinear media. *International Journal for Numerical Methods in Engineering*, **15**, 1413–1418. 1, 39

HUGHES, T.J.R. (1987). *The Finite Element Method*. Prentice-Hall, Englewood Cliffs, NJ. 128

HUGHES, T.J.R. & LIU, W.K. (1981). Nonlinear finite element analysis of shells. part ii: Two dimensional shells. *Computer Methods in Applied Mechanics and Engineering*, **27**, 167–182. 130

HUGHES, T.J.R. & TEZDUYAR, T. (1981). Finite elements based upon Mindlin plate theory with particular reference to the four-node isoparametric element. *Journal of Applied Mechanics*, **48**, 587–596. 3, 73, 98

HUGHES, T.J.R., TAYLOR, R.L. & KANOKNUKULCHAI, W. (1977). Simple and efficient element for plate bending. *International Journal for Numerical Methods in Engineering*, **11**, 1529–1543. 1, 73, 98

HUGHES, T.J.R., COHEN, M. & HAROUN, M. (1978). Reduced and selective integration techniques in finite element method of plates. *Nuclear Engineering Design*, **46**, 203–222. 1, 73, 98

IDELSOHN, S. (1974). *Analyse statique et dynamique des coques par la méthod des éléments finis*. Ph.D. thesis, LTAS, Faculté des Sciences Appliquées, Université de Liège. 127

JETTEUR, P. & CESCOTTO, S. (1991). A mixed finite element for the analysis of large inelastic strains. *International Journal for Numerical Methods in Engineering*, **31**, 229–239. 2

JOHNSON, C. & MERCIER, B. (1979). *Some equilibrium finite element methods for two-dimensional elasticity problems. In Energy methods in finite element analysis*. Wiley-Interscience, Chichester, Sussex, England. 33, 53, 156

KANSARA, K. (2004). *Development of Membrane, Plate and Flat Shell Elements in Java*. Master's thesis, Virginia Polytechnic Institute and State University. 17

KARUNASENA, W., LIEW, K.M. & AL-BERMANI, F.G.A. (1996). Natural frequencies of thick arbitrary quadrilateral plates using the pb-2 ritz method. *Journal Sound and Vibration*, **196**, 371 –385. 117, 119

KELLY, D.W. (1979). Reduced integration to give equilibrium models for assessing the accuracy of finite element analysis. In *Proceedings of Third International Conference in Australia on FEM. University of New South Wales*. 30, 53, 178, 180, 181

KELLY, D.W. (1980). Bounds on discretization error by special reduced integration of the Lagrange family of finite elements. *International Journal for Numerical Methods in Engineering*, **15**, 1489–1560. 30, 53, 178, 180

KOSCHNICK, F., BISCHOFF, M., CAMPRUBI, N. & BLETZINGER, K.U. (2005). The discrete strain gap method and membrane locking. *Computer Methods in Applied Mechanics and Engineering*, **194**, 2444–2463. 3

KOUHIA, R. (2007). On stabilized finite element methods for the reissnermindlin plate model. *International Journal for Numerical Methods in Engineering*, DOI: 10.1002/nme.2211, in press. 74, 100

LANCASTER, P. & SALKAUSKAS, K. (1981). Surfaces generated by moving least squares methods. *Mathematics of Computation*, **37**, 141–158. 4

LE, V.C., NGUYEN-XUAN, H. & NGUYEN-DANG, H. (2005). Dual limit analysis of bending plate. In *Third international Conference on advanced computational method in Engineering*, Belgium. 172

LEE, S.W. & PIAN, T.H.H. (1978). Improvement of plate and shell finite element by mixed formulation. *AIAA Journal*, **16**, 29–34. 2, 73, 98

LEE, S.W. & WONG, C. (1982). Mixed formulation finite elements for Mindlin theory plate bending. *International Journal for Numerical Methods in Engineering*, **18**, 1297–1311. 73, 98

LEGAY, A. & COMBESCURE, A. (2003). Elastoplastic stability analysis of shell using physically stabilized finite element SHB8PS. *International Journal for Numerical Methods in Engineering*, **57**, 1299 –1322. 2

LEISSA, A.W. (1969). Vibration of plates. *NASA SP-160*. 95

LI, Z.R., LIM, C.W. & WU, C.C. (2005). Bound theorem and implementation of dual finite elements for fracture assessment of piezoelectric materials. *Computational Mechanics*, **36**, 209–216. 3, 172

LIU, G.R. (2002). *Mesh-free methods: moving beyond the finite element method*. CRC-Press:, BocaRaton. 115, 116

LIU, G.R. & ZHANG, G.Y. (2007). Upper bound solution to elasticity problems: A unique property of the linearly conforming point interpolation method (LC-PIM). *International Journal for Numerical Methods in Engineering*, DOI: 10.1002/nme.2204, in press. 144, 156

LIU, G.R., LI, Y., DAI, K.Y., LUAN, M.T. & XUE, W. (2006a). A linearly conforming radial point interpolation method for solid mechanics problems. *International Journal of Computational Methods*, **3**, 401–428. 5, 144

LIU, G.R., ZHANG, G.Y., DAI, K.Y., WANG, Y.Y., ZHONG, Z.H., LI, G.Y. & HAN, X. (2006b). A linearly conforming point interpolation method (lc-pim) for 2D solid mechanics problems. *International Journal of Computational Methods*, **2**, 645–665. 5, 144

LIU, G.R., DAI, K.Y. & NGUYEN, T.T. (2007a). A smoothed finite element for mechanics problems. *Computational Mechanics*, **39**, 859–877. 5, 19, 20, 21, 22, 26, 27, 30, 32, 74, 75, 78, 98, 102, 144

LIU, G.R., NGUYEN, T.T., DAI, K.Y. & LAM, K.Y. (2007b). Theoretical aspects of the smoothed finite element method (sfem). *International Journal for Numerical Methods in Engineering*, **71**, 902–930. 5, 20, 26, 27, 52, 59, 99, 100

LIU, G.R., NGUYEN, T.T., NGUYEN-XUAN, H. & LAM, K.Y. (2007c). A node-based smoothed finite element method (n-sfem) for upper bound solutions to solid mechanics problems. *Computers and Structures*, Doi:10.1016/j.compstruc.2008.09.003, in press. 5, 7, 144, 145, 146, 147, 171

LYLY, M., STENBERG, R. & VIHINEN, T. (1993). A stable bilinear element for Reissner–Mindlin plate model. *Computer Methods in Applied Mechanics and Engineering*, **110**, 343 –357. 2, 7, 100, 102, 133

MACNEAL, R.H. & HARDER, R.L. (1985). A proposed standard set of problems to test finite element accuracy. *Finite Elements in Analysis and Design*, **1**, 1–20. 61, 130

MALKUS, D.S. & HUGHES, T.J.R. (1978). Mixed finite element methods - Reduced and selective integration technique: a unification of concepts. *Computer Methods in Applied Mechanics and Engineering*, **15**, 63–81. 1, 39

MAUNDER, E.A.W., ALEMEIDA, J.P.M. & RAMSAY, A.C.A. (1996). A general formulation of equilibrium macro-elements with control of spurious kinematic modes. *International Journal for Numerical Methods in Engineering*, **39**, 3175–3194. 3

MELENK, J.M. & BABUŠKA, I. (1996). The partition of unity finite element method: Basic theory and applications. *Computer Methods in Applied Mechanics and Engineering*, **139**, 289–314. 48

MIJUCA, D. & BERKOVIĆ, M. (1998). On the efficiency of the primal-mixed finite element scheme. *Advances in Computational Structured Mechanics*, 61–69, civil-Comp Press. 63, 161

MILITELLO, C. & FELIPPA, C.A. (1990). A variational justification of the assumed natural strain formulation of finite elements i. variational principles II. the C0 four-node plate element. *Computers and Structures*, **34**, 439–444. 3

MOËS, N., DOLBOW, J. & BELYTSCHKO, T. (1999). A finite element method for crack growth without remeshing. *International Journal for Numerical Methods in Engineering*, **46**. 164

MORLEY, L.S.D. (1963). *Skew plates and structures*. Pergamon Press: Oxford. 91

NGUYEN, H.S. (2006). *Contributions for a direct understading of the error estimation and realization of an education finite element software using Matlab*. Ph.D. thesis, LTAS, Faculté des Sciences Appliquées, Université de Liège. 165

NGUYEN, T.D. & NGUYEN-DANG, H. (2006). Regular and singular metis finite element models for delamination in composite laminates. *Finite Elements in Analysis and Design*, **42**, 650–659. 3, 73

NGUYEN, T.N., RABCZUK, T., NGUYEN-XUAN, H. & BORDAS, S. (2007a). A smoothed finite element method for shell analysis. *Computer Methods in Applied Mechanics and Engineering*, Doi: 10.1016/j.cma.2008.05.029, in press. 7, 128

NGUYEN, T.T., LIU, G.R., DAI, K.Y. & LAM, K.Y. (2007b). Selective Smoothed Finite Element Method. *Tsinghua Science and Technology*, **12**, 497–508. 5, 24, 99

NGUYEN-DANG, H. (1970). Displacement and equilibrium methods in matrix analysis of trapezoidal structures. Tech. rep., Collection des Publications de la Faculté des Sciences Appliquées, Université de Liège. 2

NGUYEN-DANG, H. (1979). Sur un classe particulière d'éléments finis hybrides: les éléments métis. In *Proceedings of International Congress on Numerical Methods for Engineering–GAMNI*, Dunod, Paris. 3

NGUYEN-DANG, H. (1980a). Finite element equilibrium analysis of creep using the mean value of the equivalent shear modulus. *Meccanica (AIMETA, Italy)*, **15**, 234–245. 175

NGUYEN-DANG, H. (1980b). On the monotony and the convergence of a special class of hybrid finite element: The Mongrel elements. In *Proceedings of the IUTAM symposium held at Northwestern University, Evanston, Illinois, USA*, Pergamon Press Oxford and New York. 3, 73

NGUYEN-DANG, H. (1985). *Sur la plasticité et le calcul des états limites par éléments finis*. Ph.D. thesis, LTAS, Faculté des Sciences Appliquées, Université de Liège. 2, 175

NGUYEN-DANG, H. & DANG, D.T. (2000). Invariant isoparametric metis displacement element. In *Proceedings of Nha Trang'2000 International Colloquium*, Vietnam. 3

NGUYEN-DANG, H. & DESIR, P. (1977). La performance numérique d'un élément fini hybrid de déplacement pour l'étude des plaques en flexion. Tech. rep., Collection des Publications de la Faculté des Sciences Appliquées, Université de Liège. 2, 3

NGUYEN-DANG, H. & TRAN, T.N. (2004). Analysis of cracked plates and shells using "metis" finite element model. *Finite Elements in Analysis and Design*, **40**, 855–878. 3, 73

NGUYEN-DANG, H., DETROUX, P., FALLA, P. & FONDER, G. (1979). Implementation of the duality in the finite element analysis of shels: mixed-metis planar shell element. In *Proceedings of World Congress on shell and Spatial structures*, Madrid. 127

NGUYEN-DANG, H., DE-SAXCE, G. & CHI-HANG, K. (1991). The computational of 2-d stress intensity factors using hybrid mongrel displacement finite element. *Engineering Fracture Mechanics*, **38**, 197–205. 3

NGUYEN-XUAN, H. & NGUYEN, T.T. (2008). A stabilized smoothed finite element method for free vibration analysis of mindlin–reissner plates. *Communications in Numerical Methods in Engineering*, DOI: 10.1002/cnm.1137, in press. 7, 99, 100, 101

NGUYEN-XUAN, H., BORDAS, S. & NGUYEN-DANG, H. (2006). Smooth strain finite elements: selective integration. In *Collection of Papers from Professor Nguyen-Dang Hungs former students*, Vietnam National University, HCM Publishing House. 6, 24

NGUYEN-XUAN, H., BORDAS, S. & NGUYEN-DANG, H. (2007a). Addressing volumetric locking by selective integration in the smoothed finite element method. *Communications in Numerical Methods in Engineering*, Doi: 10.1002/cnm.1098, in press. 24

NGUYEN-XUAN, H., BORDAS, S. & NGUYEN-DANG, H. (2007b). Smooth finite element methods: Convergence, accuracy and properties. *International Journal for Numerical Methods in Engineering*, DOI: 10.1002/nme.2146, in press. 6, 52, 99

NGUYEN-XUAN, H., BORDAS, S., NGUYEN-VINH, H., DUFLOT, M. & RABCZUK, T. (2008a). A smoothed finite element method for three dimensional elastostatics. *International Journal for Numerical Methods in Engineering*, submitted. 6, 53

NGUYEN-XUAN, H., RABCZUK, T., BORDAS, S. & DEBONGNIE, J.F. (2008b). A smoothed finite element method for plate analysis. *Computer Methods in Applied Mechanics and Engineering*, **197**, 1184–1203. 7, 74, 98, 99, 100, 102, 128

PAULINO, G.H., MENEZES, I.F.M., NETO, J.B.C. & MARTHA, L.F. (1999). A methodology for adaptive finite element analysis: Towards an integrated computational environment. *Computational Mechanics*, **23**, 361–388. 165

PIAN, T.H.H. & SUMIHARA, K. (1984). Rational approach for assumed stress finite elements. *International Journal for Numerical Methods in Engineering*, **20**, 1685–1695. 2, 161

PIAN, T.H.H. & TONG, P. (1969). Basis of finite elements for solids continua. *International Journal for Numerical Methods in Engineering*, **1**, 3–28. 2, 30, 73, 98

PIAN, T.H.H. & WU, C.C. (1988). A rational approach for choosing stress term for hybrid finite element formulations. **26**, 2331–2343. 2

PIAN, T.H.H. & WU, C.C. (2006). *Hybrid and Incompatible finite element methods*. CRC Press, Boca Raton. 3, 149

Puso, M.A. (2000). A highly efficient enhanced assumed strain physically stabilized hexahedral element. *International Journal for Numerical Methods in Engineering*, **49**, 1029–1064. 2

Puso, M.A. & Solberg, J. (2006). A stabilized nodally integrated tetrahedral. *International Journal for Numerical Methods in Engineering*, **67**, 841–867. 58, 154

Puso, M.A., Chen, J.S., Zywicz, E. & Elmer, W. (2007). Meshfree and finite element nodal integration methods. *International Journal for Numerical Methods in Engineering*, DOI: 10.1002/nme.2181, in press. 58

Rabczuk, T. & Belytschko, T. (2007). A three dimensional large deformation meshfree method for arbitrary evolving cracks,. *Computer Methods in Applied Mechanics and Engineering*, **196**, 2777–2799. 4

Rabczuk, T., Areias, P.M.A. & Belytschko, T. (2007a). A meshfree thin shell method for non-linear dynamic fracture. *International Journal for Numerical Methods in Engineering*, **72**, 524–548. 4

Rabczuk, T., Areias, P.M.A. & Belytschko, T. (2007b). A simplified meshfree method for shear bands with cohesive surfaces. *International Journal for Numerical Methods in Engineering*, **69**, 887–1107. 4

Rabczuk, T., Bordas, S. & Zi, G. (2007c). A three-dimensional meshfree method for continuous crack initiation, nucleation and propagation in statics and dynamics. *Computational Mechanics*, **40**, 473–495. 4, 5, 172

Rabczuk, T., Zi, G., Bordas, S. & Nguyen-Xuan, H. (2008). A geometrically nonlinear three dimensional cohesive crack method for reinforced concrete structures. *Engineering Fracture Mechanics*, doi:10.1016/j.engfracmech.2008.06.019, in press. 4, 5, 172

Razzaque, A. (1973). Program for triangular bending elements with derivative smoothing. *International Journal for Numerical Methods in Engineering*, **6**, 333–345. 91, 93

Reese, S. (2005). On a physically stabilized one point finite element formulation for three-dimensional finite elasto-plasticity. *Computer Methods in Applied Mechanics and Engineering*, **194**, 4685–5715. 2

Reese, S. & Wriggers, P. (2000). A stabilization technique to avoid hourglassing in finite elasticity. *International Journal for Numerical Methods in Engineering*, **48**, 79–109. 2

Richardson, L.F. (1910). The approximate arithmetical solution by finite differences of physical problems. *Trans. Roy.Soc. (London) A210*, 307–357. 44, 70

ROBERT, D.B. (1979). Formulas for natural frequency and mode shape. Tech. rep., Van Nostrand Reinhold, New York. 113, 114

SÁ, J.M.A.C.D. & JORGE, R.M.N. (1999). New enhanced strain elements for incompatible problems. *International Journal for Numerical Methods in Engineering*, **44**, 229 – 248. 3

SÁ, J.M.A.C.D., JORGE, R.M.N., VALENTE, R.A.F. & AREIAS, P.M.A. (2002). Development of shear locking-free shell elements using an enhanced assumed strain formulation. *International Journal for Numerical Methods in Engineering*, **53**, 1721–1750. 3, 127

SANDER, G. (1969). *Applications de la méthod des éléments finis à la flexion des plaques*. Ph.D. thesis, LTAS, Faculté des Sciences Appliquées, Université de Liège. 73

SAUER, R. (1998). *Eine einheitliche Finite-Element-Formulierung fur Stab-und Schalentragwerke mit endlichen Rotationen, Bericht 4 (1998)*. Institut fur Baustatik, Universitat Karlsruhe (TH). 137

SCORDELIS, A.C. & LO, K.S. (1964). Computer analysis of cylindracal shells. *Journal of the American Concrete Institute*, **61**, 539–561. 130

SIMO, J.C. & HUGHES, T.J.R. (1986). On the variational foundation of assumed strain methods. *ASME Journal of Applied Mechanics*, **53**, 51–54. 3, 19, 21, 25, 100

SIMO, J.C. & RIFAI, M.S. (1990). A class of mixed assumed strain methods and the method of incompatible modes. *International Journal for Numerical Methods in Engineering*, **29**, 1595 – 1638. 3, 19, 25, 74, 98

SIMO, J.C., FOX, D.D. & RIFAI, M.S. (1989). On a stress resultant geometrically exact shell model. part ii: The linear theory; computational aspects. *Computer Methods in Applied Mechanics and Engineering*, **73**, 53–92. 130

STOLLE, D.F.E. & SMITH, W.S. (2004). Average strain strategy for finite elements. *Finite Elements in Analysis and Design*, **40**, 20112024. 6, 53, 72

SUKUMAR, N., MORAN, B. & BELYTSCHKO, T. (1998). The natural element method in solid mechanics. *International Journal for Numerical Methods in Engineering*, **43**, 839–887. 4, 39

SZE, K. (2000). On immunizing five-beta hybrid-stress element models from trapezoidal locking in practical analyses. *International Journal for Numerical Methods in Engineering*, **47**, 907–920. 2

SZE, K.Y., CHEN, J.S., SHENG, N. & LIU, X.H. (2004). Stabilized conforming nodal integration: exactness and variational justification. *Finite Elements in Analysis and Design*, **41**, 147–171. 4

TAYLOR, R.L. (1988). *Finite element analysis of linear shell problems, in: J.R. Whiteman (Ed.), The Mathematics of Finite Elements and Applications VI (MAFELAP 1987).* Academic Press, London. 137

TAYLOR, R.L. & AURICCHIO, F. (1993). Linked interpolation for Reissner–Mindlin plate elements. Part I-a simple triangle. *International Journal for Numerical Methods in Engineering*, **36**, 3056–3066. 82

TAYLOR, R.L. & KASPERM, E.P. (2000). A mixed-enhanced strain method. *Computers and Structures*, **75**, 237–250. 133

TAYLOR, R.L., BERESFORD, P.J. & WILSON, E.L. (1976). A non-conforming element for stress analysis. *International Journal for Numerical Methods in Engineering*, **10**, 1211–1219. 3

THOMPSON, L.L. (2003). On optimal stabilized MITC4 plate bending elements for accurate frequency response analysis. *Computers and Structures*, **81**, 995–1008. 13

TIMOSHENKO, S.P. & GOODIER, J.N. (1987). *Theory of Elasticity (3rd edn)*. McGraw-Hill, New York. 31, 39, 154, 156

TURNER, M.J., CLOUGH, R.W., MARTIN, H.C. & TOPP, L.J. (1956). Stiffness and deflection analysis of complex structures. *Journal of Aeronautical Sciences*, **23**, 805–823. 1

WANG, D. & CHEN, J.S. (2004). Locking -free stabilized conforming nodal integration for meshfree Mindlin-Reissner plate formulation. *Computer Methods in Applied Mechanics and Engineering*, **193**, 1065–1083. 74

WANG, D. & CHEN, J.S. (2007). A hermite reproducing kernel approximation for thin-plate analysis with sub-domain stabilized conforming integration. *International Journal for Numerical Methods in Engineering*, DOI: 10.1002/nme.2175, in press. 5

WASHIZU, K. (1982). *Variational Methods in Elasticity and Plasticity(3rd edn)*. Pergamon Press:, New York. 1, 24, 100

WEISSMAN, S.L. & TAYLOR, R.L. (1990). Resultant fields for mixed plate bending elements. *Computer Methods in Applied Mechanics and Engineering*, **79**, 321–355. 76

WU, C.C. & CHEUNG, Y.K. (1995). On optimization approaches of hybrid stress elements. *Finite Elements in Analysis and Design*, **21**, 111–128. 2

WU, C.C. & XIAO, Q.Z. (2005). Electro-mechanical crack systems: bound theorems, dual finite elements and error estimation. *International Journal of Solids and Structures*, **42**, 5413–5425. 3, 172

WU, C.C., XIAO, Q.Z. & YAGAWA, G. (1998). Finite element methodology for path integrals in fracture mechanics. *International Journal for Numerical Methods in Engineering*, **43**, 69–91. 2, 172

WU, S., LI, G. & BELYTSCHKO, T. (2005). A dkt shell element for dynamic large deformation analysis. *Communications in Numerical Methods in Engineering*, **21**, 651–674. 127

WYART, E., COULON, D., DUFLOT, M., PARDOEN, T., REMACLE, J. & LANI, F. (2007). A substructured fe-shell/xfe 3d method for crack analysis in thin-walled structures. *International Journal for Numerical Methods in Engineering*, **72**, 757 – 779. 172

XIANG, Y. (2003). Vibration of rectangular Mindlin plates resting on non-homogenous elastic foundation. *International Journal of Mechanical sciences*, **45**, 1229–1244. 121

XIE, X. (2005). An accurate hybrid macro-element with linear displacements. *Communications in Numerical Methods in Engineering*, **21**, 1–12. 161

XIE, X. & ZHOU, T. (2004). Optimization of stress modes by energy compatibility for 4-node hybrid quadrilaterals. *International Journal for Numerical Methods in Engineering*, **59**, 293–313. 161

YEO, S.T. & LEE, B.C. (1996). Equivalence between enhanced assumed strain method and assumed stress hybrid method based on the Hellinger –Reissner principle. *International Journal for Numerical Methods in Engineering*, **39**, 3083 – 3099. 3

YOO, J.W., MORAN, B. & CHEN, J.S. (2004). Stabilized conforming nodal integration in the natural-element method. *International Journal for Numerical Methods in Engineering*, **60**, 861–890. 4, 5, 18, 21, 144

YVONNET, J., RYCKELYNCK, D., LORONG, P. & CHINESTA, F. (2004). A new extension of the natural element method for non convex and discontinuous domains: the constrained natural element method (c-nem). *International Journal for Numerical Methods in Engineering*, **60**, 1451–1474. 4, 5, 144

ZHANG, G.Y., LIU, G.R., WANG, Y.Y., HUANG, H.T., ZHONG, Z.H., LI, G.Y. & HAN, X. (2007). A linearly conforming point interpolation method (lc-pim) for three-dimensional elasticity problems. *International Journal for Numerical Methods in Engineering*, **72**, 1524 – 1543. 5, 144

ZHANG, Y.X., CHEUNG, Y.K., & CHEN, W.J. (2000). Two refined non-conforming quadrilateral at shell elements. *International Journal for Numerical Methods in Engineering*, **49**, 355–382. 127

ZHOU, T. & NIE, Y. (2001). A combined hybrid approach to finite element schemes of high performance. *International Journal for Numerical Methods in Engineering*, **51**, 181–202. 161

ZHU, Y. & CESCOTTO, S. (1996). Unified and mixed formulation of the 8-node hexahedral elements by assumed strain method. *Computer Methods in Applied Mechanics and Engineering*, **129**, 177–209. 2

ZIENKIEWICZ, O.C. & TAYLOR, R.L. (2000). *The Finite Element Method*. 5th Edition, Butterworth Heinemann, Oxford. 1, 3, 13, 14, 15, 17, 52, 74, 98, 128

ZIENKIEWICZ, O.C., TAYLOR, R.L. & TOO, J.M. (1971). Reduced intgration technique in general analysis of plates and shells. *International Journal for Numerical Methods in Engineering*, **3**, 275–290. 1, 73, 98